Technische Universität München – TUM School of Engineering and Design

Arlequin – coupling of 2-D peridynamic finite elements with an analytical Jacobian matrix

Moritz Becker M.Sc.

Lehrstuhl für Baumechanik
Technische Universität München

Arlequin - coupling of 2-D peridynamic finite elements with an analytical Jacobian matrix

Abstract

This thesis covers the solution of the 2-D bond-based peridynamic equations with finite elements for an integer ratio of peridynamic horizon and element length. The peridynamic integral is split into three sets of elements, which are solved by different quadrature techniques using midpoint rule, gaussian quadrature and subelementation with both Duffy transformation and tanh-sinh quadrature. The effect of quadrature technique, integral discretization, meshgrid density and load applications are studied in detail. Furthermore, an analytical Jacobian matrix for large deformations is derived and compared to a result from literature. The 2-D peridynamic elements are coupled with linear plane stress finite elements from classical continuum mechanics using the Arlequin method and solved with Newton's method. Furthermore, a coupling of 1-D peridynamic finite elements with an analytical solution for a harmonic excitation using Arlequin method is presented. A failure mechanism for brittle materials is implemented and compared to results from an extended finite element method with hybrid explicit-implicit crack description from literature.

Keywords:

- Peridynamics

- Finite elements

- Arlequin method

- Duffy transformation

Acknowledgements

This thesis was formed during my work as research assistant at the Chair of Structural Mechanics at Technical University of Munich between 2014 and 2020.

I owe my deep gratitude to Professor Dr. -Ing. Gerhard Müller, who gave me the opportunity to work at his chair for the last six years in a highly professional, yet fair and comfortable environment. Thank you, Professor Müller, for giving me the lecture in continuum mechanics and the scientific freedom to work on a topic I really loved.

I would like to give my sincere thanks to Professor Dr. Erkan Oterkus not just for being my second examiner, but also for supporting me superbly during the last two and a half years. I would also like to thank Professor Dr. Selda Oterkus and the team of the Peridynamic Research Center at Strathclyde University in Glasgow for the wonderful, productive research stay there.

I am very grateful to Professor Dr. -Ing. Fabian Duddeck for kindly agreeing to be chair of the examination board.

I have to thank Dr. -Ing. Martin Buchschmid, for bringing me to the chair and teaching ITM. You were an excellent teacher and an exemplary superior, but an even better friend. Martin, I'm here because of you. Thank you so much.

My deepest gratitude goes to my parents, Ruth and Gunter, to my sister Sophia, and to my uncle Gernot. I am aware of the wonderful gift of unconditional love you gave me all my life long.

My deep gratitude goes to Hannes Englert, with whom I shared the office. Often, you've explained to me what I failed to understand.

Thank you, Assistant Professor Michael Gfrerer, for the friendship with you since we have been students, and for aiding me in months of non-convergence.

My deepest thanks to Isabelle Haag, for your love and support during the difficult times of the thesis.

Thank you, Corinna Treimer, because you made a bad day good and a good day great.

Thank you, Karen Arlt, Christoph Winter, Manuela Hackenberg, Christian Weineisen, Mathias Kohrmann, Franziska Weber, Quirin Auman, Felix Schneider, Julian Freisinger, Matthias Miksch, Francesca Taddei, Raul Rodriguez Sanchez, Axel Greim, Mirjam Lainer and Aditi Kumawat. You were the best colleagues I could have wished for.

Thanks to all my friends and the countless persons who were at my side. It's due to all your combined support that led me to this point in my life.

Danke für Alles. Für Immer...

Contents

List of symbols

Greek letters

Γ_{2_t}	Boundary with force condition of classical continuum mechanics domain
Γ_{2_u}	Boundary with displacement condition of classical continuum mechanics domain
δ	Peridynamic horizon
$\delta\boldsymbol{\mu}, \delta\mu^j$	(Virtual) test Lagrange multipliers
$\delta\mathbf{v}, \delta v^j$	(Virtual) test function
$\delta\mathbf{v}^h$	Approximation of $\delta\mathbf{v}$
$\delta\bar{\mathbf{v}}$	Virtual nodal displacements
$\delta\mathbf{w}, \delta w^j$	(Virtual) test function fulfilling homogenous displacement boundary conditions
δW	Total virtual work
δW_{int}	Virtual work of internal forces
δW_{ext}	Virtual work of external forces
ϵ	Error
ϵ_{relax}	Termination threshold of adaptive dynamic relaxation
$\boldsymbol{\epsilon}, \epsilon^{ij}$	Infinitesimal strain tensor
ζ	Auxiliary parameter
$\boldsymbol{\eta}$	Difference of displacement vectors
θ	1-D approach functions
κ_1, κ_2	Coupling weighting factors
$\boldsymbol{\lambda}, \lambda^j$	Lagrange multipliers
ν	Poisson ratio
Π_{int}	Strain energy
Π_{ext}	Potential energy of external forces
Π	Total potential energy in the system
ρ^0	Material density in undeformed configuration
$\boldsymbol{\sigma}, \sigma^{ij}$	Cauchy stress tensor

$\boldsymbol{\varphi}$	Deformation map
ω_0^n	Smallest eigenfrequency in timestep n in adaptive dynamic relaxation
Ω^0	Continuum domain in the reference configuration
Ω	Continuum domain in the deformed configuration
Ω_{in}	Inner peridynamic domain
Ω_{out}	Outer peridynamic domain
Ω_c	Constrained peridynamic domain
Ω_b	Loaded peridynamic domain
$\Omega_{1_{in}}$	Inner peridynamic domain (coupled)
$\Omega_{1_{out}}$	Outer peridynamic domain (coupled)
Ω_{1_c}	Constrained peridynamic domain (coupled)
Ω_{1_b}	Loaded peridynamic domain (coupled)
Ω_2	Classical continuum mechanics domain domain
Ω_E	Domain of a finite element
Ω_e	Angular excitation frequency

Latin letters

A	Cross section of rod
$\mathbf{b}, b^j$	Vector of peridynamic external force density
c	Microelastic stiffness constant (bond constant)
c_P	Phase velocity
c_d	Damping coefficient
$[C]$	Coupling matrix
C	Coupling operator
d	Surface correction factor
$da_{\mathbf{x}}$	differential area element in deformed configuration integrating field $\mathbf{x}$
$dA_{\mathbf{X}}$	differential area element in undeformed configuration integrating field $\mathbf{X}$
$D_{\mathbf{x}}$	Family of $\mathbf{x}$ in the deformed configuration
$D_{\mathbf{X}}$	Family of $\mathbf{X}$ in the reference configuration
$[D], D_{ii}$	Diagonal density matrix
$\mathbf{d}$	Direction of a deformed bond
E	Elastic modulus
$\mathbf{e}_{i0}$	Covariant cartesian base vector
eps	Machine precision
$\mathbf{f}_{int}$	Bond force

$\mathbf{g}_i$	Covariant skew angled base vector
G_c	Critical energy release rate
h	Spacing between support points in the tanh-sinh - transformed domain
h_{min}	Shortest meshgrid length
$\mathbf{H}^1$	Hilbert space
$[J]$	Jacobian matrix
$[J]_{an}$	Analytically derived Jacobian matrix
$[J]_{num}$	Numerically derived Jacobian matrix
$[K]_{CCM}$	Stiffness matrix of CCM-system
$[K]_{loc}$	"Local" stiffness matrix in adaptive dynamic relaxation
$\mathbf{L}^2$	Vector space of square integrable functions
l_1	Length of peridynamic beam / rod
l_2	Length of CCM beam / rod
l_G	Length of gluing region
l_{tot}	Combined length of peridynamic- and CCM-beam
$\mathbf{L}$	Undeformed bond
L	Length of undeformed bond
$\mathcal{L}$	Lagrangian
$\mathbf{l}$	Deformed bond
l	Length of deformed bond
$[M]$	Master matrix
M	Number of nodes in a yet unspecified finite element meshgrid
M_1	Number of nodes in the inner peridynamic domain $\Omega_{1_{in}}$
M_2	Number of nodes in the inner CCM domain Ω_2
M_G	Number of nodes in gluing region S_G
$\bar{N}$	2-D approach function on global level
N	2-D approach function on local level
N_{cut}	Number of quadrature points in each direction of cut element
N_{inc}	Number of load increments during adaptive dynamic relaxation
N_{middle}	Number of quadrature points in each direction of middle-subelement
N_{parent}	Number of parent Gauss points in each direction
N_{uncut}	Number of Gauss points in each direction of uncut element
p	Number of time steps between bond removal
$P_{(n)}$	Legendre polynomial of order n
P	Single load
$\mathbf{p}, p^j$	Volume loads of classical continuum mechanics

$\mathbf{r}$	Resulting force of a peridynamic family
$\mathbf{R}_k$	Residual of node k
$\mathbf{R}_{k_{int}}, R^j_{k_{int}}$	Contribution of inner forces to $\mathbf{R}_k$
s	Bond stretch
s_{max}	Maximal bond stretch
S_G	Gluing region
t	Time coordinate
$\mathbf{t}, t^j$	Traction vector
$\bar{\mathbf{t}}, \bar{t}^j$	(Neumann) force boundary condition on Γ_{2_t}
$\tilde{\mathbf{u}}, \tilde{u}^j$	Displacement on Ω_c
$\mathbf{u}, u^j$	Displacement vector
$\mathbf{u_X}$	Displacement vector of material point $\mathbf{X}$
$\mathbf{u_Y}$	Displacement vector of material point $\mathbf{Y}$
$\mathbf{u}^h$	Approximation of $\mathbf{u}$
$\bar{\mathbf{u}}$	Nodal displacements
u_0	Start point displacement of analytical CCM domain
$\mathcal{U}_1$	Function space of solutions of peridynamic continuum
$\mathcal{U}_2$	Function space of solutions of classical continuum
$\mathcal{U}_g$	Function space of Lagrange multipliers
$\mathcal{U}_1^h$	Function space of approach functions of peridynamic solution
$\mathcal{U}_2^h$	Function space of approach functions of classical continuum mechanics solution
$\mathcal{U}_g^h$	Function space of approach functions of Lagrange multipliers
V	Vector space
$\mathcal{V}_1^h$	Test space of approach functions of peridynamic solution
$\mathcal{V}_2^h$	Test space of approach functions of classical continuum mechanics solution
$\mathcal{V}_g^h$	Test space of approach functions of Lagrange multipliers
$\mathcal{V}_1$	Function space of test functions of peridynamic continuum
$\mathcal{V}_2$	Function space of test functions of CCM continuum
$\mathcal{V}_g$	Function space of test functions of Lagrange multipliers
w	Micropotential
w_c	Critical strain energy density of bond
W	Strain energy density
W_{CCM}	Strain energy density of classical continuum
$\mathbf{W}^{1,2}$	Sobolev space of 1st weak derivative and $\mathbf{L}^2$ - norm

$\mathbf{x}, x^j$	Position vector of a point in Ω
$\mathbf{X}, X^j$	Position vector of a point in Ω^0 in the reference configuration
$\tilde{\mathbf{X}}, \tilde{X}^1, \tilde{X}^2$	Transformed coordinate
X_2	Position vector of 1-D CCM domain
X_P	X-coordinate of application of load P
$\mathbf{y}, y^j$	Position vector of a member of $D_\mathbf{x}$ in the deformed configuration
$\mathbf{Y}, Y^j$	Position vector of a member of $D_\mathbf{x}$ in the reference configuration

Mathematical symbols

$\mathbf{a} \cdot \mathbf{b} \mathrel{\hat{=}} a^j b_j$	Scalar product
$\mathbf{S} : \mathbf{E} \mathrel{\hat{=}} S^{ij} E_{ij}$	Double tensor contraction
$< \cdot, \cdot >$	Inner product
$\lVert \cdot \rVert_V$	Norm of vector space V
$\lvert \cdot \rvert$	Absolute value of argument
$[\cdot]$	Matrix
$\mathrm{Im}(a)$	Imaginary part of the complex number a
sgn	sign-function
$\mathbf{0}$	Zero vector
$[0]$	Zero matrix

Abbreviations

app	appendix
approx	approximately
CCM	Classical Continuum Mechanics
CFL	Courant-Friedrichs-Lewy
comp	compare
DAE	Differential Algebraic Equation
dof	degree of freedom
eq	equation
FEM	Finite Element Method
fig	figure
Gp	Gauss point
GL	Gaus-Legendre
iff	if and only if

LEFM   Linear elastic fracture mechanics
nl   nonlinear
PD   Peridynamics
w.r.t   with respect to
XFEM   Extended Finite Element Method
1-D/2-D   one/two-dimensional

1 Introduction

1.1 Motivation

Peridynamics was developed as a remedy for some of the shortcomings of classical continuum mechanics (CCM). The core of classical continuum mechanics is a set of three partial differential equations, providing displacement fields as solutions. Despite their applicability to large deformations and nonlinear stress-strain relations, being the solution of differential equations poses severe restrictions on the desired displacement field, because the solution needs to be continuous in order to be differentiable at all. Therefore, classical continuum mechanics is not seemlessly applicable to problems involving changes in topology like crack nucleation and propagation. Although the continuum domain may contain cavities or free surfaces, stresses at the tips of those surfaces can get unbound [Gerstle 2015, p.116] in terms of classical continuum mechanics. Linear elastic fracture mechanics (LEFM) and concepts like stress intensity factors or critical energy release rates provide solutions to fracture of very brittle materials, assuming that the fracture process zone, where the solutions become singular, is small enough to be negligible. Nonlinear fracture mechanics or nonlocal damage mechanics provide remedies for cases where the LEFM is not applicable any more. Still, in all fracture- and damage models, the crack needs to be represented by a pair of matching surfaces in the bulk of the continuum [Gerstle 2015, p.119], and a model must be introduced to localize the crack tip in case of crack propagation. Thus, fracture mechanics is not intrinsic to CCM.

Peridynamics was proposed in 1999 by Dr. Steward A. Silling in order to overcome CCM's limitations by an intrinsic damage capability. It combines concepts from molecular dynamics and classical continuum mechanics by keeping a continuum, but introducing an internal length scale called horizon. Material points within horizon-distance have an influence on each other through force densities. Unlike to CCM, the horizon around a material point does not vanish, and the force state in any material point is the integral of all force densities within horizon-reach. The results are three integro-differential equations for three dimensions, but without any spatial derivatives. Classical continuum mechanics is a special case of

Peridynamics, as the CCM – equation of motion is the Peridynamic one for the limit of the horizon tending to zero. In Peridynamics, the differential quotients remain quotients of the displacement fields, and thus are not restricted to continuity or differentiability. Damage and cracks are part of the model by definition, because the forces between two material points can be deleted if a damage criterion is met.

The model chosen for the force density between two material points defines the kind of peridynamic theory. The most simple case, called "bond-based" and used in the scope of this thesis, defines the forces acting between two points being equal in magnitude and collinear to the difference of their location vectors in the deformed state [Gerstle 2015, p.153]. In the second ("state-based") model, forces are still acting opposite and in line to each other, but are not equal in magnitude any more. The "non-ordinary state-based" model permits the force densities to be both unequal in magnitude and direction. State-based Peridynamics was developed because bond-based Peridynamics is restricted to one poisson ratio only and cannot distinguish between volumetric and distortional deformation [Madenci and Oterkus 2014, p.37]. Except for one-dimensional (1-D) problems, the resulting equations are nonlinear in terms of the displacement field.

As no analytical solutions for Peridynamics are known in general, numerical solutions are applied for both spatial- and time integration. In most cases, a collocation method of a meshless scheme is used for spatial integration, dividing the domain in a finite number of subdomains with associated collocation points and volumes [Madenci and Oterkus 2014, p.125], although solutions with Bubnov- and Petrov-Galerkin methods (finite elements) were proposed as well. Time integration is performed usually by finite difference explicit integration schemes or multistep methods [Madenci and Oterkus 2014, p.125].

In general, solving the peridynamic equations is computationally more expensive than classical continuum mechanics equations, regardless of the numerical solution technique. Minding that Peridynamics can play it's strength in areas of crack nucleation and propagation, whereas a CCM-model with finite element solution or even an analytical solution is superior in terms of computational effort, a connection between both models is desirable. Propositions for coupling between Peridynamics and CCM-FEM include among others the morphing method, the use of blending functions and the Arlequin method [Bobaru et al 2016, p.407-431]. In the scope of this thesis, finite elements for the solution of the peridynamic equations are chosen. Furthermore, a coupling with finite element solutions of linear elastic classical continuum mechanics and an implementation of a crack propagation mechanism into the peridynamic elements are presented.

1.2 State of knowledge

This section is restricted to a review over finite element solutions of Peridynamics and some aspects of the Arlequin method, because a solution of the peridynamic equations can be achieved in many different ways and the Arlequin method is applied to a broad range of problems. A good overview over Peridynamics in general at the state of 2014 can be found in [Madenci and Oterkus 2014, p.8-13] and in [Bobaru et al 2016] at the state of 2016.

1.2.1 Peridynamic finite elements

[Chen and Gunzburger 2011] applied continuous- and discontinuous Galerkin finite element methods to one-dimensional peridynamic rods with continuous displacement fields and displacement fields with jump discontinuities. Their finite element approximations consist of continuous linear piecewise approach functions, discontinuous constant- and discontinuous linear approach functions and are compared to analytical solutions.

[Wang and Tian 2012] developed a fast solution for a 1-D peridynamic Galerkin approximation exploiting the structure of the stiffness matrix. Furthermore, the entries of the stiffness matrix were evaluated analytically in contrast to [Chen and Gunzburger 2011], who applied Gauss-Legendre (GL) quadrature.

[Littlewood et al 2014] developed the prototype of a partial stress formulation in order to couple a CCM finite element solution with a meshfree peridynamic domain by a finite element solution of Peridynamics and applied it to a linear patch test. The partial stress incorporated into the coupling elements was derived by the divergence operator yielding stress in the CCM-sense and can be applied to a meshless approach of Peridynamics too. Furthermore, their partial stress approach is able to suppress numerical artifacts in the transition zone between the nonlocal- and local model.

[Glaws 2014] developed finite elements by a Bubnov-Galerkin approach for two-dimensional (2-D) bond-based peridynamic problems. Triangular elements with linear approach functions were chosen. The solution of the equation of motion was done with Newton's method, whose Jacobian matrix was obtained numerically from forward finite differences. The ratio between element- and horizon length in [Glaws 2014] was arbitrary, necessitating a subelementation with additional triangular subelements. Moreover, a special integral kernel of the weak form was chosen.

[Huang et al 2019] developed a peridynamic stiffness matrix. The meshgrid nodes represent peridynamic material points and are hereby center of the peridynamic families, which extend over the elements within an integer-valued horizon - element ratio. The integration of the elements within the horizon is done with the same formula for every element. Truncation of elements by the horzion is covered by a volume correction coefficient. Furthermore, the authors developed a direct coupling with a classical continuum-mechanics meshgrid by adding the respective stiffness matrix entries. Nodes of classical continuum mechanics elements are incorporated into the peridynamic families as well. The elements are applied afterwards to various numerical experiments involving fracture of domains with- and without spherical cutouts.

[Dong et al 2020] proposed a similar element like [Huang et al 2019], but for a non-ordinary state based peridynamic model. Furthermore, an improved hourglass method was introduced into the element to restrain the instability due to the zero-energy modes. The authors applied a direct coupling between Peridynamics and CCM as well, introducing a two-step interface correction method in order to improve the accuracy at the interface between the domains.

[Bode et al 2020] proposed a peridynamic Petrov-Galerkin method in order to mitigate low-frequency oscillations in a meshfree peridynamic approach. According to the authors, these oscillations occur because the peridynamic equivalent to the deformation gradient, the deformation state, cannot be retrieved sufficiently enough from the locally averaged deformation gradient, when a peridynamic material is calibrated on a CCM-material. Instead, a deformation gradient for each individual bond is proposed, allowing a more exact resolution of the deformation of each peridynamic family. This can be done by a Petrov-Galerkin approach, allowing different functions for displacement- and test fields of a finite element. Furthermore, the authors derive an analytical stiffness matrix from this approach.

1.2.2 Arlequin method

[Dhia 1998] proposed the Arlequin method as a volume coupling for various mechanical- and multiscale problems. A gluing zone is defined, where both models coexist, but are weighted. Coupling is enforced by introduction of a Lagrange multiplier field acting on the displacements of both models, which contributes to the total virtual work. Two different coupling operators, L^2- and H^1-coupling, are proposed, based on the scalar product between the space of approach functions and it's dual. Different to a surface coupling, the non-vanishing

volume of the gluing region is suitable to include the nonlocal peridynamic model.

[Guidault and Belytschko 2007] compare L^2- and H^1-coupling for overlapping domains with different discretizations. It is figured out that the weight functions for L^2-coupling have to be continuous, whereas H^1-coupling can cope with both continuous- and discontinuous weight functions. In case of different mesh densities, it was figured out that the Lagrange multiplier field for L^2-coupling must not be finer than the coarser meshgrid.

[Dhia 2008] gives further insight into the Arlequin method and provides criteria for the stability and consistency of the Arlequin framework.

[Fernier et al 2017] covers explicit time integration w.r.t. the Arlequin framework, resulting in a differential algebraic system. The influence of the Arlequin weights on the critical timestep is investigated and a remedy is proposed.

1.3 Outline of the thesis

This thesis pursues four aims:

1. Integration of the peridynamic equation of motion in the deformed configuration with finite elements on a subdivision of the integrand into middle-, uncut- and cut finite elements.

2. Development of an analytical Jacobian matrix for two dimensional peridynamic finite elements in order to use Newton's method.

3. Investigation of a coupling between peridynamic- and classical continuum mechanics (CCM) elements using the Arlequin method.

4. Incorporation of a damage model into the developed peridynamic finite elements in order to capture quasi-static crack propagation.

Chapter 2 derives the equation of motion of the bond-based peridynamics model. In chapter 3, a transformation from the deformed- to the undeformed configuration and the weak form of the 2-D peristatic equation of motion is presented. Afterwards, the weak form is discretized with two dimensional quadrilateral elements with linear approach functions. The following computation of the nodal forces necessitates a distinction between middle-, uncut- and cut finite elements in order to reduce truncation- and quadrature errors. The different

numerical integration approaches on those elements are presented. As the resulting equations are nonlinear, both Newton's method and adaptive dynamic relaxation are used. The application of Newton's method necessitates the Jacobian matrix of the discretized equations of motion w.r.t. the nodal degrees of freedom. It's derivation is explained in detail and compared with a numerical Jacobian obtained from complex step derivative. Furthermore, the structure of the Jacobian matrix in this thesis is compared to a different approach from literature. Afterwards, 1-D peridynamic finite elements are presented. Chapter 3 closes with a presentation of the surface correction factor, a damage model for quasi-static crack propagation in brittle materials and the modelling of boundary conditions for peridynamic finite elements with fixed horizon-element ratio.

Chapter 4 presents a coupling between peridynamic- and CCM finite elements. The Arlequin method was chosen, because it provides a volume coupling suitable for nonlocal Peridynamics based on Lagrange multipliers. Both L^2- and H^1- coupling are described in detail and the coupling matrices are derived from a scalar product of the Sobolev space of the approach functions.

Chapter 5 contains numerical simulations and is split into three sections. The first one compares the results for a peridynamic cantilever beam with analytical Jacobian matrix with results from literature. Afterwards, the effects of mesh refinement and discretization are investigated. Two different load types on the cantilever beam are tested and a mechanical explanation of the results is given. The section closes with the application of the elements on a large-deflection example. The second section incorporates the investigation of the coupling. Both L^2- and H^1- coupling are tested on a cantilever beam with different discretizations and coupling lengths. Furthermore, a dynamic coupling of 1-D peridynamic finite elements and an analytical solution is presented. The third section tests the damage capability of the elements. The crack paths obtained from Peridynamics are compared with results from an extended finite element method (XFEM) with hybrid explicit-implicit crack description on a square plate with a predefined crack and a three-point bending example.

Chapter 6 provides a summary and gives an outlook on further ideas, which could not be pursued in the scope of this thesis.

The appendix provides additional information to some of the used mathematical methods like complex step derivative, tanh-sinh numerical quadrature and Gauss-Legrendre quadrature, some foundations of the Arlequin method and a brief investigation of the effect of the discretization of the inner peridynamic integral.

2 Theory of Peridynamics

The aim of this chapter is to provide the bond-based peridynamic equation of motion. Prerequisites are a definition of kinematics, the deformation, and the strain energy in the peridynamic sense. Furthermore, a linear-elastic peridynamic material is introduced, together with the calibration of it's parameter by the correspondence with a linear elastic material in the classical sense. Furthermore, the limitation to one material parameter and the resulting coupling between volumetric and distortional deformation is shown. The formalism is developed under the following guideline: No spatial derivatives of the displacement field shall be necessary. Please note: In the following, base vectors are usually denoted covariant, coordinates contravariant. All derivations are done for 2-D problems, assuming that the thickness of the material bodies in X^3-direction remains constant.

2.1 Introduction

The peridynamic continuum consists of infinitely many material points [Madenci and Oterkus 2014, p.19]. In the undeformed configuration, any material point occupies a position in space $\mathbf{X}$. The position vectors of the undeformed configuration are defined w.r.t. a fixed cartesian coordinate system; their coordinates (X^1, X^2) are denoted by capital letters. If the system
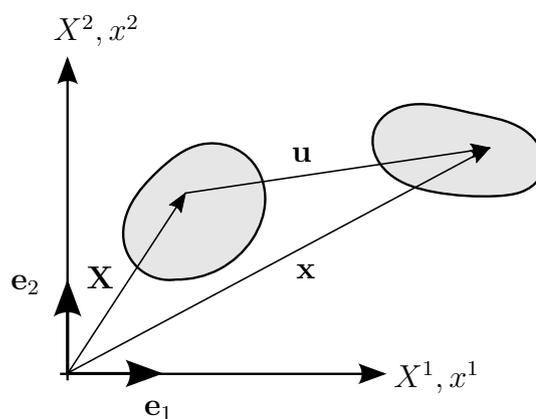

Figure 2.1: Configurations

undergoes deformation, the material points are mapped to the deformed configuration. Posi-

tion vectors in the deformed configuration $\mathbf{x}$ are defined w.r.t. a second cartesian coordinate system, which is located by convenience in the same position as the reference coordinate system. Coordinates of deformed-configuration position vectors are denoted by small letters (x^1, x^2). Undeformed and deformed position vectors $\mathbf{X}$ and $\mathbf{x}$ differ by a displacement vector $\mathbf{u}$ [Parisch 2003, p.61].

$$\mathbf{x} = \mathbf{X} + \mathbf{u} \tag{2.1}$$

Although $\mathbf{X}$ and $\mathbf{x}$ are both defined w.r.t. fixed cartesian coordinate systems, i.e. described w.r.t. the same base vectors, their coordinates are functions of each other.

$$\mathbf{x} = \boldsymbol{\varphi}(\mathbf{X}) \ , \quad x^i = \varphi^i(X^J) \ , \quad \text{e.g.} \ \ x^1 = \varphi^1(X^1, X^2, X^3) \tag{2.2}$$

$\boldsymbol{\varphi}$ denotes the deformation map. As $\boldsymbol{\varphi}$ is a function of the material coordinates X^J, it is a Lagrangian description of motion [Parisch 2003, p.62].

2.2 Bond - based Peridynamics

In Peridynamics, a material point $\mathbf{X}$ is able to interact with all material points $\mathbf{Y}$ within a finite vicinity called family $D_{\mathbf{X}}$ [Madenci and Oterkus 2014, p.19]. In two dimensions, the familiy $D_{\mathbf{X}}$ is a circle centered in $\mathbf{X}$ with radius δ called "horizon". The influence of material points on $\mathbf{X}$ beyond δ is assumed to vanish.

Connections between $\mathbf{X}$ and $\mathbf{Y}$ are called "bonds" $\mathbf{L}$. In the undeformed configuration, the
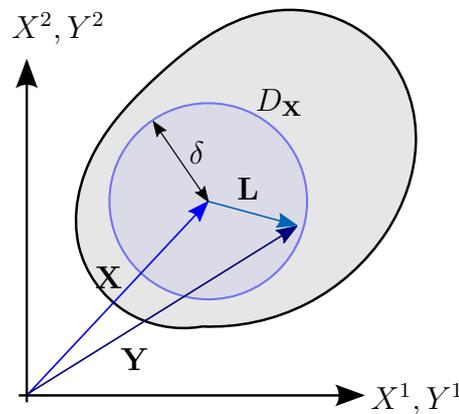

Figure 2.2: Horizon, family and undeformed bond

length of the bond L is obtained from the difference of the respective position vectors:

$$\mathbf{L} = \mathbf{Y} - \mathbf{X}$$
$$L = |\mathbf{Y} - \mathbf{X}|$$

(2.3)

Together with equation 2.1, a deformed bond $\mathbf{l}$ is defined as:

$$\mathbf{l} = \mathbf{y} - \mathbf{x} = \mathbf{Y} + \mathbf{u}_Y - \mathbf{X} - \mathbf{u}_X$$
$$l = |\mathbf{y} - \mathbf{x}| = |\mathbf{Y} + \mathbf{u}_Y - \mathbf{X} - \mathbf{u}_X|$$

(2.4)

For a later use, according to [Silling 2000, p.177], the difference of displacement vectors is defined as:

$$\boldsymbol{\eta} = \mathbf{u}_\mathbf{Y} - \mathbf{u}_\mathbf{X}$$

(2.5)

The stretch of a bond is defined as:

$$s = \frac{l - L}{L} = \frac{|\mathbf{Y} + \mathbf{u}_Y - \mathbf{X} - \mathbf{u}_X| - |\mathbf{Y} - \mathbf{X}|}{|\mathbf{Y} - \mathbf{X}|}$$

(2.6)

2.2.1 Micropotentials and strain energy

In a next step, a scalar-valued micropotential w between $\mathbf{X}$ and $\mathbf{Y}$ is defined. It depends on the material and on the absolute value of undeformed and deformed bond length. Furthermore, it is not supposed to contain any spatial derivative of the displacement field.

$$w(\mathbf{X},\mathbf{Y}) = w(|\mathbf{Y} + \mathbf{u}_Y - \mathbf{X} - \mathbf{u}_X|, |\mathbf{Y} - \mathbf{X}|) = w(|\mathbf{L} + \boldsymbol{\eta}|, |\mathbf{L}|)$$

(2.7)

This claim has the following consequences:

1. Any two bonds, regardless of their orientation in either undeformed or deformed configuration, obtain the same micropotential, if the undeformed- and deformed length coincide. This assumption will introduce an isotropic material, see [Silling 2000, p.179].

2. The micropotential is not a function of the dilatation (volumetric change) of $\mathbf{X}$ and $\mathbf{Y}$, respectively the deformation of the families $D_\mathbf{X}$ and $D_\mathbf{Y}$, see [Madenci and Oterkus 2014, p.55].

3. The micropotential remains the same if swapping $\mathbf{X}$ and $\mathbf{Y}$.

4. Since the micropotential is free of derivatives, functions for $\mathbf{u}$ need not be differentiable.

The strain energy density W in $\mathbf{X}$ is the sum of all micropotentials related to it. Since points $\mathbf{Y}$ beyond the horizon have no influence on $\mathbf{X}$, the integral over the whole configuration reduces to an integral over the horizon. (Remark: At this point, no difference is made between the integration in the reference- or undeformed configuration. This assumption is released in chapter 3).

$$W(\mathbf{X}) = \iint\limits_{\Omega^0 \cap D_{\mathbf{X}}} w(\mathbf{X}, \mathbf{Y}) \, dA_{\mathbf{Y}} \tag{2.8}$$

Thus, the strain energy of the system is the volume integral over the strain energy density function:

$$\Pi_{int} = \iint\limits_{\Omega^0} W(\mathbf{X}) \, dA_{\mathbf{X}} \tag{2.9}$$

The potential energy of the external forces is defined as:

$$\Pi_{ext} = -\iint\limits_{\Omega^0} \mathbf{b} \cdot \mathbf{u} \, dA_{\mathbf{X}} \tag{2.10}$$

The potential energy Π in the system is the sum of strain energy and the potential energy of the external forces $\mathbf{b}$:

$$\Pi = \Pi_{int} + \Pi_{ext} = \iint\limits_{\Omega^0} W(\mathbf{X}) \, dA_{\mathbf{X}} - \iint\limits_{\Omega^0} \mathbf{b} \cdot \mathbf{u} \, dA_{\mathbf{X}} \tag{2.11}$$

The kinetic energy of the whole system is denoted by:

$$T = \iint\limits_{\Omega^0} \frac{1}{2} \rho^0 \, \dot{\mathbf{u}}^T \cdot \dot{\mathbf{u}} \, dA_{\mathbf{X}} \tag{2.12}$$

The equation of motion of the system is obtained by the Euler-Lagrange equations [Nolting 2006, p.71]:

$$\frac{\partial \mathcal{L}}{\partial \mathbf{u}} - \frac{d}{dt} \frac{\partial \mathcal{L}}{\partial \dot{\mathbf{u}}} = 0 \tag{2.13}$$

with $\mathcal{L}$ being the Lagrangian:

$$\mathcal{L} = T - \Pi \tag{2.14}$$

In the following, the equation of motion is derived from eq. 2.14 for one particular material point $\mathbf{X}$, respectively $\mathbf{u_X}$. The equations of motion will consist of internal, external and inertial forces. Because the internal forces in Peridynamics are of special importance, they are derived in detail.

The potential energy in the Lagrangian is a function of the displacements $\mathbf{u}$. Deriving the strain energy at point $\mathbf{X}$ w.r.t. $\mathbf{u_X}$ yields the resulting force $\mathbf{r}$ of all (bond) forces $\mathbf{f}$ connected to $\mathbf{X}$. This implies that the derivatives of the micropotentials by the displacement vector will yield the bond forces. According to [Silling 2000, p.180], such a material is called "microelastic". Although the exact form of the micropotentials is not defined yet, the application of the chain rule reveals their structure:

$$
\frac{\partial \mathcal{L}}{\partial \mathbf{u_X}} = \frac{\partial}{\partial \mathbf{u_X}}\big(W(\mathbf{X})\big) = \mathbf{r} = \frac{\partial}{\partial \mathbf{u_X}}\Big(\iint\limits_{\Omega^0 \cap D_\mathbf{X}} w(|\mathbf{L}+\boldsymbol{\eta}|,|\mathbf{L}|)\, dA_\mathbf{Y} \Big) =
$$
$$
= \iint\limits_{\Omega^0 \cap D_\mathbf{X}} \frac{\partial w(|\mathbf{L}+\boldsymbol{\eta}|,|\mathbf{L}|)}{\partial |\mathbf{L}+\boldsymbol{\eta}|}\, \frac{\partial |\mathbf{L}+\boldsymbol{\eta}|}{\partial \mathbf{u_X}}\, dA_\mathbf{Y}
$$

(2.15)

By using eq. 2.7, the last derivative in the expression above can be broken down further. Please note: The base vectors in the background are cartesian and therefore not affected by the differentiation.

$$
\frac{\partial |\mathbf{L}+\boldsymbol{\eta}|}{\partial \mathbf{u_X}} = \begin{bmatrix} \dfrac{\partial}{\partial u_\mathbf{X}^1} \\[2ex] \dfrac{\partial}{\partial u_\mathbf{X}^2} \end{bmatrix} \Big((Y^1 + u_\mathbf{Y}^1 - X^1 - u_\mathbf{X}^1)^2 + (Y^2 + u_\mathbf{Y}^2 - X^2 - u_\mathbf{X}^2)^2 \Big)^{\frac{1}{2}} =
$$
$$
= \frac{1}{|\mathbf{L}+\boldsymbol{\eta}|} \begin{bmatrix} (Y^1 + u_\mathbf{Y}^1 - X^1 - u_\mathbf{X}^1)\,(-1) \\[1ex] (Y^2 + u_\mathbf{Y}^2 - X^2 - u_\mathbf{X}^2)\,(-1) \end{bmatrix} = - \begin{bmatrix} \dfrac{L^1 + \eta^1}{|\mathbf{L}+\boldsymbol{\eta}|} \\[2ex] \dfrac{L^2 + \eta^2}{|\mathbf{L}+\boldsymbol{\eta}|} \end{bmatrix}
$$

(2.16)

The result of equation 2.16 is a vector of unit length. It will denote the direction of the bond forces. On the other hand, the magnitude of the force vector is defined by expression:

$$
\frac{\partial\, w(|\mathbf{L}+\boldsymbol{\eta}|,|\mathbf{L}|)}{\partial |\mathbf{L}+\boldsymbol{\eta}|}
$$

(2.17)

The following claims aid in the construction of the yet missing function $w(|\mathbf{L}+\boldsymbol{\eta}|,|\mathbf{L}|)$.

1. Thought experiment: If $w(|\mathbf{L}+\boldsymbol{\eta}|,|\mathbf{L}|)$ was a linear function of $|\mathbf{L}+\boldsymbol{\eta}|$, any derivation by $\partial |\mathbf{L}+\boldsymbol{\eta}|$ (comp. eq. 2.16) would lead to a constant. Then, the force of a bond would

be constant too. In this case, any bond would yield the same inner force, regardless of it's displacement and thus deformation state. Such a micropotential could not yield the same results as classical elasticity, where the inner forces are functions of the displacements by the strain tensor.

2. Pursuing this thought, $w(|\mathbf{L} + \boldsymbol{\eta}|, |\mathbf{L}|)$ must be able to yield a force which is a linear function of the deformed bond length $|\mathbf{L} + \boldsymbol{\eta}|$ (because linear elastic material was claimed).

Therefore, the following expression for the magnitude of the internal forces vector $|\mathbf{f}|$, which is compatible with the requirements on it's indefinite integral, is demanded

$$|\mathbf{f}| = k\left(|\mathbf{L} + \boldsymbol{\eta}| - |\mathbf{L}|\right) \tag{2.18}$$

with yet to determine function k for the influence of material and horizon. Subtracting $|\mathbf{L}|$ in eq. 2.18 provides a zero-force in case $\boldsymbol{\eta} = \mathbf{0}$, in other words: in case of an undeformed bond. Integration of eq. 2.18 by $|\mathbf{L} + \boldsymbol{\eta}|$ yields the micropotential of a bond:

$$w = \frac{1}{2} k \left(|\mathbf{L} + \boldsymbol{\eta}| - |\mathbf{L}|\right)^2 + C \tag{2.19}$$

The integration constant C in expression 2.19 is omitted now. Many functions would be possible for the material parameter k. However, the derivation up to now forbids k to be a function of $\boldsymbol{\eta}$. In this case, the material is called "harmonic" [Silling 2000, p.184]. Harmonic materials are isotropic, microelastic and linear.

The strain energy in $\mathbf{X}$ is then given by:

$$W = \frac{1}{2} \iint\limits_{\Omega^0 \cap D_{\mathbf{X}}} \frac{1}{2} k \left(|\mathbf{L} + \boldsymbol{\eta}| - |\mathbf{L}|\right)^2 dA_{\mathbf{Y}} \tag{2.20}$$

The additional factor $\frac{1}{2}$ in front of expression 2.20 is applied, because the strain energy due to the bond stretch is equally shared between $\mathbf{X}$ and $\mathbf{Y}$. Please note that the peridynamic strain energy density is a function of the bonds' elongations due to displacements, but not of any derivative of the displacement field. A more complex expression for the strain energy of a linear peridynamic solid involving two material parameters can be found in [Silling et al 2007, p.173].

2.2.2 Equation of motion

With the structure of the micropotentials known, the peridynamic equation of motion can be derived from the Lagrangian for a particular material point $\mathbf{X}$:

$$\frac{d}{dt}\frac{\partial \mathcal{L}}{\partial \dot{\mathbf{u}}} = \frac{\partial \mathcal{L}}{\partial \mathbf{u}}$$

$$\frac{d}{dt}\frac{\partial T}{\partial \dot{\mathbf{u}}_{\mathbf{X}}} = -\frac{\partial U}{\partial \mathbf{u}_{\mathbf{X}}} \tag{2.21}$$

$$\rho^0 \ddot{\mathbf{u}}_{\mathbf{X}} = \mathbf{b} + \frac{1}{2}\iint\limits_{\Omega^0 \cap D_{\mathbf{X}}} k\left(|\mathbf{L} + \boldsymbol{\eta}| - |\mathbf{L}|\right)\frac{\mathbf{L} + \boldsymbol{\eta}}{|\mathbf{L} + \boldsymbol{\eta}|}\, dA_{\mathbf{Y}}$$

In Peridynamics, due to the existence of micropotentials, the inner forces in $\mathbf{X}$ are the sum of all bond forces acting upon $\mathbf{X}$ by the material points in it's family $D_{\mathbf{X}}$. Please note that the forces acting in a bond $\mathbf{L}$ are of equal magnitude and acting opposite to each other on $\mathbf{X}$ and $\mathbf{Y}$.
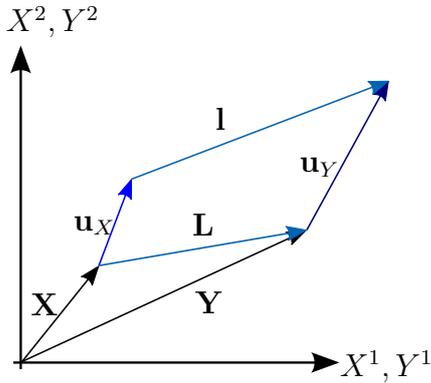

Figure 2.3: Undeformed and deformed bond
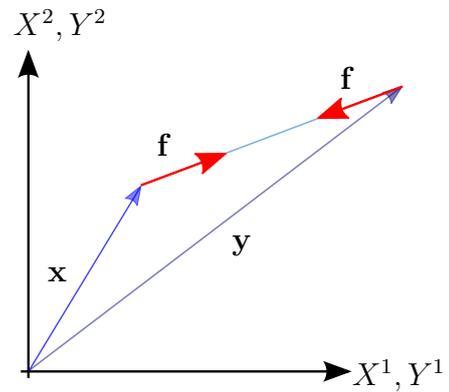
Figure 2.4: Direction of bond forces

2.3 Peridynamic material modelling

In a next step, adequate peridynamic material parameters need to be defined. The material is supposed to be isotropic linear elastic. Furthermore, the derivations are restricted on a 2-dimensional problem, see [Madenci and Oterkus 2014, p.61-66]. Two more assumptions are introduced to the model:

1. Material points $\mathbf{Y}$ with greater distance to $\mathbf{X}$ are supposed to have lesser influence on $\mathbf{X}$ than closer ones. Therefore, a hyperbola influence function is introduced into the

micropotential, taking stronger influence of closer partners into consideration.

$$k = c \frac{1}{|\mathbf{Y} - \mathbf{X}|} \tag{2.22}$$

Remark: The hyperbola influence function eq. 2.22 is not derived from a higher principal of nature, but it is a design choice.

2. A factor c in equation 2.22 remains. This parameter is called microelastic stiffness constant [Trageser and Seleson 2020, p.4] or bond constant.

Computing the microelastic stiffness constant means calibrating the peridynamic model on a corresponding classic material. This is done by equating the strain energy densities of Peridynamics and classical elasticity for two independent deformation states, comp. [Madenci and Oterkus 2014, p.61-65]. It has to be differentiated between plane stress and plane strain condition, comp. appendix A.8. The expressions below hold for a cartesian coordinate system.

The first deformation state is an isotropic expansion. In terms of classical elasticity, it means that the coefficients of the linearized strain tensor $\epsilon^{11} = \epsilon^{22} = \zeta$ are equal, ϵ^{12} resp. ϵ^{21} are zero. The resulting displacement field will lead to a change of volume, but no distortion of the continuum. On the other hand, a change of shape, but not of volume, is obtained by a simple shear deformation, $\epsilon^{11} = \epsilon^{22} = 0$, $\epsilon^{12} = \epsilon^{21} = \zeta$.

The strain energy density of a classical continuum in two dimensions is given by:

$$W_{CCM} = \frac{1}{2}\sigma_{ij}\,\epsilon^{ij} = \frac{1}{2}\left(\sigma_{11}\,\epsilon^{11} + \sigma_{12}\,\epsilon^{12} + \sigma_{21}\,\epsilon^{21} + \sigma_{22}\,\epsilon^{22}\right) \tag{2.23}$$

(Infinitesimal deformation and thus no difference between tensors in the deformed and undeformed configuration is assumed). The peridynmamic strain energy density for a hyperbola influence function is denoted by (see eq. 2.20 and 2.22):

$$W = \frac{1}{4}\iint\limits_{\Omega^0 \cap D_{\mathbf{X}}} c\frac{1}{|\mathbf{L}|}\left(|\mathbf{L} + \boldsymbol{\eta}| - |\mathbf{L}|\right)^2 dA_{\mathbf{Y}} \tag{2.24}$$

It is solved now for the bond constant c under plane stress assumption:

Isotropic expansion

Setting $\epsilon^{11} = \epsilon^{22} = \zeta$, $\epsilon^{12} = 0$ and replacing the entries of the stress tensor in 2.23 by the stress-strain relations from eq. A.8 yields the strain energy density for isotropic expansion

in classical continuum mechanics:

$$W_{CCM} = \frac{1}{2}\frac{E}{1-\nu^2}\left(\zeta^2 + \zeta^2 + 2\nu\zeta^2\right) = \frac{E}{1-\nu}\zeta^2 \tag{2.25}$$

The peridynamic strain energy density can be computed easily in polar coordinates [Madenci
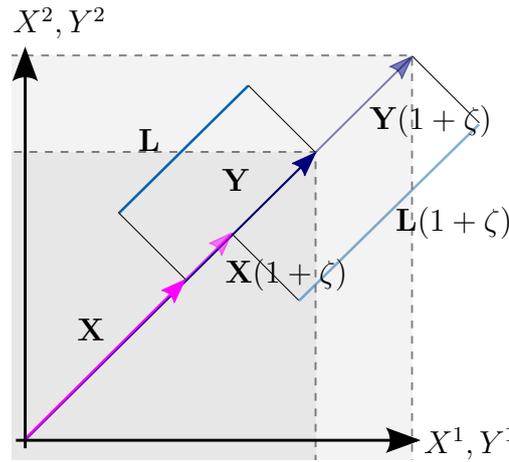
Figure 2.5: Isotropic expansion calibration

and Oterkus 2014, p.63]. By using the fact that isotropic expansion means constant strain ζ in any direction, thus also in radial one, the length of a deformed bond in polar coordinates can be denoted as:

$$|\mathbf{l}| = (1+\zeta)\,r \tag{2.26}$$

with r being the length of an undeformed bond in polar coordinates. Including eq. 2.26 into 2.24 yields:

$$W = 2\int_{-\frac{\pi}{2}}^{\frac{\pi}{2}}\int_{0}^{\delta}\frac{1}{4}c\frac{1}{r}\left((1+\zeta)\,r - r\right)^2 r\,drd\varphi = \frac{1}{2}c\int_{-\frac{\pi}{2}}^{\frac{\pi}{2}}\int_{0}^{\delta}\zeta^2\,r^2 drd\varphi = \frac{1}{6}c\,\delta^3\,\pi\,\zeta^2 \tag{2.27}$$

The bond constant is obtained by equating both expressions for the strain energy density:

$$c_{iso} = 6\,\frac{E}{1-\nu}\,\frac{1}{\pi\,\delta^3} \tag{2.28}$$

Simple shear

The classical continuum mechanics strain energy density for simple shear and plane stress is given by:

$$W_{CCM} = \frac{1}{2}\frac{E}{1-\nu^2}\, 2\,(1-\nu)\,\zeta^2 = \frac{E}{1+\nu}\,\zeta^2 \tag{2.29}$$

with $\epsilon^{11} = \epsilon^{22} = 0$, $\epsilon^{12} = \epsilon^{21} = \zeta$. The elongated bond is a function of the orientation of the
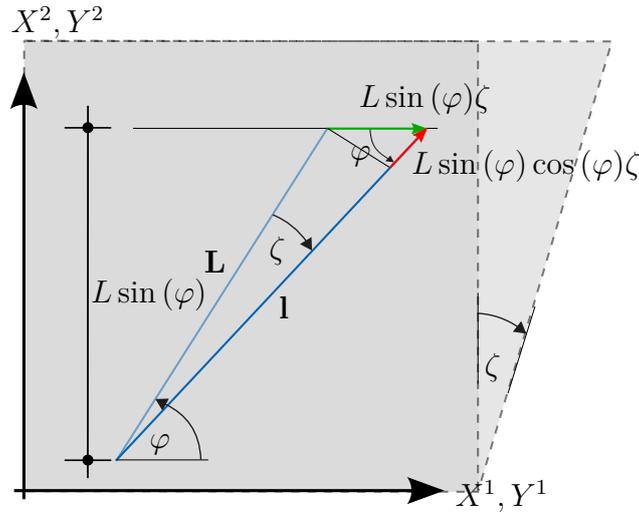

Figure 2.6: Simple shear calibration

bond [Madenci and Oterkus 2014, p.65]:

$$l = L\,(1 + \zeta\cos(\varphi)\sin(\varphi)) \tag{2.30}$$

As the length of an undeformed bond L in polar coordinates is denoted by r again, equation 2.30 in polar coordinates reads as:

$$l = r\,(1 + \zeta\cos(\varphi)\sin(\varphi)) \tag{2.31}$$

Introducing eq. 2.31 into eq. 2.24, expressed w.r.t. polar coordinates reads as:

$$W = 2\int_{-\frac{\pi}{2}}^{\frac{\pi}{2}}\int_{0}^{\delta}\frac{1}{4}c\frac{1}{r}\left((1 + (2\,\zeta)\cos(\varphi)\sin(\varphi))\,r - r\right)^2 r\,dr d\varphi = \frac{1}{12}c\,\delta^3\,\pi\,\zeta^2 \tag{2.32}$$

Remark: The expression $2\,\zeta$ in eq. 2.32 was necessary because shearing $\epsilon_{12} = \epsilon_{21} = \zeta$ in eq. 2.29, so a twofold shearing, was used. Equating expressions 2.29 and 2.32 and solving for c

yields:

$$c_{shear} = 12 \frac{E}{1 + \nu} \frac{1}{\pi \, \delta^3} \tag{2.33}$$

Expressions 2.28 and 2.33 are not equal and thus not compatible for arbitrary combinations of E and ν. Leaving the youngs modulus variable and solving for the poisson ratio yields:

$$6 \frac{E}{1 - \nu} \frac{1}{\pi \, \delta^3} = 12 \frac{E}{1 + \nu} \frac{1}{\pi \, \delta^3} \quad \leftrightarrow \quad \nu = \frac{1}{3} \tag{2.34}$$

Thus, the bond based peridynamic theory is valid for a poisson ratio $\nu = \frac{1}{3}$ only. Performing the same derivation but for the plane strain relations in W_{CCM} yields a constraint on the poisson ratio $\nu = \frac{1}{4}$ [Trageser and Seleson 2020, p.4].

This limitation arose due to the design of the structure of the micropotentials; the energy stored in the micropotential is equally distributed between $\mathbf{X}$ and $\mathbf{Y}$. In different words, their common deformation generates strain energy, but the micropotential does not differentiate between the potentially different proportions of deformations of $\mathbf{X}$ and $\mathbf{Y}$. Introducing a second bond constant would not help, as it would operate still on the same micropotential.

A way out was proposed in [Silling et al 2007] by introducing a generalized tensor concept called state, which maps the bond between $\mathbf{X}$ and $\mathbf{Y}$ to a pair of forces acting opposite to each other, but taking into consideration the potentially different deformation conditions of $D_{\mathbf{X}}$ and $D_{\mathbf{Y}}$ into the respective micropotentials and thus enabling the pairwise forces being of different magnitude.

In the scope of this thesis, the bond-based model is pursued. The bond constant c is taken from eq. 2.28 under the prerequisite $\nu = \frac{1}{3}$ for plane stress:

$$c = \frac{6 \, E}{\pi \, \delta^3 \, (1 - \nu)} \tag{2.35}$$

With the bond constant defined, the expressions for the force density and equation of motion can be denoted:

$$\rho^0 \, \ddot{\mathbf{u}}_{\mathbf{X}} = \mathbf{b} + \frac{1}{2} \iint_{\Omega^0 \cap D_{\mathbf{X}}} c \frac{1}{|\mathbf{L}|} \left(|\mathbf{L} + \boldsymbol{\eta}| - |\mathbf{L}| \right) \frac{\mathbf{L} + \boldsymbol{\eta}}{|\mathbf{L} + \boldsymbol{\eta}|} \, dA_{\mathbf{Y}} \tag{2.36}$$

The internal forces can be expressed w.r.t. the stretch of a bond s as well, comp. eq. 2.6:

$$\rho^0\,\ddot{\mathbf{u}}_{\mathbf{X}} = \mathbf{b} + \frac{1}{2} \iint\limits_{\Omega^0 \cap D_{\mathbf{X}}} c\,s\,\frac{\mathbf{L} + \boldsymbol{\eta}}{|\mathbf{L} + \boldsymbol{\eta}|}\,dA_{\mathbf{Y}} \tag{2.37}$$

The peristatic equation of motion is obtained by omitting the inertial forces in eq. 2.36.

$$0 = \mathbf{b} + \frac{1}{2} \iint\limits_{\Omega^0 \cap D_{\mathbf{X}}} c\,\frac{1}{|\mathbf{L}|}\left(|\mathbf{L} + \boldsymbol{\eta}| - |\mathbf{L}|\right)\frac{\mathbf{L} + \boldsymbol{\eta}}{|\mathbf{L} + \boldsymbol{\eta}|}\,dA_{\mathbf{Y}} \tag{2.38}$$

3 Peridynamic Finite Elements

Different to the majority of peridynamic simulations, the peridynamic equation of motion shall be solved by using the finite element method (FEM) in the scope of this work. This decision is based on the widespread use of the FEM in engineering applications. Peridynamic finite elements could be applied more easily by an engineer already familiar with finite element method and the respective modeling. Furthermore, a simple coupling between peridynamic finite elements and classical finite elements can be developed. Therefore, it is possible to model those parts of the system prone to discontinuities in the displacement field with peridynamic finite elements, whereas the rest of the structure is modeled with the computationally cheaper classical finite elements, combining the strengths of both Peridynamics and classical continuum mechanics.

This chapter provides the finite element formulations of the equations derived in chapter 2 for one- and two dimensional problems, including boundary conditions, the implementation of the static crack propagation and adaptive dynamic relaxation.

3.1 Finite elements for a 2-D problem

Different to peridynamic finite elements in one dimension, the discretization of the two-dimensional peridynamic equation of motion leads to a nonlinear problem. Although a linearization is possible [Glaws 2014, p.17], the loss in precision is significant for large deformations and therefore not advisable. The derivation begins with the peridynamic equation of motion from chapter 2.

3.1.1 Derivation of the weak form

The force density in a bond between point $\mathbf{X}$ and $\mathbf{Y}$ for a microelastic material and a hyperbola – influence function is denoted by [Madenci and Oterkus 2014]:

$$\mathbf{f}(\mathbf{X},\mathbf{Y}) = c \, \frac{\delta}{|\mathbf{Y} - \mathbf{X}|} \left(|\mathbf{y} - \mathbf{x}| - |\mathbf{Y} - \mathbf{X}| \right) \frac{\mathbf{y} - \mathbf{x}}{|\mathbf{y} - \mathbf{x}|} \tag{3.1}$$

Using $\mathbf{X}$ and $\mathbf{Y}$ as arguments for $\mathbf{f}$ implies that the equilibrium is expressed with respect to the undeformed configuration Ω^0. Although the force between start and end of the bond is generated by a relative displacement between them both, the displacement is assumed to be small enough not to change the original geometry significantly. From a certain degree on, the magnitude of displacements necessitates the equilibrium being expressed with respect to the deformed configuration Ω in order to consider nonlinear relations between displacements and deformations, as well as additional stabilizing/destabilizing effects of loads on finite displacements [Parisch 2003, p.107]. It holds: (compare section A.1.1)

$$\mathbf{x} = \varphi(\mathbf{X}) = \mathbf{X} + \mathbf{u} \tag{3.2}$$

By this connection, a position vector $\mathbf{x}$ of the deformed configuration is expressed with respect to the known undeformed configuration Ω^0. Now, the use of $\mathbf{x}$ and $\mathbf{y}$ states that this equation is written in the deformed configuration.

$$\mathbf{f}(\mathbf{x},\mathbf{y}) = c \, \frac{\delta}{|\mathbf{Y} - \mathbf{X}|} \, \left(|\mathbf{y} - \mathbf{x}| - |\mathbf{Y} - \mathbf{X}| \right) \frac{\mathbf{y} - \mathbf{x}}{|\mathbf{y} - \mathbf{x}|} \tag{3.3}$$

Although equations 3.1 and 3.3 share the same structure, eq. 3.3 has to be transformed back to the reference configuration before integration.

Adaption to large displacements

Because the base vectors of the deformed configuration are dependent on the yet unknown displacement field, the position vectors $\mathbf{x}$ and $\mathbf{y}$ have to be expressed w.r.t. the undeformed configuration:

$$\begin{aligned}
\mathbf{x} &= \varphi(\mathbf{X}) = \mathbf{X} + \mathbf{u_X} \\
\mathbf{y} &= \varphi(\mathbf{Y}) = \mathbf{Y} + \mathbf{u_Y}
\end{aligned} \tag{3.4}$$

Introducing eq. 3.4 into eq. 3.3 yields the bond force vector in the deformed state (equilibrium state), expressed w.r.t. the undeformed configuration.

$$\begin{aligned}
\mathbf{f}(\mathbf{x},\mathbf{y}) &= \mathbf{f}(\varphi(\mathbf{X}), \varphi(\mathbf{Y})) = \\
&= c \, \frac{\delta}{|\mathbf{Y} - \mathbf{X}|} \, \left(|\mathbf{Y} + \mathbf{u_Y} - \mathbf{X} - \mathbf{u_X}| - |\mathbf{Y} - \mathbf{X}| \right) \frac{\mathbf{Y} + \mathbf{u_Y} - \mathbf{X} - \mathbf{u_X}}{|\mathbf{Y} + \mathbf{u_Y} - \mathbf{X} - \mathbf{u_X}|}
\end{aligned} \tag{3.5}$$

The resulting force $\mathbf{r}$ in $\mathbf{x}$ is the integral over all bonds in the horizon $D_{\mathbf{x}}$. Since this integral is defined w.r.t. the (yet unknown) deformed configuration, the integrand is transformed to

the undeformed configuration by the functional determinant of the map $\mathbf{y} = \varphi(\mathbf{Y}) = \mathbf{Y} + \mathbf{u_Y}$ (compare appendix A.1.1):

$$
\begin{aligned}
\mathbf{r} &= \iint\limits_{\Omega \cap D_{\mathbf{x}}} \mathbf{f}(\mathbf{x,y})\, da_{\mathbf{y}} \;=\; \iint\limits_{\Omega^0 \cap D_{\mathbf{x}}} \mathbf{f}(\varphi(\mathbf{X}), \varphi(\mathbf{Y}))\, \det D\varphi(\mathbf{Y})\, dA_{\mathbf{Y}} \\
&= \iint\limits_{\Omega^0 \cap D_{\mathbf{x}}} \mathbf{f}\big(\mathbf{X} + \mathbf{u_X}, \mathbf{Y} + \mathbf{u_Y} \big)\, \det D\varphi(\mathbf{Y})\, dA_{\mathbf{Y}}
\end{aligned}
\tag{3.6}
$$

3.1.2 Weak form

As no general analytical solution is currently known for equation 2.38, a weak form of the equilibrium must serve, which fulfills the equilibrium in an integral sense. In order to obtain a weak form, both inner peridynamic force-field $\mathbf{r}(\mathbf{x})$ and the vector of the external loads function $\mathbf{b}(\mathbf{x})$ are multiplied with a virtual test field $\delta\mathbf{v}(\mathbf{x})$ and integrated over the whole deformed domain Ω. The weak form of the integral equation 2.38 then reads as [Steeb 2021], [John 2009, p.47]:

$$
\begin{aligned}
\mathbf{given} :\; &\mathbf{b} : \Omega \to \mathbb{R}^2 \;\text{ with }\; \Omega \subset \mathbb{R}^2 \\
&\text{boundary region values:} \\
&\mathbf{u} = \tilde{\mathbf{u}} \;\text{ on }\; \Omega_c \\
\mathbf{goal} :\; &\text{find a function} \\
&\mathbf{u} \in \mathcal{U}_1 := \left\{ \mathbf{u} \in \big(\mathbf{H}^1(\Omega) \big)^2 \,|\, \mathbf{u} = \tilde{\mathbf{u}} \;\text{ on }\; \Omega_c \right\} \\
&\text{such that for all} \\
&\delta\mathbf{v} \in \big(\mathbf{H}_0^1(\Omega) \big)^2 ,\, \delta\mathbf{v} = \mathbf{0} \;\text{ on }\; \Omega_c \Big\} \\
&\text{the equation} \\
&\delta W = \iint\limits_{\Omega} \Big(\iint\limits_{\Omega \cap D_{\mathbf{x}}} \mathbf{f}(\mathbf{u})\, da_{\mathbf{y}} + \mathbf{b} \Big) da_{\mathbf{y}} \cdot \delta\mathbf{v}\, da_{\mathbf{x}} = 0 \\
&\text{is fulfilled.}
\end{aligned}
\tag{3.7}
$$

As area and shape of the deformed area of integration are not known in advance, again the integral is modified with the functional determinant of the gradient of the map $\varphi(\mathbf{x})$. The result can be considered as the virtual work of internal and external forces w.r.t. the

undeformed configuration:

$$
\begin{aligned}
\delta W_{int} &= \iint_{\Omega} \delta \mathbf{v}(\mathbf{x}) \cdot \mathbf{r}(\mathbf{x}) \, da_{\mathbf{x}} = \\
&= \iint_{\Omega^0} \delta \mathbf{v}(\varphi(\mathbf{X})) \cdot \iint_{\Omega^0 \cap D_{\mathbf{X}}} \mathbf{f}(\varphi(\mathbf{X}), \, \varphi(\mathbf{Y})) \det D\varphi(\mathbf{Y}) \, dA_{\mathbf{Y}} \det D\varphi(\mathbf{X}) \, dA_{\mathbf{X}}
\end{aligned}
\tag{3.8}
$$

$$
\delta W_{ext} = \iint_{\Omega} \delta \mathbf{v}(\mathbf{x}) \cdot \mathbf{b}(\mathbf{x}) \, da_{\mathbf{x}} = \iint_{\Omega^0} \delta \mathbf{v}(\varphi(\mathbf{X})) \cdot \mathbf{b}(\varphi(\mathbf{X})) \det D\varphi(\mathbf{X}) \, dA_{\mathbf{X}}
$$

3.1.3 Discretization

The aim is now to find a vector-valued function $\mathbf{u}$, which sets the sum of the virtual works of all internal and external forces to zero:

$$
\delta W = \delta W_{int}(\mathbf{u}, \delta \mathbf{v}) + \delta W_{ext}(\delta \mathbf{v}) = 0
\tag{3.9}
$$

The principle of virtual work states that the force state of a system in equilibrium will not perform work on a "small" virtual displacement which is compatible with the system's kinematics. As both $\mathbf{u}$ and $\delta \mathbf{v}$ are elements of infinite-dimensional function spaces, finite-dimensional approximations for the function spaces $\mathcal{U}_1$ and $\mathcal{V}_1$ have to be made. An approach for $\mathbf{u}$ and $\delta \mathbf{v}$ is introduced in order to obtain a finite amount of equations:

$$
\begin{aligned}
\mathbf{u} &\approx \mathbf{u}^h \\
\delta \mathbf{v} &\approx \delta \mathbf{v}^h
\end{aligned}
\tag{3.10}
$$

with

$$
\begin{aligned}
\mathbf{u}^h &\in \mathcal{U}_1^h := \left\{ \mathbf{u}^h \in \left(\mathbf{H}^1(\Omega) \right)^2 \,|\, \mathbf{u}^h(\mathbf{X}) = \tilde{\mathbf{u}}^h(\mathbf{X}) + \sum_{n=1}^{M_1} \mathbf{A}_n(\mathbf{X}) \cdot \bar{\mathbf{u}}_n \right\} \subset \mathcal{U}_1 \\
\delta \mathbf{v}^h &\in \mathcal{V}_1^h := \left\{ \delta \mathbf{v}^h \in \left(\mathbf{H}_0^1(\Omega) \right)^2 \,|\, \delta \mathbf{v}^h(\mathbf{X}) = \sum_{l=1}^{M_1} \mathbf{B}_l(\mathbf{X}) \cdot \delta \bar{\mathbf{v}}_l \right\} \subset \mathcal{V}_1
\end{aligned}
\tag{3.11}
$$

$\tilde{\mathbf{u}}^h(\mathbf{X})$ is a field with constrained nodal displacements and ensures that the equivalents to the Dirichlet boundary conditions are met. Until specified in detail, it shall be assumed that the discretized parts of $\mathbf{u}^h$ and $\delta \mathbf{v}^h$ are built of M_1 sums of products between approach functions $\bar{N}$ and the yet unknown coefficients $\bar{\mathbf{u}}$. Following a Bubnov-Galerkin approach, the same approach functions are used for discretization of $\mathbf{u}$ and $\delta \mathbf{v}$, therefore $\mathbf{A}_n(\mathbf{X}) = \mathbf{B}_n(\mathbf{X})$

[Steeb 2021]:

$$
\begin{aligned}
\mathbf{A}_n(\mathbf{X}) \cdot \bar{\mathbf{u}}_n &= \begin{bmatrix} \bar{N}_n(X^1, X^2) & 0 \\ 0 & \bar{N}_n(X^1, X^2) \end{bmatrix} \begin{bmatrix} \bar{u}_n^1 \\ \bar{u}_n^2 \end{bmatrix} \\
\mathbf{B}_l(\mathbf{X}) \cdot \delta\bar{\mathbf{v}}_l &= \begin{bmatrix} \bar{N}_l(X^1, X^2) & 0 \\ 0 & \bar{N}_l(X^1, X^2) \end{bmatrix} \begin{bmatrix} \delta\bar{v}_1^l \\ \delta\bar{v}_2^l \end{bmatrix}
\end{aligned}
\tag{3.12}
$$

The approach functions $\bar{N}_n(X^1, X^2)$ ($\bar{N}_l(X^1, X^2)$ analogously), (comp. appendix eq. A.89) are a product of $\bar{N}_n(X^1)$ and $\bar{N}_n(X^2)$:

$$
\bar{N}_n(X^1) = \begin{cases} +\dfrac{1}{\Delta}(X^1 - X_n^1) + 1 & \text{for } X_n^1 - \Delta \leq X^1 \leq X_n^1 \\ -\dfrac{1}{\Delta}(X^1 - X_n^1) + 1 & \text{for } X_n^1 < X^1 \leq X_n^1 + \Delta \\ 0 & \text{else} \end{cases}
\tag{3.13}
$$

$$
\bar{N}_n(X^2) = \begin{cases} +\dfrac{1}{\Delta}(X^2 - X_n^2) + 1 & \text{for } X_n^2 - \Delta \leq X^2 \leq X_n^2 \\ -\dfrac{1}{\Delta}(X^2 - X_n^2) + 1 & \text{for } X_n^2 < X^2 \leq X_n^2 + \Delta \\ 0 & \text{else} \end{cases}
\tag{3.14}
$$

with Δ being the element length and (X_n^1, X_n^2) being the coordinates of the n'th finite element node. In order to be an element of the Sobolev space $(\mathbf{H}^1)^2$, all (weak) partial derivatives D^1 of first order of $\mathbf{u}^h$ and $\delta\mathbf{v}^h$ have to exist and be finite, see section appendix A.1.3.

The virtual work in Ω_1 becomes now a function of both $2M_1$ real- and virtual nodal displacements. In order to perform the upcoming derivations, the resulting force $\mathbf{r}$ of a family (see eq.3.6) has to be expressed w.r.t. the discretized displacement field $\mathbf{u}^h$:

$$
\begin{aligned}
\mathbf{r} &= \iint\limits_{\Omega} \mathbf{f}(\mathbf{x,y})\, da_{\mathbf{y}} = \iint\limits_{\Omega^0} \mathbf{f}(\varphi(\mathbf{X}), \varphi(\mathbf{Y}))\det D\varphi(\mathbf{Y})\, dA_{\mathbf{Y}} \\
&= \iint\limits_{\Omega^0} \mathbf{f}\big(\mathbf{X} + \mathbf{u_X}, \mathbf{Y} + \mathbf{u_Y}\big)\det D\varphi(\mathbf{Y})\, dA_{\mathbf{Y}} \approx \\
&\approx \iint\limits_{\Omega^0} \mathbf{f}\Big(\mathbf{X} + \sum_{n=1}^{M_1} \mathbf{A}_n(\mathbf{X}) \cdot \bar{\mathbf{u}}_n, \mathbf{Y} + \sum_{m=1}^{M_1} \mathbf{A}_m(\mathbf{Y}) \cdot \bar{\mathbf{u}}_m\Big)\det D\varphi(\mathbf{Y})\, dA_{\mathbf{Y}}
\end{aligned}
\tag{3.15}
$$

With $\mathbf{r}$ expressed w.r.t. the approximated displacement field $\mathbf{u}^h$, the virtual work on the discretized fields can be expressed:

$$\delta W = \delta W_{int} + \delta W_{ext} \approx \iint_{\Omega} \mathbf{r} \cdot \delta\mathbf{v} \, da_{\mathbf{x}} + \iint_{\Omega} \mathbf{b} \cdot \delta\mathbf{v} \, da_{\mathbf{x}} =$$

$$= \iint_{\Omega^0} \mathbf{r}(\mathbf{u}^h(\mathbf{X})) \cdot \sum_{l=1}^{M_1} \mathbf{B}_l(\mathbf{X}) \cdot \delta\bar{\mathbf{v}}_l \det D\varphi(\mathbf{X}) \, dA_{\mathbf{X}}$$

$$+ \iint_{\Omega^0} \mathbf{b} \cdot \sum_{l=1}^{M_1} \mathbf{B}_l(\mathbf{X}) \cdot \delta\bar{\mathbf{v}}_l \det D\varphi(\mathbf{X}) \, dA_{\mathbf{X}} =$$

$$= \sum_{l=1}^{M_1} \delta\bar{\mathbf{v}}_l \iint_{\Omega^0} \mathbf{B}_l^T(\mathbf{X}) \cdot \mathbf{r}(\mathbf{u}^h(\mathbf{X}))) \det D\varphi(\mathbf{X}) \, dA_{\mathbf{X}} + \tag{3.16}$$

$$+ \sum_{l=1}^{M_1} \delta\bar{\mathbf{v}}_l \iint_{\Omega^0} \mathbf{B}_l^T(\mathbf{X}) \cdot \mathbf{b} \det D\varphi(\mathbf{X}) \, dA_{\mathbf{X}} =$$

$$= \sum_{l=1}^{M_1} \delta\bar{\mathbf{v}}_l \iint_{\Omega^0} \mathbf{B}_l^T(\mathbf{X}) \cdot \mathbf{r}(\sum_{l=1}^{M_1} \mathbf{A}_l(\mathbf{X}) \cdot \bar{\mathbf{U}}_l) \det D\varphi(\mathbf{X}) \, dA_{\mathbf{X}} +$$

$$+ \sum_{l=1}^{M_1} \delta\bar{\mathbf{v}}_l \iint_{\Omega^0} \mathbf{B}_l^T(\mathbf{X}) \cdot \mathbf{b} \det D\varphi(\mathbf{X}) \, dA_{\mathbf{X}}$$

Every summand of 3.16 is now a part of the virtual work of the system. The test field is an arbitrary linear combination of products of the virtual nodal displacements $\delta\bar{v}_l^s$ and their respective approach function $\bar{N}_l$. Setting all but one nodal test displacement $\delta\bar{v}_k^s$ to zero poses a valid test field too (the virtual work must vanish for all possible test fields) and yields an equation for the $2M_1$ unknown real nodal displacements $\bar{u}_n^s$. Setting all but one virtual nodal displacement to zero can be repeated $2M_1$ times, where every obtained equation represents the virtual work of all forces in direction s related with the finite element node k; the virtual displacement $\delta\bar{v}_k^s$ of every equation can be canceled out, because it is multiplied with both external and internal forces. The result is a system of $2M_1$ equations.

$\mathbf{R}_k$ denotes the residual vector in node k.

$$\mathbf{R}_k = \iint\limits_{\Omega^0} \mathbf{B}_k^T(\mathbf{X}) \cdot \mathbf{r}(\mathbf{u}^h(\mathbf{X})) \det D\varphi(\mathbf{X}) \, dA_{\mathbf{X}} + \iint\limits_{\Omega^0} \mathbf{B}_k^T(\mathbf{X}) \cdot \mathbf{b} \det D\varphi(\mathbf{X}) \, dA_{\mathbf{X}} =$$

$$= \iint\limits_{\Omega^0} \mathbf{B}_k^T(\mathbf{X}) \cdot \mathbf{r}(\sum_{n=1}^{M_1} \mathbf{A}_n(\mathbf{X}) \cdot \bar{\mathbf{u}}_n) \det D\varphi(\mathbf{X}) \, dA_{\mathbf{X}} + \iint\limits_{\Omega^0} \mathbf{B}_k^T(\mathbf{X}) \cdot \mathbf{b} \det D\varphi(\mathbf{X}) \, dA_{\mathbf{X}} =$$

$$= \iint\limits_{\Omega^0} \mathbf{B}_k^T(\mathbf{X}) \cdot \iint\limits_{\Omega^0 \cap D_{\mathbf{X}}} \mathbf{f}(\sum_{n=1}^{M_1} \mathbf{A}_n(\mathbf{X}) \cdot \bar{\mathbf{u}}_n, \sum_{m=1}^{M_1} \mathbf{A}_m(\mathbf{Y}) \cdot \bar{\mathbf{u}}_m) \det D\varphi(\mathbf{Y}) \, dA_{\mathbf{Y}} \det D\varphi(\mathbf{X}) \, dA_{\mathbf{X}} +$$

$$+ \iint\limits_{\Omega^0} \mathbf{B}_k^T(\mathbf{X}) \cdot \mathbf{b} \det D\varphi(\mathbf{X}) \, dA_{\mathbf{X}}$$

$$(3.17)$$

Because this system of equation is nonlinear in $\mathbf{u}$ due to the nonlocality of $\mathbf{r}$ (compare eq. 3.6 and eq. 3.17) and analytical solutions are not available in general, it has to be solved by numerical methods. In this section, a solution with Newton's method is chosen (compare section A.2). In order to obtain the Jacobian matrix, every equation of the inner forces 3.17 has to be derived by every unknown nodal displacement $\bar{u}_k^s$. This could be done by numerical manners, e.g. forward differences [Glaws 2014, p.23] or complex step derivative, compare appendix section A.3. In the scope of this thesis, an analytical expression for the derivative of eq. 3.8 was developed and implemented as follows.

Analytical Jacobian matrix

$\mathbf{R}_{k_{int}}$ denotes the result of the inner forces in node k, comp. expression 3.17:

$$\mathbf{R}_{k_{int}} = \iint\limits_{\Omega^0} \mathbf{B}_k^T(\mathbf{X}) \cdot \mathbf{r}(\mathbf{u}^h(\mathbf{X})) \det D\varphi(\mathbf{X}) \, dA_{\mathbf{X}} \qquad (3.18)$$

Deriving $\mathbf{R}_{k_{int}}$ by a nodal degree of freedom (dof) $\bar{u}_k^s$ yields two entries of the Jacobian matrix. (Two, because $\mathbf{R}_{k_{int}}$ is a vector with a force component in X^1 - and X^2 - direction). Because of the derivation, all maps from $\mathbf{x}$ to $\bar{u}_k^s$ have to be considered now:

$$\frac{\partial \mathbf{R}_{k_{int}}}{\partial \bar{u}_k^s} = \iint\limits_{\Omega^0} \mathbf{B}_k^T(\mathbf{X}) \cdot \frac{\partial}{\partial \bar{u}_k^s} \Big(\mathbf{r}(\varphi(\mathbf{X})) \det D\varphi(\mathbf{X}) \Big) \, dA_{\mathbf{X}} =$$

$$= \iint\limits_{\Omega^0} \mathbf{B}_k^T(\mathbf{X}) \cdot \Big(\frac{\partial \mathbf{r}(\varphi(\mathbf{X}))}{\partial \bar{u}_k^s} \det D\varphi(\mathbf{X}) + \mathbf{r}(\varphi(\mathbf{X})) \frac{\partial}{\partial \bar{u}_k^s} \Big(\det D\varphi(\mathbf{X}) \Big) \Big) \, dA_{\mathbf{X}}$$

$$(3.19)$$

Expressing eq. 3.3 w.r.t. the undeformed configuration and therefore multiplication with the functional determinant necessitates the application of the product rule in expression 3.19. The occuring expressions are listed below:

$$\mathbf{r}(\varphi(\mathbf{X})) = \begin{bmatrix} r^1(\varphi(\mathbf{X})) \\ r^2(\varphi(\mathbf{X})) \end{bmatrix} \tag{3.20}$$

The indices in r^1 and r^2 denote the components of $\mathbf{r}$ in along the cartesian base vectors $\mathbf{e}_1$ and $\mathbf{e}_2$.

$$\frac{\partial \mathbf{r}(\varphi(\mathbf{X}))}{\partial \bar{u}_k^s} = \begin{bmatrix} \dfrac{\partial\, r^1(\varphi(\mathbf{X}))}{\partial \bar{u}_k^s} \\ \dfrac{\partial r^2(\varphi(\mathbf{X}))}{\partial \bar{u}_k^s} \end{bmatrix} \tag{3.21}$$

The derivative of the result of the force densities $\mathbf{r}(\mathbf{x})$ necessitates a derivative of the inner integral.

$$\frac{\partial \mathbf{r}(\varphi(\mathbf{X}))}{\partial \bar{u}_k^s} = \iint\limits_{\Omega^0 \cap D_{\mathbf{X}}} \left(\frac{\partial \mathbf{f}(\varphi(\mathbf{Y}))}{\partial \bar{u}_k^s} \det D\varphi(\mathbf{Y}) + \mathbf{f}(\varphi(\mathbf{Y})) \frac{\partial}{\partial \bar{u}_k^s}\Big(\det D\varphi(\mathbf{Y}) \Big) \right) dA_{\mathbf{Y}} \tag{3.22}$$

Next, the expressions for the functional determinants are developed:

$$\det D\varphi(\mathbf{Y}) = \det D\Big(\mathbf{Y} + \mathbf{u}^h(\mathbf{Y}) \Big) =$$

$$= \det \begin{bmatrix} \dfrac{\partial}{\partial Y^1} \\ \dfrac{\partial}{\partial Y^2} \end{bmatrix} \begin{bmatrix} Y^1 + u^{h1}(\mathbf{Y}) & Y^2 + u^{h2}(\mathbf{Y}) \end{bmatrix} = \tag{3.23}$$

$$= \left(1 + \frac{\partial u^{h1}(\mathbf{Y})}{\partial Y^1}\right)\left(1 + \frac{\partial u^{h2}(\mathbf{Y})}{\partial Y^2}\right) - \frac{\partial u^{h1}(\mathbf{Y})}{\partial Y^2}\frac{\partial u^{h2}(\mathbf{Y})}{\partial Y^1} =$$
$$= 1 + \frac{\partial u^{h1}(\mathbf{Y})}{\partial Y^1} + \frac{\partial u^{h2}(\mathbf{Y})}{\partial Y^2} + \frac{\partial u^{h1}(\mathbf{Y})}{\partial Y^1}\frac{\partial u^{h2}(\mathbf{Y})}{\partial Y^2} - \frac{\partial u^{h1}(\mathbf{Y})}{\partial Y^2}\frac{\partial u^{h2}(\mathbf{Y})}{\partial Y^1}$$

The derivation of the functional determinant by the degrees of freedom is derived by using

equations 3.11 and 3.23: (Repetition eq. 3.11)

$$\mathbf{u}^h(\mathbf{Y}) = \tilde{\mathbf{u}}^h(\mathbf{Y}) + \sum_{n=1}^{M_1} \mathbf{A}_n(\mathbf{Y}) \cdot \bar{\mathbf{u}}_n \tag{3.24}$$

Introducing equation 3.12 into 3.24 yields the displacement field, expressed w.r.t. the nodal displacements, by which the derivation is done:

$$\mathbf{u}^h(\mathbf{Y}) = \begin{bmatrix} u^{h^1}(\mathbf{Y}) \\ u^{h^2}(\mathbf{Y}) \end{bmatrix} = \begin{bmatrix} \tilde{u}^{h^1}(\mathbf{Y}) \\ \tilde{u}^{h^2}(\mathbf{Y}) \end{bmatrix} + \sum_{n=1}^{M_1} \begin{bmatrix} \bar{N}_n(Y^1, Y^2) & 0 \\ 0 & \bar{N}_n(Y^1, Y^2) \end{bmatrix} \begin{bmatrix} \bar{u}_n^1 \\ \bar{u}_n^2 \end{bmatrix} \tag{3.25}$$

With eq. 3.25, the derivation of the functional determinant can be carried out:

$$\frac{\partial}{\partial \bar{u}_k^1}\left(\det D\varphi(\mathbf{Y})\right) = \frac{\partial N_j(\mathbf{Y})}{\partial Y^1} + \frac{\partial N_j(\mathbf{Y})}{\partial Y^1}\frac{\partial u^{h^2}(\mathbf{Y})}{\partial Y^2} - \frac{\partial N_j(\mathbf{Y})}{\partial Y^2}\frac{\partial u^{h^2}(\mathbf{Y})}{\partial Y^1} \tag{3.26}$$

$$\frac{\partial}{\partial \bar{u}_k^2}\left(\det D\varphi(\mathbf{Y})\right) = \frac{\partial N_j(\mathbf{Y})}{\partial Y^2} + \frac{\partial N_j(\mathbf{Y})}{\partial Y^2}\frac{\partial u^{h^1}(\mathbf{Y})}{\partial Y^1} - \frac{\partial N_j(\mathbf{Y})}{\partial Y^1}\frac{\partial u^{h^1}(\mathbf{Y})}{\partial Y^2} \tag{3.27}$$

In a next step, the derivation of a bond force in equation 3.22 has to be done. For this purpose, equation 3.5 is reformulated to an easier form.

$$\mathbf{f} = c\left(\frac{l-L}{L}\right)\left(\frac{\mathbf{l}}{l}\right) = c\,\epsilon\,\mathbf{d} \tag{3.28}$$

with

$$L = |\mathbf{Y} - \mathbf{X}|$$

$$\mathbf{l} = \mathbf{Y} + \mathbf{u_Y} - \mathbf{X} - \mathbf{u_X}$$

$$l = |\mathbf{l}| \tag{3.29}$$

$$\epsilon = \frac{l-L}{L}$$

$$\mathbf{d} = \frac{\mathbf{l}}{l}$$

The derivation of $\mathbf{f}$ with respect to a degree of freedom leads to:

$$\frac{\partial \mathbf{f}(\mathbf{x})}{\partial \bar{u}_k^s} = c \left(\frac{\partial \epsilon}{\partial \bar{u}_k^s} \mathbf{d} + \epsilon \frac{\partial \mathbf{d}}{\partial \bar{u}_k^s} \right) \tag{3.30}$$

The derivatives in equation 3.30 are:

$$\frac{\partial \epsilon}{\partial \bar{u}_k^s} = \frac{\partial}{\partial \bar{u}_k^s} \left(\frac{l - L}{L} \right) = \frac{1}{L} \frac{\partial l}{\partial \bar{u}_k^s} \tag{3.31}$$

$$\frac{\partial \mathbf{d}}{\partial \bar{u}_k^s} = \frac{\partial}{\partial \bar{u}_k^s} \left(\frac{\mathbf{l}}{|\mathbf{l}|} \right) = \frac{1}{l} \frac{\partial \mathbf{l}}{\partial \bar{u}_k^s} - \frac{\mathbf{l}}{l^2} \frac{\partial l}{\partial \bar{u}_k^s} \tag{3.32}$$

with:

$$\frac{\partial l}{\partial \bar{u}_k^s} = \frac{\partial}{\partial \bar{u}_k^s} \left(|\mathbf{l}| \right) = \frac{1}{|\mathbf{l}|} \frac{\partial \mathbf{l}}{\partial \bar{u}_k^s} \cdot \mathbf{l} \tag{3.33}$$

$$\frac{\partial \mathbf{l}}{\partial \bar{u}_k^s} = \frac{\partial}{\partial \bar{u}_k^s} \left(\mathbf{Y} + \mathbf{u_Y} - \mathbf{X} - \mathbf{u_X} \right) = \left(N_j(\mathbf{Y}) - N_j(\mathbf{X}) \right) \mathbf{e}_s \tag{3.34}$$

Equations 3.33 and 3.34 express the change of length and direction of a deformed bond due to a variation of the degrees of freedom of the underlying element. As a bond is defined by its origin $\mathbf{x}$ and its end $\mathbf{y}$, the possibility arises that $\mathbf{x}$ and $\mathbf{y}$ are not located within the same, but adjacent elements which share a degree of freedom. The behavior of an entry of the Jacobian matrix is therefore significantly influenced by the discretization. Furthermore, the circular shape of the influence region $D_\mathbf{X}$ is not compatible with a meshgrid built of quadrilateral-shaped finite elements. Therefore, the inner integral of eq. 3.8 has to be examined in detail.

3.1.4 Numerical integration

For both the computation of the resulting force $\mathbf{r}$ in a point $\mathbf{x}$ (compare eq. 3.6) as well as the derivative of the latter (compare eq. 3.22), an integration over $D_\mathbf{X}$ is necessary. At this point, four central assumptions for this thesis are made.

1. The discretization is done with 4-node quadrilateral elements with element length Δ

and linear shape functions.

2. The length of the peridynamic horizon δ is fixed to an integer-multiple of Δ. Unless mentioned otherwise, $\delta = 3\,\Delta$ shall hold.

3. The discretizations of outer- and inner integral are chosen independently.

4. The outer integral is solved by using Gauss-Legendre quadrature.

The choice of an integer ratio between $\frac{\delta}{\Delta}$ provides an easier-to-implement template for $D_{\mathbf{X}}$, as if δ could be chosen freely. However, a release of this assumption could be implemented with the manageable effort using the subelementation techniques in subsections on pages 31 ff. , 34 ff. and 39 ff. The choice $\delta = 3\,\Delta$ provides the best tradeoff between accuracy and computational costs according to some preliminary tests not presented in the scope of this thesis. An independent choice of the discretizations of outer- and inner integral was chosen in order to investigate the results of different combinations of discretizations, because its effects could not be foreseen in advance. A computational setup using the same discretization for inner- and outer integral can be found in [Messmer 2020, p.35-36].

The following minimal example should aid up in the following derivations. Figure 3.1 displays a fully embedded peridynamic finite element. Fully embedded implies that the influence regions $D_{\mathbf{X}}$ of every point $\mathbf{X}$ inside the element are completely covering subelements. The system is minimal because it is described by eight degrees of freedom only. The nodal displacements of all embedding elements are set to zero in this example. (This assumption will be released at a further point). The whole meshgrid has dimensions $7\Delta \times 7\Delta$, and the domain of the outer integral Ω^0 is the ochre element in the middle. If not stated differently, all elements have the Young's modulus $E = 2.1 \cdot 10^{11}[\frac{\text{kN}}{\text{m}^2}]$ and $\Delta = 1[\text{m}]$.

The outer integral $\iint_{\Omega} da_{\mathbf{x}}$ is discretized with $N_{parent} = 2$, so called parent Gauss points (parent Gp) in each direction. The inner integral is evaluated in every parent Gauss point. Applying the second assumption from above, this means there is an individual influence region $D_{\mathbf{X}}$ originating from every parent Gauss point, depicted in colorful pairs of Gauss points and respective influence region in figure 3.1. As these influence regions are circular in shape with a fixed horizon length $\delta = 3\,\Delta$, there will be a number of elements which lie not within the horizon but are cut by it.
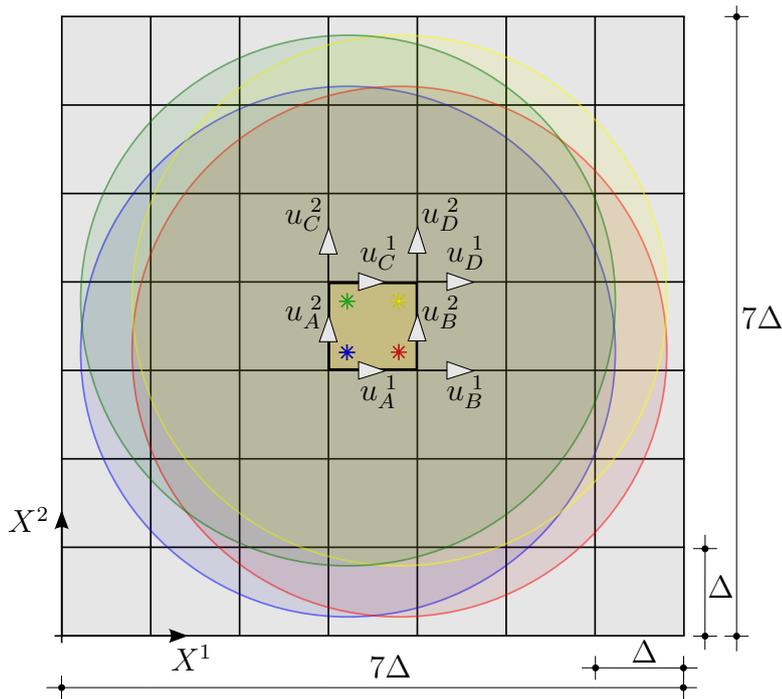
**Figure 3.1:** Minimal example ($N_{parent} = 2$)
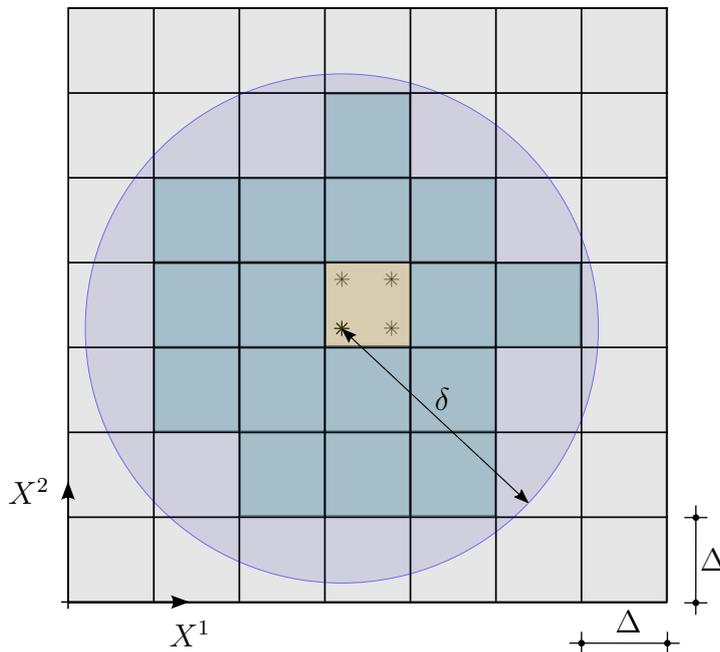
Figure 3.2: Middle element, uncut elements, cut elements of one parent Gauss point

For further reference, the element containing the parent Gauss point shall be called "middle element", the elements surrounding the middle element, but fully included in $D_{\mathbf{X}}$ are called "uncut elements", and the elements cut by $D_{\mathbf{X}}$ are denoted as "cut elements". The integrand over the uncut elements will be integrated using Gauß-Legendre (GL) quadrature,

see subsection appendix A.4.1. A requirement for GL quadrature to yield reliable results is
the continuity of the integrand, because GL quadrature uses Legendre-polynomials for the
approximation of the latter, which are continuous and smooth themselves. Discontinuous
integrands can lead to a severe loss in accuracy of the solution, as the jump in the inte-
grand must be approximated by Legendre polynomials of high order, which requires a high
number of Gauss points in return. Although the existence and continuity of the integrand
for physically meaningful displacement fields was proven in appendix A.1.2, GL quadrature
is not applicable to the inner element or the cut elements. Furthermore, it was shown in
app. A.1.2 that the integrand over the inner element is not defined for $\mathbf{X} = \mathbf{Y}$ and that this
discontinuity could not be removed. Therefore, GL quadrature needs a modification on the
inner element.

Figure 3.2 demonstrates that the cut elements are only partly covered by $D_{\mathbf{X}}$. The integrand
outside of the influence region is set to zero, regardless of being zero or not. This introduces a
discontinuity into the cut elements which needs to be treated by another quadrature scheme.

In the following sections, the numerical integration of the components of equation 3.19,
the resulting inner force

$$\mathbf{r}(\mathbf{x}) \;=\; \iint\limits_{\Omega^0 \cap D_{\mathbf{X}}} \mathbf{f}(\varphi(\mathbf{X}),\varphi(\mathbf{Y})) \det D\varphi(\mathbf{Y}) \, dA_{\mathbf{Y}}$$

and the derivative of the resulting inner force

$$\frac{\partial \mathbf{r}(\varphi(\mathbf{X}))}{\partial \bar{u}_k^s} \;=\; \iint\limits_{\Omega^0 \cap D_{\mathbf{X}}} \left(\frac{\partial \mathbf{f}(\varphi(\mathbf{Y}))}{\partial \bar{u}_k^s} \det D\varphi(\mathbf{Y}) + \mathbf{f}(\varphi(\mathbf{Y})) \frac{\partial}{\partial \bar{u}_k^s} \Big(\det D\varphi(\mathbf{Y}) \Big) \right) dA_{\mathbf{Y}}$$

are discussed.

Integration of uncut elements

The uncut elements are each discretized with N_{uncut} quadrature points in each direction.
The integrand over the middle elements is continuous and smooth and therefore suitable for
GL quadrature.

An important effect for the computation of the Jacobian matrix occurs from equation 3.34

when applied to the uncut elements (Repetition equation 3.34).

$$\frac{\partial \mathbf{l}}{\partial \bar{u}_k^s} = \frac{\partial}{\partial \bar{u}_k^s}\Big(\mathbf{Y} + \mathbf{u_Y} - \mathbf{X} - \mathbf{u_X}\Big) = \Big(N_j(\mathbf{Y}) - N_j(\mathbf{X})\Big)\mathbf{e}_s \tag{3.35}$$

The expression above computes the change of the vector of a deformed bond by the change of a nodal displacement. Because there is a set of uncut elements adjacent to the middle element and a set not in contact with them, eq. 3.34 can lead to two different cases:

Case 1: Adjacent

Computing a line of the Jacobian matrix of Newton's method (compare eq. A.56) can be interpreted as listing up the contributions of all nodal displacements that have an influence upon the resulting force in one specific degree of freedom. That specific degree of freedom must be a dof of the middle element of a family, depicted in ochre in figure 3.3. As the domain of integration is discretized by a meshgrid, begin and end of a bond and therefore the force acting between those points will be expressed by the nodal displacements of the elements containing begin and end.
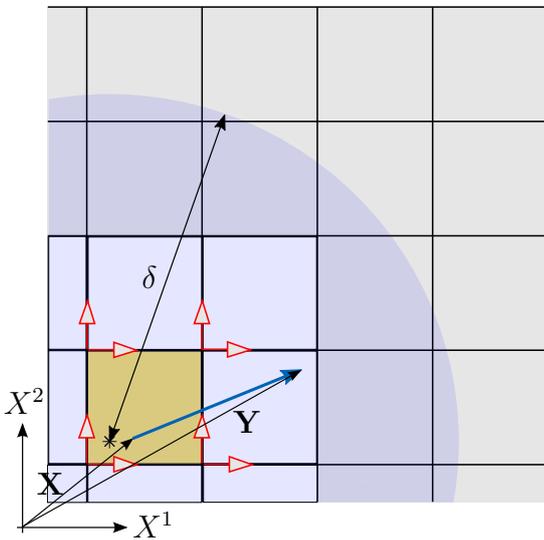

Figure 3.3: Shared dofs between middle- and adjacent uncut elements
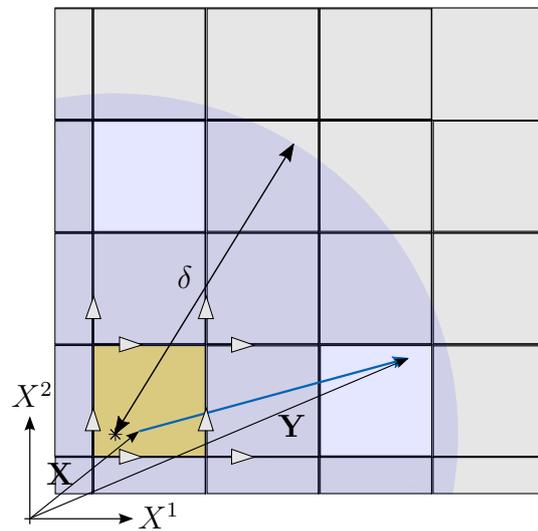

Figure 3.4: Shared dofs between middle- and non-adjacent uncut elements

As depicted in fig. 3.3, eight dofs (depicted in red) are shared between the ochre middle element and the surrounding uncut elements. This means that both begin and end of the blue bond will be affected by deriving by a shared dof, because both are "moved" when

shifting the position of the connecting node. Mathematically, this means that both terms

$$\frac{\partial \mathbf{l}}{\partial \bar{u}_k^s} = \Big(N_j(\mathbf{Y}) - N_j(\mathbf{X}) \Big) \mathbf{e}_s$$

in equation 3.35 exist.

Case 2: Not adjacent

A second subset of the uncut elements has no common dofs with the middle elements. Therefore, deriving by one of the middle element's dofs will not cause any change in position of the bond's end $\mathbf{Y}$, setting the end's contribution to 0.

$$\frac{\partial \mathbf{l}}{\partial \bar{u}_k^s} = \Big(\cancel{N_j(\mathbf{Y})}^{\ 0} - N_j(\mathbf{X}) \Big) \mathbf{e}_s$$

However, even non-adjacent uncut elements have a contribution to the main diagonal entries of the Jacobian matrix J of Newton's method, because the non-locality of the theory extends over the elements' boundaries. The displacement of the begin of the bonds connecting middle element and non-adjacent elements is a function of the dofs of the middle element. Although some uncut elements are not connected to the middle element in terms of dofs, they are connected indirectly by the bonds between them.

The rate of convergence of the integral over the uncut elements is determined by a minimal example, consisting of one fully embedded peridynamic element. The example will have an 8×8 - Jacobian matrix, because it consists of eight degrees of freedom. It's Jacobian was computed for an isotropic expansion of $0.01[\text{m}]$, compare figure 3.5.
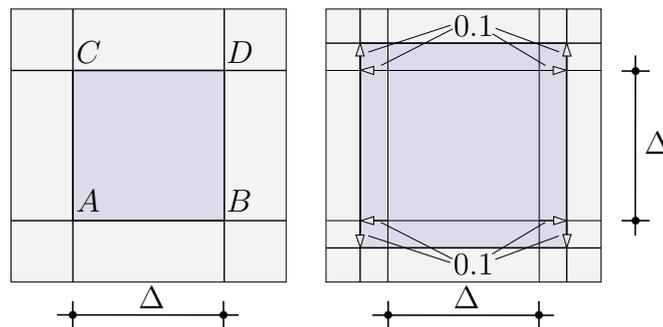

Figure 3.5: Isotropic expansion of an element

Figure 3.6 displays the rate of convergence of the resulting force r^1 in the lower left parent Gauss point due to the interaction with the uncut elements. The error of step i is defined as the difference between the results R_i and R_n of current- and final step n, based on the final

result:

$$\epsilon_i = \frac{r_i - r_n}{r_n} \tag{3.36}$$
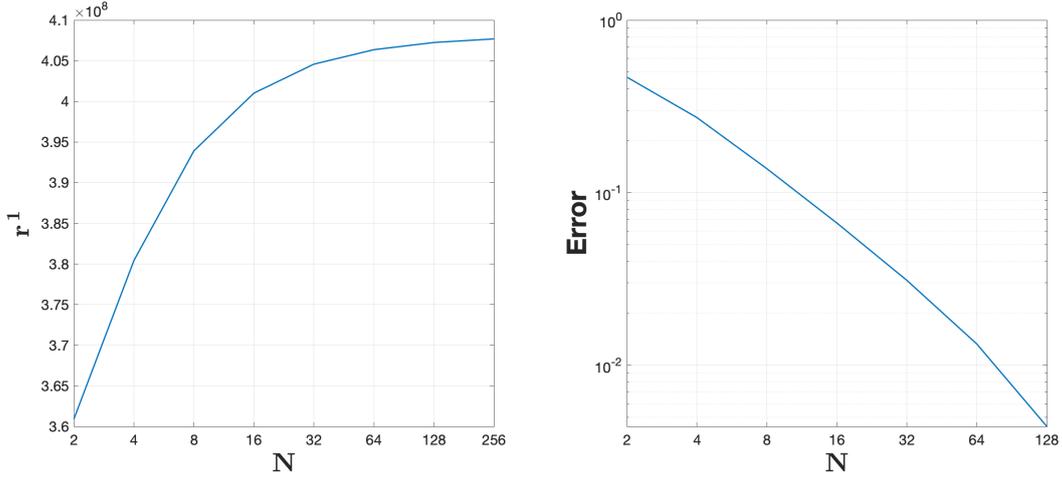
Figure 3.6: Convergence and error of uncut elements for isotropic expansion

In every iteration, the number of Gauss points was doubled. It can be seen that the convergence rate is low however, because even a doubling from 64 to 128 subordinate Gauss points results in a low difference of about $15 \cdot 10^{-3}$.

Integration of cut elements

As only a part of a cut element is covered by $D_{\mathbf{X}}$, the integrand over the element is truncated and therefore discontinuous. GL quadrature runs into difficulties here, because it relies on a polynomial p_n in order to approximate a discontinuous integrand $f(x)$, compare appendix A.4.1. As the polynomial $p_n(x)$ is a sum of products of constant coefficients a_i and powers of x, the polynomial is always continuous, because it is a composition of continuous functions [Meyberg and Vachenauer 1999, p.108]. Therefore, only a slow convergence with an increasing number of gauss points has to be expected.

An alternative to GL quadrature would be an integration with midpoint rule on a subelementation of the cut elements. The formula of the two-dimensional midpoint rule is given

by:

$$\int\limits_{X^1=a}^{b}\int\limits_{X^2=c}^{d} f(X^1,X^2)\,dX^2 dX^1 \approx \Delta_{X^1}\Delta_{X^2}\sum_{i=1}^{N_{X^1}}\sum_{j=1}^{N_{X^2}} f(X_i^1,X_j^2)$$

with

$$X_i^1 = a + i\frac{(b-a)}{N_{X^1}} \tag{3.37}$$

$$X_j^2 = c + j\frac{(d-c)}{N_{X^2}}$$

$$\Delta_{X^1} = \frac{(b-a)}{N_{X^1}} \;,\; \Delta_{X^2} = \frac{(d-c)}{N_{X^2}}$$

N_{X^1} and N_{X^2} hereby denote the numbers of subelements in both directions. In the scope of this work, both elements and subelements are quadrilaterals, therefore it holds: $N_{X^1} = N_{X^2} = N_{cut}$.
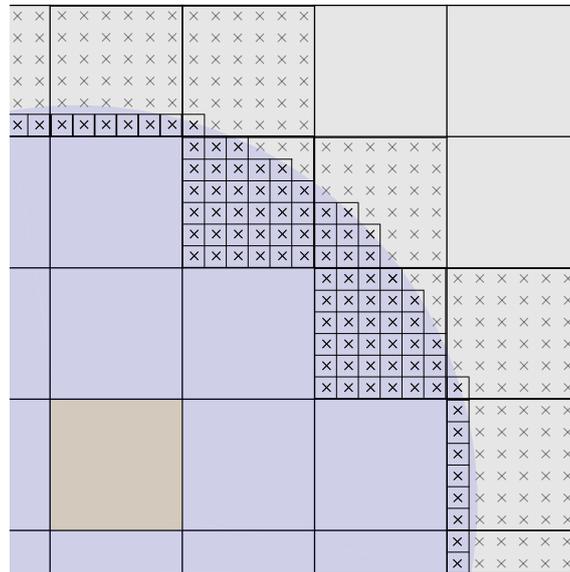

Figure 3.7: Quadrature points inside and outside $D_{\mathbf{X}}$ (N_{cut} = 6)

As depicted in figure 3.7, N_{cut} quadrature points are distributed in both directions X^1 and X^2. The quadrature points are located at the center of every subelement, while the integrand in the quadrature points outside the horizon is set to zero. It is obvious that subelements can

just approximate the shape of the circular influence region. So, there will be subelements which protrude over the edge of $D_{\mathbf{X}}$ and there will be indentations. This effect is reduced with increasing number of subelements per element.
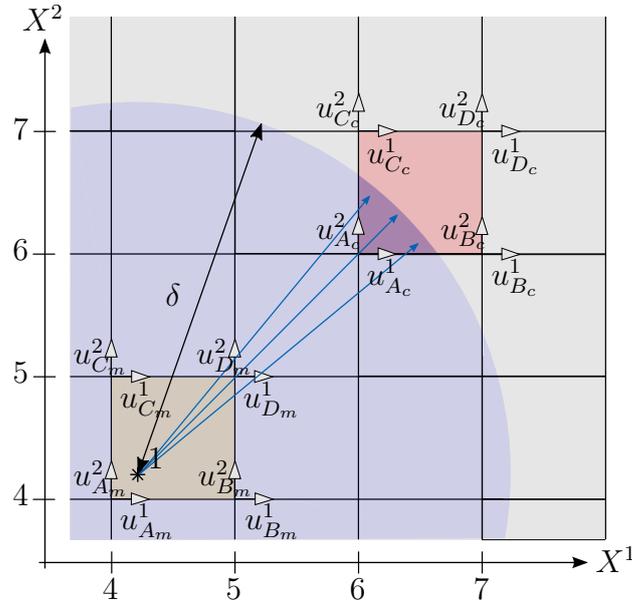

Figure 3.8: Minimal example for Gauss- and midpoint quadrature of cut element

Returning to the minimal example, the behavior of the numerical integration of a cut element is investigated now. The parent element is discretized with two parent gauss points in both directions. The depicted cut element is integrated with both GL quadrature and midpoint rule. The cut element has been given degrees of freedom for this particular example. The nodal displacements of both elements' nodes are given below:

$$\text{middle element:} \begin{bmatrix} u^1_{A_m} \\ u^1_{B_m} \\ u^1_{C_m} \\ u^1_{D_m} \\ u^2_{A_m} \\ u^2_{B_m} \\ u^2_{C_m} \\ u^2_{D_m} \end{bmatrix} = \begin{bmatrix} -0.01 \\ +0.01 \\ -0.01 \\ +0.01 \\ -0.01 \\ -0.01 \\ +0.01 \\ +0.01 \end{bmatrix} \quad ; \quad \text{cut element:} \begin{bmatrix} u^1_{A_c} \\ u^1_{B_c} \\ u^1_{C_c} \\ u^1_{D_c} \\ u^2_{A_c} \\ u^2_{B_c} \\ u^2_{C_c} \\ u^2_{D_c} \end{bmatrix} = \begin{bmatrix} 0 \\ 0 \\ 0.1 \\ 0.1 \\ 0 \\ 0.1 \\ 0 \\ 0.1 \end{bmatrix}$$

Figure 3.9 and 3.10 display the X^1 - component of the resulting force in parent gauss point 1.
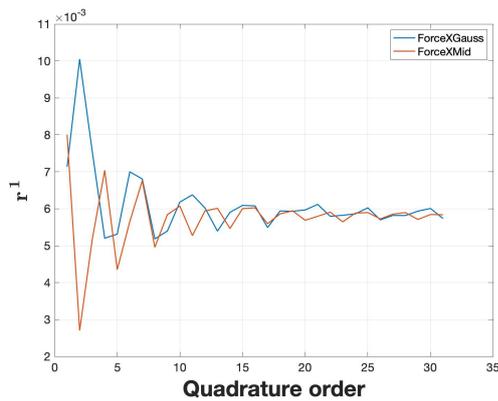
**Figure 3.9:** Comparison forces in X^1 direction Gauss - midpoint
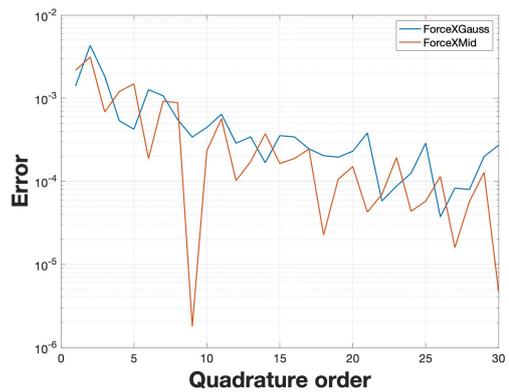
Figure 3.10: Comparison error in X^1 direction Gauss - midpoint

Both quadrature methods converge, and both methods oscillate heavily for few quadrature points. However, the error of GL quadrature vanishes more slowly than the error of the midpoint rule. Furthermore, GL quadrature yields larger results for r^1 than midpoint rule results. The reason for the oscillatory behavior for few quadrature points lies in the insufficient resolution of the domain of integration by both subelements and Gauss points. Both numerical methods split up the domain of integration into sets of sub-quadrilaterals respectively a set of sub-rectangles for Gaussian integration, because the weights of GL quadrature are not equal in size.
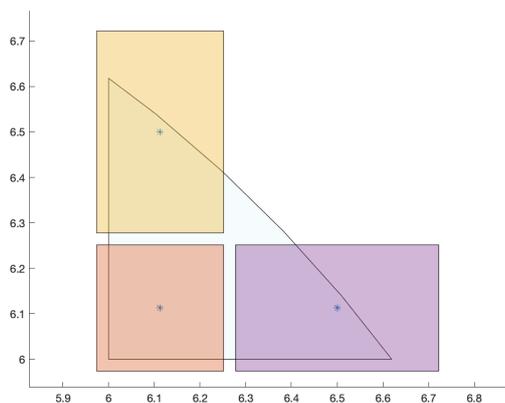
Figure 3.11: 3 x 3 Gauss points
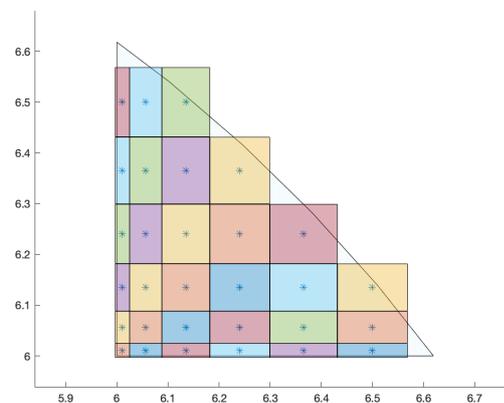
Figure 3.12: 11 x 11 Gauss points

As already depicted in figure 3.7, the subelements are just an approximation to the real shape of $D_{\mathbf{X}}$ over the cut element. Especially for a low number of quadrature points, this approximation can highly over- and underestimate the domain of integration, because the subelements either protrude over the edge of $D_{\mathbf{X}}$ or leave areas of it uncovered, compare figures 3.11 and 3.12. Here, the weights of the respective Gauss points were interpreted as areas. The result oscillates, because the coverage of the cut area changes with increasing

number of quadrature points.

The influence of the cut elements in comparison to the uncut elements to the Jacobian matrix has to be determined yet. The uncut elements cover a larger part of $D_\mathbf{X}$, as the ratio of their areas demonstrate:

$$\frac{A_{cut}}{A_{uncut}} = \frac{\Delta^2 \pi - 1 - 16}{16} = 0{,}705$$

On average, the cut elements have greater distance to the origin of $D_\mathbf{X}$ than the uncut elements. Because the force density of a bond is reciprocal to it's length (compare denominator in eq. 3.3), it can be assumed, that the cut elements will contribute less to the Jacobian matrix than the uncut elements. An exact ratio of the contributions to the Jacobian matrix however has to be left to the respective problem.

In a last step, the Frobenius norm of the Jacobian matrix resulting from the cut elements with midpoint rule is computed for an increasing number of subelements. The Frobenius norm serves as a measure for the similarity of the Jacobian matrices for different subelementations. For a $N \times M$ - matrix A, it is given by: [Bollhöfer and Mehrmann 2013, p.115]

$$\|A\| = \sqrt{\sum_{i=1}^{N} \sum_{j=1}^{M} (A_{ij})^2} \tag{3.38}$$

The results in the table below 3.1 show that the changes in the Frobenius norm are small. The convergence of the inner integral over the cut elements is depicted in figure 3.10. Again,

N_{cut}	$\|J_{cut}\|$
2	8.5005e+09
4	8.9542e+09
8	8.8495e+09
16	8.8555e+09
32	8.8588e+09
64	8.8533e+09
128	8.8574e+09

Table 3.1: Frobenius norm of Jacobian matrix

the setup was an isotropic expansion by an absolute value for the nodal displacements of 0.01, evaluated in one of the four parent Gauss points.
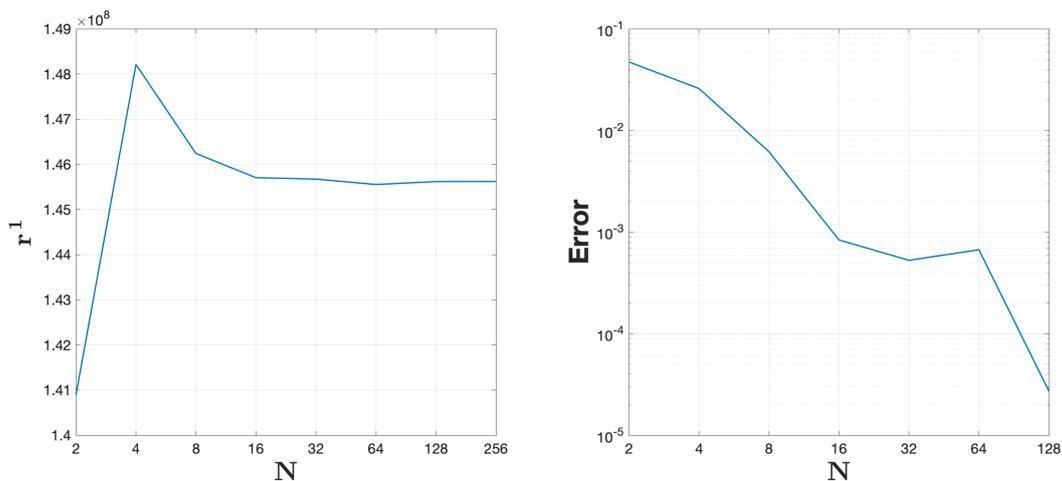
Figure 3.13: Convergence and error of cut elements for isotropic expansion

In comparison to the integral over the uncut elements (see figure 3.6), the rate of convergence in figure 3.13 is higher. The oscillatory behavior of the integral remains even for a high number of quadrature points. A detailed convergence study of systems consisting of more than one element will be done in chapter 5.2.1.

Integration of the inner element

A straightforward discretization of the integral over the middle element in $\mathbf{Y}$ with N_{middle} Gauss points (see figure 3.14) displays strong oscillatory behavior and yields unreliable results, compare figure 3.15.
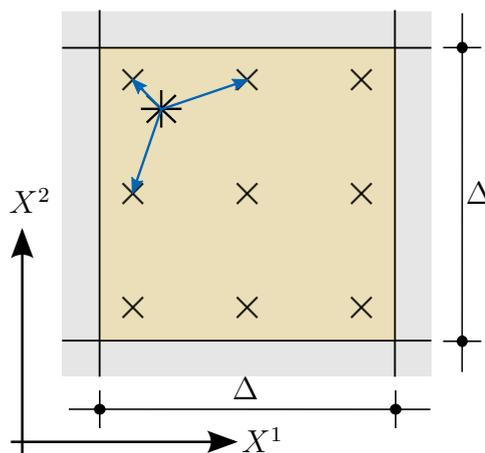
Figure 3.14: 2 Parent Gauss points, 3 middle element Gauss points

Figure 3.15 displays the resulting force in X^1 - direction for the middle element of the minimal example for an isotropic expansion by $u = 0.1$ of the element and a material parameter $c = 1$.

The results are not reliable even for 28 Gauss points in both directions in this particular example.
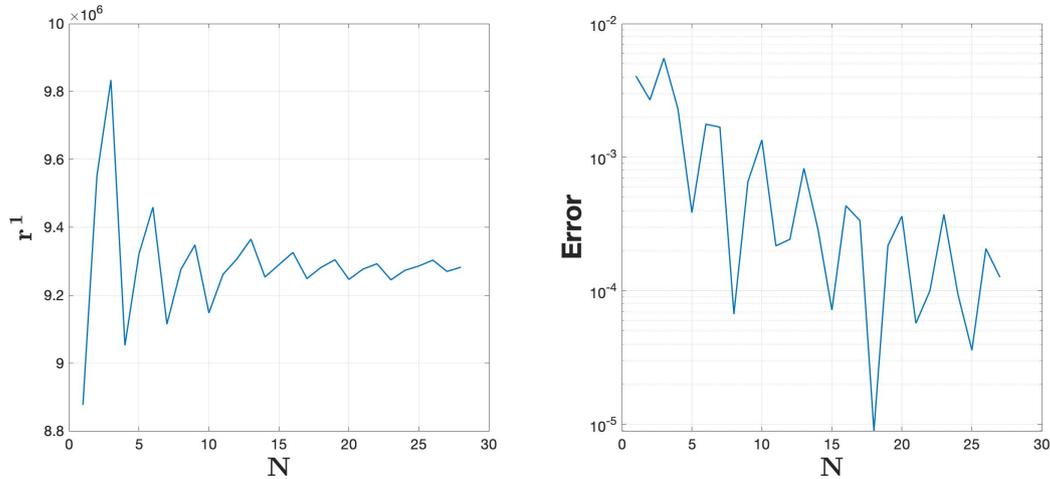
Figure 3.15: Oscillations and error of straightforward quadrature for isotropic expansion of the middle element

As explained in section appendix A.1.2 and depicted in figure appendix A.3, the integrand is not continuous for $\mathbf{X} = \mathbf{Y}$ and displays strong gradients close to this point, compare figure 3.16.
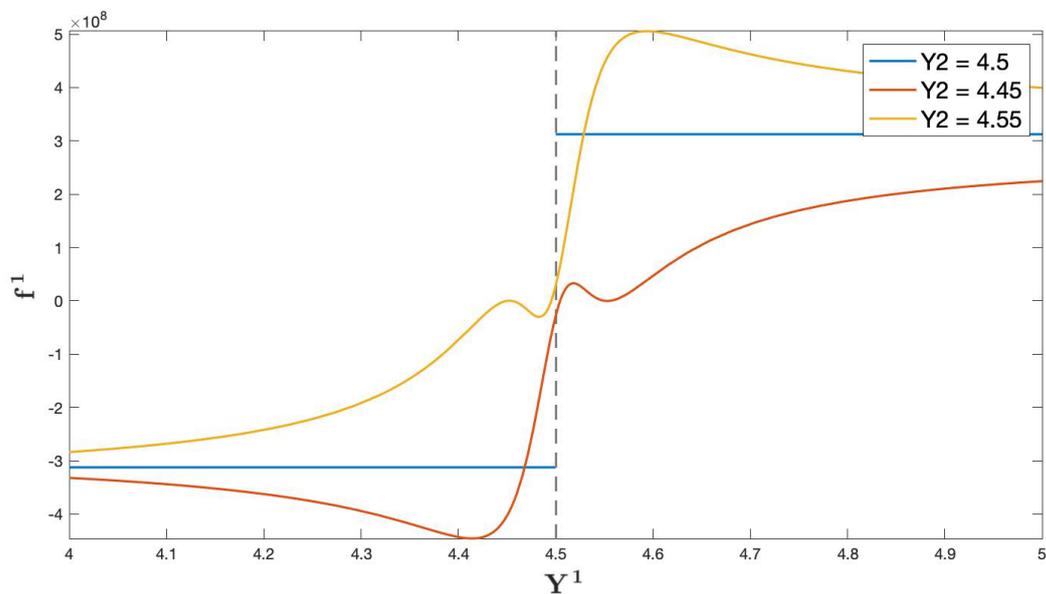
Figure 3.16: Discontinuity for $\mathbf{X} = \mathbf{Y} = \begin{bmatrix} 4.5 \\ 4.5 \end{bmatrix}$ of middle element

Depicted are three cuts through the graph of the X^1 - component of the force density over the middle element with respect to $\mathbf{X} = [4.5 \, ; 4.5]$. The blue line represents the cut through

this point along the Y^1- axis, jumping left and right of $Y^1 = 4.5$. The lines in orange and yellow are cuts parallel to the blue one at adjacent X^2 - coordinates. Even a straightforward quadrature of the inner element should avoid a coincidence of parent Gauss point and subordinate Gauss point, thus averting an evaluation of the inner integral in a point where the integrand is not defined. However, classical GL quadrature suffers from a severe loss of precision in vicinity of singularities or regions of insufficient smoothness as jumps in the integrand are poorly approximated by continuous polynomials. Furthermore, the meshgrids of parent- and subordinate Gauss points are not coordinated to each other. The oscillations in fig. 3.15 result from oscillating distances between parent- and subordinate quadrature points due to a refinement of the subordinate meshgrid and therefore an oscillating resolution of the input-sensitive denominators of eq. 3.5.

The problem is overcome by a subelementation of the middle element itself. In the scope of this thesis, this is done in two different ways explained in the following.

A: Duffy transformation

The Duffy transformation is a variable transformation method to integrate weakly singular integrands [Mousavi and Sukumar 2010, p.1] by mapping the domain of integration onto a parent domain and shorten out the singularity with the Jacobian of the map [Mousavi and Sukumar 2010, p.2]. Equation 3.6 and it's derivatives consist of integrals over the deformed configuration which were expressed w.r.t. the undeformed configuration by substitution of the deformed coordinates $\mathbf{y}$ by maps of the undeformed ones $\varphi(\mathbf{Y})$. This transformation was necessary to pull back the domain of integration to a known configuration. The same approach is now applied successively in order to transform the integral into a form which is more suitable for GL quadrature. The necessary transformations are depicted in figure 3.18. As the derivations shall be valid for large displacements, the integral to begin with is over the deformed configuration, compare step 4 in fig. 3.18. Because the change from the deformed to the deformed basis has to be done for all together cut, uncut and middle elements, this transformation

$$\mathbf{r}(\mathbf{x}) = \iint\limits_{\Omega \cap D_{\mathbf{x}}} \mathbf{f}(\mathbf{x},\mathbf{y}) \, da_{\mathbf{y}} = \iint\limits_{\Omega^0 \cap D_{\mathbf{X}}} \mathbf{f}(\varphi(\mathbf{X}), \varphi(\mathbf{Y})) \det D\varphi(\mathbf{Y}) \, dA_{\mathbf{Y}}$$

is explained in appendix A.1.1.

The undeformed configuration of an element itself is image of a function κ, which represents the undeformed geometry by a sum of products of form functions and the respective

nodal coordinates:

$$\mathbf{Y} \;=\; \kappa(\boldsymbol{\theta}) \;\; \text{by} \;\; \begin{bmatrix} Y^1 \\ Y^2 \end{bmatrix} = \begin{bmatrix} N_1(\boldsymbol{\theta})R_A^1 + N_2(\boldsymbol{\theta})R_B^1 + N_3(\boldsymbol{\theta})R_C^1 + N_4(\boldsymbol{\theta})R_D^1 \\ N_1(\boldsymbol{\theta})R_A^2 + N_2(\boldsymbol{\theta})R_B^2 + N_3(\boldsymbol{\theta})R_C^2 + N_4(\boldsymbol{\theta})R_D^2 \end{bmatrix} \tag{3.39}$$

As depicted in 3.18, the set of departure of map κ is a unit-quadrilateral. The θ^1, θ^2 - coordinate system is located in the lower left corner of this quadrilateral. By this choice of origin, the form functions are the following:

$$\begin{aligned} N_1(\theta^1, \theta^2) &= (1 - \theta^1)(1 - \theta^2) \\ N_2(\theta^1, \theta^2) &= (\theta^1)(1 - \theta^2) \\ N_3(\theta^1, \theta^2) &= (1 - \theta^1)(\theta^2) \\ N_3(\theta^1, \theta^2) &= (\theta^1)(\theta^2) \end{aligned} \tag{3.40}$$

Furthermore, it has to be noted that the position of the parent Gauss points is now computed by the map κ too. The position of the parent Gauss point is denoted by P in the unit quadrilateral.

$$\mathbf{X} \;=\; \kappa\left(\boldsymbol{\theta}_P\right) \tag{3.41}$$

The coordinates $\boldsymbol{\theta}_P$ are the points obtained from GL quadrature on the interval $[0,1]$. The integral over the middle element $D_{\mathbf{X}m}$ in eq. 3.6 can now be pulled back to the θ^1, θ^2 - coordinate system:

$$\begin{aligned} \iint\limits_{\Omega \cap D_{\mathbf{x}m}} \mathbf{f}(\mathbf{x}, \mathbf{y}) \, dy^2 dy^1 &= \iint\limits_{\Omega^0 \cap D_{\mathbf{X}m}} \mathbf{f}(\varphi(\mathbf{X}), \varphi(\mathbf{Y})) \det D\varphi(\mathbf{Y}) \, dY^2 dY^1 = \\ &= \iint\limits_{\Omega^0 \cap D_{\mathbf{X}m}} \mathbf{f}(\varphi(\mathbf{X}), \varphi(\mathbf{Y})) \det D\varphi(\mathbf{Y}) \det D\kappa(\boldsymbol{\theta}) \, dY^2 dY^1 \\ &= \int_0^1 \int_0^1 \mathbf{f}\left(\varphi(\kappa(\boldsymbol{\theta}_{\mathbf{P}})), \, \varphi(\kappa(\boldsymbol{\theta}))\right) \det\left(\frac{\partial y^i}{\partial Y^j}\right) \det\left(\frac{\partial Y^k}{\partial \theta^l}\right) d\theta^2 d\theta^1 \end{aligned} \tag{3.42}$$

with:

$$\det\left(\frac{\partial Y^k}{\partial \theta^l}\right) = \begin{vmatrix} \dfrac{\partial Y^1}{\partial \theta^1} & \dfrac{\partial Y^1}{\partial \theta^2} \\[2em] \dfrac{\partial Y^2}{\partial \theta^1} & \dfrac{\partial Y^2}{\partial \theta^2} \end{vmatrix}$$

$$\begin{aligned}
\frac{\partial Y^1}{\partial \theta^1} &= (-R_A^1 + R_B^1) + \theta^2(R_A^1 - R_B^1 - R_C^1 + R_D^1) \\
\frac{\partial Y^1}{\partial \theta^2} &= (-R_A^1 + R_C^1) + \theta^1(R_A^1 - R_B^1 - R_C^1 + R_D^1) \\
\frac{\partial Y^2}{\partial \theta^1} &= (-R_A^2 + R_B^2) + \theta^2(R_A^2 - R_B^2 - R_C^2 + R_D^2) \\
\frac{\partial Y^2}{\partial \theta^2} &= (-R_A^2 + R_C^2) + \theta^1(R_A^2 - R_B^2 - R_C^2 + R_D^2)
\end{aligned}$$

(3.43)

Up to now, the integral was expressed w.r.t the θ^1, θ^2 - coordinate system. $\boldsymbol{\theta_P}$ denotes the position of the parent Gauss point on this area. As explained in appendix A.1.2, the integrand is not continuous for $\mathbf{X} = \mathbf{Y}$, respectively $\boldsymbol{\theta} = \boldsymbol{\theta_P}$. The integral over the unit-quadrilateral is now divided into four sub-triangles (compare figure 3.18). This subdivision places the discontinuity into the corners of the four subtriangles. Now, the Duffy transformation can be applied. According to [Mousavi and Sukumar 2010, p.2], standard Duffy transformation is a map of an integral over a triangle to a quadrilateral:
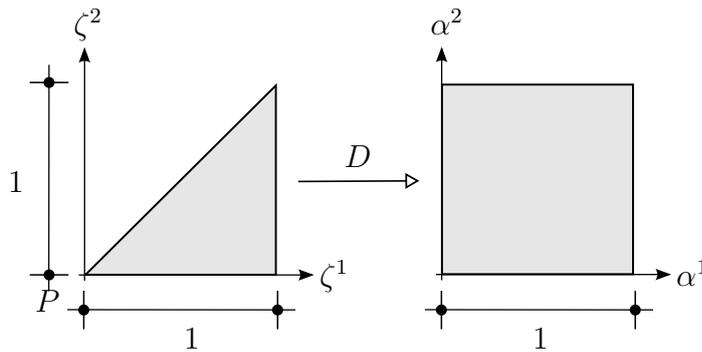

Figure 3.17: Duffy transformation

Duffy transformation for $1/r$ - singularity:

$$\boldsymbol{\zeta} = D(\boldsymbol{\alpha}) \quad \text{by} \quad \begin{bmatrix} \zeta^1 \\ \zeta^2 \end{bmatrix} = \begin{bmatrix} \alpha^1 \\ \alpha^1 \alpha^2 \end{bmatrix}$$

(3.44)

The Jacobian of the Duffy transformation enables shortening out a component of the denom-

inator, thus rendering the kernel of the integral smooth enough for GL quadrature [Mousavi and Sukumar 2010, p.2]:

$$
\begin{aligned}
\int_{\zeta^1=0}^{1} \int_{\zeta^2=0}^{\zeta^1} \frac{f(\zeta^1, \zeta^2)}{(\zeta^{1^2} + \zeta^{2^2})^{\frac{1}{2}}} \, d\zeta^2 d\zeta^1 \; &= \\
= \int_{\alpha^1=0}^{1} \int_{\alpha^2=0}^{1} \frac{f(\alpha^1, \alpha^2)}{(\alpha^{1^2} + (\alpha^1 \alpha^2)^2)^{\frac{1}{2}}} \, \det\left(\frac{\partial \zeta^i}{\partial \alpha^j}\right) d\alpha^2 d\alpha^1 \; &= \\
= \int_{\alpha^1=0}^{1} \int_{\alpha^2=0}^{1} \frac{f(\alpha^1, \alpha^2)}{(\alpha^{1^2} + (\alpha^1 \alpha^2)^2)^{\frac{1}{2}}} \, \alpha^1 d\alpha^2 d\alpha^1 \; &= \\
= \int_{\alpha^1=0}^{1} \int_{\alpha^2=0}^{1} \frac{f(\alpha^1, \alpha^2)}{(1 + \alpha^{2^2})^{\frac{1}{2}}} \, d\alpha^2 d\alpha^1 &
\end{aligned}
\tag{3.45}
$$

It is evident that the denominator of 3.45 cannot become 0 for $[\alpha^1, \alpha^2] \in [0,1]$. In a last step, the sub-triangles from step 2 in equation 3.18 have to be mapped to the Duffy-triangle. The map is done by a parametrization of the sub-triangles with the $[\zeta^1, \zeta^2]$ - coordinates of the Duffy-triangle:

$$
\boldsymbol{\theta} = \Psi(\boldsymbol{\zeta}) \quad \text{by} \quad \begin{bmatrix} \theta^1 \\ \theta^2 \end{bmatrix} = \begin{bmatrix} P^1 + \zeta^1(A_j^1 - P^1) + \zeta^2(A_{j+1}^1 - A_j^1) \\ P^2 + \zeta^1(A_j^2 - P^2) + \zeta^2(A_{j+1}^2 - A_j^2) \end{bmatrix} \quad, \quad \zeta^2 \leq \zeta^1
\tag{3.46}
$$

All transformations mentioned above are depicted in fig. 3.18. It depicts the Duffy quadrilateral at the bottom, mapped to consecutive configurations and ending up in the deformed configuration. In order to express the integral over the deformed configuration by the gauss points over the Duffy-quadrilateral, the steps 1 to 4 in fig. 3.18 have to be done in reverse order.

Step 4: Map undeformed to deformed element:

$$\mathbf{y} = \varphi(\mathbf{Y}) \quad \text{by} \quad \begin{bmatrix} y^1 \\ y^2 \end{bmatrix} = \begin{bmatrix} Y^1 + U^1(Y^1, Y^2) \\ Y^2 + U^2(Y^1, Y^2) \end{bmatrix}$$

compare subsection appendix A.1.1.

Step 3: Map unit quadrilateral to undeformed element in meshgrid:

$$\mathbf{Y} = \kappa(\boldsymbol{\theta}) \quad \text{by} \quad \begin{bmatrix} Y^1 \\ Y^2 \end{bmatrix} =$$

$$= \begin{bmatrix} N_1(\boldsymbol{\theta})R_A^1 + N_2(\boldsymbol{\theta})R_B^1 + N_3(\boldsymbol{\theta})R_C^1 + N_4(\boldsymbol{\theta})R_D^1 \\ N_1(\boldsymbol{\theta})R_A^2 + N_2(\boldsymbol{\theta})R_B^2 + N_3(\boldsymbol{\theta})R_C^2 + N_4(\boldsymbol{\theta})R_D^2 \end{bmatrix}$$

Step 2: Map triangle on sub-triangle:

$$\boldsymbol{\theta} = \Psi(\boldsymbol{\zeta}) \quad \text{by} \quad \begin{bmatrix} \theta^1 \\ \theta^2 \end{bmatrix} =$$

$$= \begin{bmatrix} P^1 + \zeta^1(A_j^1 - P^1) + \zeta^2(A_{j+1}^1 - A_j^1) \\ P^2 + \zeta^1(A_j^2 - P^2) + \zeta^2(A_{j+1}^2 - A_j^2) \end{bmatrix} \ , \ \zeta^2 \le \zeta^1$$

Step 1: Duffy transformation:

$$\boldsymbol{\zeta} = D(\boldsymbol{\alpha}) \quad \text{by} \quad \begin{bmatrix} \zeta^1 \\ \zeta^2 \end{bmatrix} = \begin{bmatrix} \alpha^1 \\ \alpha^1 \alpha^2 \end{bmatrix}$$

Figure 3.18: Steps of transformation from deformed configuration to Duffy-quadrilateral

The expressions A_j^1, A_{j+1}^1, ... denote the nodal coordinates of the θ^1, θ^2 - quadrilateral. Please note that their numeration deviates from the nodal order of the X^1, X^2 - quadrilateral.

Combining all transformation steps above leads to an integral over the Duffy-quadrilateral:

$$
\iint\limits_{\Omega \cap D_{\mathbf{x}m}} \mathbf{f}(\mathbf{x}, \mathbf{y}) \, dy^2 dy^1 =
$$

$$
= \int_0^1 \int_0^1 \mathbf{f}\Big(\varphi(\kappa(\boldsymbol{\theta}_\mathbf{P})) , \, \varphi(\kappa(\psi(D(\boldsymbol{\alpha})))) \Big) \det\left(\frac{\partial y^i}{\partial Y^j}\right) \det\left(\frac{\partial Y^k}{\partial \theta^l}\right) \det\left(\frac{\partial \theta^m}{\partial \zeta^n}\right) \det\left(\frac{\partial \zeta^o}{\partial \alpha p}\right) d\alpha^2 d\alpha^1
$$

$$
(3.47)
$$

A convergence analysis of the Duffy-subelementation is done together with the tanh-sinh-quadrature, discussed in the following.

B: Subelementation and tanh-sinh quadrature

The tanh-sinh quadrature (compare subsection appendix A.4.2) is a quadrature method insensitive to certain endpoint singularities and therefore very promising for the integration of the middle element on a subelementation with the following transformation rule (1-D):

$$
I \;=\; \int_{-1}^{1} f(x)\, dx \;=\; \int_{-\infty}^{\infty} f(\psi(t))\, \psi^{'}(t)\, dt
$$

by

$$
\psi(t) \;=\; \tanh(\lambda\, \sinh(t))
$$

$$
\psi^{'}(t) \;=\; \frac{\lambda \cosh(t)}{\cosh^{2}(\lambda\, \sinh(t))}
$$

$$
\text{with } \lambda \;=\; \frac{\pi}{2}
$$

(3.48)

In a discretized form, the integral from $-\infty$ to ∞ is replaced by a finite sum:

$$
\int_{-\infty}^{\infty} f(\psi(t))\, \psi^{'}(t)\, dt \;\approx\; h \sum_{j=-n}^{n} f(\psi(j \cdot h))\, \psi^{'}(j \cdot h)
$$

(3.49)

This approximation achieves remarkable precision with a relatively small number of support points in positive and negative direction, compare appendix A.4.2. Furthermore, the quadrature can be easily expended to two dimensions.

The peridynamic integrand has no singularity, but it is not defined for $\mathbf{Y} = \mathbf{X}$. As derived in app. A.1.2, this gap cannot be removed, so the function remains discontinuous.
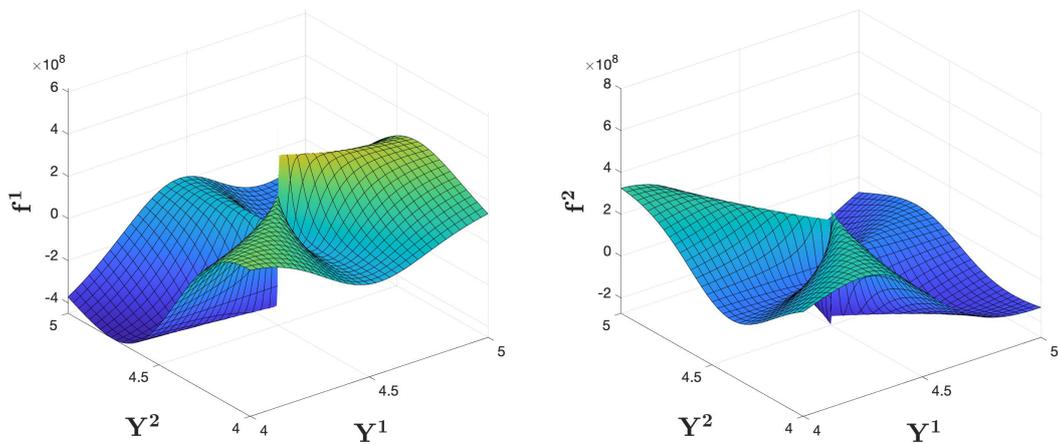

Figure 3.19: Discontinuity of middle element's integrand for $\mathbf{X} = \mathbf{Y} = \begin{bmatrix} 4.5 \\ 4.5 \end{bmatrix}$

The domain of integration is split into four subrectangles (compare fig. 3.20), which intersect at **X**. The integral over the middle element is then divided into four subintegrals, which are evaluated with tanh-sinh quadrature:

Step 4 + Step 3:
compare figure 3.18

Step 2: Map quadrilateral on sub-rectangle:

$$\boldsymbol{\theta} = \gamma(\boldsymbol{\psi}) \text{ by } \begin{bmatrix} \theta^1 \\ \theta^2 \end{bmatrix} =$$

$$= \begin{bmatrix} N_1(\boldsymbol{\psi})a_s^1 + N_2(\boldsymbol{\psi})b_s^1 + N_3(\boldsymbol{\psi})c_s^1 + N_4(\boldsymbol{\psi})d_s^1 \\ N_1(\boldsymbol{\psi})a_s^2 + N_2(\boldsymbol{\psi})b_s^2 + N_3(\boldsymbol{\psi})c_s^2 + N_4(\boldsymbol{\psi})d_s^2 \end{bmatrix}$$

with $s = 1, 2, 3, 4$

Step 1: tanh-sinh - quadrature:

$$\psi^1(t_j^1) = \tanh(\frac{1}{2}\pi \sinh(j \cdot h))$$

$$\psi^2(t_k^2) = \tanh(\frac{1}{2}\pi \sinh(k \cdot h))$$
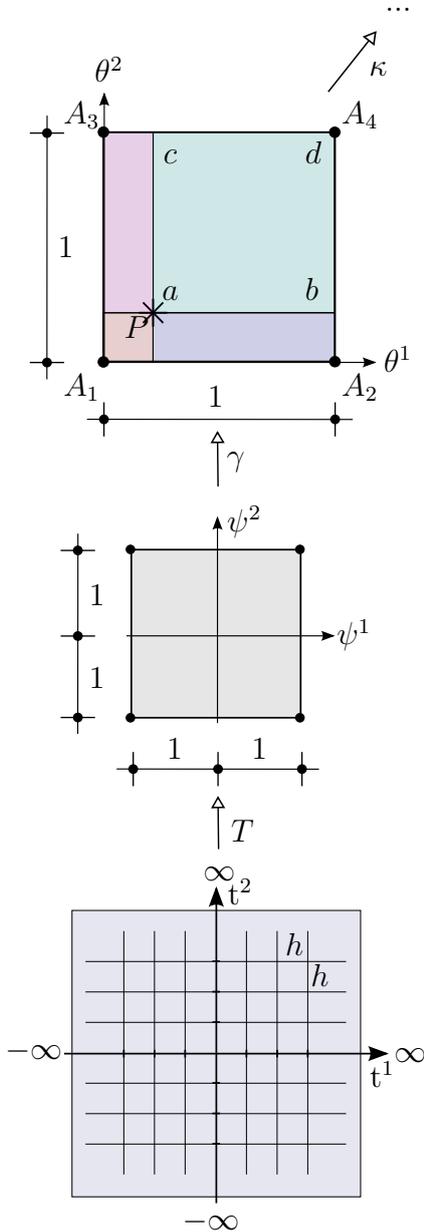
Figure 3.20: Steps of transformation from deformed configuration to tanh-sinh - domain

It has to be noted that in figure 3.20, step 4, the already discretized coordinates t_j^1 and t_k^2 have been used.

As explained in subsection appendix A.1.2, the integrand is continuous for physically rea-

sonable displacement fields, implying the continuity of the integrand over the subquadrilaterals. The tanh-sinh quadrature owes it's insensitivity to endpoint singularities the double-exponential decline of the differentiated substitution functions when t^1, $t^2 \rightarrow \infty$. The transformation of the integral over a rectangular, two dimensional problem is given below. Because the domain of integration is rectangular, the coordinates t^1, t^2 are independent of each other, simplifying the functional determinant to a simple product of the derivatives of $v^1(t^1), v^2(t^2)$:

$$\boldsymbol{\psi} = T(\mathbf{t})$$

$$\begin{bmatrix} \psi^1 \\ \psi^2 \end{bmatrix} = \begin{bmatrix} \tanh(\lambda \ \sinh(t^1)) \\ \tanh(\lambda \ \sinh(t^2)) \end{bmatrix}$$

$$\int_{-1}^{1} \int_{-1}^{1} f(\psi^1, \ \psi^2) \, d\psi^2 \, d\psi^1 = \int_{-\infty}^{\infty} \int_{-\infty}^{\infty} f(\psi^1(t^1), \psi^2(t^2)) \, \det D\,T(\mathbf{t}) \, dt^2 dt^1$$

$$\det D\,T(\mathbf{t}) = \det\left(\frac{\partial \psi^o}{\partial t^p}\right) = \det \begin{bmatrix} \dfrac{\partial \psi^1}{\partial t^1} & \dfrac{\partial \psi^1}{\partial t^2} \\[2ex] \dfrac{\partial \psi^2}{\partial t^1} & \dfrac{\partial \psi^2}{\partial t^2} \end{bmatrix} = \det \begin{bmatrix} \dfrac{\lambda \cosh(t^1)}{\cosh^2(\lambda \ \sinh(t^1))} & 0 \\[3ex] 0 & \dfrac{\lambda \cosh(t^2)}{\cosh^2(\lambda \ \sinh(t^2))} \end{bmatrix} =$$

$$= \left(\frac{\lambda \cosh(t^1)}{\cosh^2(\lambda \ \sinh(t^1))}\right)\left(\frac{\lambda \cosh(t^2)}{\cosh^2(\lambda \ \sinh(t^2))}\right)$$

$$(3.50)$$

Together with equation 3.50, the approximation of the inner integral of the middle element with the tanh-sinh-quadrature can be written down:

$$I = \iint\limits_{\Omega \cap D_{\mathbf{x}m}} \mathbf{f}(\mathbf{x}, \mathbf{y}) \, dy^2 dy^1 =$$

$$= \int_{-\infty}^{\infty} \int_{-\infty}^{\infty} \mathbf{f}\Big(\varphi(\kappa(\boldsymbol{\theta}_{\mathbf{P}})), \ \varphi(\kappa(\gamma(T(\mathbf{t}))))\Big) \det\left(\frac{\partial y^i}{\partial Y^j}\right) \det\left(\frac{\partial Y^k}{\partial \theta^l}\right) \det\left(\frac{\partial \theta^m}{\partial \psi^n}\right) \det\left(\frac{\partial \psi^o}{\partial t^p}\right) dt^2 dt^1$$

$$(3.51)$$

After the discretization, one obtains:

$$I \approx \sum_{a=-n}^{n} \sum_{b=-n}^{n} \mathbf{f}\left(\varphi(\kappa(\boldsymbol{\theta_P})) ,\, \varphi(\kappa(\gamma(T(\, a{\cdot}h,\, b{\cdot}h\,)))) \right) \det\left(\frac{\partial y^i}{\partial Y^j} \right) \det\left(\frac{\partial Y^k}{\partial \theta^l} \right) \det\left(\frac{\partial \theta^m}{\partial \psi^n} \right) \det\left(\frac{\partial \psi^o}{\partial t^p} \right) h^2$$

(3.52)

Depicted in fig. 3.21 are the weights for 5×5 quadrature points [Ata and Sahin 2018, p.31]. In comparison to the GL quadrature, the abscissas ψ^1, ψ^2 are approaching the domain's limits $1/-1$ extremely fast due to the double exponential dependency on their parameters t^1, t^2.
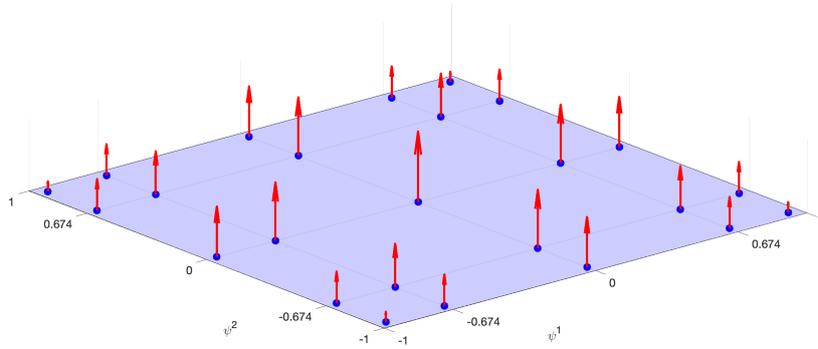
Figure 3.21: Weights of the tanh-sinh quadrature

Depicted in figure 3.22 are cuts through the right graph in figure 3.19, once for the X^2-values kept constant, once for the X^1-values kept constant throughout the cut. The yellow line, passing through the the point $\mathbf{Y} = \mathbf{X}$ is not continuous there. Although the integrand can have large gradients, especially in the vicinity of the discontinuity, their behavior is not exponential and therefore effectively suppressed by the double-exponentially decaying derivatives of the substitution function.
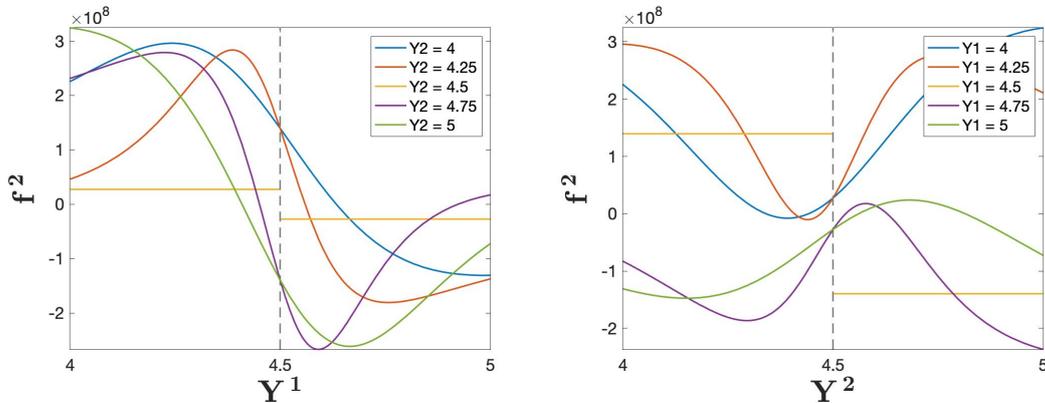
Figure 3.22: Cuts through the integrand of the middle element

A comparison of the results of Duffy transformation and tanh-sinh quadrature are represented below. At first, the tanh-sinh quadrature was applied to the problem. As explained in subsection A.4.2, it is not known in advance how many quadrature points are necessary to obtain a desired accuracy, so, the tanh-sinh quadrature is applied iteratively with the distance h between the support points in the transformed domain halved in every iteration cycle k. The middle element was subjected to two different displacement fields; an isotropic expansion by the nodal displacements $u_j^1, u_j^2 = 0.1$, for which the direct integration has failed prior (compare figure 3.15), and a displacement field with randomized nodal displacements $|u_j^1|, |u_j^2| \leq 0.1$. Remark: The material parameter c was set to 1 in the following figures.
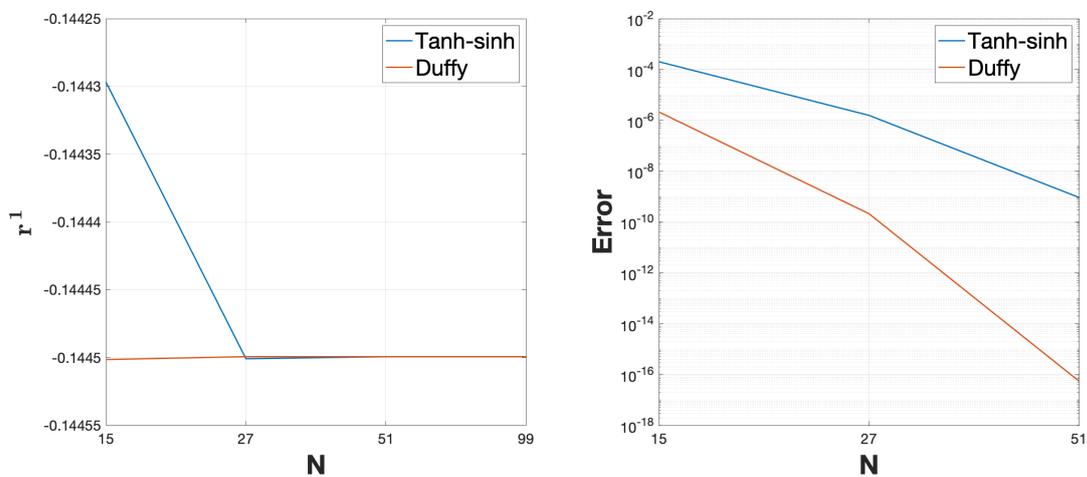
Figure 3.23: r^1 by Tanh-sinh quadrature and Duffy transformation, isotropic expansion
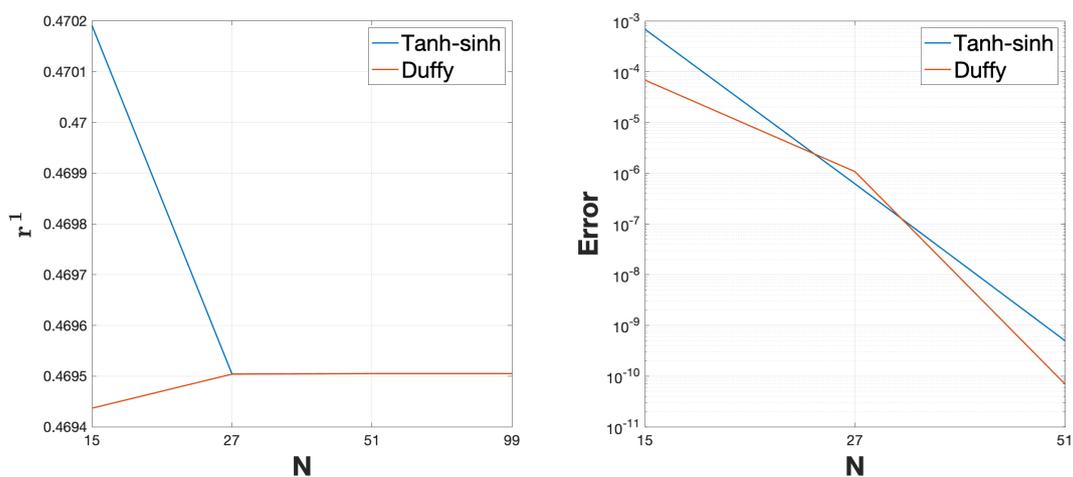
Figure 3.24: r^1 by Tanh-sinh quadrature and Duffy transformation, random nodal displacements

For both displacement fields, four iteration cycles k where necessary in order to obtain an

absolute value of 1^{-10} for the error of the resulting integral between two successive iterations. The same number of support points was available to the subelements of the Duffy transformation afterwards.

Both quadrature methods show good convergence behavior and are therefore suitable for the integration of the middle element. In case of the isotropic expansion, the Duffy transformation yields even faster convergence and reaches the desired precision with approx. 30 support points. In case of the randomized nodal displacements, both quadrature methods are almost equal in their convergence rate. An experimental order of convergence (EOC) [Axthelm 2020, p.37] can be computed for both Duffy- and tanh-sinh-quadrature.

$$\alpha = \frac{\ln\left(\frac{E_{k+1}}{E_k}\right)}{\ln\left(\frac{E_k}{E_{k-1}}\right)} \tag{3.53}$$

k in eq. 3.53 denotes the level of iteration, E_k denotes the error of the current iteration step k, and α denotes the approximated order of convergence. The error is defined as

$$E_k = \|I_k - I\| \tag{3.54}$$

with $I_{k_{k\in\mathbb{N}}}$ being the result of the numerical quadrature in step k and I being the true solution of the integral. Equation 3.53 is an experimental measure of the convergence order, assuming that the errors E_{k+1} and E_k of two successive steps k are related by:

$$E_{k+1} \approx E_k{}^\alpha \tag{3.55}$$

According to [Axthelm 2020, p.37], the EOC is the more valid the more the series E_k converges. Regarding however the good convergence behavior in figure 3.24, using the EOC is exemplarily justifiable. The convergence orders are computed for the curves in 3.24 and yield:

$$
\begin{aligned}
\alpha_{\text{tanh-sinh}} &\approx \frac{\ln\left(\frac{5\cdot 10^{-10}}{6\cdot 10^{-7}}\right)}{\ln\left(\frac{6\cdot 10^{-7}}{7\cdot 10^{-4}}\right)} = 1.0040 \\[2ex]
\alpha_{\text{Duffy}} &\approx \frac{\ln\left(\frac{5\cdot 10^{-10}}{6\cdot 10^{-7}}\right)}{\ln\left(\frac{6\cdot 10^{-7}}{7\cdot 10^{-4}}\right)} = 1.1089
\end{aligned}
\tag{3.56}
$$

Because in addition, the rate of convergence μ

$$\lim_{k \to \infty} \frac{\|I_{k+1} - I\|}{\|I_k - I\|} = \mu < 1 \tag{3.57}$$

is smaller than 1 (the error in fig. 3.23 and fig. 3.24 becomes even infinitesimally small), at least a linear convergence may be assumed.
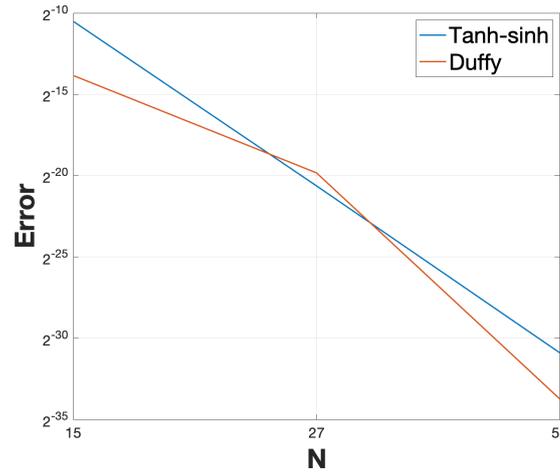
Figure 3.25: f^1 by Tanh-sinh quadrature and Duffy transformation, random nodal displacements

The number of support points in both directions Y^1, Y^2 is roughly quadrupled (doubled in each direction) during the iteration cycles k, compare e.g. figure 3.24. In figure 3.25, the error is displayed w.r.t basis 2 instead of 10. It can be seen that quadrupling the number of support points leads to a reduction of the error by a factor of roughly $\frac{1}{1024}$. An a priori error estimation of the Tanh-Sinh-quadrature can be found in [Vanherck et al 2020, p.3].

3.1.5 Investigation of the Jacobian matrix

In this part, the structure of the Jacobian matrix will be examined for a single peridynamic element which is fully embedded. Because the derivative of the force state, eq. 3.6 incorporates the inner integral over middle-, uncut- and cut elements, the Jacobian matrix can be split down into three contributions as well. For the computation, the setup

1. $N_{parent} = 2$

2. $N_{cut} = 2^3$

3. $N_{uncut} = 2^3$

4. $N_{middle} = 2^3$

was used. The Jacobian matrices for a zero - initial displacement are given by:

$$[J_{uncut}] = 1 \cdot 10^9 \begin{bmatrix} -5.56 & -2.15 & -2.58 & -0.82 & +0.58 & -0.48 & -0.48 & +0.55 \\ -2.15 & -5.56 & -0.82 & -2.58 & +0.48 & -0.58 & -0.55 & +0.48 \\ -2.58 & -0.82 & -5.56 & -2.15 & +0.48 & -0.55 & -0.58 & +0.48 \\ -0.82 & -2.58 & -2.15 & -5.56 & +0.55 & -0.48 & -0.48 & +0.58 \\ +0.58 & -0.48 & -0.48 & +0.55 & -5.56 & -2.58 & -2.15 & -0.82 \\ +0.48 & -0.58 & -0.55 & +0.48 & -2.58 & -5.56 & -0.82 & -2.15 \\ +0.48 & -0.55 & -0.58 & +0.48 & -2.15 & -0.82 & -5.56 & -2.58 \\ +0.55 & -0.48 & -0.48 & +0.58 & -0.82 & -2.15 & -2.58 & -5.56 \end{bmatrix} \quad (3.58)$$

$$[J_{cut}] = 1 \cdot 10^9 \begin{bmatrix} -2.69 & -1.35 & -1.35 & -0.67 & -0.07 & 0 & 0 & 0 \\ -1.35 & -2.69 & -0.67 & -1.35 & 0 & +0.07 & 0 & 0 \\ -1.35 & -0.67 & -2.69 & -1.35 & 0 & 0 & +0.07 & 0 \\ -0.67 & -1.35 & -1.35 & -2.69 & 0 & 0 & 0 & -0.07 \\ -0.07 & 0 & 0 & 0 & -2.69 & -1.35 & -1.35 & -0.67 \\ 0 & +0.07 & 0 & 0 & -1.35 & -2.69 & -0.67 & -1.35 \\ 0 & 0 & +0.07 & 0 & -1.35 & -0.67 & -2.69 & -1.35 \\ 0 & 0 & 0 & -0.07 & -0.67 & -1.35 & -1.35 & -2.69 \end{bmatrix} \quad (3.59)$$

$$[J_{middle}] = 1 \cdot 10^8 \begin{bmatrix} -4.48 & +2.56 & -1.08 & +2.99 & -1.98 & +0.06 & +0.06 & +1.86 \\ +2.56 & -4.48 & +2.99 & -1.08 & -0.06 & -1.98 & -1.86 & -0.06 \\ -1.08 & +2.99 & -4.48 & +2.56 & -0.06 & -1.86 & -1.98 & -0.06 \\ +2.99 & -1.08 & +2.56 & -4.48 & +1.86 & +0.06 & +0.06 & -1.98 \\ -1.98 & +0.06 & +0.06 & +1.86 & -4.48 & -1.08 & +2.56 & +2.99 \\ -0.06 & -1.98 & -1.86 & -0.06 & -1.08 & -4.48 & +2.99 & +2.56 \\ -0.06 & -1.86 & -1.98 & -0.06 & +2.56 & +2.99 & -4.48 & -1.08 \\ +1.86 & +0.06 & +0.06 & -1.98 & +2.99 & +2.56 & -1.08 & -4.48 \end{bmatrix} \quad (3.60)$$

The complete Jacobian matrix is given by:

$$[J] = [J_{uncut}] + [J_{cut}] + [J_{middle}] \quad (3.61)$$

The force- and displacement vector corresponding to the matrices above have the following order of indices:

$$
\mathbf{u} =
\begin{bmatrix}
\bar{u}_1^1 \\
\bar{u}_2^1 \\
\bar{u}_3^1 \\
\bar{u}_4^1 \\
\bar{u}_1^2 \\
\bar{u}_2^2 \\
\bar{u}_3^2 \\
\bar{u}_4^2
\end{bmatrix}
\quad ; \quad
\mathbf{f} =
\begin{bmatrix}
f_1^1 \\
f_2^1 \\
f_3^1 \\
f_4^1 \\
f_1^2 \\
f_2^2 \\
f_3^2 \\
f_4^2
\end{bmatrix}
$$
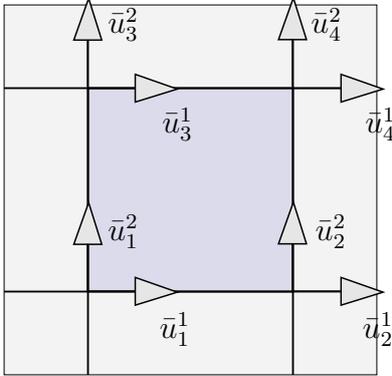
Forces are supposed to point in the same direction as the respective dofs in the figure above. The indices of the approach functions N_1 ... N_4 are related to the indices of the dofs as well.

All Jacobian matrices have a blockwise structure, resulting from the order of the degrees of freedom. The "parallel-blocks" represent the changes of forces due to changes of nodal displacements acting in the same respective direction. These blocks are symmetric for all three matrices. The "perpendicular-blocks", representing changes of nodal forces due to perpendicular nodal displacements, are equal above and below the main diagonal. Furthermore, the entries opposite to each other are of equal absolute value, yet some have opposite sign. This special structure contradicts the claim of [Glaws 2014, p.24], stating that the Jacobian matrix has to be symmetric. Both results can be explained however by a detailed investigation of the structure of the inner integrals.

Structure of Jacobian matrix from [Glaws 2014]

The different results w.r.t. symmetry are examined by a derivation of two entries of the Jacobian matrix which oppose in sign. For the minimal example above with 8 global dofs, the entries

$$
\frac{\partial R_1^1}{\partial \bar{u}_3^2} = J_{17}
$$

$$
\frac{\partial R_3^2}{\partial \bar{u}_1^1} = J_{71}
$$

are compared to each other. The indices i, j in J_{ij} refer to the global dofs with i being the index of the dof-force which is derived by dof j. The Jacobian matrix is built from deriving the (weak) inner forces, compare eq. 3.19. In order to enable a comparison with

[Glaws 2014], the functional determinant from the transition from deformed to undeformed configuration is omitted in the following comparison. The expressions J_{17} and J_{71} in the context of [Glaws 2014, p.23] are then given by:

$$J_{17} = \frac{\partial R_1^1}{\partial u_3^2} = \iint_{\Omega^0} \iint_{\Omega^0 \cap D_{\mathbf{X}}} \left({\color{blue} N_1(\mathbf{Y})} - N_1(\mathbf{X}) \right) \frac{\partial f^1}{\partial \bar{u}_3^2} \, dA_{\mathbf{Y}} \, dA_{\mathbf{X}} \qquad (3.62)$$

respectively

$$J_{71} = \frac{\partial R_3^2}{\partial u_1^1} = \iint_{\Omega^0} \iint_{\Omega^0 \cap D_{\mathbf{X}}} \left({\color{blue} N_3(\mathbf{Y})} - N_3(\mathbf{X}) \right) \frac{\partial f^2}{\partial \bar{u}_1^1} \, dA_{\mathbf{Y}} \, dA_{\mathbf{X}} \qquad (3.63)$$

The appearence of the blue term in 3.62 introduced in [Glaws 2014, p.23] is different to the approach in this thesis. Nevertheless, it can be introduced into the derivation of the analytical Jacobian matrix. By recalling the expressions from eq. 3.28,

$$\mathbf{f} = \begin{bmatrix} f^1 \\ f^2 \end{bmatrix} = c\,\epsilon\,\mathbf{d}$$

$$L = |\mathbf{Y} - \mathbf{X}|$$

$$\mathbf{u_X} = \begin{bmatrix} \sum_{i=1}^4 N_i(\mathbf{X})\,\bar{u}_i^1 \\ \sum_{i=1}^4 N_i(\mathbf{X})\,\bar{u}_i^2 \end{bmatrix} \quad , \, \mathbf{u_Y} = \begin{bmatrix} \sum_{i=1}^4 N_i(\mathbf{Y})\,\bar{u}_i^1 \\ \sum_{i=1}^4 N_i(\mathbf{Y})\,\bar{u}_i^2 \end{bmatrix}$$

$$\mathbf{l} = \begin{bmatrix} l^1 \\ l^2 \end{bmatrix} = \mathbf{Y} + \mathbf{u_Y} - \mathbf{X} - \mathbf{u_X} = \begin{bmatrix} Y^1 - X^1 + \sum_{i=1}^4 (N_i(\mathbf{Y}) - N_i(\mathbf{X}))\,\bar{u}_i^1 \\ Y^2 - X^2 + \sum_{i=1}^4 (N_i(\mathbf{Y}) - N_i(\mathbf{X}))\,\bar{u}_i^2 \end{bmatrix}$$

$$l = |\mathbf{l}|$$

$$\epsilon = \frac{l - L}{L}$$

$$\mathbf{d} = \frac{\mathbf{l}}{l}$$

equation 3.62 can be developed into: (compare appendix A.6)

$$J_{17} = \iint_{\Omega^0} \iint_{\Omega^0 \cap D_{\mathbf{X}}} \left(\frac{1}{L} \frac{l^1 l^2}{(l)^2} - \epsilon \frac{l^1 l^2}{(l)^3} \right) \left(N_1(\mathbf{Y}) - N_1(\mathbf{X}) \right) \left(N_3(\mathbf{Y}) - N_3(\mathbf{X}) \right) dA_{\mathbf{Y}} \, dA_{\mathbf{X}} \quad (3.64)$$

Doing the same derivation for J_{71} leads to:

$$J_{71} = \iint_{\Omega^0} \iint_{\Omega^0 \cap D_{\mathbf{X}}} \left(\frac{1}{L} \frac{l^1 l^2}{(l)^2} - \epsilon \frac{l^1 l^2}{(l)^3} \right) \left(N_3(\mathbf{Y}) - N_3(\mathbf{X}) \right) \left(N_1(\mathbf{Y}) - N_1(\mathbf{X}) \right) dA_{\mathbf{Y}} \, dA_{\mathbf{X}} \quad (3.65)$$

The indices of the two differences of form functions are related to the index of derived nodal force and deriving dof. Swapping those indices means computing the opposite Jacobian matrix entry. As swapping does not change the product of the difference of the approach functions, the Jacobian matrix will always be symmetric, proving the claim.

Structure of Jacobian matrix in this thesis

The Jacobian matrices 3.60, 3.59 and 3.58 in this thesis are not symmetric, although entries opposite to each other are always of same absolute value. This structure results from a different weighting approach in this thesis. Computing the entries J_{17} and J_{71} is done by

$$
J_{17} = \iint\limits_{\Omega^0} N_1(\mathbf{X}) \iint\limits_{\Omega^0 \cap D_\mathbf{X}} \left(\frac{1}{L} \frac{l^1 \, l^2}{(l)^2} (N_3(\mathbf{Y}) - N_3(\mathbf{X})) - \epsilon \frac{l^1 \, l^2}{(l)^3} (N_3(\mathbf{Y}) - N_3(\mathbf{X})) \right) dA_\mathbf{Y} \, dA_\mathbf{X} =
$$
$$
= \iint\limits_{\Omega^0} N_1(\mathbf{X}) \iint\limits_{\Omega^0 \cap D_\mathbf{X}} \left(\frac{1}{L} \frac{l^1 \, l^2}{(l)^2} - \epsilon \frac{l^1 \, l^2}{(l)^3} \right) \left(N_3(\mathbf{Y}) - N_3(\mathbf{X}) \right) dA_\mathbf{Y} \, dA_\mathbf{X}
$$

$$(3.66)$$

respectively

$$
J_{71} = \iint\limits_{\Omega^0} N_3(\mathbf{X}) \iint\limits_{\Omega^0 \cap D_\mathbf{X}} \left(\frac{1}{L} \frac{l^1 \, l^2}{(l)^2} - \epsilon \frac{l^1 \, l^2}{(l)^3} \right) \left(N_1(\mathbf{Y}) - N_1(\mathbf{X}) \right) dA_\mathbf{Y} \, dA_\mathbf{X} \tag{3.67}
$$

Because the test function is a function only of $\mathbf{X}$, it does not contribute to the inner integral over $\mathbf{Y}$, which is fulfilled therefore in a strong sense. Swapping the indices of derived nodal force and deriving dof yields different expressions for the products of the formfunctions, compare equations 3.66 and 3.67. However, the fact that opposite entries of the Jacobian matrix are of equal magnitude can be explained without loss of generality by the following minimal example.

The example consists of the inner integral over the middle element itself. A single parent Gauss point is used, therefore located in the middle of the element. The coordinate system, measuring both (X^1, X^2) and (Y^1, Y^2) is located in the center too for the sake of simplicity. All subelementations are using one quadrature point, compare figure 3.26. The Jacobian matrix is computed for a zero initial displacement; therefore, no bonds undergo a change in their length:

$$
\epsilon = (\frac{l}{L} - 1) = 0 \tag{3.68}
$$
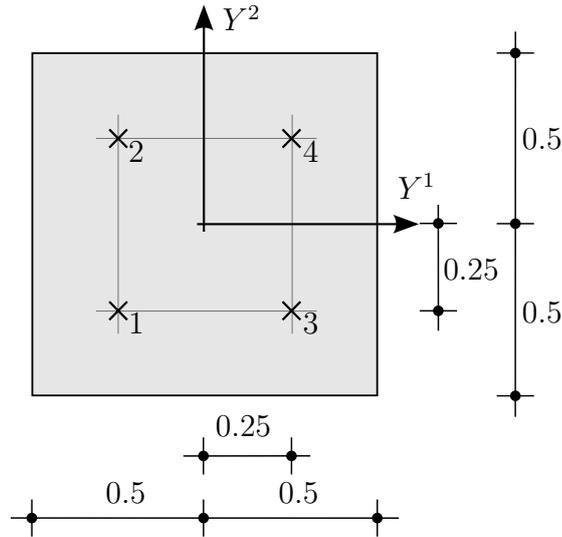
Figure 3.26: Minimal example on the inner element

Introducing these simplifications into equation 3.66 and replacing the integrals by a numerical quadrature yields:

$$\frac{\partial R_1^1}{\partial \bar{u}_3^2} = N_1(\mathbf{X}_p) \sum_{n=1}^{4} \frac{l^1 \, l^2}{L \, (l)^2} \Big(N_3(\mathbf{Y}_n) - N_3(\mathbf{X}_p) \Big) w_n^1 \, w_n^2 \cdot 1 \cdot 1 \tag{3.69}$$

As just one parent Gauss point was used, the outer integral degenerates to one single Gauss quadrature evaluation with weight $1 \cdot 1$. Due to the zero initial displacement and the location of the coordinate system in the middle of the element, the lengths of the deformed bonds simplify to their endpoint coordinates:

$$
\begin{aligned}
l^1 &= Y^1 + \cancelto{0}{u^1(\mathbf{Y})} - \cancelto{0}{X^1} - \cancelto{0}{u^1(\mathbf{X})} = Y^1 \\
l^2 &= Y^2 + \cancelto{0}{u^2(\mathbf{Y})} - \cancelto{0}{X^2} - \cancelto{0}{u^2(\mathbf{X})} = Y^2
\end{aligned}
\tag{3.70}
$$

The evaluation of all four approach functions $N_i(\mathbf{X}_p)$ in the parent Gauss point at the center of the coordinate system yields a value of $\frac{1}{4}$. The weights w_n^1, w_n^2 for four quadratic subelements is $\frac{1}{4}$ too. Introducing these simplifications into eq. 3.69 provides the following expression:

$$\frac{\partial R_1^1}{\partial \bar{u}_3^2} = \frac{1}{4} \sum_{n=1}^{4} Y_n^1 \, Y_n^2 \, \frac{1}{L^3} \left(N_3(\mathbf{Y}_n) - \frac{1}{4} \right) \frac{1}{16} \tag{3.71}$$

(All four bonds have the same length L). Doing the same derivation for $\dfrac{\partial R_3^2}{\partial \bar{u}_1^1}$ yields:

$$\frac{\partial R_3^2}{\partial \bar{u}_1^1} = \frac{1}{4} \sum_{n=1}^{4} Y_n^1 Y_n^2 \frac{1}{L^3} \left(N_1(\mathbf{Y}_n) - \frac{1}{4} \right) \frac{1}{16} \tag{3.72}$$

The sums in equations 3.71 and 3.72 are evaluated in tables 3.2 and 3.3.   Comparing the

QP	Y^1	Y^2	$N_3(Y_i^1, Y_i^2)$	$Y_i^1 Y_i^2 \cdot \left(N_3(Y_i^1, Y_i^2) - \frac{1}{4} \right)$
1	-0.25	-0.25	0.188	$(-0.25)(-0.25) \cdot (0.188 - 0.25) = -0.004$
2	-0.25	+0.25	0.562	$(-0.25)(+0.25) \cdot (0.562 - 0.25) = -0.012$
3	+0.25	-0.25	0.063	$(+0.25)(-0.25) \cdot (0.063 - 0.25) = +0.012$
4	+0.25	+0.25	0.188	$(+0.25)(+0.25) \cdot (0.188 - 0.25) = -0.004$
				$\sum$ -0.008

Table 3.2: $\dfrac{\partial R_1^1}{\partial \bar{u}_3^2}$

QP	Y^1	Y^2	$N_1(Y_i^1, Y_i^2)$	$Y_i^1 Y_i^2 \cdot \left(N_1(Y_i^1, Y_i^2) - \frac{1}{4} \right)$
1	-0.25	-0.25	0.562	$(-0.25)(-0.25) \cdot (0.562 - 0.25) = +0.012$
2	-0.25	+0.25	0.188	$(-0.25)(+0.25) \cdot (0.188 - 0.25) = +0.004$
3	+0.25	-0.25	0.188	$(+0.25)(-0.25) \cdot (0.188 - 0.25) = +0.004$
4	+0.25	+0.25	0.063	$(+0.25)(+0.25) \cdot (0.063 - 0.25) = -0.012$
				$\sum$ 0.008

Table 3.3: $\dfrac{\partial R_3^2}{\partial \bar{u}_1^1}$

outcomes of tables 3.2 and 3.3 proves that the Jacobian matrix entries opposite to each other are different in sign, but equal in magnitude.

Comparison of analytical- and numerical Jacobian matrix

In a last step, the analytical Jacobian matrix is compared with the one obtained from a complex step derivative; this serves as a validation, as the complex step derivative (compare section A.3) builds the Jacobian matrix by using the inner peridynamic forces 3.17 only, but not it's derivative w.r.t the dofs in the sense of equation 3.19. The analytical Jacobian matrices from cut-, uncut and middle elements (3.58, 3.59, 3.60) were recomputed numerically; their deviation to their analytical counterparts was examined by the relative error of their Frobenius norms (eq. 3.38) in table 3.4: A second example covers a cantilever beam built from 30×3 elements with $\Delta = 1$ under end load $F = 10$, providing a 248×248 - Jacobian matrix. For this particular example, the elastic modulus was set to $3 \cdot 10^6$. The

	$\|[J]_{an}\|$	$\|[J]_{num}\|$	$\|[J]_{an} - [J]_{num}\|$	$\dfrac{\|[J]_{an}\| - \|[J]_{num}\|}{[J]_{an}}$
uncut	$1.8746 \cdot 10^{10}$	$1.8746 \cdot 10^{10}$	$1.3337 \cdot 10^{-5}$	$2.0349 \cdot 10^{-16}$
cut	$9.5270 \cdot 10^{9}$	$9.5270 \cdot 10^{9}$	$5.1745 \cdot 10^{-5}$	$-2.0021 \cdot 10^{-16}$
middle	$1.8801 \cdot 10^{9}$	$1.8801 \cdot 10^{9}$	$2.3776 \cdot 10^{-5}$	$-1.2681 \cdot 10^{-16}$
total	$2.8978 \cdot 10^{10}$	$2.8978 \cdot 10^{10}$	$1.5309 \cdot 10^{-5}$	$-1.3164 \cdot 10^{-16}$

Table 3.4: Comparison of Frobenius norms of Jacobian matrices

problem was solved using Newton's method with both analytical and numerical Jacobian matrix. The termination threshold of the computation was set to 10^{-7}, and the Frobenius norms of both Jacobian matrices from the last iteration steps were compared in table 3.5: As can be seen from tables 3.4 and 3.5, numerical and analytical Jacobian matrices display

	$\|[J]_{an}\|$	$\|[J]_{num}\|$	$\|[J]_{an} - [J]_{num}\|$	$\dfrac{\|[J]_{an}\| - \|[J]_{num}\|}{[J]_{an}}$
-	$9.1077 \cdot 10^{6}$	$9.1077 \cdot 10^{6}$	75.70	$4.926 \cdot 10^{-8}$

Table 3.5: Comparison of Frobenius norms of Jacobian matrices

very good coincidence.

3.1.6 Implementation of surface correction factor

A surface correction factor takes the truncated families close to free surfaces into account and is of crucial importance for the convergence to the correct results for the peridynamic finite elements. The following example illustrates the problem.
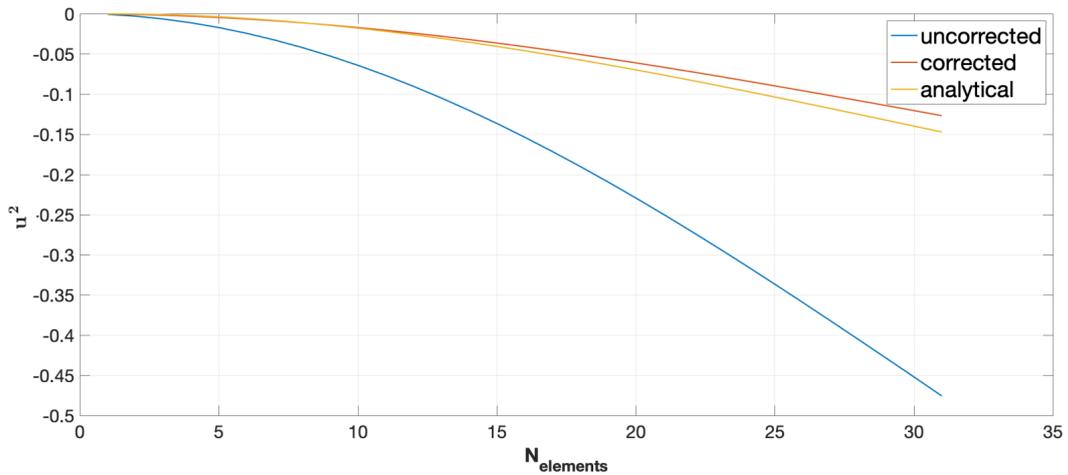

Figure 3.27: Configuration A. Comparison between uncorrected, corrected and analytical solution, 30×3 elements
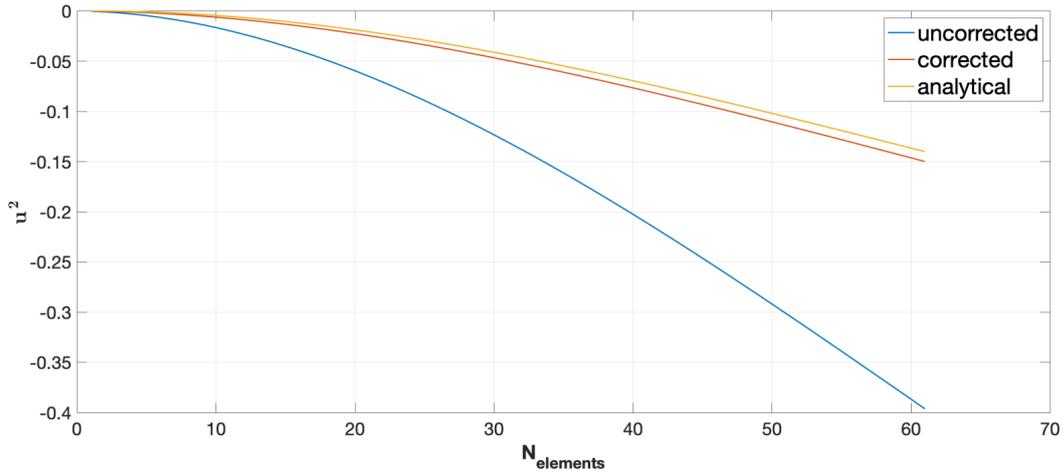
Figure 3.28: Configuration B. Comparison between uncorrected, corrected and analytical solution, 60×6 elements

The simulation displays the vertical displacements of a cantilever beam with a single load applied to the free end (right end in figure 3.27 and 3.28). The system had the following properties: $\frac{l}{h} = 10$, $l = 30$, $h = 3$. Discretization A was done with 30×3 elements, discretization B was done with 60×6 elements. Both discretizations had four parent Gauss points per element and a fixed horizon length $\delta = 3\,\Delta$. Therefore, the coarser configuration A has twice the horizon length as configuration B. Both problems were solved by Newton's method with the iteration terminated as soon as $\epsilon = |I_{n-1} - I_n| \leq 1e^{-8}$.

Both simulations display large deviations between the results with discretization A showing a deviation of $223\,\%$ in comparison to the analytical solution, and discretization B having an error of $182\,\%$. The reason for the error lies in the calibration of the peridynamic model by the equivalence of the strain energy in Peridynamics and classical elasticity theory, aggreviated by a long, slender structure with large surfaces like a cantilever beam. Thinking in terms of Euler Bernoulli beam theory, the maximum strains will occur in the topmost and bottommost material fibers, storing the highest strain energy there. The nonlocal nature of Peridynamics obtains the strain energy in $\mathbf{X}$ by integration over the strain energy densities in it's respective bonds $D_\mathbf{x}$:

$$\Pi_{\mathbf{x}_I} = \iint\limits_{D_\mathbf{X}} \frac{1}{2} \frac{c\,\delta}{|\mathbf{Y} - \mathbf{X}|}\, s^2 \det D\varphi(\mathbf{Y})\, dY^2 dY^1$$

with

$$s = \left(|\mathbf{y} - \mathbf{x}| - |\mathbf{Y} - \mathbf{X}| \right)$$

(3.73)

Different to classical elasticity with it's vanishing horizon length and depending on the ratio

between δ and the element length Δ, the surroundings of a point $\mathbf{X}$ close to a boundary is only partly covered by material (compare fig. 3.29):
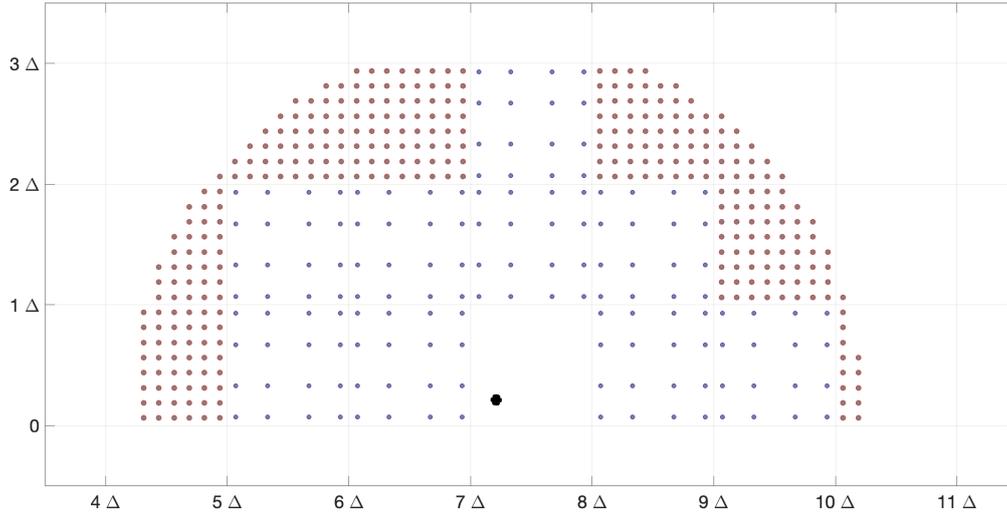
Figure 3.29: Truncated family, 30×3 elements, Δ = 3

This truncation introduces an error in comparison to local classical elasticity, because the calibration of the peridynamic material parameters (see section 2.3) was done with a completely covered vicinity of $\mathbf{X}$. Configuration A suffers even more from this truncation error due to it's coarser meshgrid, comparatively more strain energy-providing area was truncated. This effect was enhanced by the mechanics of the cantilever beam, as the truncated boundary vicinities are responsible at the same time for the highest strain energy density.

A surface correction factor d, according to [Madenci and Oterkus 2014, p.68 ff.] has to be introduced. This factor takes into account, that even a truncated family must be able to produce the same strain energy as a complete one by enlarging the material parameter of the truncated family. In the scope of this thesis, a correction factor is computed element-wise by averaging the strain energies of each parent Gauss points family. The surface correction factor results from the quotient of averaged truncated strain energy and the strain energy of a complete family. Both complete and truncated strain energy are computed for the same

calibration shear displacement field [Madenci and Oterkus 2014, p.70 ff.]:

$$
\begin{bmatrix} y^1 \\ y^2 \end{bmatrix} = \begin{bmatrix} 1 & \zeta \\ \zeta & 1 \end{bmatrix} \begin{bmatrix} Y^1 \\ Y^2 \end{bmatrix}
$$

$$
\begin{bmatrix} x^1 \\ x^2 \end{bmatrix} = \begin{bmatrix} 1 & \zeta \\ \zeta & 1 \end{bmatrix} \begin{bmatrix} X^1 \\ X^2 \end{bmatrix} \quad , \quad \zeta \in [0\,,\,0.5]
$$
(3.74)

Thus, the averaged strain energy of the truncated vicinities of the N parent Gauss points equals:

$$
\tilde{W}_{\mathbf{x}_I} = \frac{1}{N} \sum_{k=1}^{N} \iint_{D_{\mathbf{X_k}}} \frac{1}{2} \frac{c}{|\mathbf{Y} - \mathbf{X_k}|} s^2 \det D\varphi(\mathbf{Y})\, dY^2 dY^1
$$
(3.75)

The surface correction factor d then can be obtained by division:

$$
d = \frac{W_{\mathbf{x}_I}}{\tilde{W}_{\mathbf{x}_I}}
$$
(3.76)

With $W_{\mathbf{x}_I}$ being the untruncated strain energy due to the calibration shear field and a plate-thickness $h = 1$ (compare eq. 2.32):

$$
W_{\mathbf{x}_I} = \frac{1}{12}\,\pi\,c\,\delta^3\,\zeta^2
$$

The orange displacement fields in figures 3.27 and 3.28 display the corrected displacement fields. It can be seen that due to the surface correction, different to [Glaws 2014, p.28], even the coarse mesh 30×3 reduces the error from former $223\,\%$ to $13.7\,\%$ in comparison to the analytical solution from Euler Bernoulli beam theory.

3.2 Finite elements for a 1-D problem

Some of the complexity of the 2-D peridynamic elements arose due to the differentiation of the product of the absolute value of the deformed bond and the orientation vector w.r.t. the nodal degrees of freedom. The result were sums of changes of bond forces, which could be arbitrarily orientated in the 2-D - plane. Reducing the model to a 1-D-problem leaves the bond forces to point in either positive- or negative bar direction only. This significant restriction of allowed bond directions leads to a linear dependency of the bond forces on the elements' degrees of freedom. Furthermore, 1-D elements can be coupled to analytical

solutions more easily.

3.2.1 1-D equation of motion

Beginning the derivation with the peridynamic equation of motion, eq. 2.36, and reducing it to one dimension yields:

$$\rho\,\ddot{u} = \int\limits_{X-\delta}^{X+\delta} c\,\frac{1}{|Y-X|}\left(|u_Y + Y - u_X - X| - |Y - X|\right) \operatorname{sgn}\left(u_Y + Y - u_X - X\right) dY + b \quad (3.77)$$

The sgn - function in eq. 3.77 takes into consideration the direction of the bond (left or right), whereas the difference of the absolute values differentiates between compression or elongation of the bond. The same behavior of the sign of the resulting force in X can be obtained by the following expression:

$$\rho\,\ddot{u} = \int\limits_{X-\delta}^{X+\delta} c\,\frac{u_Y - u_X}{|Y - X|}\,dY + b \tag{3.78}$$

The validity of equation 3.78 is shown in figure 3.30. Depicted there are one-dimensional
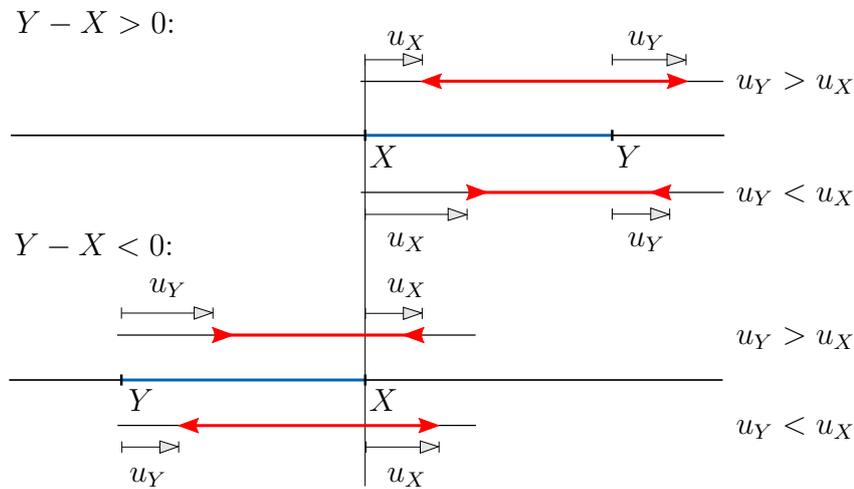
Figure 3.30: Directions of bond forces

bonds for both cases $Y - X > 0$ and $Y - X < 0$. The undeformed, blue bonds in fig. 3.30 are depicted in red after the deformation. The arrows at the ends of the bond denote tensile- or compressional bond forces. Obviously, u_Y being larger than u_X leads to tension if $Y - X > 0$ and compression, if $Y - X < 0$. However, due to the denominator in eq. 3.78, the difference of the bond end displacements are divided by the absolute value of the undeformed bond orientation $|Y - X|$. Therefore, bonds orientated in the negative direction

will be multiplied by -1 additionally, thus providing the same signs of the resulting force in X w.r.t. endpoint displacements, regardless of the bond orientation. The resulting equation 3.78 is still nonlocal, but linear in u.

3.2.2 Weak form and discretization

The weak form of equilibrium is generated by weighting eq. 3.78 with a virtual displacement field v_X and integrating [Chen and Gunzburger 2011, p.7-9]:

$$
\int_{\Omega^0} \rho \, \ddot{u} \, v_X \, dX \;=\; \int_{\Omega^0} \int_{X-\delta}^{X+\delta} c \, \frac{u_Y - u_X}{|Y - X|} \, dY \, v_X \, dX \;+\; \int_{\Omega^0} b \, v_X \, dX
\tag{3.79}
$$

Both real- and virtual displacement fields u and v are discretized with triangular "hat" functions θ_i:

$$
\theta_i(X) \;=\; \begin{cases} \frac{1}{\Delta}\Big(X + \Delta - i\Delta\Big) & (i-1)\Delta \leq X \leq i\Delta \\ \frac{1}{\Delta}\Big(-(X - \Delta - i\Delta)\Big) & i\Delta \leq X \leq (i+1)\Delta \\ 0 & \text{else} \end{cases}
\tag{3.80}
$$

Thus, the discretized real- and virtual displacement fields are:

$$
\begin{aligned}
u_X &= \sum_{i}^{N} \theta_i(X)\, \bar{u}_i \\
v_X &= \sum_{j}^{N} \theta_j(X)\, \bar{1}
\end{aligned}
\tag{3.81}
$$

Since external- and inertial forces are straightforward (the mass matrix of a truss element can be found in e.g. [Mehlhorn 1996a, p.119]), the computation of the integral of the weighted inner forces $R(X)$ is examined now in detail. The aim is the development of the stiffness matrix for a peridynamic truss element between nodes $k - 1$ and k. The evaluation of the outer integral in X will be a function of the two dofs $k - 1$ and k left and right of X:

$$
R(X) = \int_{(k-1)\Delta}^{k\Delta} \int_{x-3\Delta}^{x+3\Delta} c \, \frac{\sum\limits_{s=k-4}^{k+3} \theta_s(Y)\bar{u}_s - \Big(\theta_{k-1}(X)\bar{u}_{k-1} + \theta_k(X)\bar{u}_k\Big)}{|Y - X|} \, dY \, \Big(\theta_{k-1}(X) + \theta_k(X)\Big) \, dX
\tag{3.82}
$$

Equal to 2-D peridynamic finite elements, the horizon in 1-D Peridynamics δ is set to 3Δ.
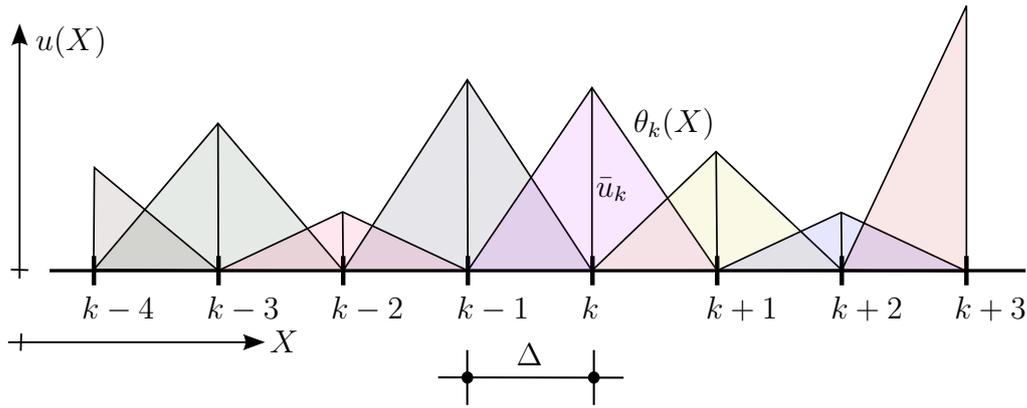
Figure 3.31: 1-D hat functions

The integral above can be split down into eight components [Chen and Gunzburger 2011, p.9]:

$$
R(x) = c \int\limits_{(k-1)\Delta}^{k\Delta} \Bigg(- \int\limits_{(k-4)\Delta}^{(k-3)\Delta} \frac{\theta_{k-4}(Y)\bar{u}_{k-4} + \theta_{k-3}(Y)\bar{u}_{k-3}}{Y - X} \, dY -
$$

$$
- \int\limits_{(k-3)\Delta}^{(k-2)\Delta} \frac{\theta_{k-3}(Y)\bar{u}_{k-3} + \theta_{k-2}(Y)\bar{u}_{k-2}}{Y - X} \, dY - \int\limits_{(k-2)\Delta}^{(k-1)\Delta} \frac{\theta_{k-2}(Y)\bar{u}_{k-2} + \theta_{k-1}(Y)\bar{u}_{k-1}}{Y - X} \, dY -
$$

$$
- \int\limits_{(k-1)\Delta}^{X} \frac{\theta_{k-1}(Y)\bar{u}_{k-1} + \theta_{k}(Y)\bar{u}_{k} - u(X)}{Y - X} \, dY + \int\limits_{X}^{k\Delta} \frac{\theta_{k-1}(Y)\bar{u}_{k-1} + \theta_{k}(Y)\bar{u}_{k} - u(X)}{Y - X} \, dY +
$$

$$
+ \int\limits_{k\Delta}^{(k+1)\Delta} \frac{\theta_{k}(Y)\bar{u}_{k} + \theta_{k+1}(Y)\bar{u}_{k+1}}{Y - X} \, dY + \int\limits_{(k+1)\Delta}^{(k+2)\Delta} \frac{\theta_{k+1}(Y)\bar{u}_{k+1} + \theta_{k+2}(Y)\bar{u}_{k+2}}{Y - X} \, dY +
$$

$$
+ \int\limits_{(k+2)\Delta}^{(k+3)\Delta} \frac{\theta_{k+2}(Y)\bar{u}_{k+2} + \theta_{k+3}(Y)\bar{u}_{k+3}}{Y - X} \, dY \Bigg) \theta_{k-1}(X) \, dX
$$

$$(3.83)$$

with

$$
u(X) = \theta_{k-1}(X)\bar{u}_{k-1} + \theta_{k}(X)\bar{u}_{k} \tag{3.84}
$$

and a microelastic stiffness constant c for 1-D problems [Madenci and Oterkus 2014, p.68]:

$$
c = \frac{2\,E}{A\,\delta^2} \tag{3.85}
$$

with A denoting the cross sectional area of the truss.

The integrals in expression 3.83 can be solved analytically. For a truss element between nodes $k-1$ and k, the force densities can be weighted with $\theta_{k-1}(X)\,\bar{1}$ and $\theta_k(X)\,\bar{1}$, providing two independent equations for the resulting inner forces in nodes $k-1$ and k. Those can be written down as a nonlocal, non-quadratic stiffness matrix:

$$
\begin{bmatrix} R_{k-1} \\ R_{k+0} \end{bmatrix} = c\,\Delta \begin{bmatrix} 0.046 & 0.22 & 0.45 & -1.03 & -0.18 & 0.33 & 0.19 & 0.015 \\ 0.015 & 0.19 & 0.33 & -0.18 & -1.03 & 0.45 & 0.22 & 0.046 \end{bmatrix} \begin{bmatrix} \bar{u}_{k-4} \\ \bar{u}_{k-3} \\ \bar{u}_{k-2} \\ \bar{u}_{k-1} \\ \bar{u}_{k+0} \\ \bar{u}_{k+1} \\ \bar{u}_{k+2} \\ \bar{u}_{k+3} \end{bmatrix} \quad (3.86)
$$

Depending on the length of the horizon, the elements within a δ - range at both ends of the rod need to be surface-corrected according to subsection 3.1.6. An example of a coupling between a peridynamic- and CCM-rod is given in subsection 5.3.2.

3.3 Boundary conditions

Boundary conditions in Peridynamics differ in several ways from classical elasticity's concept. In the later, constraining the displacement field or it's derivatives on a boundary with vanishing volume is sufficient to impose displacement- and force boundary conditions on the problem. As the peridynamic forces and thus the underlying displacement field is built from the integration over force densities within a finite region of space, "local" boundary conditions on a vanishing volume need to be replaced by boundary conditions with spatial extent. Furthermore, force boundary conditions in Peridynamics are not expressed by derivatives of the displacement field on the boundary. Following the nonlocal concept, pointwise boundary tractions do not directly appear in Peridynamics [Madenci and Oterkus 2014, p.30]. Instead, force boundary conditions are introduced by prescribing the external force density on a finite boundary domain, displacement boundary conditions are realized by constraining the displacements on a nonvanishing boundary domain. Thus, the Peridynamic domain Ω has to be split into two subdomains.

Depicted below is the peridynamic finite element model. The peridynamic domain Ω is
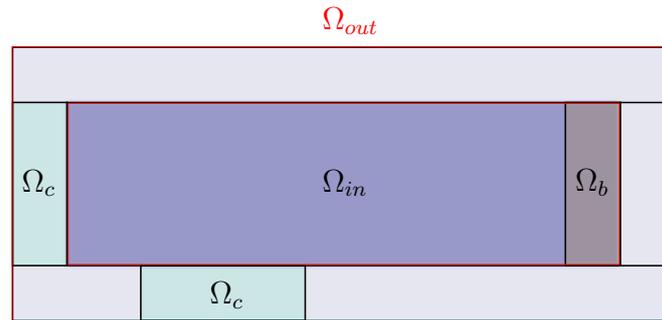
Figure 3.32: Inner and outer peridynamic domain, force- and displacement domains

split into an inner domain Ω_{in}, and a surrounding, outer domain Ω_{out}. The inner domain is defined as the set of finite elements, whose degrees of freedom are all unconstrained. The outer layer consists of those elements, whose degrees of freedom are all constrained plus a layer of elements, surrounding Ω_{in}, whose dofs are partly unconstrained and partly constrained.
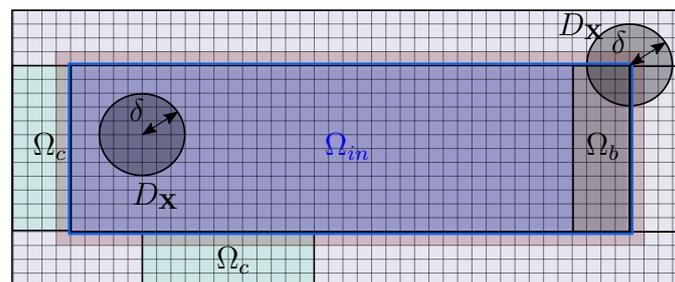
Figure 3.33: Meshed domains

Displacement boundary conditions

The nodal displacements of all elements of Ω_{out}, except for those elements adjacent to Ω_{in}, are set to 0 by default. The dofs of the layer of elements connected to Ω_{in} (depicted in reddish) are unconstrained, if they coincide with a dof of Ω_{in}, otherwise they are set to 0. In order not to constrain the complete outer region by this design choice, the material parameter c of the elements in Ω_{out} can be varied. Setting c to zero equals a free surface (compare grey elements in figure 3.33), whereas having the same c in Ω_{out} and Ω_{in} yields a constrained region Ω_c, which can be used to model supports, compare the mint-colored elements in 3.33. The bonds emanating from elements in Ω_{in} find in those constrained (mint) elements immovable partners with non-vanishing material constants.

The material value c of the outer elements adjacent to Ω_{in} (reddish shade in figures 3.33 and 3.34) depends on the intended boundary condition beyond. In case of a free surface (compare blue family at lower edge of Ω_{in} in figure 3.34), the material constant of the respective elements in Ω_{out} is set to 0. In this case, only the elements in Ω_{in} have non-vanishing material, whereas the bonds to elements in Ω_{out} have zero bond constant, indicated by the dotted lines in fig. 3.34.
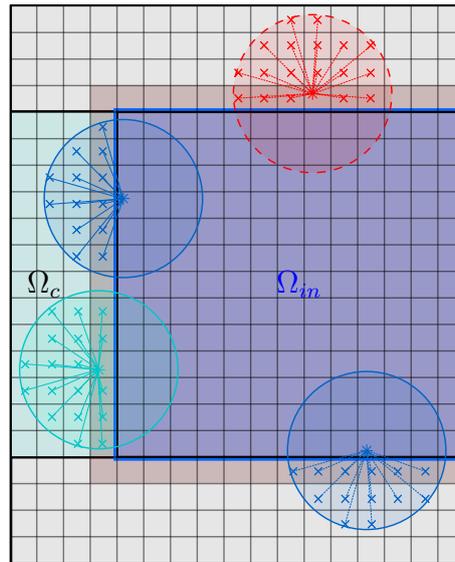
Figure 3.34: Families and bonds

In case of a constrained region behind the inner region (compare blue and cyan family at left edge), the elements in between Ω_{in} and those elements of Ω_{out} with all dofs constrained share c with Ω_{in}. The difference between the blue and the cyan family lies in the origin of the parent Gauss point; the blue family is originating from an element in Ω_{in}, but the cyan family is originating from an element with both unconstrained and constrained dofs. Since the mint elements in the surrounding belong to a support region and have non-vanishing material, the parent element contributes to the force state of the problem, although the element itself is not in Ω_{in}. The red family at the upper element demonstrates the opposite. The originating element belongs to Ω_{out}, has therefore both constrained and unconstrained dofs and could contribute to the Jacobian. But this surface is supposed to be a free one, therefore, the parent-element material is set to 0 and all bonds have no force.

Although inner-region-dofs are unconstrained by default, they can be assigned arbitrary displacements, thus enabling a displacement-controlled solution with adaptive dynamic relaxation, compare subsection 3.4.2.

Force boundary conditions

Force boundary conditions can be applied in Ω_b, a subset of Ω_{in}. Since the peridynamic equations are solved by finite elements, it is possible to apply the forces directly on the elements nodes.

3.4 Quasi - static crack propagation

In this thesis focus is set to a quasi-static crack propagation. Inertial effects like generation of stress waves due to a further opening of the crack tip are neglected. To justify the neglection of wave motion of the continuum, loads are applied slowly (quasi static) [Madenci and Oterkus 2014, p.171]. Since no plastic deformation is incorporated in the underlying peridynamic model, according to the assumptions of linear elastic fracture mechanics (LEFM), only a brittle material can be simulated, where the plastic deformations around the crack tip are assumed to be small in comparison to the size of the crack [Mehlhorn 1996b, p.160].

3.4.1 Damage model

Damage in Peridynamics is introduced by irreversibly deleting bonds between material points, leading to a redistribution of the forces [Madenci and Oterkus 2014, p.114]. Different to Peridynamics on a particle level, the bonds in the present finite elements exist between a parent gauss point $\mathbf{X}$ and it's subordinate quadrature points $\mathbf{Y}$ throughout the element itself and the elements in it's family. Thus, the parent Gauss points are not connected to each other by bonds directly, but by the dofs defining the displacement fields of the elements. Deleting bonds of a family $D_{\mathbf{X}}$ however softens up the element containing $\mathbf{X}$ and all potential $\mathbf{Y}$ in that element, because larger nodal displacements are necessary for a thinned out family to yield the same force state in $\mathbf{X}$ as an undamaged one. The following derivations hold for a 2-D problem:

In Peridynamics, a new surface (crack) A is created, if all bonds passing through A are deleted [Madenci and Oterkus 2014, p.116]. Those are all bonds within a circle of radius δ around A.
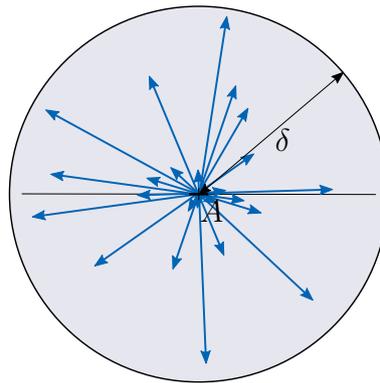
Figure 3.35: All bonds through A

A bond is deleted if it's stretch s exceeds the critical stretch s_c, which is defined in the following:

$$s = \frac{|\mathbf{Y} + \mathbf{u_Y} - \mathbf{X} - \mathbf{u_X}| - |\mathbf{Y} - \mathbf{X}|}{|\mathbf{Y} - \mathbf{X}|}$$

Independent of Peridynamics, a new surface A is created, if the strain energy in A surpasses the material dependent critical energy release rate G_c. Thus, by equating G_c with the strain energy of all bonds passing through A at $s = s_c$ yields an expression to compute the critical stretch of a bond. The strain energy of all bonds passing through A can be computed using a shift and integration in polar coordinates, compare [Silling and Askari 2005]:
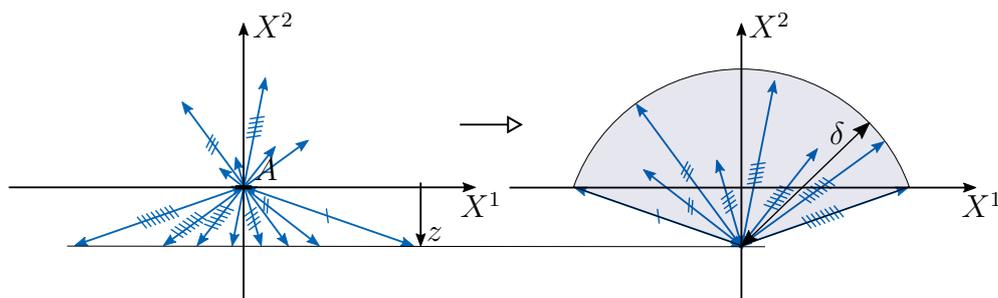
Figure 3.36: Shift of all bonds on same X^2 level

Depicted in the left of figure 3.36 are all bonds passing through A, whose lower ends have all the same X^2 coordinate. Depicted right in figure 3.36 are all those bonds shifted to the same X^1-coordinate with their lower ends. Although the bonds do not pass through the same surface A any more by this shift, it represents the same physical state. Repeating this step for all bond ends with equal X^2 - coordinate yields figure 3.37, which is suitable for integration in polar coordinates to obtain the strain energy density in A, compare [Madenci and Oterkus 2014, p.119]:
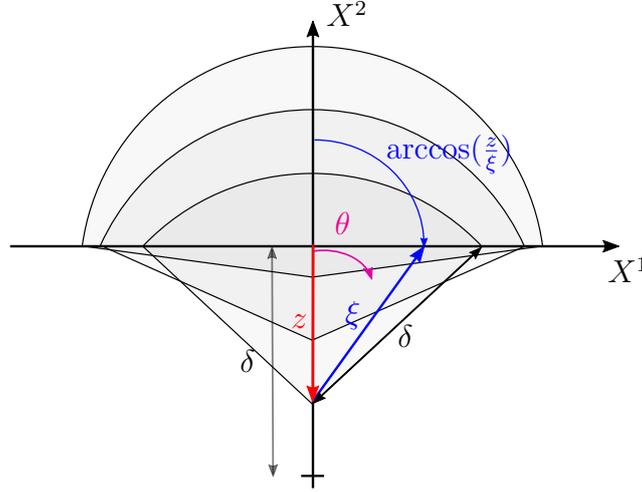
Figure 3.37: Coordinate system for integration of strain energy

$$
W \;=\; 2 \int\limits_{z=0}^{\delta} \int\limits_{\xi=z}^{\delta} \int\limits_{\theta=0}^{\arccos \frac{z}{\xi}} w(\xi)\, \xi\, d\theta d\xi dz \tag{3.87}
$$

ξ in equation 3.87 denotes the undeformed length of the bonds and is a radius in polar coordinates. The critical strain energy density $w_c(\xi)$ of a bond in polar coordinates is given by [Madenci and Oterkus 2014, p.119]:

$$
w_c(\xi) \;=\; \int\limits_{r=0}^{\xi} \frac{1}{2} c\, s_c^2\, dr \;=\; \frac{1}{2} c\, s_c^2\, \xi \tag{3.88}
$$

where $\frac{1}{2} c\, s_c^2$ denotes the micropotential of a bond at maximum stretch, see eq. 2.19. Inserting expression 3.88 into 3.87 denotes the amount of strain energy, which would cause all bonds passing A to reach their critical stretch and therefore fail:

$$
W \;=\; 2 \int\limits_{z=0}^{\delta} \int\limits_{\xi=z}^{\delta} \int\limits_{\theta=0}^{\arccos \frac{z}{\xi}} \frac{1}{2} c\, s_c^2\, \xi^2\, d\theta d\xi dz \;=\; c\, s_c^2\, \frac{\delta^4}{4} \tag{3.89}
$$

Equating expression 3.89 with the critical energy release rate G_c, introducing the bond constant c from equation 2.35 and solving for s_c yields an expression for the critical stretch:

$$s_c = \sqrt{\frac{2\,G_c\,\pi}{9\,\kappa\,\delta}} = \sqrt{\frac{4\,(1-\nu)\,G_c\,\pi}{9\,E\,\delta}} \tag{3.90}$$

During computation, the stretch of every bond can be easily compared with s_c. Bonds exceeding this stretch are terminated, introducing damage to the peridynamic finite elements.

3.4.2 Adaptive dynamic relaxation

As soon as the damage model is taken into the simulation, a different solution technique becomes necessary. (Unmodified) Newton's method cannot cope with unstable crack propagation, e.g. in a crack path analysis, because the system will be in no more equilibrium state as soon as crack propagation has begun. A different approach for quasi-static crack propagation was suggested by [Kilic and Madenci 2010] and can be found in [Madenci and Oterkus 2014, p.136 - p.138].

The peridynamic equilibrium equation $\mathbf{R}$ (compare equation 3.17) is reformulated into a pseudo-time dependent problem

$$[D]\,\ddot{\bar{\mathbf{u}}}(t) + c_d\,[D]\,\dot{\bar{\mathbf{u}}}(t) = \mathbf{R}(\bar{\mathbf{u}}(t)) \tag{3.91}$$

with yet to determine diagonal density matrix $[D]$. Vector $\mathbf{R}$ in eq. 3.91 denotes the vector of the resulting forces in the nodes of the finite element meshgrid, and c_d stands for a (yet to determine) artificial damping coefficient. The aim is to render equation system 3.91 into a critically damped problem, that shall reach the steady-state solution (the static equilibrium) as soon as possible by an explicit time-integration scheme [Madenci and Oterkus 2014, p.136]. According to an explicit time integration scheme with central differences, the displacement in the next time step $\bar{\mathbf{u}}^{(n+1)}$ is derived from the known displacement and velocity from prior time steps:

$$\bar{\mathbf{u}}^{(n+1)} = \bar{\mathbf{u}}^{(n)} + \Delta t\,\dot{\bar{\mathbf{u}}}^{(n+\frac{1}{2})} \tag{3.92}$$

The velocity in eq. 3.92 is evaluated in the middle of the time interval $[n\Delta t,\ (n+1)\Delta t]$ by a central difference approach:

$$\dot{\bar{\mathbf{u}}}^{(n+\frac{1}{2})} = \frac{(2 - c_d^{(n)}\,\Delta t)\dot{\bar{\mathbf{u}}}^{(n-\frac{1}{2})} + 2\Delta t[D]^{-1}\mathbf{R}(\bar{\mathbf{u}}^{(n)})}{(2 + c_d^{(n)}\Delta t)} \tag{3.93}$$

Because no velocity at time step $n = -\frac{1}{2}$ is available, the algorithm is started with

$$\dot{\bar{\mathbf{u}}}^{(\frac{1}{2})} = \frac{\Delta t \, [D]^{-1} \, \mathbf{R}(\bar{\mathbf{u}}^{(0)})}{2} \tag{3.94}$$

The iteration is terminated as soon the absolute value of the difference of two successive steps falls below a user-defined threshold ϵ_{relax}:

$$\left| \bar{\mathbf{u}}^{(n+1)} - \bar{\mathbf{u}}^{(n)} \right| \leq \epsilon_{relax} \tag{3.95}$$

The time t is a pseudo-time and has no mechanical meaning. Therefore, the timestep length Δt can be chosen to 1.

In the following, the yet unknown matrix $[D]$ is derived. Central difference explicit time integration is conditionally stable. A necessary condition for stability is given by the Courant-Friedrichs-Lewy (CFL) condition [Dang and Meguid 2010, p.126]:

$$1 \geq \frac{\Delta t \, v_{max}}{h_{min}} \quad \Leftrightarrow \quad 1 \geq \frac{1}{4} \, (\Delta t)^2 \, \omega^2_{max} \tag{3.96}$$

ω_{max} in eq. 3.96 denotes the largest angular eigenfrequency of the system. The condition above guarantees, that the product of largest phase velocity v_{max} of a wave and the time step length is shorter than the shortest meshgrid length h_{min}. Since the phase velocity is directly proportional to the eigenfrequency of the wave, the entries of the density matrix $[D]$ must be computed in such a way that the phase velocity of the highest eigenvalue (eigenfrequency) resulting from [D] and [K] does not violate the CFL condition. "An upper bound to the maximum eigenvalue (eigenfrequency) can be obtained from Gerschgorin's theorem" [Dang and Meguid 2010, p.126]:

$$\omega^2_{max_i} \leq \max \sum_j \frac{\left| K_{ij} \right|}{D_{ii}} \tag{3.97}$$

D_{ii} in eq. 3.97 stands for the main diagonal matrix elements. In the current context, $[D]$ is comparable to a mass matrix. Inserting eq. 3.97 into 3.96 and solving for D_{ii} provides a formalism to compute a density matrix $[D]$ that fulfills the CFL condition.

$$D_{ii} \geq \frac{1}{4} \, (\Delta t)^2 \max \sum_j \left| K_{ij} \right| \tag{3.98}$$

To be precise, the peridynamic equilibrium $\mathbf{R}$ (compare equation 3.17) is nonlinear in $\bar{\mathbf{u}}$ and thus cannot be expressed by a stiffness matrix $[K]$. The approximation by a stiffness matrix is therefore valid only for a fixed timestep in order to direct the pseudo-dynamical problem to a steady state solution. Madenci and Oterkus propose a peridynamic stiffness matrix derived from linearized Peridynamics in [Madenci and Oterkus 2014, p.138] for $[K]$ in 3.96. In the scope of this work, the analytical Jacobian matrix $[J]$ from subsection 3.1.3, evaluated at the initial displacement vector $\bar{\mathbf{u}}^{(n=0)}$ is used instead.

According to [Dang and Meguid 2010, p.126], the optimal convergence rate is obtained for the damping parameter $c_d^{(n)}$ being:

$$c_d^{(n)} \leq 2\,\omega_0 \tag{3.99}$$

where $\omega_0^{(n)}$ denotes the smallest eigenvalue, which can be computed by Rayleigh's quotient [Madenci and Oterkus 2014, p.138]:

$$\omega_0^{(n)} = \sqrt{\frac{\bar{\mathbf{u}}^T [K]_{loc}\, \bar{\mathbf{u}}}{\bar{\mathbf{u}}^T [D]\, \bar{\mathbf{u}}}} \tag{3.100}$$

$[K]_{loc}$ denotes the diagonal local stiffness matrix:

$$K_{ii_{loc}} = -\frac{f_i^{(n)} - f_i^{(n-1)}}{\lambda_{ii}\,\Delta\,\dot{u}^{(n-\frac{1}{2})}} \tag{3.101}$$

Equation 3.101 is an approximation of the current stiffness of the system, as no linear connection between internal forces and nodal displacements is available.

4 Coupling

The developed peridynamic finite elements require a higher computational effort than e.g. local, eight-noded two dimensional finite elements. The former's raison d'être lies in the simulation of regions where crack initiation and propagation is likely. Therefore, a coupling between both local and nonlocal finite elements would combine both computational efficiency and a change in topology if needed. In the scope of this thesis, an energy-based coupling (Arlequin method) is used. The "local" finite elements in the scope of this thesis have the same element length Δ like the peridynamic finite elements.

4.1 Arlequin method

The Arlequin method [Dhia 1998] is a coupling method to create a multi-model framework [Dhia and Rateau 2005, p.1443] and can be used to combine a local- and nonlocal model. It does not rely on adding the stiffness matrix entries of both subsystems on a coupling surface, but allows both models to exist parallel to each other in a finite gluing region S_G with compatibility between both being enforced by Lagrange multipliers [Bobaru et al 2016, p.410]. Because the coupling is not done by a sum of nodal forces of domains 1 and 2 in shared dofs, but their compatibility is enforced by the virtual work of a Lagrange multiplier field on a common overlap zone, a coupling of non-conforming meshgrids would be possible with the Arlequin framework too [Dhia and Rateau 2005, p.1444].

4.1.1 Setup

The coupled problem is visualized in figure 4.1 with the following relations between the sets holding:
Ω_1 denotes the peridynamic domain and Ω_2 denotes the CCM domain. As depicted in fig. 4.1, the gluing region S_G is the overlap zone between the inner peridynamic region $\Omega_{1_{in}}$ and Ω_2. In general, no coupling exists between $\Omega_{1_{out}}$ and Ω_2. Loads in the scope of this work are supposed to exist on Ω_2 only. According to [Dhia and Rateau 2005, p.1447], the coupled
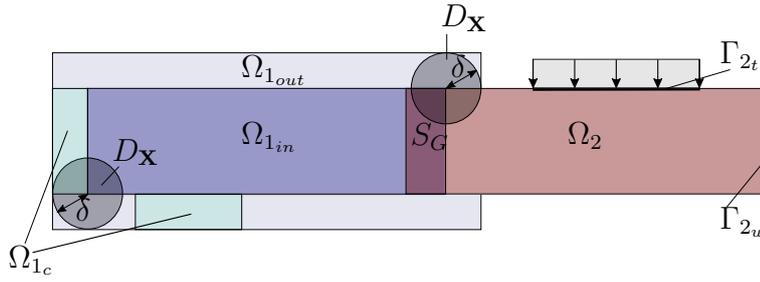
Figure 4.1: Coupled system – definition of domains and surfaces

$$
\begin{aligned}
\Omega_1 &= \Omega_{1_{in}} \cup \Omega_{1_{out}} \\
S_G &= \Omega_{1_{in}} \cap \Omega_2 \\
\Omega_{1_{out}} \cap \Omega_2 &= \emptyset \\
\Omega_{1_b} &= \emptyset
\end{aligned}
\qquad (4.1)
$$

problem reads as:

given : $\mathbf{p} : \Omega_2 \to \mathbb{R}^2$ with $\Omega_2 \subset \mathbb{R}^2$

boundary region values:

$\mathbf{u}_1 = \tilde{\mathbf{u}}_1$ on Ω_{1_c}

$\mathbf{u}_2 : \boldsymbol{\sigma} \cdot \mathbf{n} = \mathbf{t} = \bar{\mathbf{t}}$ on Γ_{2_t}

goal : find functions

$$\mathbf{u}_1 \in \mathcal{U}_1 := \left\{ \mathbf{u}_1 \in \left(\mathbf{H}^1(\Omega_1) \right)^2 \,|\, \mathbf{u}_1 = \tilde{\mathbf{u}}_1 \text{ on } \Omega_{1_c} \right\}$$

$$\mathbf{u}_2 \in \mathcal{U}_2 := \left\{ \mathbf{u}_2 \in \left(\mathbf{H}^1(\Omega_2) \right)^2 \,|\, \mathbf{u}_2 = \tilde{\mathbf{u}}_2 \text{ on } \Gamma_{2_u} \right\}$$

$$\boldsymbol{\lambda} \in \mathcal{U}_G := \left\{ \boldsymbol{\lambda} \in \left(\mathbf{H}^1(S_G) \right)^2 \right\}$$

such that for all

$$\delta\mathbf{v}_1 \in \mathcal{V}_1 := \left\{ \delta\mathbf{v}_1 \in \left(\mathbf{H}_0^1(\Omega) \right)^2 \,|\, \delta\mathbf{v}_1 = \mathbf{0} \text{ on } \Omega_c \right\}$$

$$\delta\mathbf{v}_2 \in \mathcal{V}_1 := \left\{ \delta\mathbf{v}_2 \in \left(\mathbf{H}_0^1(\Omega) \right)^2 \,|\, \delta\mathbf{v}_2 = \mathbf{0} \text{ on } \Gamma_{2_u} \right\}$$

$$\delta\boldsymbol{\mu} \in \mathcal{V}_G := \left\{ \delta\boldsymbol{\mu} \in \left(\mathbf{H}^1(S_G) \right)^2 \right\}$$

the equations

$$\delta W = \iint\limits_{\Omega_1} \alpha_1 \left(\iint\limits_{\Omega_1 \cap D_{\mathbf{x}_1}} \mathbf{f}(\mathbf{u}_1) \, da_{\mathbf{y}_1} \right) \cdot \delta\mathbf{v}_1 \, da_{\mathbf{x}} + \iint\limits_{\Omega_2} \alpha_2 \left(\boldsymbol{\sigma}(\mathbf{u}_2) : \boldsymbol{\epsilon}(\delta\mathbf{v}_2) \right) dA_{\mathbf{X}_2} +$$

$$+ \, C\left(\boldsymbol{\lambda}, \delta\mathbf{v}_1 - \delta\mathbf{v}_2 \right) = \int\limits_{\Gamma_{2_t}} \mathbf{t} \cdot \delta\mathbf{v}_2 \, d\Gamma_2 + \iint\limits_{\Omega_2} \mathbf{p} \cdot \delta\mathbf{v}_2 \, dA_{\mathbf{X}_2}$$

$$C\left(\mathbf{u}_1 - \mathbf{u}_2, \delta\boldsymbol{\mu} \right) = \mathbf{0}$$

are fulfilled.

$$(4.2)$$

4.1.2 Coupling operator

The first of the equations represents the virtual work of the interior and exterior forces in both peridynamic and CCM-domain, supplemented by a coupling operator C, which acts on the gluing regions $\Omega_1 \cap S_G$ and $\Omega_2 \cap S_G$. The coupling operator will include a Lagrange multiplier field $\boldsymbol{\lambda}$, but because the Arlequin method is a volume coupling instead of a surface coupling, the structure of the coupling operator is not clear right from the start. It's task is to enforce a weak equivalence of the displacements in the gluing region S_G. In order to fit the virtual work of Ω_1 and Ω_2, the coupling operator has to yield a virtual work too. According to [Dhia 2008, p.5], the beginning of the developement of the coupling operator is a look on the Hilbert space the functions $\boldsymbol{\lambda}$, $\delta\mathbf{v}_1$ and $\delta\mathbf{v}_2$ will originate from. The coupling operator is a linear, continuous bilinear form, mapping the Lagrange multipliers and the test fields to the real numbers. Because the test functions originate from a Hilbert space, Riesz representation theorem is applicable, see appendix A.1.3. It states, that in a Hilbert space V, every linear continuous functional $l(\mathbf{v})$, $l : \text{V} \to \mathbb{R}$, can be expressed by the scalar product of a unique vector $\boldsymbol{\lambda} \in V$ and $\mathbf{v}$.

$$l(\mathbf{v}) = <\boldsymbol{\lambda}, \mathbf{v}> \text{ for all } \mathbf{v} \in V \tag{4.3}$$

The yet unknown coupling operator C can be seen as this scalar product.

$$C(\boldsymbol{\lambda}, \mathbf{v}) = <\boldsymbol{\lambda}, \mathbf{v}> \text{ for all } \mathbf{v} \in V \tag{4.4}$$

The unknown vector $\boldsymbol{\lambda}$ can be interpreted as a Lagrange multiplier field. The structure of the scalar product in 4.3 can be derived from the Hilbert space the test functions $\mathbf{v}$ (and $\boldsymbol{\lambda}$) exist in.

$\mathbf{H}^1$ is the space of the L^2 - functions which have additionally a weak first derivative. (Please note that belonging to the space L^2 poses no requirement on the differentiability of the functions; only their squared integral over Ω has to remain finite; a further restriction of the function space is therefore necessary in order to obtain e.g. test functions for the CCM-domain Ω_2, which must have a weak derivative). Therefore, the approach functions should originate from the Sobolev space $\mathbf{W}^{1,2}$ (comp. A.1.3) with the inner product:

$$<f, g>_{\mathbf{H}^1} = \int_\Omega f(x)\, g(x)\, +\, D^1 f(x)\, D^1 g(x)\, dx \tag{4.5}$$

D^1 stands for the weak first derivative. Because the domain S_G are both two dimensional, D^1 represents all weak partial first derivatives. The inner product of the Sobolev space

therefore incorporates the gradient:

$$< f, g >_{\mathbf{H^1}} = \iint_{S_G} f(\mathbf{x}) \, g(\mathbf{x}) \, + \, \nabla f(\mathbf{x}) \, \nabla g(\mathbf{x}) \, dX^2 dX^1 \tag{4.6}$$

By introducing eq. 4.6 into eq. 4.4, replacing $f(\mathbf{x})$ by $\boldsymbol{\lambda}$ and $g(\mathbf{x})$ by $\delta\mathbf{v}_1 - \delta\mathbf{v}_2$, one obtains a valid description of the coupling operator C:

$$\begin{aligned} C(\boldsymbol{\lambda},\mathbf{v}) \, &= \, C(\boldsymbol{\lambda}, \delta\mathbf{v}_1 - \delta\mathbf{v}_2) \, = \, C(\boldsymbol{\lambda}, \delta\mathbf{v}_1) \, - \, C(\boldsymbol{\lambda}, \delta\mathbf{v}_2) \, = \\ &= \iint_{S_G} \boldsymbol{\lambda} \cdot \delta\mathbf{v}_1 + \nabla\boldsymbol{\lambda} : \nabla\delta\mathbf{v}_1 \, dX^2 dX^1 \, - \, \iint_{S_G} \boldsymbol{\lambda} \cdot \delta\mathbf{v}_2 + \nabla\boldsymbol{\lambda} : \nabla\delta\mathbf{v}_2 \, dX^2 dX^1 \end{aligned} \tag{4.7}$$

Please note that the integration over S_G is done w.r.t. the undeformed configuration, because the coupled CCM-domain is based on an infinitesimal strain theory, such that deformed and undeformed configuration coincide. The scalar product in eq.4.7 can be split in two, because the scalar product is by definition linear in it's arguments. The splitting in the components $\delta\mathbf{v}_1$ and $\delta\mathbf{v}_2$ is necessary, because the Lagrange multipliers will act by definition opposite to each other on $\delta\mathbf{v}_1$ and $\delta\mathbf{v}_2$. In order to select only parts of the complete coupling operator, two factors (κ_1, κ_2) are introduced. (Their existence however cannot be deduced from the scalar product itself).

$$\begin{aligned} C(\boldsymbol{\lambda}, \delta\mathbf{v}_1 - \delta\mathbf{v}_2) \, &= \iint_{S_G} \kappa_1 \boldsymbol{\lambda} \cdot \delta\mathbf{v}_1 \, + \, \kappa_2 \nabla\boldsymbol{\lambda} : \nabla\delta\mathbf{v}_1 \, dX^2 dX^1 - \\ &- \iint_{S_G} \kappa_1 \boldsymbol{\lambda} \cdot \delta\mathbf{v}_2 \, + \, \kappa_2 \nabla\boldsymbol{\lambda} : \nabla\delta\mathbf{v}_2 \, dX^2 dX^1 \end{aligned} \tag{4.8}$$

A choice $(\kappa_1, \kappa_2) = (1,0)$ yields the $\mathcal{L}^2$ - coupling. According to [Dhia 2008, p.5], this coupling can be understood as a Lagrange multiplier field homogenous to a force - density field, acting on the virtual displacements. However, although this choice of coupling seems natural on a first glance, it represents an incomplete coupling operator for a volume coupling which can lead to an ill-conditioned problem, as parts of the scalar product eq. 4.7 are missing and the operator is not coercive any more. One of the requirements of an operator is to be coercive [Hartmann 2008, p.5]:

$$C(\mathbf{v}, \, \mathbf{v}) \, \geq \, k\|\mathbf{v}\|_V \, \|\mathbf{v}\|_V \tag{4.9}$$

with a constant $k > 0$. Coercivity means that the result of C operating on an infinitely large input must not remain finite. In a non-coercive coupling operator, the Lagrange multipliers could tend to infinity in their vain attempt to generate enough virtual work to ensure the coupling. Furthermore, infinitley large values for the Lagrange multipliers would violate the condition that $\boldsymbol{\lambda} \in \mathbf{L}^2$[Dhia 2008, p.13, p.14]. In case that the complete scalar product of

the Sobolev space $\mathbf{H}^1$ is used for the coupling operator, the Lagrange multiplier field becomes homogenous to a displacement field [Dhia 2008, p.5]. This operator is denoted $\mathcal{H}^1$ - coupling and is realized by setting $(\kappa_1, \kappa_2) = (1,1)$ in equation 4.8.

The factors α_1 and α_2 in 4.2 are weight parameters in order not to count the energy in the gluing region twice [Dhia and Rateau 2005, p.1446]:

$$\begin{aligned} \alpha_i &= 1 \text{ in } \Omega_i \, S_G \\ \alpha_1 + \alpha_2 &= 1 \text{ in } S_G \end{aligned} \tag{4.10}$$

4.1.3 Matrix form of coupled problem

With the coupling operator C defined, the contributing, discretized vector fields can be put into the equation 4.2 in order to obtain a system of $2\,(M_1 + M_2 + M_G)$ equations. M_1 denotes the number of nodes in the inner peridynamic domain $\Omega_{1_{in}}$, M_2 the number of nodes in the CCM-domain Ω_2, and M_G the number of nodes in the gluing region S_G. Both real- and virtual Lagrange multiplier fields $\boldsymbol{\lambda}$ and $\delta\boldsymbol{\mu}$ are discretized with piecewise linear "hat" - functions:

$$\begin{aligned} \boldsymbol{\lambda} &\approx \boldsymbol{\lambda}^h \\ \delta\boldsymbol{\mu} &\approx \delta\boldsymbol{\mu}^h \end{aligned} \tag{4.11}$$

with

$$\begin{aligned} \boldsymbol{\lambda}^h \in \mathcal{U}_1^h &:= \left\{ \boldsymbol{\lambda}^h \in \left(\mathbf{H}^1(S_G)\right)^2 \,|\, \boldsymbol{\lambda}^h(\mathbf{X}) = \sum_{n=1}^{M_G} \mathbf{A}_n(\mathbf{X}) \cdot \bar{\boldsymbol{\lambda}}_n \right\} \subset \mathcal{U}_1 \\ \delta\boldsymbol{\mu}^h \in \mathcal{V}_1^h &:= \left\{ \delta\boldsymbol{\mu}^h \in \left(\mathbf{H}^1(S_G)\right)^2 \,|\, \delta\boldsymbol{\mu}^h(\mathbf{X}) = \sum_{l=1}^{M_G} \mathbf{B}_l(\mathbf{X}) \cdot \delta\bar{\boldsymbol{\mu}}_l \right\} \subset \mathcal{V}_1 \end{aligned} \tag{4.12}$$

with the already defined matrices $\mathbf{A}_k, \mathbf{B}_k$ from eq. 3.12. Introducing the discretized fields into the coupling operator transforms the coupling operator into a linear equation system. The derivation of a coupling element is exemplarily done for $\delta\mathbf{v}$ now:

$$\begin{aligned} C(\boldsymbol{\lambda}, \delta\mathbf{v}) &= \iint_{S_G} \kappa_1 \boldsymbol{\lambda} \cdot \delta\mathbf{v} + \kappa_2 \nabla\boldsymbol{\lambda} : \nabla\delta\mathbf{v} \, dX^2 dX^1 = \\ &= \iint_{S_G} \kappa_1 \boldsymbol{\lambda} \cdot \delta\mathbf{v} \, dX^2 dX^1 + \iint_{S_G} \kappa_2 \nabla\boldsymbol{\lambda} : \nabla\delta\mathbf{v} \, dX^2 dX^1 \end{aligned} \tag{4.13}$$

For a better overview, the two equations 4.13 are treated separately, beginning with the left one:

$$\iint_{S_G} \kappa_1 \boldsymbol{\lambda} \cdot \delta \mathbf{v} \, dX^2 dX^1 \approx \sum_{l=1}^{M_G} \delta \bar{\mathbf{v}}_l^T \iint_{S_G} \kappa_1 \, \mathbf{B}_l^T(\mathbf{X}) \cdot \sum_{n=1}^{M_G} \mathbf{A}_n(\mathbf{X}) \cdot \bar{\boldsymbol{\lambda}}_n \, dX^2 dX^1 \qquad (4.14)$$

This expression provides $2M_G$ equations, because $2M_G$ coefficients $\delta \bar{v}_l$ of the test function exist. By setting one particular $\delta \bar{v}_k$ to 1 and the others to 0, one can isolate the virtual work of $\boldsymbol{\lambda}$ on node k:

$$\iint_{S_G} \kappa_1 \sum_{n=1}^{M_G} \begin{bmatrix} \bar{N}_l(X^1, X^2) \, \bar{N}_n(X^1, X^2) & 0 \\ 0 & \bar{N}_l(X^1, X^2) \, \bar{N}_n(X^1, X^2) \end{bmatrix} \begin{bmatrix} \bar{\lambda}_1^n \\ \bar{\lambda}_2^n \end{bmatrix} dX^2 dX^1 \quad (4.15)$$

The right integral in eq. 4.13 contains the double contraction of the gradients of $\boldsymbol{\lambda}$ and $\delta \mathbf{v}$. The gradient of a vector field w.r.t. a curvilinear coordinate system is defined as: [Klingbeil 1966, p.88]

$$\begin{aligned} \boldsymbol{\lambda} &= \lambda^i \, \mathbf{g}_i \\ \nabla \boldsymbol{\lambda} &= \lambda^i_{,j} \, \mathbf{g}_i \otimes \mathbf{g}^j \\ &\text{with} \\ \lambda^i_{,j} &= \frac{\partial \lambda^{k0}}{\partial X^l} \frac{\partial X^l}{\partial \theta^j} \frac{\partial \theta^i}{\partial X^{k0}} + \lambda^{k0} \frac{\partial^2 \theta^i}{\partial X^{k0} \partial X^l} \frac{\partial X^l}{\partial \theta^j} \end{aligned} \qquad (4.16)$$

In case that $\mathbf{g}_i = \mathbf{e}_i$ and $\theta^i = X^i$, expression 4.16 simplifies to:

$$\lambda^i_{,j} = \frac{\partial \lambda^{k0}}{\partial X^l} \frac{\partial X^l}{\partial X^j} \frac{\partial X^i}{\partial X^{k0}} + \lambda^{k0} \frac{\partial^2 X^i}{\partial X^{k0} \partial X^l} \frac{\partial X^l}{\partial X^j} \qquad (4.17)$$

All terms $k_0 \neq i$ and $l \neq j$ will vanish. The only remaining terms are then:

$$\lambda^i_{,j} = \frac{\partial \lambda^i}{\partial X^j} \frac{\partial X^j}{\partial X^j} \frac{\partial X^i}{\partial X^i} + \lambda^i \underbrace{\frac{\partial^2 X^i}{\partial X^i \partial X^j}}_{0} \frac{\partial X^j}{\partial X^j} = \frac{\partial \lambda^i}{\partial X^j} \qquad (4.18)$$

Because co- and contravariant base vectors coincide in Cartesian coordinates and because the christoffel symbols vanish when applying the gradient to a vector field in Cartesian coordinates, the contraction can be written down in an simple way [Parisch 2003, p.21]:

$$\begin{aligned} \nabla \boldsymbol{\lambda} : \nabla \delta \mathbf{v} &= \left(\lambda^i_{,j} \, \mathbf{e}_i \otimes \mathbf{e}^j \right) : \left(\delta V^s_{,k} \, \mathbf{e}_s \otimes \mathbf{e}^k \right) = \lambda^i_{,j} \, \delta V^k_{,s} \, \delta_{is} \, \delta^{jk} = \lambda^i_{,j} \, \delta V^j_{,i} = \\ &= \lambda^1_{,1} \, \delta v^1_{,1} + \lambda^1_{,2} \, \delta v^2_{,1} + \lambda^2_{,1} \, \delta v^1_{,2} + \lambda^2_{,2} \, \delta v^2_{,2} = \\ &= \frac{\partial \lambda^1}{\partial X^1} \frac{\partial \delta v^1}{\partial X^1} + \frac{\partial \lambda^1}{\partial X^2} \frac{\partial \delta v^2}{\partial X^1} + \frac{\partial \lambda^2}{\partial X^1} \frac{\partial \delta v^1}{\partial X^2} + \frac{\partial \lambda^2}{\partial X^2} \frac{\partial \delta v^2}{\partial X^2} \end{aligned} \qquad (4.19)$$

Substituting the discretized fields into eq. 4.19 and integration over S_G provides the following scheme to build up the equation system resulting from the second part of the coupling operator according to 4.15. Remark: The coordinates (X^1, X^2) are omitted in the matrix below.

$$\iint_{S_G} \kappa_2 \, \nabla \boldsymbol{\lambda} \, : \, \nabla \delta \mathbf{v} \, dX^2 dX^1 \approx$$

$$\approx \sum_{l=1}^{M_G} \delta \bar{\mathbf{v}}_l^T \iint_{S_G} \kappa_2 \sum_{n=1}^{M_G} \begin{bmatrix} \dfrac{\partial \bar{N}_n}{\partial X^1} \dfrac{\partial \bar{N}_l}{\partial X^1} & \dfrac{\partial \bar{N}_n}{\partial X^1} \dfrac{\partial \bar{N}_l}{\partial X^2} \\[2mm] \dfrac{\partial \bar{N}_n}{\partial X^2} \dfrac{\partial \bar{N}_l}{\partial X^1} & \dfrac{\partial \bar{N}_n}{\partial X^2} \dfrac{\partial \bar{N}_l}{\partial X^2} \end{bmatrix} \begin{bmatrix} \bar{\lambda}_n^1 \\[2mm] \bar{\lambda}_n^2 \end{bmatrix} dX^2 dX^1 \tag{4.20}$$

The complete coupling operator finally becomes:

$$C(\boldsymbol{\lambda}, \delta \mathbf{v}) = \sum_{l=1}^{M_G} \delta \bar{\mathbf{v}}_l^T \iint_{S_G} \sum_{n=1}^{M_G} \left[\kappa_1 \begin{bmatrix} \bar{N}_l \, \bar{N}_n & 0 \\ 0 & \bar{N}_l \, \bar{N}_n \end{bmatrix} + \kappa_2 \begin{bmatrix} \dfrac{\partial \bar{N}_n}{\partial X^1} \dfrac{\partial \bar{N}_l}{\partial X^1} & \dfrac{\partial \bar{N}_n}{\partial X^1} \dfrac{\partial \bar{N}_l}{\partial X^2} \\[2mm] \dfrac{\partial \bar{N}_n}{\partial X^2} \dfrac{\partial \bar{N}_l}{\partial X^1} & \dfrac{\partial \bar{N}_n}{\partial X^2} \dfrac{\partial \bar{N}_l}{\partial X^2} \end{bmatrix} \right] \begin{bmatrix} \bar{\lambda}_n^1 \\[2mm] \bar{\lambda}_n^2 \end{bmatrix} dX^2 dX^1 \tag{4.21}$$

In order to obtain the stiffness matrix of one coupling finite element, the integration over the whole domain S_G has to be replaced by an integral over the element area Ω_E. For a four-noded quadrilateral element, this leaves four approach functions $\bar{N}_n(X^1, X^2)$ covering the domain of integration Ω_E, thus building the Lagrange multiplier field over the element from four contributing approach functions. Weighting this field with four independent test functions yields four vectorial equations. These equations can be assembled to the coupling matrix of one element.

Final matrix form with Newton's method

With the coupling operator defined, the complete coupled problem eq. 4.2 can be written down in matrix form. It must be solved iteratively, because it is a combination of nonlinear equations (the virtual work of Peridynamics) and linear equations (virtual work of classical continuum mechanics and Lagrange multipliers). During every iteration step n, The peridynamic Jacobian matrix $[J]^{(n)}$ is computed from $\mathbf{u}_{1_n}$ and assembled into the master matrix $[M]^{(n)}$.

$$[M]^{(n)} = \begin{bmatrix} [J]^{(n)} & [0] & [C(\boldsymbol{\lambda}, \delta\mathbf{v}_1)]^T \\ [0] & [K_{\mathrm{CCM}}] & -[C(\boldsymbol{\lambda}, \delta\mathbf{v}_2)]^T \\ [C(\mathbf{u}_1, \delta\boldsymbol{\mu})] & -[C(\mathbf{u}_2, \delta\boldsymbol{\mu})] & [0] \end{bmatrix} \tag{4.22}$$

This master matrix serves as new Jacobian matrix for Newton's method. During every iteration step, the equation system (comp. A.59) has to be solved

$$[M]^{(n)} \cdot \Delta\bar{\mathbf{u}} = -\mathbf{f}(\bar{\mathbf{u}}^{(n)})$$

with

$$\mathbf{f}(\bar{\mathbf{u}}^{(n)}) = \mathbf{r}^{(n)} + \mathbf{b} \tag{4.23}$$

where $\Delta\bar{\mathbf{u}}$ denotes an increment in vector $\bar{\mathbf{u}}$. The vector $\bar{\mathbf{u}}^{(n)}$ represents the vector of all unknown nodal displacements respectively Lagrange multipliers in the n'th iteration cycle.

$$\bar{\mathbf{u}}^{(n)} = \begin{bmatrix} \bar{\mathbf{u}}_1 \\ \bar{\mathbf{u}}_2 \\ \bar{\boldsymbol{\lambda}} \end{bmatrix} \tag{4.24}$$

with $\mathbf{r}$ being the vector of the inner nodal forces and $\mathbf{b}$ being the vector of the external nodal forces. Because the problem consists of a linear and a nonlinear part, $\mathbf{r}$ is composed of two parts too:

$$\mathbf{r} = \mathbf{r}_{Peri} + \mathbf{r}_{Rest} \tag{4.25}$$

$\mathbf{r}_{Rest}$ is computed form the constant parts of the master matrix $[M]$:

$$\mathbf{r}_{Rest} = \begin{bmatrix} [0] & [0] & [C(\boldsymbol{\lambda}, \delta\mathbf{v}_1)]^T \\ [0] & [K_{\mathrm{CCM}}] & -[C(\boldsymbol{\lambda}, \delta\mathbf{v}_2)]^T \\ [C(\mathbf{u}_1, \boldsymbol{\mu})] & -[C(\mathbf{u}_2, \delta\boldsymbol{\mu})] & [0] \end{bmatrix} \bar{\mathbf{u}}^{(n)} \tag{4.26}$$

$$\mathbf{r}_{Peri} = \begin{bmatrix} \mathbf{R}_{1_{int}} \\ \vdots \\ \mathbf{R}_{k_{int}} \\ \vdots \\ \mathbf{R}_{M_{1_{int}}} \end{bmatrix}$$

with

$$\mathbf{R}_{k_{int}} = \iint\limits_{\Omega^0} \mathbf{B}_k^T(\mathbf{X}) \cdot \mathbf{r}(\,\bar{\mathbf{u}}_1(\mathbf{X})\,) \, \det D\varphi(\mathbf{X}) \, dA_{\mathbf{X}}$$

$\mathbf{r}_{Peri}$ is the vector of the peridynamic inner nodal forces (in a weak sense), compare equation 3.18:

5 Numerical examples

This chapter presents some simulations using the elements and techniques mentioned before. At first, a validation of the peridynamic finite elements and the analytical Jacobian matrix is presented. Afterwards, the effects of different element lengths, discretizations of the peridynamic integrals and load applications are investigated, followed by an analysis of the result for a coupled problem. The results are compared to solutions obtained from analytical solutions or classical finite element analysis. The last two examples consist of an application of the crack propagation option of the developed elements, compared to the results of an XFEM-analysis performed in [Fries et al 2013, p.32 - 36].

5.1 Validation

Before the elements can be applied to various experiments, their convergence to classical solutions has to be shown. The test setup is a cantilever beam (compare [Glaws 2014, p.27]) with fixed displacements on the left- and a single load on the right hand side:

Figure 5.1: Cantilever beam setup

5.1.1 Comparison with results from literature

In a first step, the results of the four-node quadrilateral elements shall be compared to the results from [Glaws 2014, p.26 - 28], obtained by triangular finite elements. The setup of the problems consisted of:

1. $l = 35$

2. $h = 2$

3. $F = 10$

4. $E = 3000000$

5. $\nu = 0.25$

6. $b = 1$

The use of poisson ratio in [Glaws 2014] of $\nu = 0.25$ in a peridynamic simulation indicates that a plane-strain state was intended. In order to present a valid comparison, $\nu = 0.25$ is used in this subsection. Because the elements in this thesis are restricted to quadrilateral shape, the original mesh density in [Glaws 2014] of 200 nearly uniform elements with 260 dofs cannot be reproduced exactly.

All simulations are compared to an analytical solution obtained from a solution of Airy's stress function for a cantilevered beam with a single load on one end, compare [Bower 2008]. For better readability, the variables X_1, X_2, u_1, u_2 are expressed w.r.t. the contravariant cartesian base vectors. The displacement fields in u_1 and u_2 are given by:

$$u_1 = \frac{3\,F}{4\,E\,h^3\,b}\,(X_1 - l)^2 X_2 \;-\; \frac{F}{4\,E\,h^3\,b}(2 + \nu)\,X_2^3 \;+\; \frac{3\,F}{2\,E\,h^3\,b}(1 + \nu)\,h^2\,X_2 \;-\; \frac{3\,F\,l^2}{4\,E\,h^3\,b}\,X_2$$

$$u_2 = -\nu\,\frac{3\,F}{4\,E\,h^3\,b}\,(X_1 - l)X_2^2 \;-\; \frac{F}{4\,E\,h^3\,b}\,(X_1 - l)^3 \;+\; \frac{3\,F\,l^2}{4\,E\,h^3\,b}\,(X_1 - l) \;-\; \frac{F\,l^3}{2\,E\,h^3\,b}$$

$$(5.1)$$

[Glaws 2014] presents the maximum difference between peridynamic finite element solution and the solution obtained from Airy's stress function for an increasing horizon distance (compare the figure below): Figure 5.2 displays the deviation of both horizontal- and vertical displacement for four different horizon radii $\delta = 0.5/1/1.5/2$. The deviation diminishes for the horizon approaching 0, but increases with increasing horizon length. This behavior does not change with increasing mesh density, although a higher mesh density yields a better approximation to the results of classical continuum mechanics. It has to be noted that the parameter h in figure 5.2 was not defined; therefore, it has to be assumed that h denotes the average element length. Comparing the used h's with the choices for δ reveals that the horizon lengths were smaller or in the same range as the element lengths in most cases. The
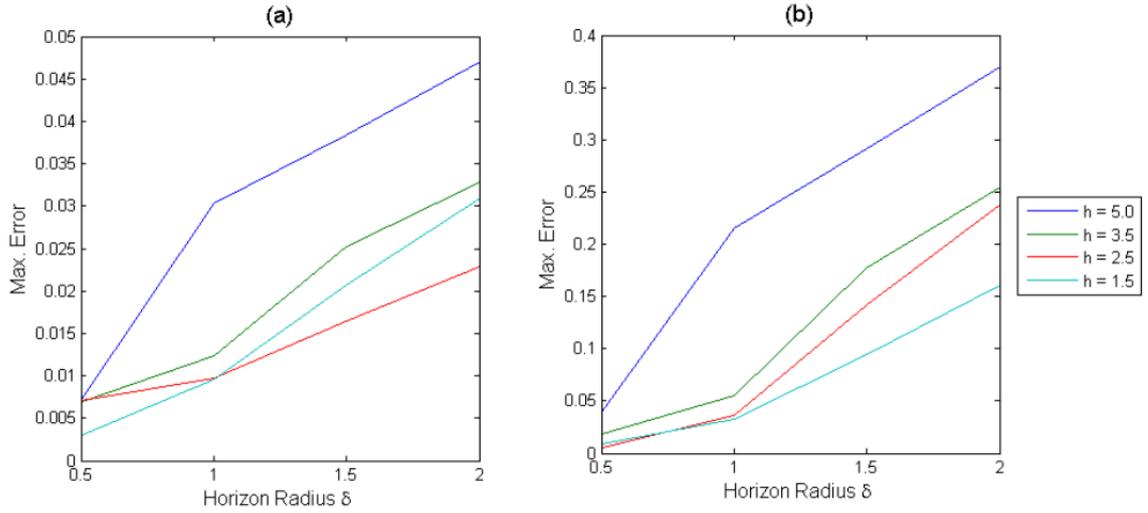
Figure 5.2: Maximum differences between the peridynamic and the classical solutions for (a) horizontal and (b) vertical displacements [Glaws 2014, p.28]

highest accuracy was obtained for horizons within the respective element length, although this does not exclude intersection with neighboring elements, as the mesh in fig. 5.2 was a non-uniform mesh built of triangles. Unfortunately, figure 5.2 does neither tell if the peridynamic displacement is larger or smaller than the CCM solution, nor was the point (X_1, X_2) of the maximum displacement specified. Although the average element length h was given in fig. 5.2, it is not possible to deduce the number of dofs of the respective meshes. Moreover, no information about the number of quadrature points was available. Therefore, the following simulations are just an attempt to reproduce a similar test environment.

The quadrilateral peridynamic elements from chapter 3 were applied to the same test setup in four different mesh densities. All meshes had the following number of quadrature points:

1. $N_{parent} = 2$

2. $N_{cut} = 2^3$

3. $N_{uncut} = 2^3$

4. $N_{middle} = 2^3$

N_{middle} denotes the number of quadrature points of each subelement of the middle element in each direction (compare subsection 3.1.4). The inner integral over the middle elements was solved with Duffy-transformation in this example. Each computation was done with Newton's method and the analytical Jacobian matrix; the threshold ϵ to terminate the computation was set to $1e^{-7}$. According to [Glaws 2014], the maximum deviation between finite element- and analytical solution was determined. To achieve this, the analytical solution was evaluated on the same meshgrid as the peridynamic computation.
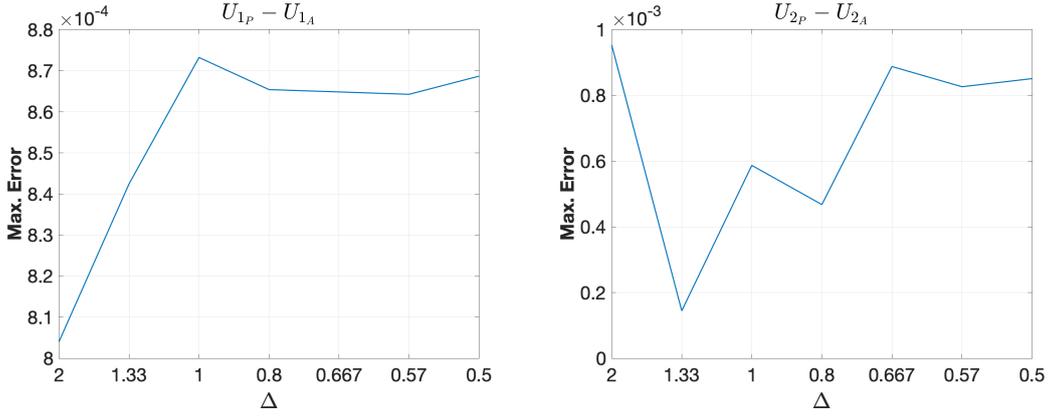
Figure 5.3: Maximum deviation between results from analytical computation and quadrilateral peridynamic elements ($\nu = 0.25$)

Figure 5.3 displays the results obtained from quadrilateral peridynamic finite elements. The error of a discretization is obtained by:

$$
\begin{aligned}
\epsilon_1 &= \max \left| u_{1_{P_i}} - u_{1_{A_i}} \right| \qquad i = 1 \dots N \\
\epsilon_2 &= \max \left| u_{2_{P_i}} - u_{2_{A_i}} \right| \qquad i = 1 \dots N
\end{aligned}
\tag{5.2}
$$

Because the horizon length δ is fixed to three times the element length Δ, an independent change of δ and Δ is not possible, thus making a direct comparison between figures 5.2 and 5.3 impossible, because the maximum ratio $\frac{\delta}{h}$ is restricted to $\frac{2}{1.5} \approx 1.33$ in figure 5.2.

A comparison of the errors for a similar element length is done for $h = 1.5$ (cyan graph in fig. 5.2) and $\Delta = 1.33$. In order to achieve maximum similarity, the horizon length $\delta = 2$ in fig. 5.2 is chosen. This leads to the following error ratios:

$$
\begin{aligned}
\frac{u_{1_{Tri}}}{u_{1_{Quad}}} &\approx \frac{3.1e^{-2}}{8.43e^{-4}} \approx 36.7 \\
\frac{u_{2_{Tri}}}{u_{2_{Quad}}} &\approx \frac{1.6e^{-1}}{1.44e^{-4}} \approx 1111.1
\end{aligned}
\tag{5.3}
$$

Thus results from figures 5.2 and 5.3 are separated by a large deviation for comparable parameters. The reason for this large deviation is unknown; a possible explanation would be a missing of the surface correction in [Glaws 2014]. This would explain the increasing deviation in the results with increasing horizon length, but remains speculation.

The results obtained with quadrilateral peridynamic elements are of same magnitude as the analytical results. The setup of 2×17 elements in figure 5.3 provides the largest deviation; the meshgrid with the given density of the quadrature points is too coarse to capture the displacement field correctly despite surface correction. Moreover, it has to be noted that finer discretizations do not meet the analytical solution from Airy's function exactly either [Bower 2008]. The following table 5.1 displays the maximum deviation between analytical and finite element solution, referred to the analytical solution: In the figure below depicted

Discretization	Δ	δ	Deviation [%]
2×17	2	6	-9.61
3×26	1.33	3.99	1.48
4×35	1	3	6.03
5×44	0.8	2.4	4.81
6×52	0.667	2.1	9.66
7×61	0.57	1.71	8.91
8×70	0.5	1.5	9.12

Table 5.1: Maximum deviation Peridynamics - analytical solution $\nu = \frac{1}{4}$

are the displacements in Y_2 - direction for different discretizations. All but one discretization yield displacements which are larger than the analytical solution, indicating that the finite element solution is "softer" than the analytical one. Remembering that the finite element approximation of the true displacement field is just an approximation with piecewise-linear approach functions, a larger FEM-solution is unusual, as the strain energy in the approximated displacement field should be overestimated due to the limited modeshapes of the finite element meshgrid. As soon as a poisson ratio $\nu = \frac{1}{3}$ is used, the peridynamic solution behaves stiffer than the analytical one, compare figure 5.6.
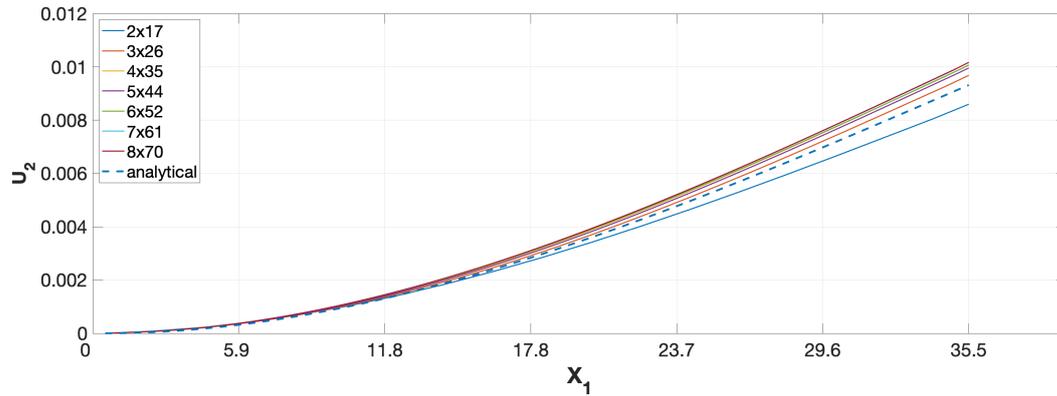
Figure 5.4: Comparison peridynamic and analytical vertical deflection ($\nu = 0.25$)

The series of peridynamic displacements converges to a limit (comp. u_2 in figures 5.2 and 5.4), but the dependence of this limit on discretization, quadrature point distribution, load- and boundary condition application and overall size of the deformation has to be investigated in detail.

5.1.2 Convergence analysis

At first, the experiment from the last subsection is repeated with a poisson ration $\nu = \frac{1}{3}$, assuming now a plane stress problem. The results for different meshgrids are given below. Please note that the analytical plate-in-membrane-action solution has been recomputed with the updated poisson ratio too:
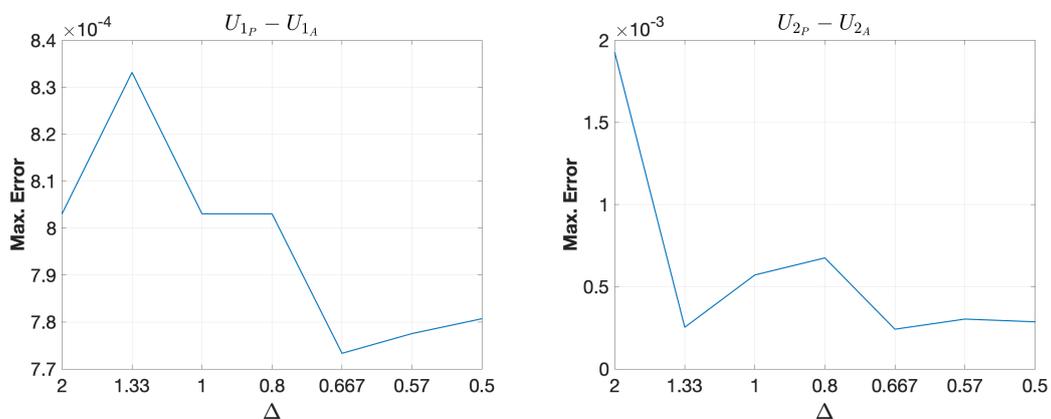
Figure 5.5: Maximum deviation between analytical computation and quadrilateral peridynamic elements ($\nu = 0.33$)
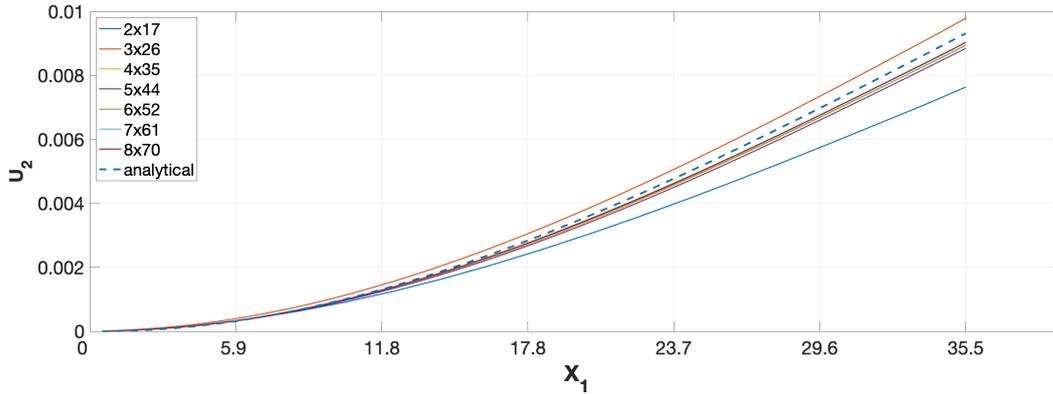
Figure 5.6: Comparison peridynamic and analytical vertical deflection ($\nu = 0.33$)

The maximum deviation between analytical and peridynamic results has reduced to:

Discretization	Δ	δ	Deviation [%]
2×17	2	6	-19.65
3×26	1.33	3.99	-2.61
4×35	1	3	-5.74
5×44	0.8	2.4	-6.83
6×52	0.667	2.1	-2.52
7×61	0.57	1.71	-3.18
8×70	0.5	1.5	-2.99

Table 5.2: Maximum deviation Peridynamics - analytical solution $\nu = \frac{1}{3}$

Comparing the results of figures 5.3 with 5.5, respectively tables 5.1 with 5.2 demonstrates that the $\nu = \frac{1}{3}$ results in the peridynamic elements behave stiffer than the analytical solution. As the analytical solution was computed with the new poisson ratio as well, it can be stated that the plane stress assumption results in a different element behavior. The reason for the strong deviation of the 3×26 could not be figured out by the end of this thesis. Please note that the diameters of the peridynamic families ($2\,\delta$) in tables 5.1 and 5.2 result in a truncation of most of the peridynamic families, because the height $h = 4$ is of the same magnitude of the horizon, emphasizing the importance of the surface correction for peridynamic elements with horizon extending over adjacent the element boundaries.

5.2 Simulation 1: Peridynamic beam

In this section, the influence of the discretization of the inner integral on the convergence behavior is examined on the example of a cantilever beam with single load on one end, together with a large deformation example. The behavior of the peridynamic elements under a line load is examined by both cantilever- and a beam with both ends clamped. Throughout all 2-D computations in the following, two parent gauss points per direction and middle element were used.

5.2.1 Cantilever beam – inner integral discretizations

The termination threshold of the solver is set to $1 \cdot 10^{-7}$, $E = 3 \cdot 10^6$. Investigated are three different ratios $\frac{h}{l}$ in order to check for differences in the behavior of a long, slender beam and a more squat structure. The height is hereby kept constant $h = 2$, the length adjusted accordingly. Furthermore, two different mesh densities are used in order to investigate the result of different inner-integral discretizations on a refinement of the mesh. The results are compared to an analytical solution with Airy's function again. The magnitude of the load is chosen such that small displacements can be assumed. An investigation of larger displacements is done in subsection 5.2.3. It furthermore holds $\delta = 3\Delta$. The deviation is compared by the difference of the maximal displacements (occuring for this system at the loaded end of the beam), and on the other hand by the relative difference of the the norms of the displacement fields. The discussion of the results follows on page 99.

$$\frac{\mathbf{h}}{\mathbf{l}} = \frac{1}{15}$$

Spatial discretization A is done with 3×45 elements, $\Delta = 0.667$, discretization B with 6×90 elements, $\Delta = 0.333$. The discretization of the inner integral is denoted by $N_{middle} \times N_{uncut} \times N_{cut}$, in which N_{ii} denotes the number of quadrature points in each direction.

(3×45) $N_{middle} \times N_{uncut} \times N_{cut}$	$\frac{u^1(l) - u^1_{\mathrm{Airy}}(l)}{u^1_{\mathrm{Airy}}(l)}$ [%]	$\frac{\left|u^1(\mathbf{X})\right| - \left|u^1_{\mathrm{Airy}}(\mathbf{X})\right|}{\left|u^1_{\mathrm{Airy}}(\mathbf{X})\right|}$ [%]
$4 \times 4 \times 4$	6.9	12.7
$8 \times 8 \times 8$	-9.12	-6.99
$16 \times 16 \times 16$	-16.7	-16.1
$32 \times 32 \times 32$	-15.3	-14.4

Table 5.3: Maximum- and avergage deviation u^1 for $\frac{h}{l} = \frac{1}{15}$, $\Delta = 0.67$ in [%]

(6×90) $N_{middle} \times N_{uncut} \times N_{cut}$	$\frac{u^1(l) - u^1_{\mathrm{Airy}}(l)}{u^1_{\mathrm{Airy}}(l)}$ [%]	$\frac{\left|u^1(\mathbf{X})\right| - \left|u^1_{\mathrm{Airy}}(\mathbf{X})\right|}{\left|u^1_{\mathrm{Airy}}(\mathbf{X})\right|}$ [%]
$4 \times 4 \times 4$	-9.11	-7.63
$8 \times 8 \times 8$	-15.4	-15.4
$16 \times 16 \times 16$	-11.5	-10.7
$32 \times 32 \times 32$	-14.1	-13.9

Table 5.4: Maximum- and avergage deviation u^1 for $\frac{h}{l} = \frac{1}{15}$, $\Delta = 0.33$ in [%]

(3×45) $N_{middle} \times N_{uncut} \times N_{cut}$	$\frac{u^2(l) - u^2_{\mathrm{Airy}}(l)}{u^2_{\mathrm{Airy}}(l)}$ [%]	$\frac{\left|u^2(\mathbf{X})\right| - \left|u^2_{\mathrm{Airy}}(\mathbf{X})\right|}{\left|u^2_{\mathrm{Airy}}(\mathbf{X})\right|}$ [%]
$4 \times 4 \times 4$	14.1	16
$8 \times 8 \times 8$	-6.83	-6.55
$16 \times 16 \times 16$	-16.5	-16.9
$32 \times 32 \times 32$	-14.7	-15

Table 5.5: Maximum- and avergage deviation u^2 for $\frac{h}{l} = \frac{1}{15}$, $\Delta = 0.67$ in [%]

(6×90) $N_{middle} \times N_{uncut} \times N_{cut}$	$\frac{u^2(l) - u^2_{\mathrm{Airy}}(l)}{u^2_{\mathrm{Airy}}(l)}$ [%]	$\frac{\left|u^2(\mathbf{X})\right| - \left|u^2_{\mathrm{Airy}}(\mathbf{X})\right|}{\left|u^2_{\mathrm{Airy}}(\mathbf{X})\right|}$ [%]
$4 \times 4 \times 4$	-7.76	-7.82
$8 \times 8 \times 8$	-16	-16.8
$16 \times 16 \times 16$	-11.1	-11.6
$32 \times 32 \times 32$	-14.4	-15.1

Table 5.6: Maximum- and avergage deviation u^2 for $\frac{h}{l} = \frac{1}{15}$, $\Delta = 0.33$ in [%]
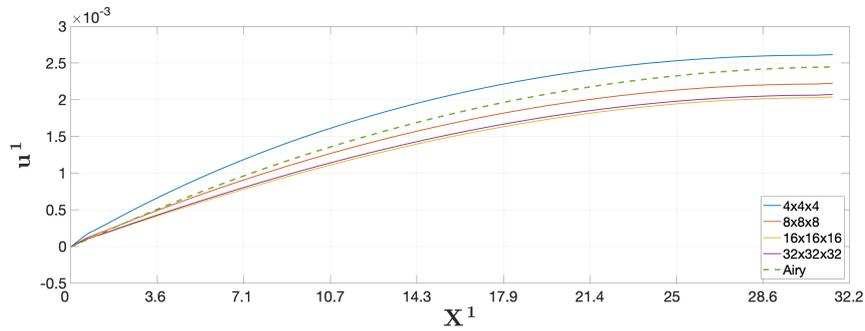
Figure 5.7: Comparison peridynamic and analytical horizontal deflection for $\frac{h}{l} = \frac{1}{15}$, $\Delta = 0.667$, $Y^2 = \frac{h}{2}$
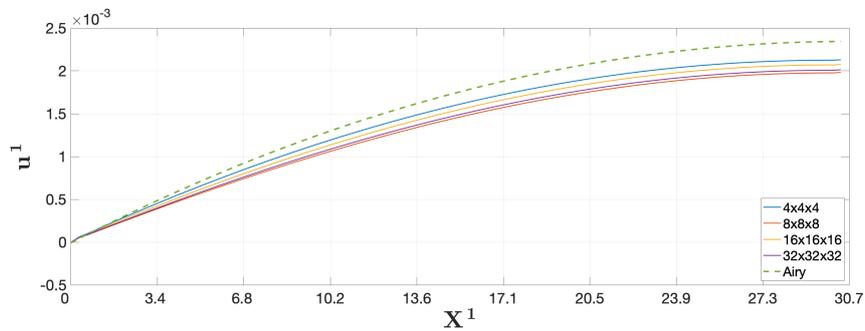

Figure 5.8: Comparison peridynamic and analytical horizontal deflection for $\frac{h}{l} = \frac{1}{15}$, $\Delta = 0.333$, $Y^2 = \frac{h}{2}$
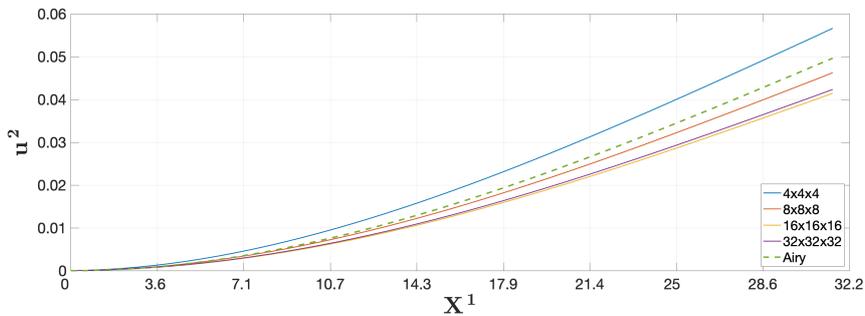

Figure 5.9: Comparison peridynamic and analytical vertical deflection for $\frac{h}{l} = \frac{1}{15}$, $\Delta = 0.667$, $Y^2 = \frac{h}{2}$
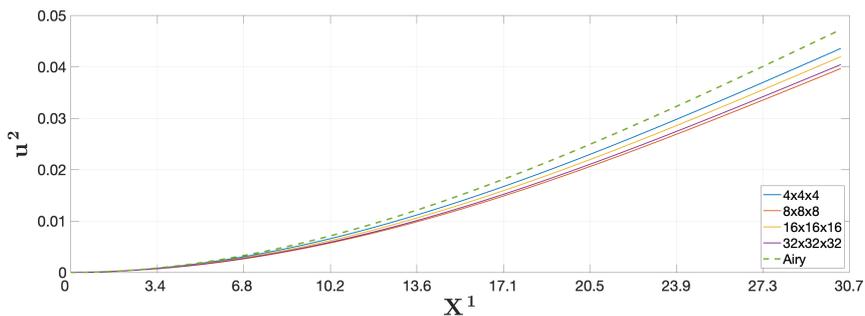
Figure 5.10: Comparison peridynamic and analytical vertical deflection for $\frac{h}{l} = \frac{1}{15}$, $\Delta = 0.333$, $Y^2 = \frac{h}{2}$

$$\frac{\mathbf{h}}{\mathbf{l}} = \frac{1}{10}$$

Spatial discretization A is done with 3×30 elements and $\Delta = 0.667$, discretization B with 6×60 elements and $\Delta = 0.333$.

(3×30) $N_{middle} \times N_{uncut} \times N_{cut}$	$\dfrac{u^1(l) - u^1_{\text{Airy}}(l)}{u^1_{\text{Airy}}(l)}$ [%]	$\dfrac{\left|u^1(\mathbf{X})\right| - \left|u^1_{\text{Airy}}(\mathbf{X})\right|}{\left|u^1_{\text{Airy}}(\mathbf{X})\right|}$ [%]
$4 \times 4 \times 4$	-0.74	1.89
$8 \times 8 \times 8$	-7.32	-6.07
$16 \times 16 \times 16$	-10.9	-10.3
$32 \times 32 \times 32$	-10.2	-9.47

Table 5.7: Maximum- and avergage deviation u^1 for $\frac{h}{l} = \frac{1}{10}$, $\Delta = 0.67$ in [%]

(6×60) $N_{middle} \times N_{uncut} \times N_{cut}$	$\dfrac{u^1(l) - u^1_{\text{Airy}}(l)}{u^1_{\text{Airy}}(l)}$ [%]	$\dfrac{\left|u^1(\mathbf{X})\right| - \left|u^1_{\text{Airy}}(\mathbf{X})\right|}{\left|u^1_{\text{Airy}}(\mathbf{X})\right|}$ [%]
$4 \times 4 \times 4$	-5.97	-5.23
$8 \times 8 \times 8$	-8.2	-8.07
$16 \times 16 \times 16$	-6.1	-5.68
$32 \times 32 \times 32$	-7.47	-7.24

Table 5.8: Maximum- and avergage deviation u^1 for $\frac{h}{l} = \frac{1}{10}$, $\Delta = 0.33$ in [%]

(3×30) $N_{middle} \times N_{uncut} \times N_{cut}$	$\dfrac{u^2(l) - u^2_{\text{Airy}}(l)}{u^2_{\text{Airy}}(l)}$ [%]	$\dfrac{\left|u^2(\mathbf{X})\right| - \left|u^2_{\text{Airy}}(\mathbf{X})\right|}{\left|u^2_{\text{Airy}}(\mathbf{X})\right|}$ [%]
$4 \times 4 \times 4$	2.87	4.16
$8 \times 8 \times 8$	-5.69	-5.15
$16 \times 16 \times 16$	-10.2	-9.99
$32 \times 32 \times 32$	-9.31	-9.06

Table 5.9: Maximum- and avergage deviation u^2 for $\frac{h}{l} = \frac{1}{10}$, $\Delta = 0.67$ in [%]

(6×60) $N_{middle} \times N_{uncut} \times N_{cut}$	$\dfrac{u^2(l) - u^2_{\text{Airy}}(l)}{u^2_{\text{Airy}}(l)}$ [%]	$\dfrac{\left|u^2(\mathbf{X})\right| - \left|u^2_{\text{Airy}}(\mathbf{X})\right|}{\left|u^2_{\text{Airy}}(\mathbf{X})\right|}$ [%]
$4 \times 4 \times 4$	-5.23	-5
$8 \times 8 \times 8$	-8.32	-8.43
$16 \times 16 \times 16$	-5.82	-5.78
$32 \times 32 \times 32$	-7.46	-7.52

Table 5.10: Maximum- and avergage deviation u^2 for $\frac{h}{l} = \frac{1}{10}$, $\Delta = 0.33$ in [%]
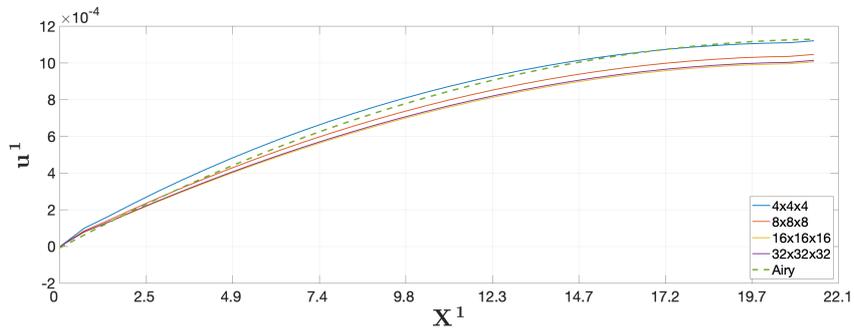
Figure 5.11: Comparison peridynamic and analytical horizontal deflection for $\frac{h}{l} = \frac{1}{10}$, $\Delta = 0.667$, $Y^2 = \frac{h}{2}$
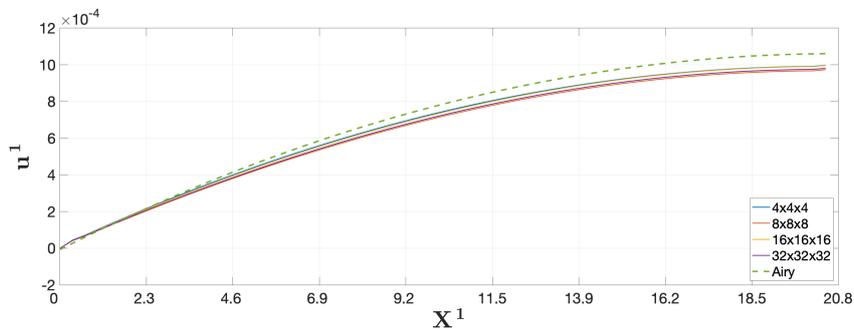

Figure 5.12: Comparison peridynamic and analytical horizontal deflection for $\frac{h}{l} = \frac{1}{10}$, $\Delta = 0.333$, $Y^2 = \frac{h}{2}$
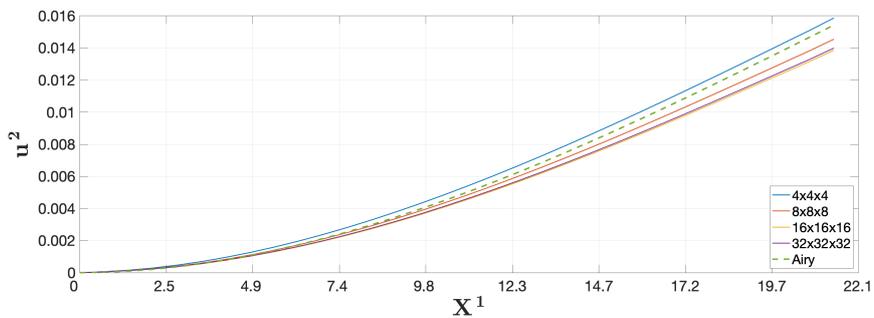

Figure 5.13: Comparison peridynamic and analytical vertical deflection for $\frac{h}{l} = \frac{1}{10}$, $\Delta = 0.667$, $Y^2 = \frac{h}{2}$
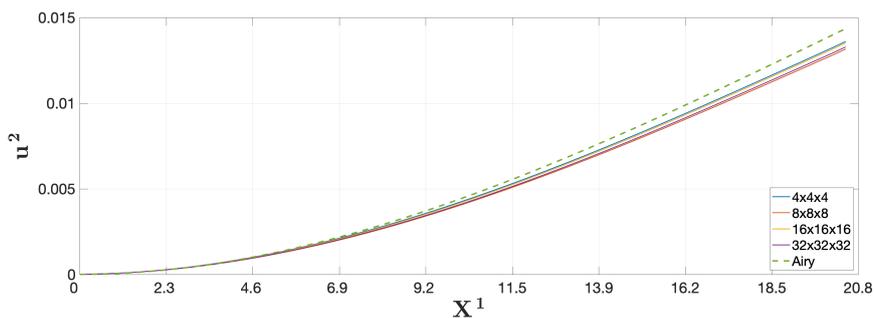
Figure 5.14: Comparison peridynamic and analytical vertical deflection for $\frac{h}{l} = \frac{1}{10}$, $\Delta = 0.333$, $Y^2 = \frac{h}{2}$

$$\frac{\mathbf{h}}{\mathbf{l}} = \frac{\mathbf{1}}{\mathbf{5}}$$

Spatial discretization A is done with 3×15 elements and $\Delta = 0.667$, discretization B with 6×30 elements and $\Delta = 0.333$.

(3×15) $N_{middle} \times N_{uncut} \times N_{cut}$	$\dfrac{u^1(l) - u^1_{\text{Airy}}(l)}{u^1_{\text{Airy}}(l)}$ [%]	$\dfrac{\left|u^1(\mathbf{X})\right| - \left|u^1_{\text{Airy}}(\mathbf{X})\right|}{\left|u^1_{\text{Airy}}(\mathbf{X})\right|}$ [%]
$4 \times 4 \times 4$	-5.02	-4.1
$8 \times 8 \times 8$	-5.85	-5.3
$16 \times 16 \times 16$	-6.68	-6.36
$32 \times 32 \times 32$	-6.52	-6.14

Table 5.11: Maximum- and avergage deviation u^1 for $\frac{h}{l} = \frac{1}{5}$, $\Delta = 0.67$ in [%]

(6×30) $N_{middle} \times N_{uncut} \times N_{cut}$	$\dfrac{u^1(l) - u^1_{\text{Airy}}(l)}{u^1_{\text{Airy}}(l)}$ [%]	$\dfrac{\left|u^1(\mathbf{X})\right| - \left|u^1_{\text{Airy}}(\mathbf{X})\right|}{\left|u^1_{\text{Airy}}(\mathbf{X})\right|}$ [%]
$4 \times 4 \times 4$	-2.78	-2.5
$8 \times 8 \times 8$	-2.28	-2.17
$16 \times 16 \times 16$	-1.44	-1.27
$32 \times 32 \times 32$	-1.93	-1.81

Table 5.12: Maximum- and avergage deviation u^1 for $\frac{h}{l} = \frac{1}{5}$, $\Delta = 0.33$ in [%]

(3×15) $N_{middle} \times N_{uncut} \times N_{cut}$	$\dfrac{u^2(l) - u^2_{\text{Airy}}(l)}{u^2_{\text{Airy}}(l)}$ [%]	$\dfrac{\left|u^2(\mathbf{X})\right| - \left|u^2_{\text{Airy}}(\mathbf{X})\right|}{\left|u^2_{\text{Airy}}(\mathbf{X})\right|}$ [%]
$4 \times 4 \times 4$	-2.85	-1.98
$8 \times 8 \times 8$	-4.29	-3.66
$16 \times 16 \times 16$	-5.45	-4.96
$32 \times 32 \times 32$	-5.22	-4.69

Table 5.13: Maximum- and avergage deviation u^2 for $\frac{h}{l} = \frac{1}{5}$, $\Delta = 0.67$ in [%]

(6×30) $N_{middle} \times N_{uncut} \times N_{cut}$	$\dfrac{u^2(l) - u^2_{\text{Airy}}(l)}{u^2_{\text{Airy}}(l)}$ [%]	$\dfrac{\left|u^2(\mathbf{X})\right| - \left|u^2_{\text{Airy}}(\mathbf{X})\right|}{\left|u^2_{\text{Airy}}(\mathbf{X})\right|}$ [%]
$4 \times 4 \times 4$	-2.39	-1.99
$8 \times 8 \times 8$	-2.19	-1.9
$16 \times 16 \times 16$	-1.26	-0.94
$32 \times 32 \times 32$	-1.83	-1.53

Table 5.14: Maximum- and avergage deviation u^2 for $\frac{h}{l} = \frac{1}{5}$, $\Delta = 0.33$ in [%]
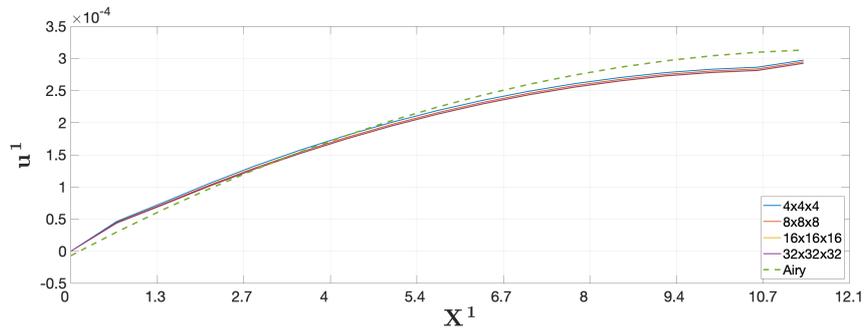
Figure 5.15: Comparison peridynamic and analytical horizontal deflection for $\frac{h}{l} = \frac{1}{5}$, $\Delta = 0.667$, $Y^2 = \frac{h}{2}$
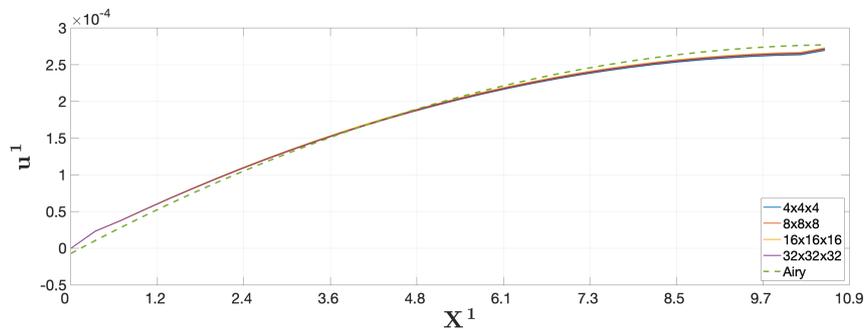

Figure 5.16: Comparison peridynamic and analytical horizontal deflection for $\frac{h}{l} = \frac{1}{5}$, $\Delta = 0.333$, $Y^2 = \frac{h}{2}$
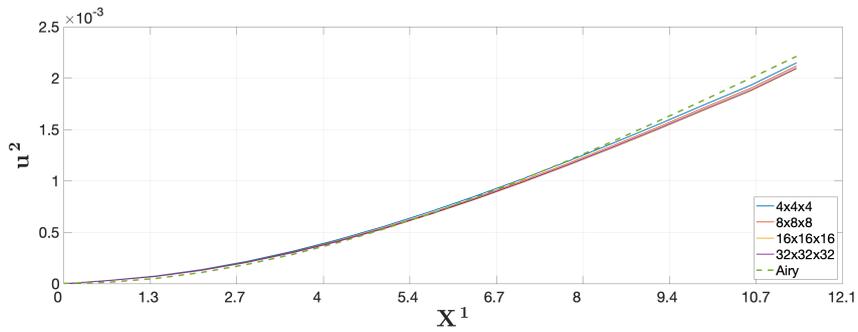

Figure 5.17: Comparison peridynamic and analytical vertical deflection for $\frac{h}{l} = \frac{1}{5}$, $\Delta = 0.667$, $Y^2 = \frac{h}{2}$
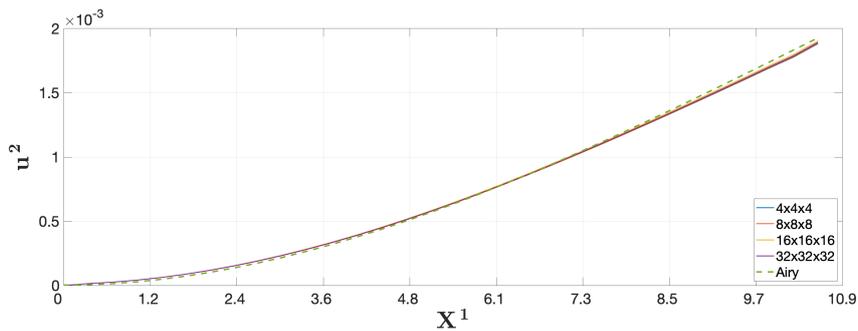
**Figure 5.18:** Comparison peridynamic and analytical vertical deflection for $\frac{h}{l} = \frac{1}{5}$, $\Delta = 0.333$, $Y^2 = \frac{h}{2}$

Discussion of the results

Comparing the range of deviations for the three investigated ratios $\frac{h}{l}$ at first, it reveals, that the deviation gets smaller with decreasing beam length. Although all examples have reached convergence, it is obvious that especially in case $\frac{h}{l} = \frac{1}{15}$, the limits of Peridynamics and Airy's function do not coincide. The peridynamic elements behave, with exception of a few weakly discretized examples, stiffer than the analytical solution, which is not in contradiction to finite element analysis in general. A "sparse" discretization with $4 \times 4 \times 4$ quadrature points resulted in a max. deviation of $+14.1\%$ of the vertical displacements for the coarse discretization, comp. table 5.5 and figure 5.9. Switching to a finer spatial discretization but keeping the inner integral's one reduces the error to -7.76%, approaching the Airy-solution now "from below". In this case, spatial refinement has a large effect. Regarding however the behavior of the solutions with an increasing number of quadrature points ($16 \times 16 \times 16$ or $32 \times 32 \times 32$), both spatial discretizations yield approximately the same results with an error of -14.7/-14.1% in the vertical direction. The horizontal displacements show similar behavior. Thus, for a long peridynamic beam, there is little benefit from increasing the spatial discretization as long as a sufficient number of quadrature points was used. A fine spatial refinement together with a coarse discretization of the inner integral produces a relatively good deviation of -7.76%, but this result is still far from the convergence limit. Furthermore, the peridynamic elements behave clearly stiffer than the analytical solution for a long and slender structure, which is dominated by bending deflections.

Also in case $\frac{h}{l} = \frac{1}{10}$, the peridynamic solutions converge, but are stiffer than the analytical ones. However, halving the element length reduces the error from -9.31% to -7.46% for the highest resolution of the inner integral, thus it has a larger influence on the results than in the previous example. Moreover, oscillatory behavior of the error can be observed too, compare table 5.10. On page 37, the oscillatory behavior of the cut elements' integration was stated despite a high number of subelements in the cut elements. Thus, keeping the number of cut element quadrature points constant, varying the number of uncut- and middle element quadrature points and observing the solutions behavior poses a test, if the oscillations in the deviation result from the cut elements:

(3×30) $N_{middle} \times N_{uncut} \times N_{cut}$	$\dfrac{u^1(l) - u^1_{\text{Airy}}(l)}{u^1_{\text{Airy}}(l)}$ [%]	$\dfrac{\left|u^1(\mathbf{X})\right| - \left|u^1_{\text{Airy}}(\mathbf{X})\right|}{\left|u^1_{\text{Airy}}(\mathbf{X})\right|}$ [%]
$4 \times 4 \times 32$	-4.87	-3.27
$8 \times 8 \times 32$	-10	-9.25
$16 \times 16 \times 32$	-10.2	-9.45
$32 \times 32 \times 32$	-10.2	-9.47

Table 5.15: Maximum- and avergage deviation u^1 for $\frac{h}{l} = \frac{1}{10}$, $\Delta = 0.67$ in [%], $N_{cut} = 5$

(3×30) $N_{middle} \times N_{uncut} \times N_{cut}$	$\dfrac{u^2(l) - u^2_{\text{Airy}}(l)}{u^2_{\text{Airy}}(l)}$ [%]	$\dfrac{\left|u^2(\mathbf{X})\right| - \left|u^2_{\text{Airy}}(\mathbf{X})\right|}{\left|u^2_{\text{Airy}}(\mathbf{X})\right|}$ [%]
$4 \times 4 \times 32$	-2.75	-2.03
$8 \times 8 \times 32$	-9.08	-8.82
$16 \times 16 \times 32$	-9.29	-9.04
$32 \times 32 \times 32$	-9.31	-9.06

Table 5.16: Maximum- and avergage deviation u^2 for $\frac{h}{l} = \frac{1}{10}$, $\Delta = 0.67$ in [%], $N_{cut} = 5$
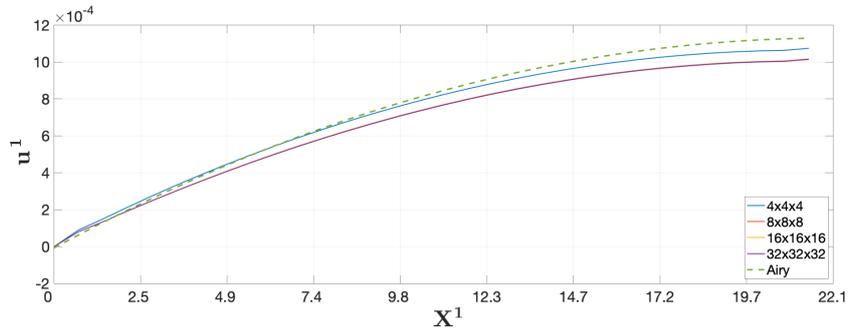
Figure 5.19: Comparison peridynamic and analytical horizontal deflection for $\frac{h}{l} = \frac{1}{10}$, $\Delta = 0.667$, $Y^2 = \frac{h}{2}$, $N_{cut} = 5$
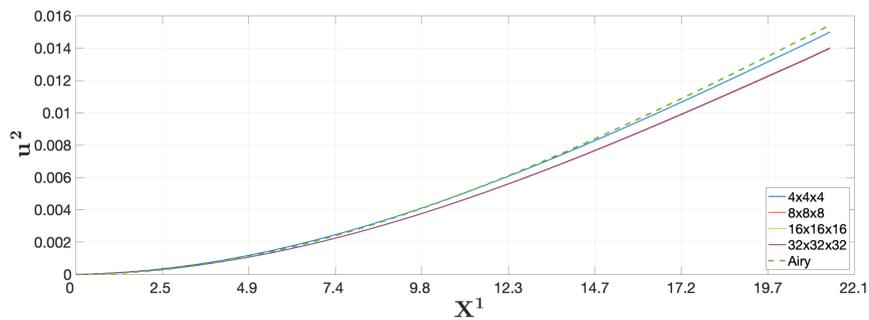
**Figure 5.20:** Comparison peridynamic and analytical vertical deflection for $\frac{h}{l} = \frac{1}{10}$, $\Delta = 0.667$, $Y^2 = \frac{h}{2}$, $N_{cut} = 5$

Comparing figures 5.19 + 5.20 and tables 5.15 + 5.16 with the previous ones display quite unambiguoulsy, that the oscillatory behavior results from the cut elements indeed. As depicted on page 39, this effect can be mitigated only by a very high number of subelements per cut elements.

In case of the squattest structure, doubling the spatial discretization leads to a significant improvement of the results towards the analytical solution, more than halving the distance to the reference results. This effect is especially visible for finer discretizations of the inner integral. Furthermore, all tested configurations achieve smaller displacements than the analytical result. The largest deviation (-5.45 %) was achieved on the coarse spatial meshgrid with 16 quadrature points in each direction. Even a fine discretization of the inner integral with 32 quadrature points on the coarse spatial mesh yields with -5.22 % nearly twice the deviation than the coarsest inner integral discretization on the finer spatial mesh with -2.39 %. At this point, it can be said that the peridynamic approximation is the better the shorter the beam becomes. Please note furthermore the additional inclination of the last peridynamic element in the horizontal displacement figures 5.15 and 5.16. This increased elongation can bee observed throughout the upmost and lowest load bearing elements (compare fig. 5.21),
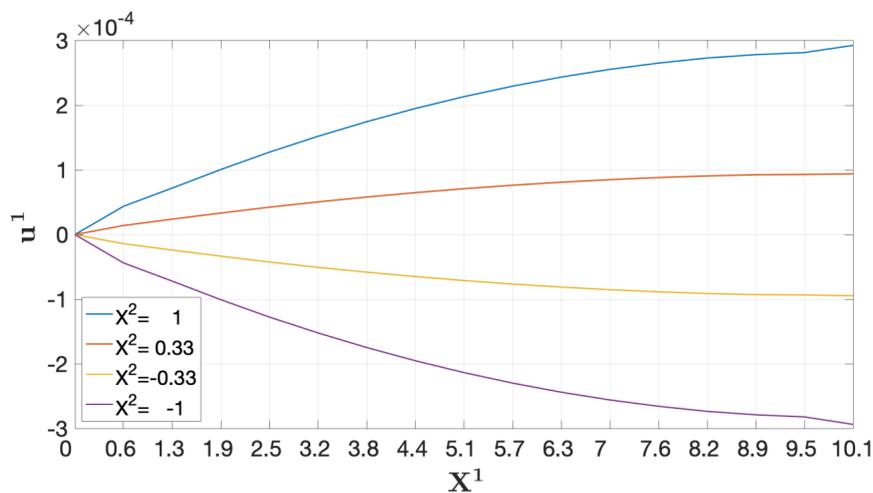
Figure 5.21: Horizontal deflection for $\frac{h}{l} = \frac{1}{5}$, $\Delta = 0.667$

and arises, because all nodes at $x = l$ were loaded equally, thus loading those two elements at the corners proportionally more. In comparison to the $\frac{h}{l} = \frac{1}{10}$ - computation, one can observe a better convergence of the peridynamic results to a common limit, although this limit is not the analytical one, see figures 5.16 and 5.18.

5.2.2 Cantilever beam – line load

The experiment above is repeated with a constant line load $q = \frac{20}{l}$ on top of the cantilever beam above for a ratio $\frac{h}{l} = \frac{1}{10}$. The results for a spatial discretization of 3×30 elements and inner integral discretizations ranging from $4 \times 4 \times 4$ to $32 \times 32 \times 32$ quadrature points are shown below in figures $5.22 + 5.23$ and tables $5.17 + 5.18$.

(3×30) $N_{middle} \times N_{uncut} \times N_{cut}$	$\dfrac{u^1(l) - u^1_{\mathrm{Airy}}(l)}{u^1_{\mathrm{Airy}}(l)}$ [%]	$\dfrac{\left\|u^1(\mathbf{X})\right\| - \left\|u^1_{\mathrm{Airy}}(\mathbf{X})\right\|}{\left\|u^1_{\mathrm{Airy}}(\mathbf{X})\right\|}$ [%]
$4 \times 4 \times 32$	87.9	93.2
$8 \times 8 \times 32$	82.1	86.5
$16 \times 16 \times 32$	78	81.8
$32 \times 32 \times 32$	78.9	82.8

Table 5.17: Maximum- and avergage deviation u^1 for $\frac{h}{l} = \frac{1}{10}$, $\Delta = 0.67$ in [%]

(3×30) $N_{middle} \times N_{uncut} \times N_{cut}$	$\dfrac{u^2(l) - u^2_{\mathrm{Airy}}(l)}{u^2_{\mathrm{Airy}}(l)}$ [%]	$\dfrac{\left\|u^2(\mathbf{X})\right\| - \left\|u^2_{\mathrm{Airy}}(\mathbf{X})\right\|}{\left\|u^2_{\mathrm{Airy}}(\mathbf{X})\right\|}$ [%]
$4 \times 4 \times 32$	94.7	96.7
$8 \times 8 \times 32$	87.5	89
$16 \times 16 \times 32$	82.6	83.8
$32 \times 32 \times 32$	83.7	84.9

Table 5.18: Maximum- and avergage deviation u^2 for $\frac{h}{l} = \frac{1}{10}$, $\Delta = 0.67$ in [%]
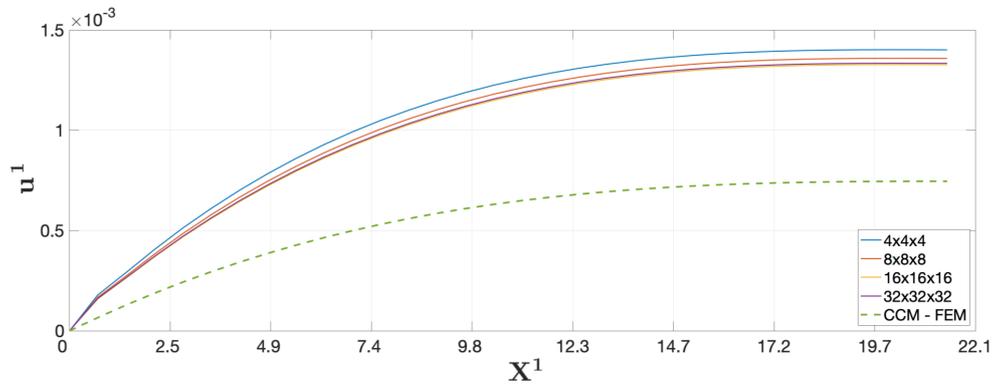

Figure 5.22: Comparison of peridynamic and analytical horizontal deflection for $\frac{h}{l} = \frac{1}{10}$, $\Delta = 0.667$, $Y^2 = \frac{h}{2}$
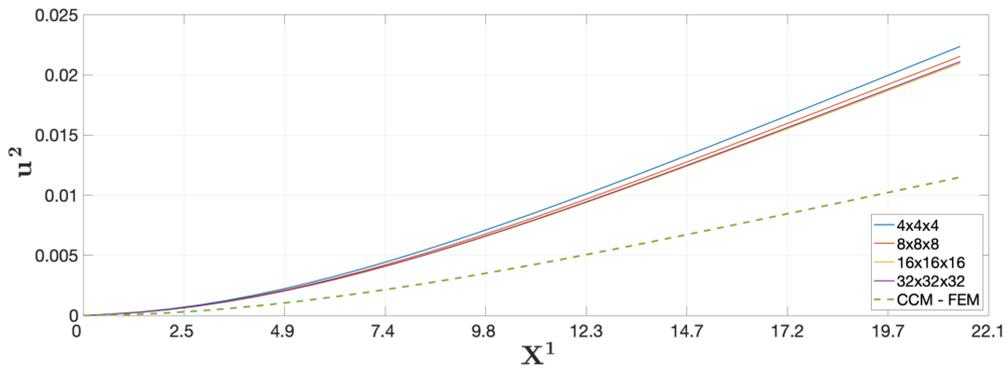
Figure 5.23: Comparison of peridynamic and analytical vertical deflection for $\frac{h}{l} = \frac{1}{10}$, $\Delta = 0.667$, $Y^2 = \frac{h}{2}$

The deviation in u^2 - direction between a finite element analysis based on classical elasticity for a plane stress problem and the peridynamic elements goes up to 94.7 % for the coarsest discretization of the inner integral. Even a refinement of the inner integral discretization, especially of the cut elements does not result in a significant improvement, regarding 83.7 % deviation even for the finest discretization. In figures 5.26 + 5.27 and tables 5.19 + 5.20, the experiment is repeated with doubling the number of elements in both directions:

(6×60) $N_{middle} \times N_{uncut} \times N_{cut}$	$\dfrac{u^1(l) - u^1_{\mathrm{Airy}}(l)}{u^1_{\mathrm{Airy}}(l)}$ [%]	$\dfrac{\left\|u^1(\mathbf{X})\right\| - \left\|u^1_{\mathrm{Airy}}(\mathbf{X})\right\|}{\left\|u^1_{\mathrm{Airy}}(\mathbf{X})\right\|}$ [%]
$4 \times 4 \times 32$	30	31.8
$8 \times 8 \times 32$	29.6	31.1
$16 \times 16 \times 32$	31.9	33.5
$32 \times 32 \times 32$	30.6	32.2

Table 5.19: Maximum- and avergage deviation u^1 for $\frac{h}{l} = \frac{1}{10}$, $\Delta = 0.33$ in [%]

(6×60) $N_{middle} \times N_{uncut} \times N_{cut}$	$\dfrac{u^2(l) - u^2_{\mathrm{Airy}}(l)}{u^2_{\mathrm{Airy}}(l)}$ [%]	$\dfrac{\left\|u^2(\mathbf{X})\right\| - \left\|u^2_{\mathrm{Airy}}(\mathbf{X})\right\|}{\left\|u^2_{\mathrm{Airy}}(\mathbf{X})\right\|}$ [%]
$4 \times 4 \times 32$	32	32.5
$8 \times 8 \times 32$	31.2	31.5
$16 \times 16 \times 32$	33.7	34.1
$32 \times 32 \times 32$	32.3	32.6

Table 5.20: Maximum- and avergage deviation u^2 for $\frac{h}{l} = \frac{1}{10}$, $\Delta = 0.33$ in [%]
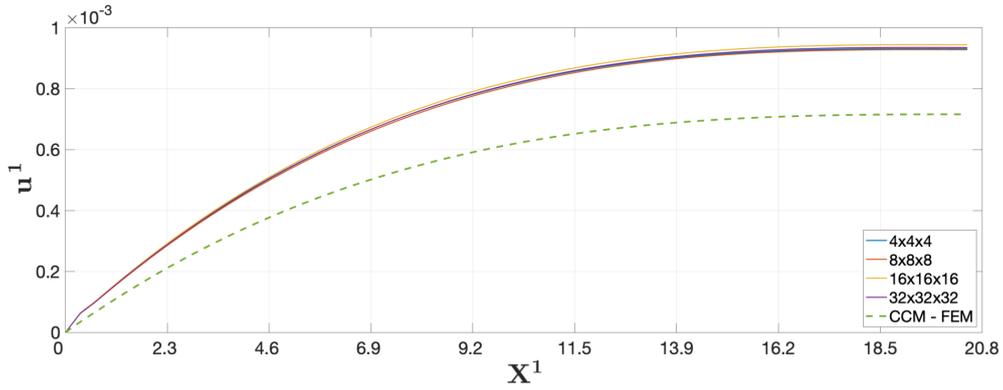
Figure 5.24: Comparison of peridynamic and analytical horizontal deflection for $\frac{h}{l} = \frac{1}{10}$, $\Delta = 0.333$, $Y^2 = \frac{h}{2}$
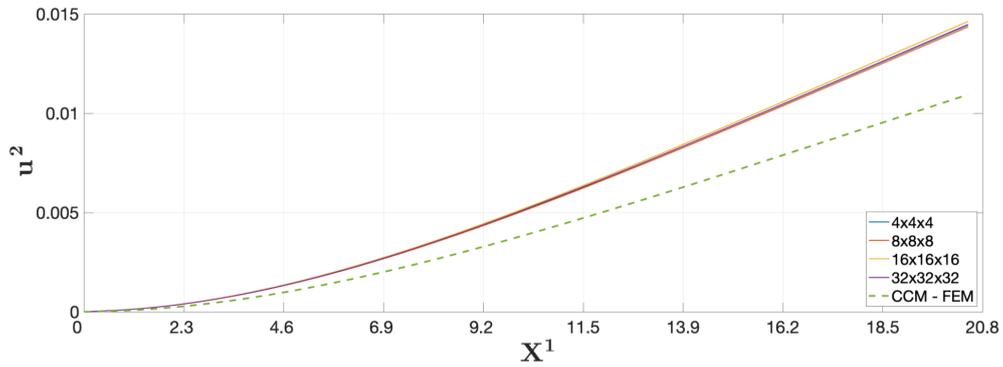

Figure 5.25: Comparison of peridynamic and analytical vertical deflection for $\frac{h}{l} = \frac{1}{10}$, $\Delta = 0.333$, $Y^2 = \frac{h}{2}$

Improving the spatial discretization resulted in a significant improvement of the results. Since even a coarse discretization of the inner integral by $4 \times 4 \times 4$ quadrature points resulted in a far better maximum difference (32 %) than the finest discretization in the previous example. Moreover, a finer integral discretization yields practically no further improvement on the results. Therefore, a better coincidence seems to be achievable only by a further spatial refinement. The simulation is repeated once more with twice as many elements in both directions:

(12×120) $N_{middle} \times N_{uncut} \times N_{cut}$	$\dfrac{u^1(l) - u^1_{\mathrm{Airy}}(l)}{u^1_{\mathrm{Airy}}(l)}$ [%]	$\dfrac{\left\lvert u^1(\mathbf{X})\right\rvert - \left\lvert u^1_{\mathrm{Airy}}(\mathbf{X})\right\rvert}{\left\lvert u^1_{\mathrm{Airy}}(\mathbf{X})\right\rvert}$ [%]
$4 \times 4 \times 32$	12.2	13.2

Table 5.21: Maximum- and avergage deviation u^1 for $\frac{h}{l} = \frac{1}{10}$, $\Delta = 0.17$ in [%]

(12×120) $N_{middle} \times N_{uncut} \times N_{cut}$	$\dfrac{u^2(l) - u^2_{\text{Airy}}(l)}{u^2_{\text{Airy}}(l)}$ [%]	$\dfrac{\left|u^2(\mathbf{X})\right| - \left|u^2_{\text{Airy}}(\mathbf{X})\right|}{\left|u^2_{\text{Airy}}(\mathbf{X})\right|}$ [%]
$4 \times 4 \times 32$	13.3	13.6

Table 5.22: Maximum- and avergage deviation u^2 for $\frac{h}{l} = \frac{1}{10}$, $\Delta = 0.17$ in [%]
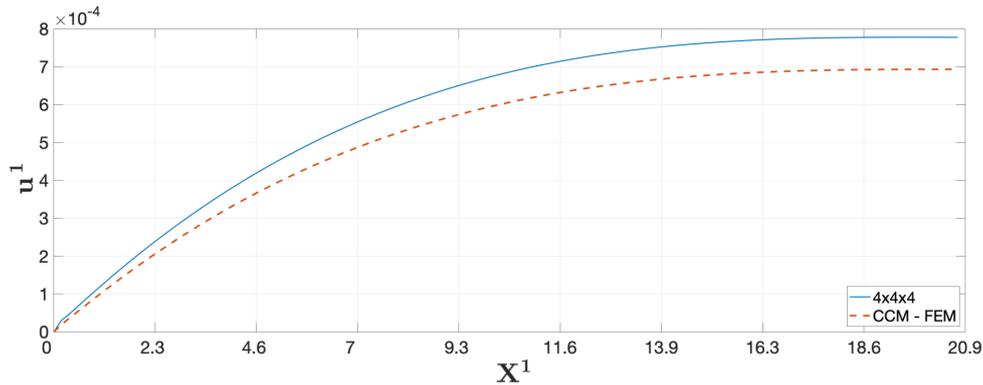
Figure 5.26: Comparison of peridynamic and analytical horizontal deflection for $\frac{h}{l} = \frac{1}{10}$, $\Delta = 0.167$, $Y^2 = \frac{h}{2}$
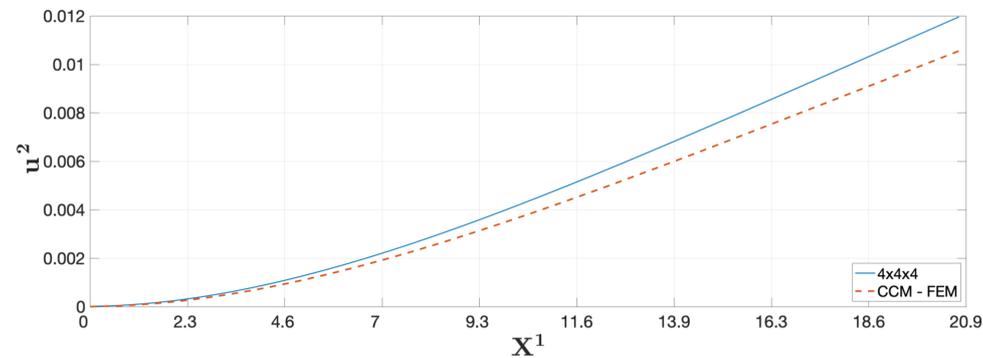
Figure 5.27: Comparison of peridynamic and analytical vertical deflection for $\frac{h}{l} = \frac{1}{10}$, $\Delta = 0.167$, $Y^2 = \frac{h}{2}$

Even with a fine discretization of 120×12 elements, a maximum deviation of 13.3 % in u^2 - direction remains. As evident from prior computations, a refinement of the inner integral discretization has little influence on the results.

The observed deviation for coarse meshgrids results from a too large peridynamic horizon δ in comparison to local changes of the displacement field. Thinking in terms of an Euler-Bernoulli beam theory, the change from a single- to a line load means an increase of the polynomial degree of the respective displacement fields by one, compare equation 5.4

and 5.5:

Cantilever beam under single load F:

$$u^2(X^1) \; = \; \frac{F}{6EI}\Big(3\,l\,(X^1)^2 \; - \; (X^1)^3\Big)$$

$$u^1(X^1,X^2) \; = \; \varphi(X^1)\cdot X^2 \; = \; \frac{F}{6EI}\Big(6\,l\,(X^1) \; - \; 3\,(X^1)^2\Big)\cdot X^2$$

(5.4)

Cantilever beam under line load q:

$$u^2(X^1) \; = \; \frac{q}{24EI}\Big(6\,l^2\,(X^1)^2 \; - \; 4\,l\,(X^1)^3 \; + \; (X^1)^4\Big)$$

$$u^1(X^1,X^2) \; = \; \frac{q}{24EI}\Big(12\,l^2\,(X^1) \; - \; 12\,l\,(X^1)^2 \; + \; 4\,(X^1)^3\Big)\cdot X^2$$

(5.5)

The transverse deflection u^2 for the line load-system is here of order 4. Although Bernoulli theory's assumption of the cross sections remaining even and perpendicular to the neutral axis is not valid for a plate in membrane action any more, it's kinematics from equations 5.5 serves a demonstrator of the effect of the element length in case of peridynamic elements and a line load for a beam with acceptable ratio $\frac{h}{l} = \frac{1}{10}$. Now, the peridynamic force densities (compare equation 3.5) are integrated for the displacement fields of a line-loaded Euler-Bernoulli beam 5.5. To keep the derivation as simple as possible, the X^2 - coordinate of the origin of the peridynamic families is kept constant to meet the upper edge of the beam $X^2 = \frac{h}{2}$. The X^1 - coordinates of the families are equally distributed along the upper edge; the distance in between is $\frac{l}{20}$, compare figure 5.28.
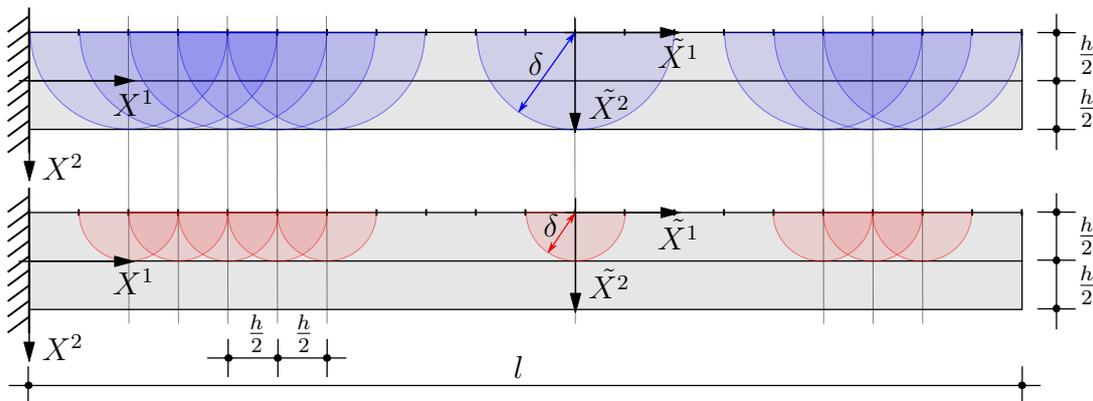
Figure 5.28: Cantilever beam setup

The resulting peridynamic forces r^1, r^2 (the resultants of the respective families) are now

computed in a first step for a fixed horizon length $\delta = h$, integrating equation 3.5 (repetition):

$$\mathbf{r}\left(\mathbf{X},\mathbf{Y}\right) = \iint\limits_{\Omega^0 \cap D_{\mathbf{X}}} c\, \frac{1}{|\mathbf{Y} - \mathbf{X}|}\left(|\mathbf{Y} + \mathbf{u}_{\mathbf{Y}} - \mathbf{X} - \mathbf{u}_{\mathbf{X}}| - |\mathbf{Y} - \mathbf{X}|\right)\cdot$$
$$\cdot\frac{\mathbf{Y} + \mathbf{u}_{\mathbf{Y}} - \mathbf{X} - \mathbf{u}_{\mathbf{X}}}{|\mathbf{Y} + \mathbf{u}_{\mathbf{Y}} - \mathbf{X} - \mathbf{u}_{\mathbf{X}}|}\, dA_{\mathbf{Y}} \tag{5.6}$$

and using a change of variables

$$\tilde{X}^1 = X^1 - n \cdot \frac{h}{2} \quad \Leftrightarrow \quad X^1 = \tilde{X}^1 + n \cdot \frac{h}{2}$$
$$\tilde{X}^2 = X^2 - \frac{h}{2} \quad \Leftrightarrow \quad X^2 = \tilde{X}^2 + \frac{h}{2} \tag{5.7}$$

on the displacement field of the Euler-Bernoulli beam, see eq. 5.5. Due to the change of variables to the $\tilde{X}^1, \tilde{X}^2$ coordinate system, $\mathbf{X}$ in eq. 5.6 can be set to 0, simplifying the resulting forces integral 5.6 to:

$$\mathbf{r}\left(\tilde{\mathbf{X}},\tilde{\mathbf{Y}}\right) = \iint\limits_{\Omega^0 \cap D_{\tilde{\mathbf{X}}}} c\, \frac{1}{|\tilde{\mathbf{Y}}|}\left(\left|\tilde{\mathbf{Y}} + \mathbf{u}_{\tilde{\mathbf{Y}}} - \mathbf{u}_{\tilde{\mathbf{X}}}\right| - \left|\tilde{\mathbf{Y}}\right|\right)\frac{\tilde{\mathbf{Y}} + \mathbf{u}_{\tilde{\mathbf{Y}}} - \mathbf{u}_{\tilde{\mathbf{X}}}}{\left|\tilde{\mathbf{Y}} + \mathbf{u}_{\tilde{\mathbf{Y}}} - \mathbf{u}_{\tilde{\mathbf{X}}}\right|}\, dA_{\tilde{\mathbf{Y}}} \tag{5.8}$$

Inserting the material parameter

$$c = \frac{6\,E}{\pi\,\delta^3\,(1-\nu)}$$

from section 2.3 and setting the horizon length δ to be the height h of the Euler-Bernoulli beam, the resulting force $\mathbf{r}$ gets the following shape:

$$\mathbf{r}\left(\tilde{\mathbf{X}},\tilde{\mathbf{Y}}\right) = \iint\limits_{\Omega^0 \cap D_{\tilde{\mathbf{X}}}} \frac{6\,E}{\pi\,(1-\nu)\,h^3}\, \frac{1}{|\tilde{\mathbf{Y}}|}\left(\left|\tilde{\mathbf{Y}} + \mathbf{u}_{\tilde{\mathbf{Y}}} - \mathbf{u}_{\tilde{\mathbf{X}}}\right| - \left|\tilde{\mathbf{Y}}\right|\right)\frac{\tilde{\mathbf{Y}} + \mathbf{u}_{\tilde{\mathbf{Y}}} - \mathbf{u}_{\tilde{\mathbf{X}}}}{\left|\tilde{\mathbf{Y}} + \mathbf{u}_{\tilde{\mathbf{Y}}} - \mathbf{u}_{\tilde{\mathbf{X}}}\right|}\, dA_{\tilde{\mathbf{Y}}} \tag{5.9}$$

The resulting integral is transformed to polar coordinates and afterwards solved numerically. In m successive steps, the horizon length h is halved, yielding $\frac{h}{2}, \frac{h}{4}, \frac{h}{8}$, and equation 5.9 is reevaluated for the same origins. The result are the resulting forces in the same locations along the beams upper edge, but now with halved horizon length.

The problem would be horizon- (and therefore element-length) independent, if the ratio

of the resulting forces 5.9 in the same point $\mathbf{X}$,

$$\frac{r^i(h \cdot 2^{-j})}{r^i(h \cdot 2^{-(j+1)})} = \frac{4}{1} \cdot \frac{(h \cdot 2^{-(j+1)})^3}{(h \cdot 2^{-(j)})^3} = 4 \cdot \frac{1}{8} = \frac{1}{2} \tag{5.10}$$

would hold. This case represents the same homogenous displacement field which has calibrated the peridynamic model, compare subsection 2.3 and 2.3. In case of a nonlinear displacement field however, the radius of the influence region can become too large to capture the local behavior of the system correctly, causing considerable deviations in the resulting inner forces.
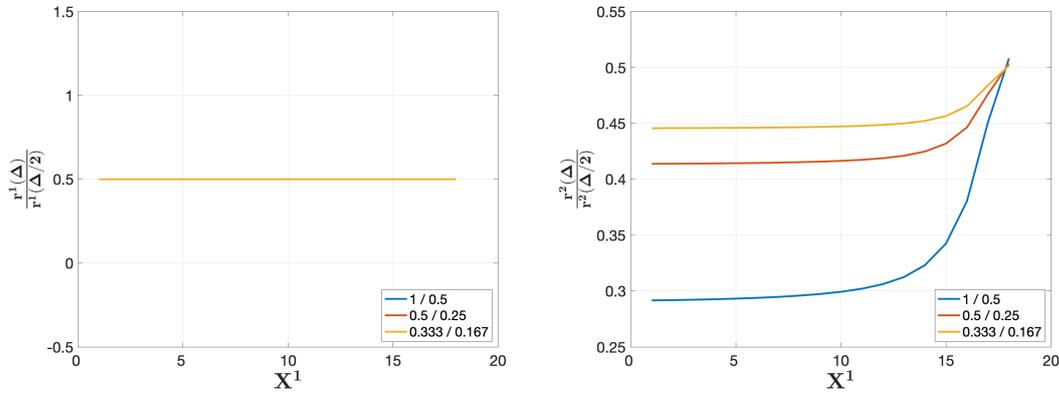
Figure 5.29: Cantilever beam under line load, ratios of r^1 and r^2 for halving the horizon lengths

Depicted in figure 5.29 are those ratios, evaluated along the upper edge of the cantilever beam for three different horizon lengths and their respective half. From the right plot, it is clearly visible that the analytical ratio from eq. 5.10 is achieved best by the yellow line, which has a starting horizon length of $\delta = 0.333$, which corresponds to an element length of $\frac{h}{6}$. Even for this subelementation, the desired ratio of $\frac{1}{2}$ is achieved only at the right end of the cantilever beam, because there, the change of the vertical displacement u^2 is lowest, corresponding to the slope $\frac{d u^2(X^1)}{dX^1}$. Recalling the meaning of $\mathbf{r}$ as the internal force in $\mathbf{X}$, the lower quotient of the blue and orange line in figure 5.29 means that the internal forces obtained on the coarser discretizations are lower than they are supposed to be, explaining the too large displacements in figures 5.22 and 5.23. The ratio of the horizontal forces however is close to the analytical results, indicating that the local changes of the horizontal displacements throughout a peridynamic influence region are small enough to fit the calibration of the model.

The explanations up to now were based on the behavior of the Bernoulli beam theory, which does not incorporate shear deformations. For a rectangular cross-sectioned cantilever

beam, this approach is valid, because even for a squat cantilever beam with a ratio $\frac{h}{l} = \frac{1}{5}$, the shear deflection makes up only 3.49 % of the total deflection according to a Timoshenko beam theory, [Becker 2011, p.62], with longer beams having an even lower shear-deflection contribution. Therefore, the behavior of an example with a higher influence of shear deflections is examined by a beam with both ends clamped.

The ratio $\frac{h}{l}$ is again fixed to $\frac{1}{10}$ with $h = 2$ in this example, the line load is set again to $q = \frac{20}{l}$. For this particular ratio, the contribution of shear deflections to the total deflection in terms of a Timoshenko beam theory is with 13.86 % higher than the 0.89 % of a cantilever beam with the same ratio. Although the peridynamic finite elements are not based on the kinematics of the Timoshenko beam theory, the latter allows an estimate of the contribution of shear deflections on the overall displacement. The problem setup is the same as in 5.2.1.

	$\dfrac{u^1(l) - u^1_{\text{Airy}}(l)}{u^1_{\text{Airy}}(l)}$ [%]	$\dfrac{u^2(l) - u^2_{\text{Airy}}(l)}{u^2_{\text{Airy}}(l)}$ [%]
30×3	-13.9	122
60×6	17.1	46
120×12	17.6	15.8

Table 5.23: Maximum deviation u^1 and u^2 for beam with clamped ends and line load
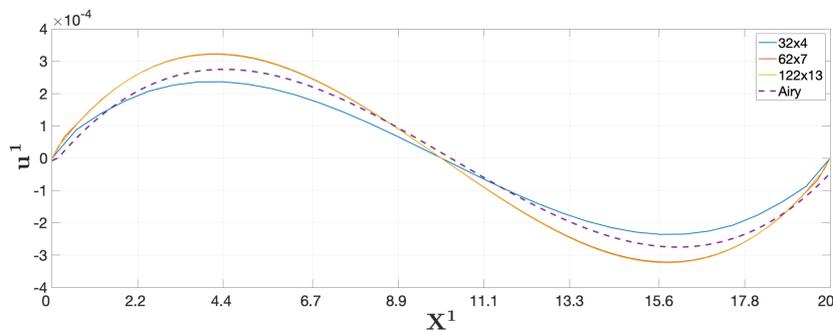
Figure 5.30: Comparison peridynamic and analytical horizontal deflection for $\frac{h}{l} = \frac{1}{10}$
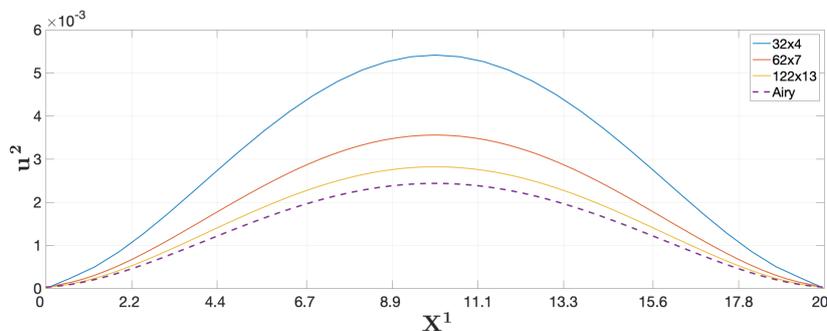
Figure 5.31: Comparison peridynamic and analytical vertical deflection for $\frac{h}{l} = \frac{1}{10}$

Table 5.23 and figures 5.30 and 5.31 display the results for an inner integral discretization of $4 \times 4 \times 4$, compared to an analytical solution obtained from [Zhan and Liu 2015, p.810]. The system's behavior under line load is similar to the cantilever beam under line load, but with even higher deviations for the respective spatial discretizations, compare tables 5.23 and tables 5.18, 5.20 and 5.22. A possible explanation could be the even more complicated deformation of the continuum due to shear deflections and cross sectional warping, which necessitates an even shorter horizon length to be resolved correctly.

5.2.3 Cantilever beam – large displacement example – outlook

The peridynamic force state and Jacobian matrix are tested on an example sustaining large displacements, driving the model to it's limits. A cantilever beam with ratio $\frac{h}{l} = \frac{1}{10}$ and material parameters from the examples above was subjected to a single load $F = 10.667$ on the right end. The load was distributed equally to the element nodes on the right edge of the system. The discretization was done with 30×3 elements and $4 \times 4 \times 4$ quadrature points for the inner integral. The solution was obtained using a Jacobian matrix derived numerically with complex step derivative.
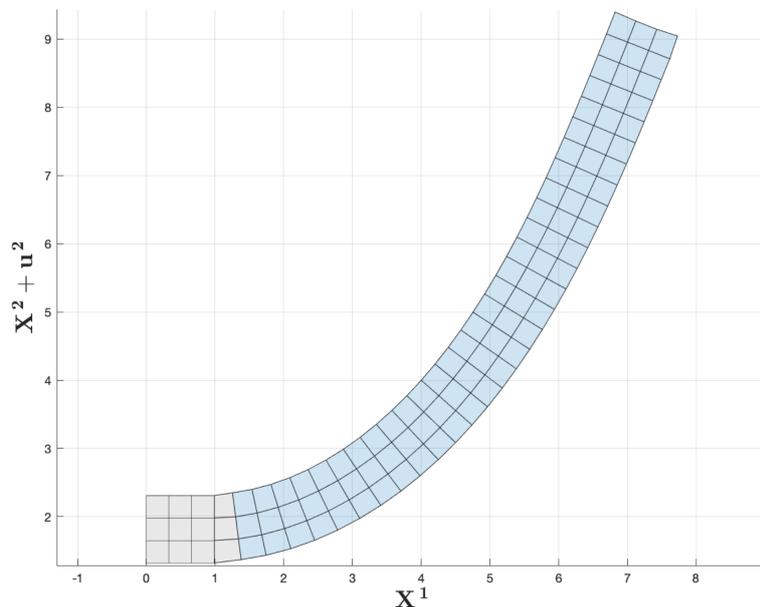
Figure 5.32: Large deformation example

As depicted in figure 5.32, the chosen load caused displacements of the same magnitude as the beam length. Thinking in terms of CCM beam theory, a portion of F will be carried by bending deflections, whereas another part of F is carried by a tensile deformation of the bar. As the tensile stiffness is several magnitudes higher than the bending stiffness, a significant

reduction in the displacements w.r.t. a theory based on small deformations can be expected.

	$u^2 \left(X^2 = l \right)$	$\frac{\left| u^2 \left(X^2 = l \right) \right| - \left| u_{nl}^2 \left(X^2 = l \right) \right|}{\left| u_{nl}^2 \left(X^2 = l \right) \right|}$ [%]
Peri	7.39	4.1
CCM - nonlinear (nl)	7.10	0
CCM - linear	15.23	114.51

Table 5.24: Comparison end displacement for large deformations

Table 5.24 displays the right-end displacements in the middle axis of the cantilever beam computed with both Peridynamics and classical elasticity, once for small- and once for large deformations. CCM computations were done by aid of the commercial finite element code ANSYS©, using the 2-D, large-deflection capable elastic beam element BEAM3©. A comparison of the ANSYS-results for nonlinear- and linear computation reveals the significant reduction of the displacements as soon as finite strains are considered. The Peridynamic computation deviates 4.1 % from the nonlinear CCM-results.

Although the displacement field is comparable to a CCM - solution in both shape and displacement magnitude, the validity of the example and the application to large-displacement computation must be seen critically at this stage. Especially since no measures were taken to keep those bonds from leaving the physical domain of the material body, which are located close to the surface and which extend over several elements. Furthermore, Newton's method with the analytical Jacobian matrix did not converge any more for loads causing displacements as large as depicted in figure 5.32, whereas the numerical Jacobian matrix derived with complex step derivative obtained stable solutions for displacements up to three times as large as in figure 5.32. The cause for the non-convergence of the analytical Jacobian matrix was not known by the end of this thesis.

5.3 Simulation 2: Coupled systems

In a next step, the results of the Arlequin-coupling are examined. A cantilever beam and a simple peridynamic rod serve as a demonstrator. Tested are the effect of both L^2- and H^1-coupling for different compositions of peridynamic- and CCM-domains for varying spatial- and inner integral discretizations.

5.3.1 Coupled cantilever beam

The investigated system consists of two domains, compare figure 5.33.
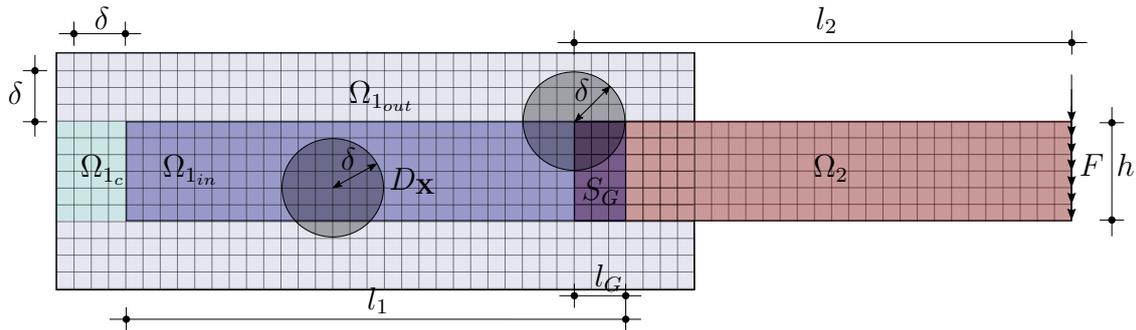
Figure 5.33: Coupled cantilever beam – domains

The inner peridynamic domain $\Omega_{1_{in}}$, is surrounded by the $\Omega_{1_{out}}$. Except for the peridynamic constraint region Ω_{1_c}, the material constant in $\Omega_{1_{out}}$ is set to 0. The constraint region has the same material constant as the inner peridynamic domain, but all nodal displacements in Ω_{1_c} are set to 0, thus modeling the clamped end. The length l_G of the gluing region S_G can be chosen arbitrarily and is not restricted à priori to the horizon length δ. The CCM-domain Ω_2 does interact exclusively with $\Omega_{1_{in}}$ via the gluing region; no interaction between Ω_2 and $\Omega_{1_{out}}$ occurs. The CCM-domain is modeled with 4 node quadrilateral plane stress elements, compare A.7. The single load F is distributed evenly along the nodes on the right hand side of Ω_2.

$$\dfrac{\mathbf{h}}{\mathbf{l_1}} = \dfrac{\mathbf{1}}{\mathbf{10}}, \dfrac{\mathbf{h}}{\mathbf{l_2}} = \dfrac{\mathbf{1}}{\mathbf{10}}, \mathbf{l_G} = \mathbf{1}\,\boldsymbol{\Delta}$$

(3×59) $N_{middle} \times N_{uncut} \times N_{cut}$	$\dfrac{u^1(l_{tot}) - u^1_{\mathrm{Airy}}(l_{tot})}{u^1_{\mathrm{Airy}}(l_{tot})}$ [%]	$\dfrac{\left|u^1(\mathbf{X})\right| - \left|u^1_{\mathrm{Airy}}(\mathbf{X})\right|}{\left|u^1_{\mathrm{Airy}}(\mathbf{X})\right|}$ [%]
$4 \times 4 \times 32$	12.3	18.4
$8 \times 8 \times 32$	2.33	5.64
$16 \times 16 \times 32$	-2.63	-0.58
$32 \times 32 \times 32$	-1.77	0.5

Table 5.25: H^1, Maximum- and avergage deviation u^1 for $\frac{h}{l_1} = \frac{1}{10}$, $\frac{h}{l_2} = \frac{1}{10}$, $\Delta = 0.67$ in [%]

(3×59) $N_{middle} \times N_{uncut} \times N_{cut}$	$\dfrac{u^1(l_{tot}) - u^1_{\mathrm{Airy}}(l_{tot})}{u^1_{\mathrm{Airy}}(l_{tot})}$ [%]	$\dfrac{\left|u^1(\mathbf{X})\right| - \left|u^1_{\mathrm{Airy}}(\mathbf{X})\right|}{\left|u^1_{\mathrm{Airy}}(\mathbf{X})\right|}$ [%]
$4 \times 4 \times 32$	12.3	18.4
$8 \times 8 \times 32$	2.33	5.64
$16 \times 16 \times 32$	-2.63	-0.58
$32 \times 32 \times 32$	-1.77	0.5

Table 5.26: L^2, Maximum- and avergage deviation u^1 for $\frac{h}{l_1} = \frac{1}{10}$, $\frac{h}{l_2} = \frac{1}{10}$, $\Delta = 0.67$ in [%]

(3×59) $N_{middle} \times N_{uncut} \times N_{cut}$	$\dfrac{u^2(l_{tot}) - u^2_{\mathrm{Airy}}(l_{tot})}{u^2_{\mathrm{Airy}}(l_{tot})}$ [%]	$\dfrac{\left|u^2(\mathbf{X})\right| - \left|u^2_{\mathrm{Airy}}(\mathbf{X})\right|}{\left|u^2_{\mathrm{Airy}}(\mathbf{X})\right|}$ [%]
$4 \times 4 \times 32$	20	22.4
$8 \times 8 \times 32$	5.95	6.68
$16 \times 16 \times 32$	-0.89	-0.93
$32 \times 32 \times 32$	0.31	0.4

Table 5.27: H^1, Maximum- and avergage deviation u^2 for $\frac{h}{l_1} = \frac{1}{10}$, $\frac{h}{l_2} = \frac{1}{10}$, $\Delta = 0.67$ in [%]

(3×59) $N_{middle} \times N_{uncut} \times N_{cut}$	$\dfrac{u^2(l_{tot}) - u^2_{\mathrm{Airy}}(l_{tot})}{u^2_{\mathrm{Airy}}(l_{tot})}$ [%]	$\dfrac{\left|u^2(\mathbf{X})\right| - \left|u^2_{\mathrm{Airy}}(\mathbf{X})\right|}{\left|u^2_{\mathrm{Airy}}(\mathbf{X})\right|}$ [%]
$4 \times 4 \times 32$	20	22.4
$8 \times 8 \times 32$	5.95	6.68
$16 \times 16 \times 32$	-0.89	-0.93
$32 \times 32 \times 32$	0.31	0.4

Table 5.28: L^2, Maximum- and avergage deviation u^2 for $\frac{h}{l_1} = \frac{1}{10}$, $\frac{h}{l_2} = \frac{1}{10}$, $\Delta = 0.67$ in [%]
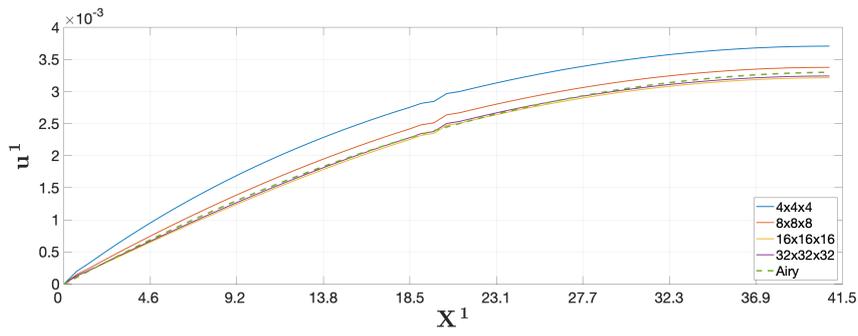
Figure 5.34: u^1, H^1 - coupling, $\Delta = 0.67$, $\frac{h}{l}_1 = \frac{1}{10}$, $\frac{h}{l}_2 = \frac{1}{10}$, $l_G = 1\Delta$
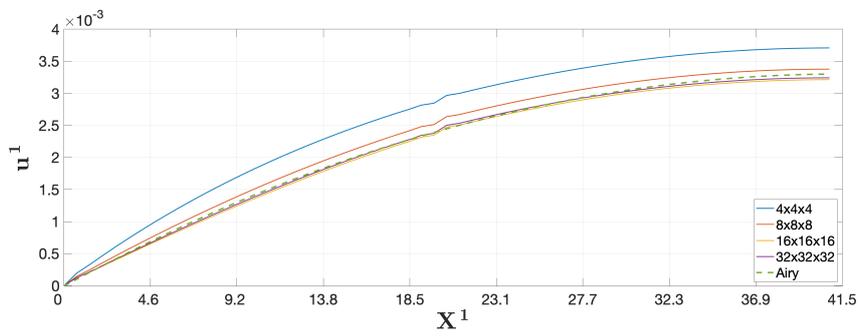
Figure 5.35: u^1, L^2 - coupling, $\Delta = 0.67$, $\frac{h}{l}_1 = \frac{1}{10}$, $\frac{h}{l}_2 = \frac{1}{10}$, $l_G = 1\Delta$
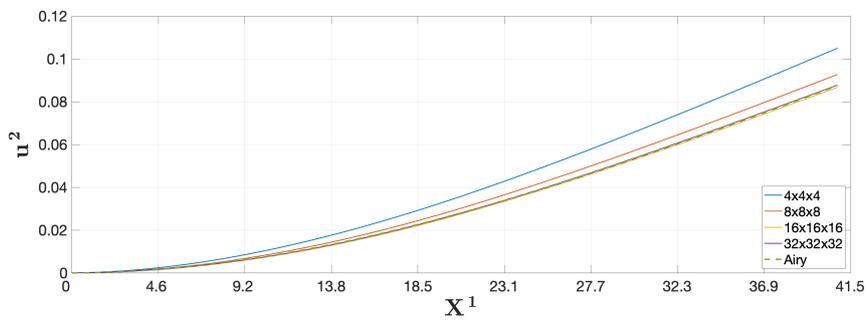

Figure 5.36: u^2, H^1 - coupling, $\Delta = 0.67$, $\frac{h}{l}_1 = \frac{1}{10}$, $\frac{h}{l}_2 = \frac{1}{10}$, $l_G = 1\Delta$
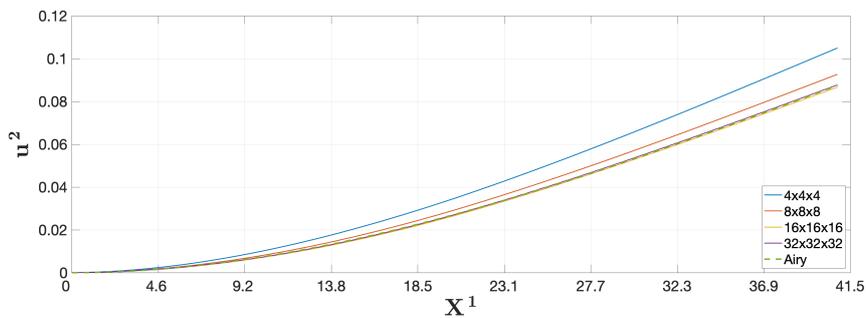

Figure 5.37: u^2, L^2 - coupling, $\Delta = 0.67$, $\frac{h}{l}_1 = \frac{1}{10}$, $\frac{h}{l}_2 = \frac{1}{10}$, $l_G = 1\Delta$

The results in tables 5.25, 5.27, 5.26 and 5.28 display very good coincidence with the analytical solution for denser inner integral discretizations, whereas too coarse discretizations behave less stiff than a solution obtained from Airy's function. For the coupling length $l_G = \Delta$, there was no observable difference between the results of L^2- and H^1- coupling. In the plots of the horizontal displacements (compare figures 5.36 and 5.37) the effect of the gluing region S_G can be observed, resulting in a local disturbance of the displacement field by the Lagrange multipliers.

In a next step, the coupling length l_G is varied. Depicted in 5.38 is the relative error at the right end of the cantilever beam for a setup with 3×30 elements for both peridynamic and CCM-domain. Increasing the coupling length results in an increased overlap between Ω_1 and Ω_2.
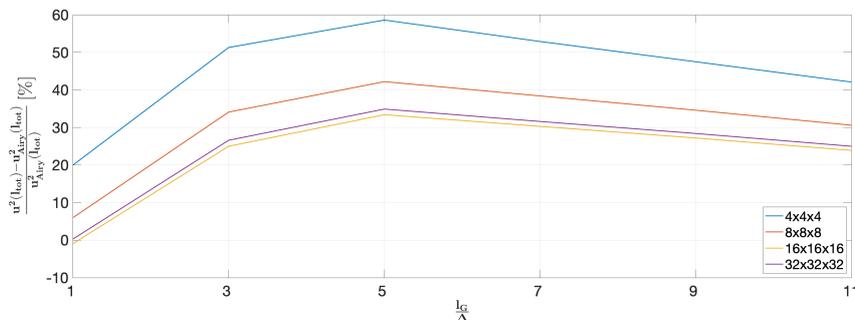
Figure 5.38: Relative error at $X^1 = l_{tot}$ for different coupling lengths, H^1 - coupling, 30×3 elements

The extended coupling length results in an increase of the relative error up to 58 %. Although the error is reduced with a further increase of l_G, it remains significant. Furthermore, the the discretization of the inner integral is resulting in a difference of up to 26 %. Repeating the experiment with half the element length yields an error of 17 % for a coupling length of $l_G = 1\,\Delta$. With increasing coupling length, the error increases similar to figure 5.38 with L^2-coupling not converging for a coupling length larger than $l_G = 5\,\Delta$. No loss of coercivity was observed on the Lagrange multiplier field however. This effect was observed by using both analytically- and numerically derived Jacobian matrix. A similar observation was made in [Guidault and Belytschko 2007, p.19] with results improving for shorter coupling lengths.

5.3.2 Coupled rods

This example covers the 1-D peridynamic elements from section 3.2. Investigated is a coupled, dynamic problem. The setup uses a fixed ratio of element length and horizon $\frac{\delta}{\Delta} = 3$. A rod of total length l is built up from a peridynamic subdomain l_1 and a CCM-subdomain

l_2.
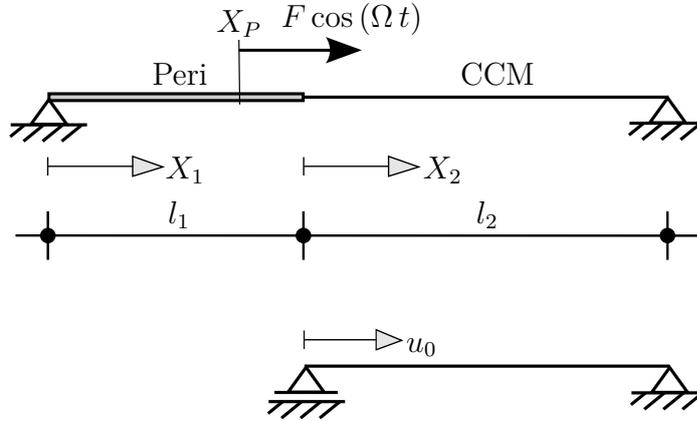
Figure 5.39: Coupled Peri- and CCM rods

The aim is to reproduce the steady state solution of the rod due to excitation with an oscillating single load. The peridynamic part of the system is modeled with 1-D peridynamic finite elements, whereas an analytical solution for the CCM-subsystem can be found:

$$u_2(X_2) = u_0 \cdot \left(\cos \left(\frac{\Omega X_2}{c_P} \right) - \sin \left(\frac{\Omega X_2}{c_P} \right) \frac{\cos \left(\frac{\Omega l_2}{c_P} \right)}{\sin \left(\frac{\Omega l_2}{c_P} \right)} \right) \qquad (5.11)$$

The respective virtual displacement field is denoted by:

$$\delta v_2(X_2) = 1 \cdot \left(\cos \left(\frac{\Omega_e X_2}{c_P} \right) - \sin \left(\frac{\Omega_e X_2}{c_P} \right) \frac{\cos \left(\frac{\Omega_e l_2}{c_P} \right)}{\sin \left(\frac{\Omega_e l_2}{c_P} \right)} \right) \qquad (5.12)$$

Equation 5.11 describes the displacement field of a rod with fixed right end under harmonically oscillating left end. Ω_e in this context denotes the excitation frequency, u_0 the amplitude of oscillation on the CCM-part's left end, and c_P denotes the phase-velocity in the CCM rod:

$$c_P = \sqrt{\frac{E}{\rho}} \qquad (5.13)$$

The ability to express the behavior of the analytical subsystem completely by it's start point displacement u_0 is advantageous, because both virtual work of internal and dynamic forces of the CCM-subsystem can be expressed w.r.t. one degree of freedom only. The virtual work

of the internal forces w.r.t. u_0 on a virtual displacement $\delta v(X_2)$ is denoted by:

$$\delta W_{2_{int}}(t) = \int_0^{l_2} EA\, u^{'}(X_2)\, \delta v^{'}(X_2) dX = EA u_0\, 1\, \Omega_e\, \frac{\left(c\, \sin\left(\frac{\Omega_e l_2}{c}\right)\, \cos\left(\frac{\Omega_e l_2}{c}\right)\, +\, \Omega_e\, l_2\right)}{2\, c^2\, \sin\left(\frac{\Omega_e l_2}{c}\right)^2} \tag{5.14}$$

The virtual work of the inertial forces in the CCM-domain is given by:

$$\delta W_{2_{kin}}(t) = \int_0^{l_2} A\rho\, \dot{u}(X_2)\, \delta\dot{v}(X_2) dX = A\,\rho\, u_0\, 1\, \Omega_e\, \frac{\left(c\, \sin\left(\frac{\Omega_e l_2}{c}\right)\, \cos\left(\frac{\Omega_e l_2}{c}\right)\, -\, \Omega_e\, l_2\right)}{2\, \sin\left(\frac{\Omega_e l_2}{c}\right)^2} \tag{5.15}$$

The virtual work of the inertial forces is now added to the Arlequin equations, compare 4.2:

$$\delta W_{1_{kin}}(t)\, +\, \delta W_{2_{kin}}(t)\, +\, \delta W_{1_{int}}(t)\, +\, W_{2_{int}}(t)\, +\, C(\lambda, +\delta v_1)\, +\, C(\lambda, -\delta v_2)\, =\, P\, \delta v_1(X_{1_P})$$
$$C\left(u_1, \delta\mu\right)\, +\, C\left(-u_2, \delta\mu\right)\, =\, 0 \tag{5.16}$$

The coupling operator $C(\lambda, -\delta v_2)$ is defined in the L^2- sense. The coupling length is chosen to be of Δ- length

$$C(\lambda, -\delta v_2) = \int_{X_2=0}^{X_2=\Delta} \left(\theta_0(X_2)\bar{\lambda}_0\, +\, \theta_1(X_2)\, \bar{\lambda}_1\right) \delta v_2(X_2)\, dX_2 \tag{5.17}$$

with δv_2 defined in eq. 5.12. The integral in eq. 5.17 is solved using gaussian quadrature. The following figures display the resulting, steady-state solutions in the peridynamic domain of the rod. Two different excitation frequencies and points of load introduction were chosen, together with the following simulation parameters:

1. $E = 2.1 \cdot 10^9 [\frac{N}{m^2}]$

2. $A = 0.01 [m^2]$

3. $P = 1 \cdot 10^5 [N]$

4. $l_1 = 1 [m]$, $l_2 = 1.5 [m]$

The excitation frequencies Ω_e are denoted in $[\frac{rad}{s}]$. The system is excited by a harmonically oscillating single load $P(t) = P \cos\left(\Omega_e\, t\right)$.

Example 1: Ω_e **= 1000,** $X_P = \frac{3\,l_1}{10}$

Displayed below are the displacement fields of the peridynamic domain for three different discretizations. A computation with linear CCM truss elements serves as validation.
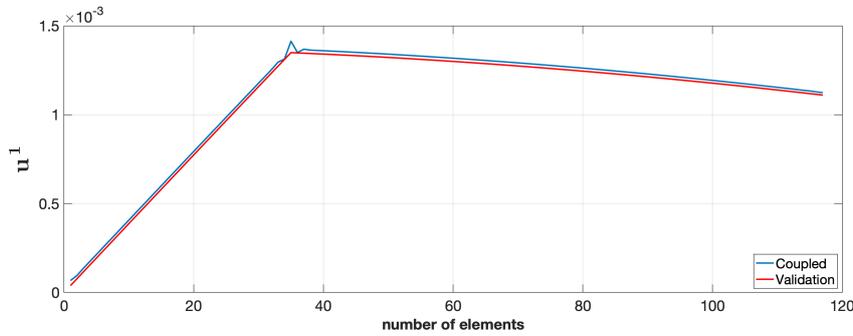

**Figure 5.40:** u_1, N = 120
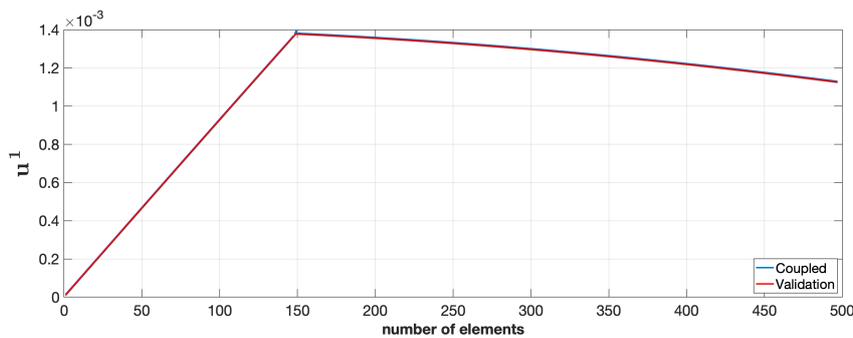
Figure 5.41: u_1, N = 500
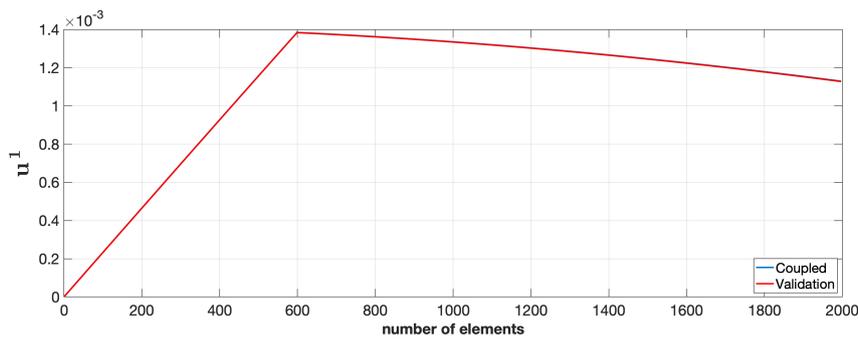
Figure 5.42: u_1, N = 2000

All three discretizations display good coincidence between coupled problem and reference solution. The sharp bend in the displacement fields results from the application of the single load. Due to the nonlocal interaction of elements with their family members in Peridynamics, the area of load introduction is disturbed in comparison to the reference solution, compare zigzag-pattern in figures 5.40 and 5.41.

Example 2: Ω_e **= 34000**
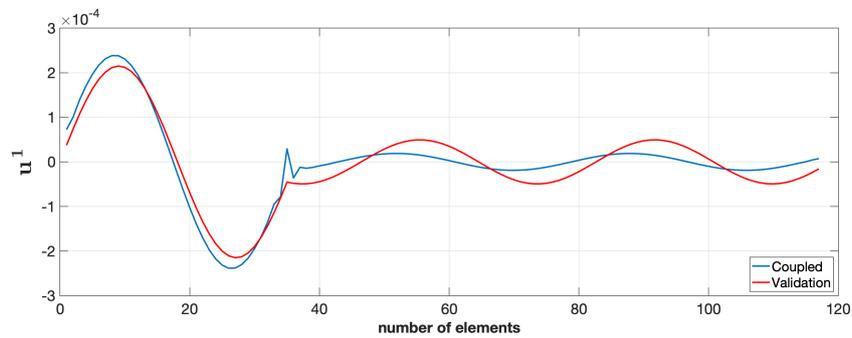
Figure 5.43: u_1, N = 120
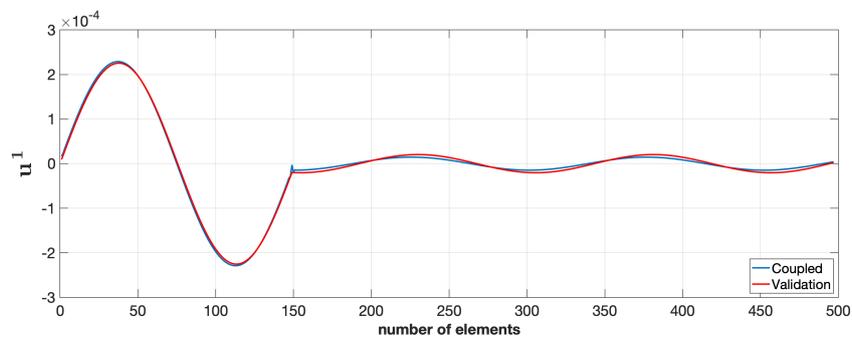
Figure 5.44: u_1, N = 500
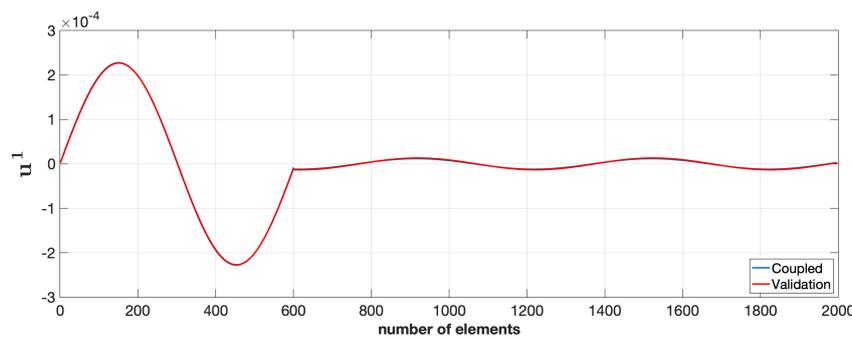
Figure 5.45: u_1, N = 2000

For a higher excitation frequency, the quality of the solution is more dependent of the element length. Although the meshgrid in figure 5.43 surpasses the claim of at least five elements per wavelength, the amplitude of the peridynamic solution especially for $X > X_P$ does not meet the reference solution.

For a sufficient number of elements however, the coupling with an analytical solution proves

to be an effective reduction technique. The best coincidence with the reference solution was obtained for coupling lengths as short as possible, thus $l_G = \Delta$.

5.4 Simulation 3: Quasi - static crack propagation in plate

The last simulation uses the incorporated failure mode of the peridynamic elements (see subsection 3.4.1) by comparing the crack path in peridynamic elements with the results obtained from an extended finite element method (XFEM) with hybrid explicit-implicit crack description, compare [Fries et al 2013, p.33, p.34]. Like mentioned in [Fries et al 2013, p.32], only the crack propagation is of interest, but no crack initiation models, energy release rates or stress intensity factors.

5.4.1 Square domain with initial crack

As template for the uncoupled problem serves the square domain with initial crack from the left side to the center of the plate from [Fries et al 2013, p.33].

(a) Dimensions and supports.   (b) Mesh.
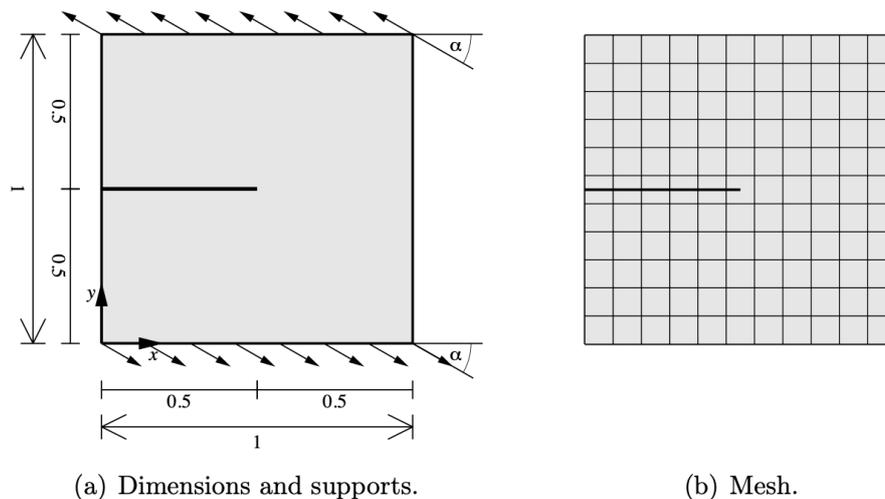
Figure 5.46: Test case with one edge crack in a unit-square specimen, [Fries et al 2013, p.33]

Investigated in [Fries et al 2013, p.32] were the crack path results for discretizations with $[11 \times 11, 21 \times 21, 41 \times 41, 81 \times 81]$ elements at an angle $\alpha = 30°$ between load and lower edge. In the XFEM-hybrid-explicit-implicit crack description, the direction of the crack propagation equals the direction of the maximum circumferential stress on circles around selected nodes close to the crack tip [Fries et al 2013, p.6]. The crack itself is built of line segments with predefined maximum length. All evaluation in [Fries et al 2013, p.34] displayed similar crack paths for the investigated combinations of stress circles radius and the resolution of

the pieced together crack path.

In Peridynamics, a predefined crack is obtained by severing all bonds passing through a predefined line. Because the number of elements per edge was chosen odd, the predefined crack extends through elements itself. The progression of the crack path can be observed by the trail of broken bonds. Similar to the highest circumferential (hoop) stress in [Fries et al 2013], the internal forces in Peridynamics will relocate due to the predefined crack, causing regions of high bond stretch. Exceeding the bond stretch leads to elimination of the respective bond, thus increasing the damage in the material. Because the influence of the surrounding elements and their respective nodal displacements on a current Gauss point is dependent on the horizon length, δ can be seen as a kind of equivalent to the radius of the stress circles in [Fries et al 2013]. Due to the design decisions of the implementation in this thesis, the horizon length cannot be chosen independently of the element length Δ. Therefore, a comparison of the effect of changing the radii of the stress circles in [Fries et al 2013] have to be realized with a varying spatial discretization in Peridynamics.

In the following, 2 parent Gauss points in each direction per element were used. $E = 3000000$, $l = h = 1$ and $b = 1$ were adopted. [Fries et al 2013] used a poisson ratio of $\nu = 0.3$ and a plane strain setup. Bond based Peridynamics cannot fulfill both of those conditions, since $\nu = 0.25$ must hold for peridynamic plane strain problems [Trageser and Seleson 2020, p.4]. The critical energy release rate G_c of the material used in [Fries et al 2013] was unknown; because bond-based quasi static crack propagation is only valid for a brittle material, a low value $G_c = 7[\frac{\text{J}}{\text{m}^2}]$ is chosen.

After the initial crack was defined, the specific limit load was computed experimentally, for which no crack growth could be observed. The problem is solved afterwards with adaptive dynamic relaxation, compare subsection 3.4.2. An additional external load, which should propagate the crack, is brought to the system. Every p'th time step, new broken bonds were removed. The p steps between the damage updates were supposed to give the system some time to equilibrate again. In case that the system reached a point of equilibrium in between the p time steps, thus the difference between two successive relaxation steps fell below a termination threshold ($\epsilon = 1 \cdot 10^{-6}$), a further incrementation of the load, up to N_{inc} times, was applied in order to guarantee a crack propagation.
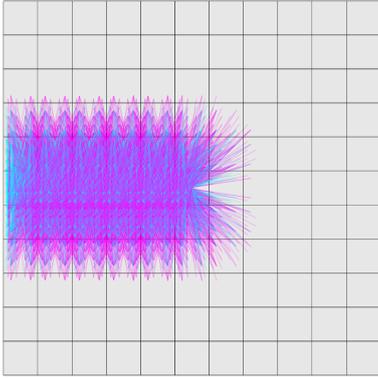
Figure 5.47: Square plate specimen, $\alpha = 90°$, $N_{cut} = 2^2$, $N_{uncut} = 2^1$, $N_{middle} = 2^2$, timestep 1
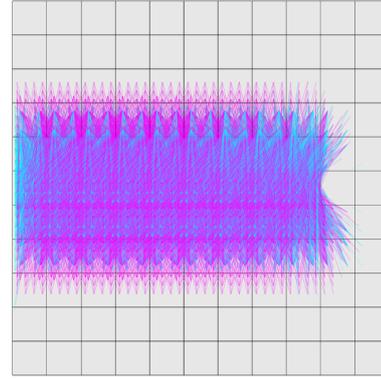

Figure 5.48: Square plate specimen, $\alpha = 90°$, $N_{cut} = 2^2$, $N_{uncut} = 2^1$, $N_{middle} = 2^2$, timestep 616

Depicted in figure 5.47 is the predefined crack through the specimen plate under a vertical load. The model consists of 11×11 elements; the load was applied to the first three layers of elements on top and bottom of the system. Different to [Fries et al 2013], the crack path is not brought into the XFEM-model from exterior, but the peridynamic crack path can be observed by the broken bonds directly. Broken bonds extending to cut elements are depicted in purple, broken bonds to uncut elements are depicted in cyan color. Broken bonds within the middle are depicted in red, but superimposed by the longer bonds. Please regard that not all colored areas are cracks; the crack in figure 5.47 and lies in the middle of the colored region where the intensity of color is highest.

The figures below depict the crack paths through the specimen plate for three different spatial discretizations. This procedure is supposed to resemble the variation of the stress circles' diameters in the XFEM-approach. According to [Fries et al 2013, p.34], the angle α between load and lower edge was fixed to 30°. The peridynamic setup used a $N_{cut} = 2^2$, $N_{uncut} = 2^2$, $N_{middle} = 2^2$ and $p = 10$; the resulting starting load was set to 75000. This load was incremented by 40000, such that the crack propagation started. No further load incrementation was necessary to continue on the crack propagation.

**11×11 elements,** $\alpha = 30°$**,** $4 \times 4 \times 4$
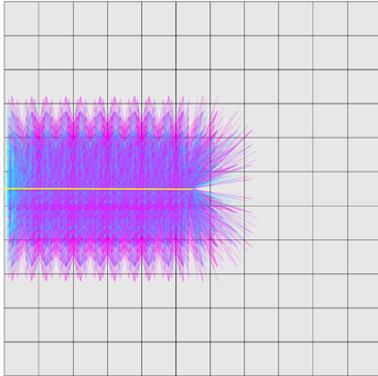

Figure 5.49: Timestep 55
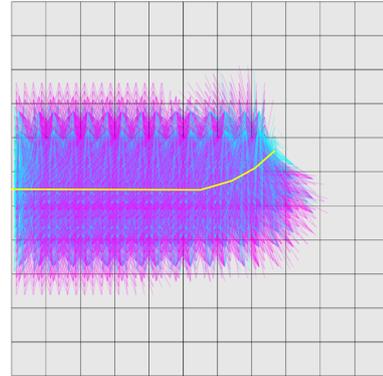

**Figure 5.50:** Timestep 275
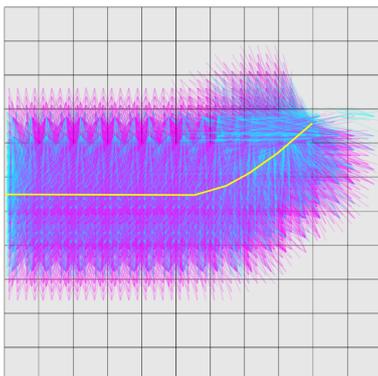
Figure 5.51: Timestep 471
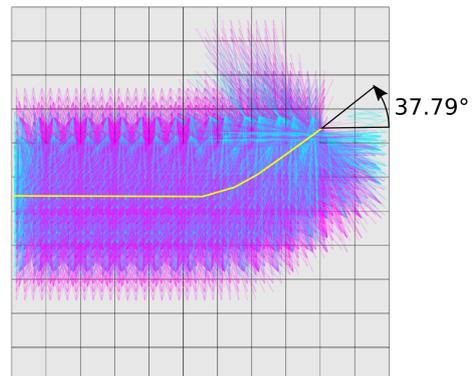
Figure 5.52: Timestep 492

The white lines in figures 5.49 to 5.52 were included manually to highlight the crack path. From timestep 471 (figure 5.51) on, additional damage at the right edge of the structure can be seen, compare the cyan broken bonds. Although direction and inclination of the crack path display good coincidence with the comparison solution (comp. figure 5.61), especially the last timestep 492 in figure 5.52 result in heavily spreading damage throughout the upper edge of the system. This damage is even increased in further timesteps not shown here. As the upper three element layers are zone of load application, an expansion of the crack path's damage into this already stressed region will probably cause a large local failure. Although this scenario is not unphysical, it could happen at too large distances between crack tip and loading zone. Reason for this is the (too) coarse spatial discretization; a peridynamic horizon

with maximum bond length $\delta = 3\,\Delta$ in this example is interfering with a large environment compared to the overall dimension of the system.

15×15 elements, $\alpha = 30°$, $3 \times 3 \times 4$

For this experiment, a coarser discretization of the cut- and uncut elements was chosen.
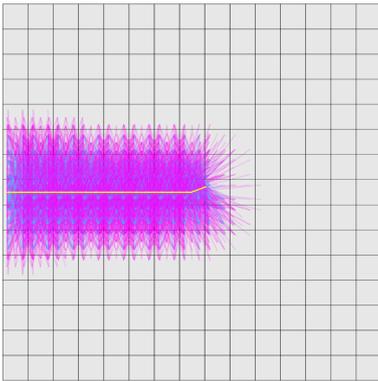

**Figure 5.53:** Timestep 225
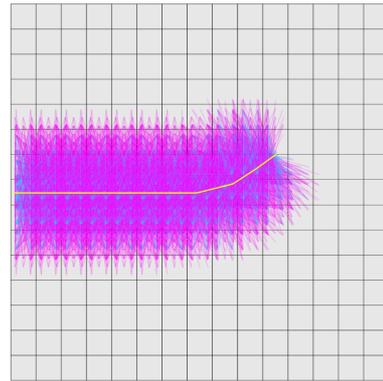
Figure 5.54: Timestep 331
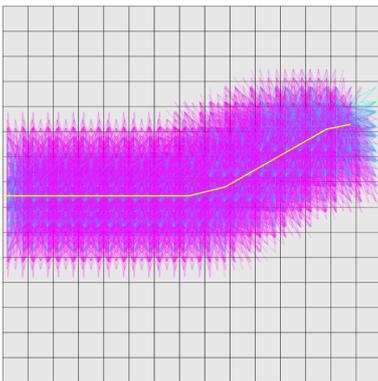
**Figure 5.55:** Timestep 475
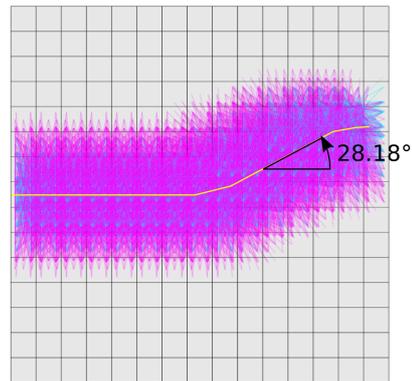
Figure 5.56: Timestep 499

Due to the finer meshgrid, very few broken bonds extend into the loading region, compare figures 5.52 and 5.56. Furthermore, a curvature of the crack path closer to the right edge can be observed in 5.56, which was not visible for the coarse 11×11 meshgrid. The coarser inner integral discretization led to a lower angle of the crack path however.

21 × 21 elements, $\alpha = 30°$**, 4 × 4 × 4**
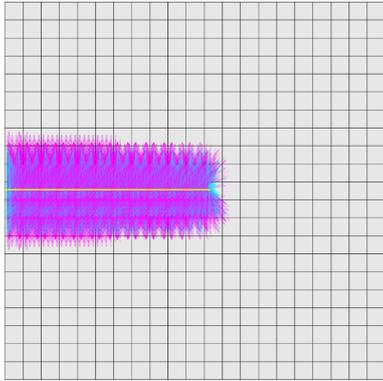
**Figure 5.57:** Timestep 225
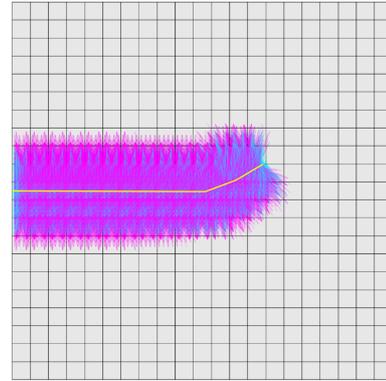

Figure 5.58: Timestep 331
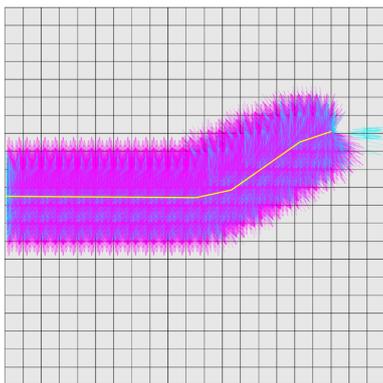

Figure 5.59: Timestep 475
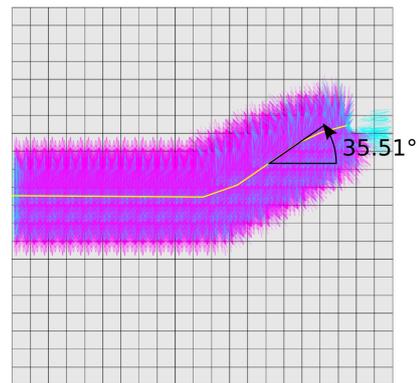
Figure 5.60: Timestep 499

The resulting angles of the crack paths are listed in table 5.29. [Fries et al 2013] obtain

	11 × 11	15 × 15	21 × 21
3 × 3 × 4	36°	28°	28°
4 × 4 × 4	38°	38°	35°

Table 5.29: Inclination of crack paths

a crack path angle of $\approx 40°$ [Fries et al 2013, p.35]. These results are met quite well by a peridynamic simulation with an inner integral discretization of $4 \times 4 \times 4$ quadrature points for cut-, uncut- and middle integral. Furthermore, the peridynamic crack paths display a similar curvature like the results from the XFEM- with hybrid explicit-implicit

crack description solution, compare figures 5.60, 5.56 and 5.61. A coarser inner integral discretization with $3 \times 3 \times 4$ quadrature points leads to a reduction of the crack path angles by 7° to 7°, depending on the discretization.


<center>(a)   (b) Detail.</center>
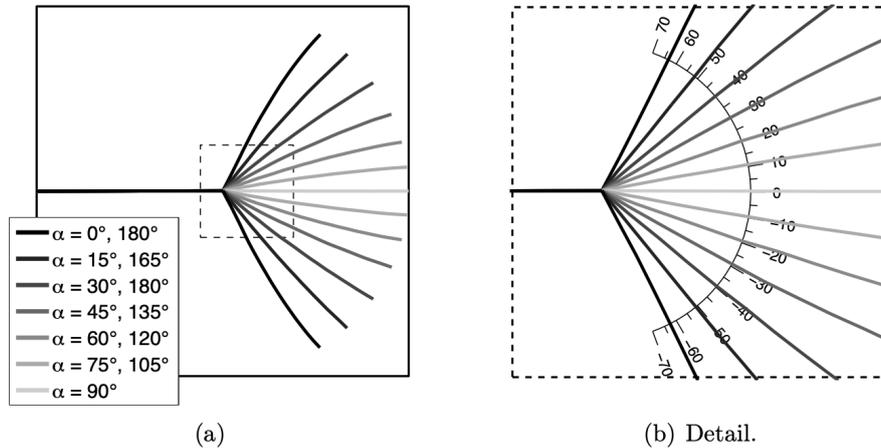
Figure 5.61: Test case with one edge crack in a unit-square specimen [Fries et al 2013, p.35]

5.4.2 Asymmetric bending of a beam

The last problem was induced by [Fries et al 2013, p.37] and "considers a beam with an eccentric edge crack under three point bending". The original experiment stems from [Gálvez et al 1998, p.732] and provided experimental crack trajectories for notched concrete beams. The experiment observed different inclinations of the resulting crack paths (compare figure 5.63) for two different support conditions; type 1 omitted the pin support on top of the structure (depicted in light grey in figure 5.62), while type 2 took this support into consideration. All dimensions are given in [mm].

Figure 5.62, lower part, displays the peridynamic model. The inner region is modeled with 15×68 and 20×90 elements, $\delta = 3\,\Delta$. The embedding region has a thickness of $\delta + 1\,\Delta = 4\,\Delta$ elements. The width of the pin supports and the area of load application is set to $3\,\Delta$ in order to prevent a local overloading, which would result in a destruction of the areas of load introduction instead of a crack propagation of the notch. According to [Madenci and Oterkus 2014, p.144], the elements close to the regions of load application were defined as "no fail" elements; bonds originating from no fail elements are not allowed to be removed although they are overstretched. Furthermore, the first check for overstretched bonds and subsequent bond removal is done after p timestep in order to give the dynamic relaxation algorithm enough time to reach a steady state condition. Afterwards, bonds are removed repeatedly after p timesteps.
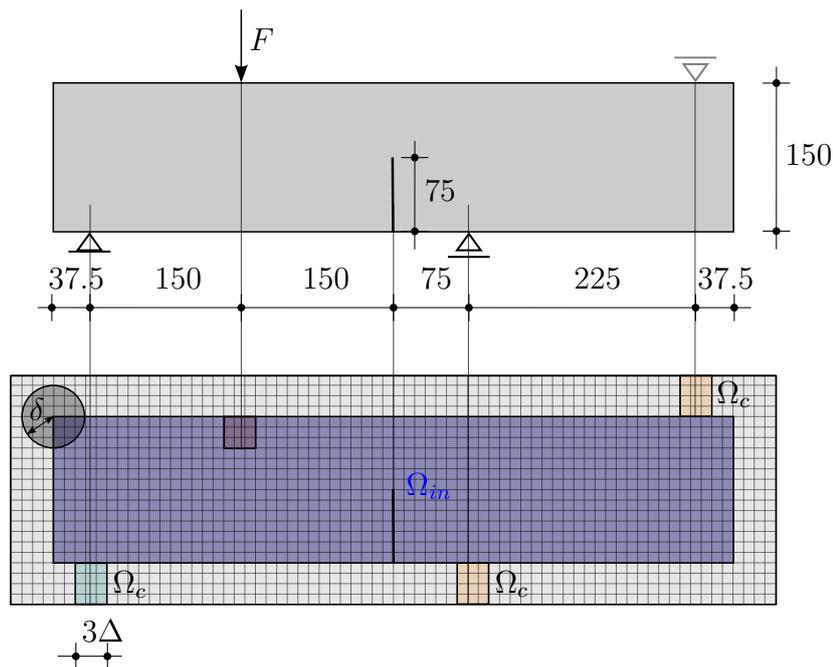
Figure 5.62: Geometry, forces and boundary conditions in mixed mode tests [Gálvez et al 1998, p.732]. Dimensions in [mm].

The pin supports on the right hand side at bottom and top of the system, depicted in orange in figure 5.62, are not compatible with the modeling of supports in subsection 3.3, because the horizontal displacement of two supports in fig. 5.62 may not be constrained. Assigning a material value $\neq 0$ to those supports would constrain the horizontal displacements however and thus generate non-intended support conditions. Solution with adaptive dynamic relaxation enables a solution to this problem. In the beginning of every timestep (before computation of the peridynamic force state), the vertical displacements of the support nodes are set to zero. As the horizontal displacements are unaffected, a vertical-only support can be generated.

Depicted in figures 5.63 and 5.64 are the crack paths for type 1 and 2 support condition from [Gálvez et al 1998, p.734] and [Fries et al 2013, p.37]. The application of a third pin support (type 2) results in a different inclination of the evolving crack path. The experimental envelope of the crack in type 1 crack has a length of approx. 35 to 40 mm, type 2 has a length of approx. 100 to 115 mm.
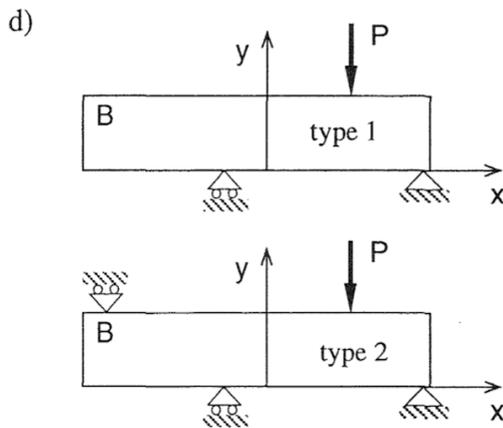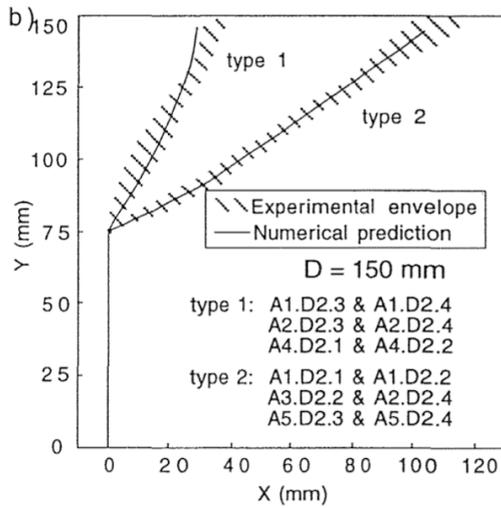
Figure 5.63: Experimental crack trajectories and numerical prediction [Gálvez et al 1998, p.734]
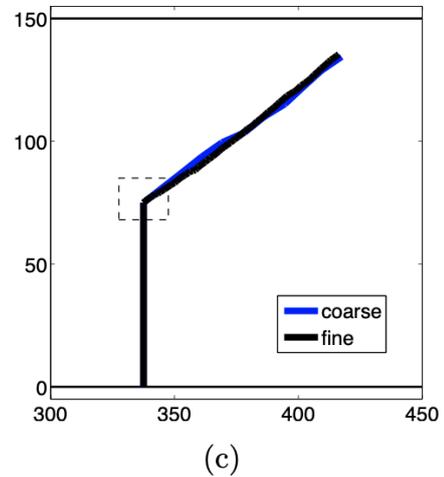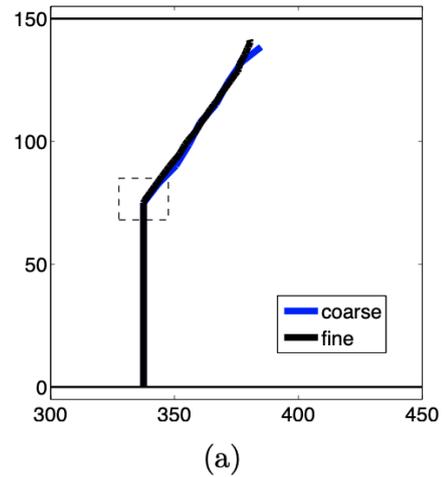
Figure 5.64: Crack inclination for coarse and fine discretization [Fries et al 2013, p.37]

The same crack patterns shall now be repeated with peridynamic finite elements. As the previous experiments have shown a certain requirement on the discretization, a minimum discretization of 15 elements in X^2- direction is chosen.

5.4.3 Discretization A, 15×68

$\Delta = 0.01$ holds for this discretization. Thus, in order to reproduce the results of [Fries et al 2013], the type 1 crack tip of the fully broken system should be located about 4 elements left of the notch, compare figure 5.63, type 2 about 10 element lengths. The discretization of the inner integral is defined as $N_{cut} \times N_{uncut} \times N_{middle}$.

Type 1 , 3 $\times$ 4 $\times$ 4
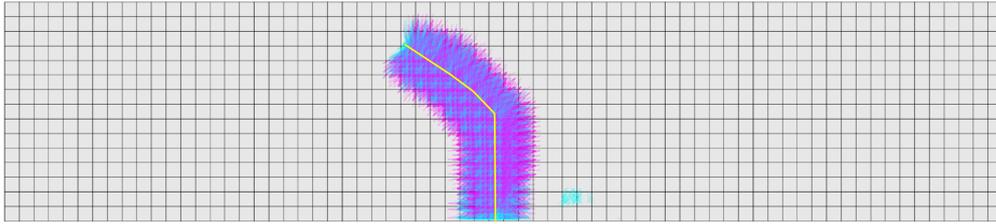
Figure 5.65: Type 1, 15 $\times$ 68, Timestep 2300, 3 $\times$ 4 $\times$ 4

Type 2 , 3 $\times$ 4 $\times$ 4
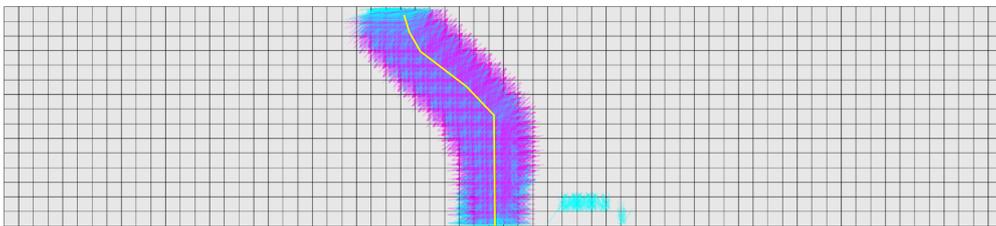
Figure 5.66: Type 2, 15 $\times$ 68, Timestep 2000, 3 $\times$ 4 $\times$ 4

Type 1 , 4 $\times$ 4 $\times$ 4
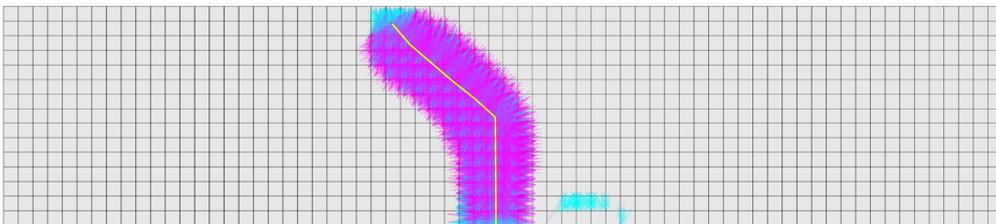
Figure 5.67: Type 1, 15 $\times$ 68, Timestep 703, 4 $\times$ 4 $\times$ 4

Type 2 , 4 $\times$ 4 $\times$ 4
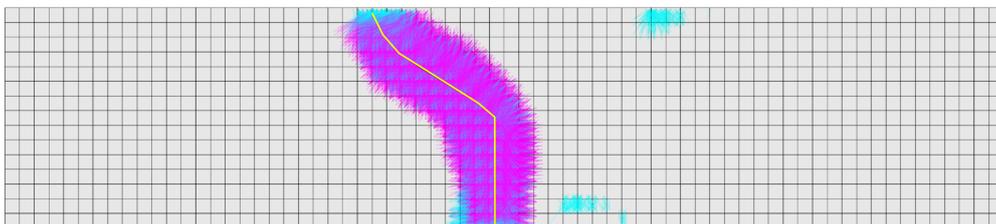
Figure 5.68: Type 2, 15 $\times$ 68, Timestep 818, 4 $\times$ 4 $\times$ 4

5.4.4 Discussion of the results

Comparing figures 5.65 and 5.66 shows that the evolution in time of the cracks is different. The crack in the type 2 system has already reached the upper edge of the system, whereas the

crack in the type 1 system has reached the upper forth. Pin support 3 of the type 2 system thus leads to a faster evolution of the crack, possibly because of the tighter constraints and therefore stiffer behavior of the system. Although the direction is as predicted, the path of broken bonds in plots 5.65 and 5.66 shows nearly no difference between both support conditions. Repeating the experiment with a finer discretization of the cut elements leads to a better distinction between the crack paths. The type 2 path displays a slightly larger inclination to the left than type - 1. Still, especially the inclination of the type - 1 crack path does not meet the predictions from figures 5.63 and 5.64. However, minding that a crack passing in between two adjacent quadrature points results in broken bonds extending to the adjacent two elements, a clear distinction between the crack paths requires at least a finer meshgrid. Depicted in table 5.30 are the horizontal distance in multiples of the element

Discretization	Experiment $[\Delta]$	$3 \times 4 \times 4$ $[\Delta]$	$4 \times 4 \times 4$ $[\Delta]$
type 1	≈ 4	-	≈ 6.5
type 2	≈ 10	≈ 7.5	≈ 8.5

Table 5.30: Horizontal distance initial notch - final crack tip

length Δ between the initial notch and the final crack tip. It displays that the inclination of the type 1 crack is too large.

5.4.5 Discretization B, 20 $\times$ 90

The experiment above is repeated with an element lenght $\Delta = 0.0075$.

Type 1 , 3 $\times$ 4 $\times$ 4
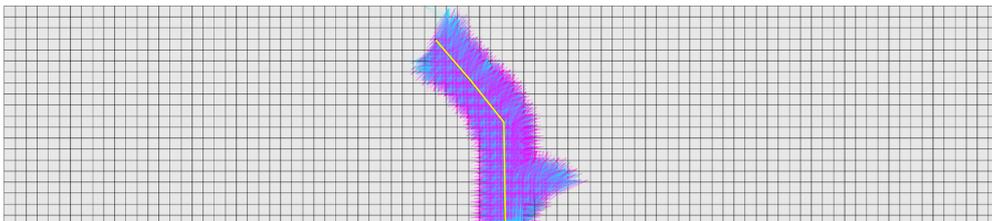
Figure 5.69: Type 1, 20 $\times$ 90, timestep 345, 3 $\times$ 4 $\times$ 4

Load introduction: $[36\Delta : 38\Delta]$

Type 2 , 3 × 4 × 4
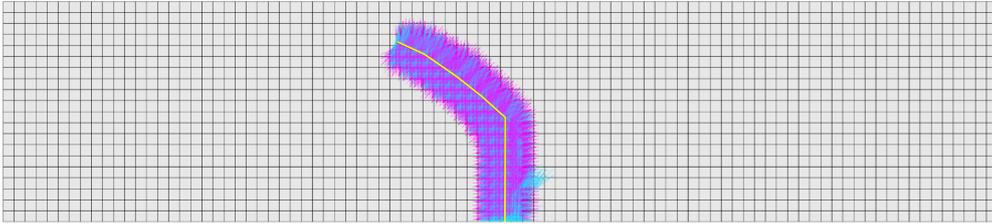
Figure 5.70: Type 2, 20 × 90, timestep 700, 3 × 4 × 4

Load introduction: $[26\Delta : 28\Delta]$

Type 1 , 4 × 4 × 4
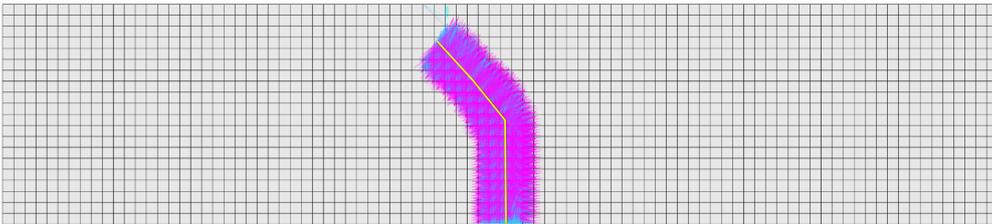
Figure 5.71: Type 1, 20 × 90, timestep 345, 4 × 4 × 4

Load introduction: $[36\Delta : 38\Delta]$

Type 2 , 4 × 4 × 4
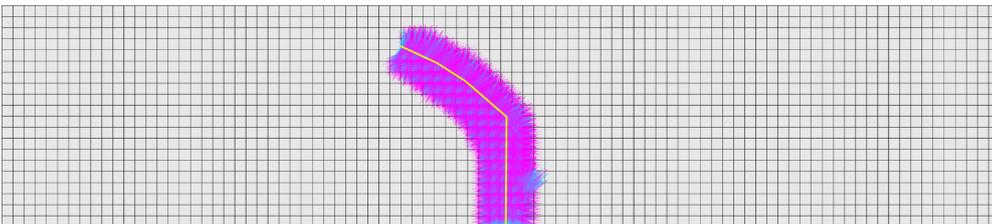
Figure 5.72: Type 2, 20 × 90, timestep 800, 4 × 4 × 4

Load introduction: $[26\Delta : 28\Delta]$

5.4.6 Discussion of the results

A refinement of the mesh alone did not result in a significant difference of the crack paths. The lower inclination of the paths in figures 5.69 and 5.71 had to be achieved by relocating

the load by a distance of 10 elements ($\approx$ 75mm) to the right. An explanation for this could be an attraction of the crack tip by the region of load introduction. As depicted in figure 5.62, the area of load introduction stretches itself several elements into the depth of the beam. This load modeling takes into consideration the non-vanishing volume of force boundaries in Peridynamics, but is necessary on the other hand to suppress an immediate destruction of the loaded elements due to overload. Extending the area of load introduction up to six elements resulted in an even more inclined crack path. Comparing the three point bending example with the cracked square plate, modeling of single loads is more challenging than line loads. Although the elements of direct load application can be defined indestructible, the resulting patch of unbreakable elements will nevertheless cause the surrounding elements to break. This effect can be observed in figure 5.68 above pin support 2; the elements with constrained nodes representing the pin supports were defined as unbreakable; the surrounding ones sustained damage. Another option would be in enlarging the area of load introduction, but this would dilute the intended single load. Therefore, enlarging the area of load introduction must be combined with a refinement of the meshgrid, also separating crack tip and area of load introduction by more elements.

Discretization	Experiment $[\Delta]$	$3 \times 4 \times 4 \ [\Delta]$	$4 \times 4 \times 4 \ [\Delta]$
type 1	≈ 6	≈ 10	≈ 10
type 2	≈ 13	≈ 16	≈ 16

Table 5.31: horizontal distance initial notch - final crack tip

6 Summary and Outlook

6.1 Summary

The topic of this thesis is a detailed investigation of the numerical integration of the inner integral of 2-D peridynamic finite elements. Thanks to the work of [Glaws 2014], a begin was available from which several starting points for this thesis could be deduced. Two goals could be identified. On the one hand, the implementation of the surface correction factor by a recalibration of the bonds' material constant provided a significant improvement of the results. Second, the development of the analytical Jacobian matrix of the peridynamic equation of motion if the solution with Newton's method was applied. Here, a different formulation for the weak form of the inner peridynamic integral than in [Glaws 2014] was chosen. Although a numerical Jacobian obtained from complex step derivative provided a good result with high computational precision, its computation time, especially for a high number of quadrature points, was significant. The analytical Jacobian matrix resulted in an acceleration by up to 15 times and provides an elegant way to obtain the Jacobian. The construction of the latter was supported by the design choice of a fixed integer ratio $\frac{\delta}{\Delta}$ because of easier implementation. Although this ratio was limited to three in this thesis, this ratio can easily be extended to non-integer ratios, although tests with ratios of four and five brought no significant improvements of the results, but a large increase in computation time. Solely the reduction of the horizon radius requires a reformulation of the integral of middle elements as soon as the middle element is not fully encircled by the horizon any more.

Unforeseen were the challenges in the numerical integration of the middle element. Non-synchronization between parent- and subordinate quadrature points posed a severe problem to the analytical Jacobian matrix, causing Newton's method not to converge. Only a subelementation of the middle element by either Duffy transformation or tanh-sinh quadrature resulted in a stable Jacobian matrix. Nevertheless, the subelementation of the cut elements remains problematic, because a high number of quadrature points is necessary to obtain low errors in the integration. Up to now, a midpoint rule provides better results of the cut elements than gauss quadrature.

Tests on a cantilever beam for single load revealed better results for squat- than for long and slender beams. Refinement of the spatial discretization provided better results in all cases. Furthermore, peridynamic elements behaved stiffer than the analytical solution except for very coarse spatial and inner element discretizations. Two further effects could be observed: Fixing spatial and increasing the inner integral discretization caused oscillations in the results, which were reduced for an increasing number of quadrature points. Especially the cut elements contributed to this behavior.

Second, the downside of the fixed horizon-element ratio became obvious for coarse grids, where the changes in the displacement field in neighborhood of the investigated material point could not be resolved adequately if the ratio between problem- and mesh size was too small. As mentioned earlier, a spatial refinement resulted in an improvement of the results; especially in case of beams under line load.

In a next step, the coupling of the peridynamic- with CCM- based elements by the Arlequin method was investigated. H^1- coupling proved to be superior to L^2- coupling with increased coupling length. Experiments on a cantilever beam showed good coincidence with analytical results for small coupling lengths with increasing errors for a longer gluing region.

A failure mechanism for brittle material could be easily implemented into the elements. Explicit time integration with adaptive dynamic relaxation was applied together with step-wise load application to pursue quasi static crack propagation. A comparison with a XFEM-hybrid-explicit-implicit crack description displayed good coincidence of the evolving crack paths for a notched square plate with line-load application. Finer meshgrids resulted in a reduction of the crack path angles in comparison to coarser ones. Furthermore, a coarser discretization of the uncut elements resulted in a significant reduction of the crack path angles throughout all tested element lengths. The three-point bending example did not yield the expected difference between type-1 and type-2 support condition. Although the crack paths evolved into the expected directions, a strong dependency of the crack path on the position of the single-load application could be observed. The desired change in inclination between type-1 and type-2 had to be achieved by relocation of the load introduction area.

6.2 Outlook

The end of this thesis is the begin of several new questions and ideas. This section presents some follow-up questions.

6.2.1 Adaptive dynamic relaxation for coupled problem

A next logical step could be the transition of the crack propagation to a coupled problem, playing at the strengths of both peridynamic finite elements with their damage capability and CCM- based finite elements with their linear relation between forces and displacements. Thus, the problem from subsection could be solved as a coupled problem, saving computational effort. To do so, the Arlequin-coupling has to be embedded into the explicit time integration scheme of the adaptive dynamic relaxation. The following expression yields a first attempt for the structure of the equations (A subindex 1 denotes the peridynamic system, subindex 2 the CCM-system):

$$
\begin{bmatrix} [D_1] & [0] & [0] \\ [0] & [D_2] & [0] \\ [0] & [0] & [0] \end{bmatrix} \begin{bmatrix} \ddot{\mathbf{u}}_1 \\ \ddot{\mathbf{u}}_2 \\ \mathbf{0} \end{bmatrix} + c^{(n)} \begin{bmatrix} [D_1] & [0] & [0] \\ [0] & [D_2] & [0] \\ [0] & [0] & [0] \end{bmatrix} \begin{bmatrix} \dot{\mathbf{u}}_1 \\ \dot{\mathbf{u}}_2 \\ \mathbf{0} \end{bmatrix} + \begin{bmatrix} [0] & [0] & [C_1]^T \\ [0] & [K_{\text{CCM}}] & -[C_2]^T \\ [C_1] & -[C_2] & [0] \end{bmatrix} \begin{bmatrix} \bar{\mathbf{u}}_1 \\ \bar{\mathbf{u}}_2 \\ \bar{\boldsymbol{\lambda}} \end{bmatrix} +
$$

$$
+ \begin{bmatrix} \mathbf{f}(\bar{\mathbf{u}}_1) \\ \mathbf{0} \\ \mathbf{0} \end{bmatrix} = \begin{bmatrix} \mathbf{b}_1 \\ \mathbf{b}_2 \\ \mathbf{0} \end{bmatrix}
$$

(6.1)

Equation 6.1 represents an Index 2 Differential Algebraic Equation (DAE), which is not compatible with an explicit treatment of the Lagrange multipliers [Peterson et al 2018, p.9], [Ascher and Petzold 1998, p.266]. By demanding a continuity of the accelerations instead of the displacements, expression 6.1 can be recast as an index 1 DAE [Peterson et al 2018, p.9]. As long as initial velocity and displacement coincide in the coupling region for both subsystems, the acceleration continuity constraint implies the original displacement continuity constraint [Peterson et al 2018, p.9]. For a better overview, the matrices are rearranged:

$$
\begin{bmatrix} [D_1] & [0] & [C_1]^T \\ [0] & [D_2] & -[C_2]^T \\ [C_1] & -[C_2] & [0] \end{bmatrix} \begin{bmatrix} \ddot{\mathbf{u}}_1 \\ \ddot{\mathbf{u}}_2 \\ \bar{\boldsymbol{\lambda}} \end{bmatrix} =
$$

$$
\begin{bmatrix} \mathbf{b}_1 \\ \mathbf{b}_2 \\ \mathbf{0} \end{bmatrix} - c^{(n)} \begin{bmatrix} [D_1] & [0] & [0] \\ [0] & [D_2] & [0] \\ [0] & [0] & [0] \end{bmatrix} \begin{bmatrix} \dot{\mathbf{u}}_1 \\ \dot{\mathbf{u}}_2 \\ \mathbf{0} \end{bmatrix} - \begin{bmatrix} [0] & [0] & [0] \\ [0] & [K_{\text{CCM}}] & [0] \\ [0] & [0] & [0] \end{bmatrix} \begin{bmatrix} \bar{\mathbf{u}}_1 \\ \bar{\mathbf{u}}_2 \\ \mathbf{0} \end{bmatrix} - \begin{bmatrix} \mathbf{f}(\bar{\mathbf{u}}_1) \\ \mathbf{0} \\ \mathbf{0} \end{bmatrix}
$$

(6.2)

The coupling matrices $[C_1]$ and $-[C_2]$ are acting now upon $\ddot{\bar{\mathbf{u}}}_1$ and $\ddot{\bar{\mathbf{u}}}_2$. Both upper lines of equation 6.2 are solved for $\ddot{\bar{\mathbf{u}}}_1$ and $\ddot{\bar{\mathbf{u}}}_2$

$$
\begin{aligned}
\ddot{\bar{\mathbf{u}}}_1 &= [D_1]^{-1} \left(\mathbf{b}_1 - \mathbf{f}(\bar{\mathbf{u}}_1) - [C_1]^T \bar{\boldsymbol{\lambda}} \right) - c^{(n)} \dot{\bar{\mathbf{u}}}_1 \\
\ddot{\bar{\mathbf{u}}}_2 &= [D_2]^{-1} \left(\mathbf{b}_2 - [K_{\mathrm{CCM}}] \bar{\mathbf{u}}_2 + [C_2]^T \bar{\boldsymbol{\lambda}} \right) - c^{(n)} \dot{\bar{\mathbf{u}}}_2
\end{aligned}
\tag{6.3}
$$

and put into the third line in order to solve for $\bar{\boldsymbol{\lambda}}$:

$$
\begin{aligned}
&[C_1] \ddot{\bar{\mathbf{u}}}_1 = [C_2] \ddot{\bar{\mathbf{u}}}_2 \\
&[C_1] \Big([D_1]^{-1} \left(\mathbf{b}_1 - \mathbf{f}_1(\bar{\mathbf{u}}_1) - [C_1]^T \bar{\boldsymbol{\lambda}} \right) - c^{(n)} \dot{\bar{\mathbf{u}}}_1 \Big) = \\
&[C_2] \Big([D_2]^{-1} \left(\mathbf{b}_2 - [K_{\mathrm{CCM}}] \bar{\mathbf{u}}_2 + [C_2]^T \bar{\boldsymbol{\lambda}} \right) - c^{(n)} \dot{\bar{\mathbf{u}}}_2 \Big)
\end{aligned}
\tag{6.4}
$$

Rearranging for $\bar{\boldsymbol{\lambda}}$ yields:

$$
\begin{aligned}
&\left([C_1][D_1]^{-1}[C_1]^T + [C_2][D_2]^{-1}[C_2]^T \right) \bar{\boldsymbol{\lambda}} = \\
&= [C_1] \Big([D_1]^{-1} \left(\mathbf{b}_1 - \mathbf{f}_1(\bar{\mathbf{u}}_1) \right) - c^{(n)} \dot{\bar{\mathbf{u}}}_1 \Big) - [C_2] \Big([D_2]^{-1} \left(\mathbf{b}_2 - [K_{\mathrm{CCM}}] \bar{\mathbf{u}}_2 \right) - c^{(n)} \dot{\bar{\mathbf{u}}}_2 \Big)
\end{aligned}
\tag{6.5}
$$

This equation is solvable for $\bar{\boldsymbol{\lambda}}$ if the coupling matrices $[C_1]$ and $[C_2]$ have full column rank [Peterson et al 2018, p.10]. As soon as the $\bar{\boldsymbol{\lambda}}$ is known, central differences can be applied in order to compute acceleration, velocity and displacements.

Obtaining a stable and reliable explicit integration of the coupled problem necessitates more research on this topic. According to [Fernier et al 2017, p.3], the stiffness matrix of the coupled problem has to be nonsingular, such that the CFL- condition for the maximum timestep length is valid; in case of CCM-Peridynamics coupling, this means that the matrix consisting blockwise of the peridynamic Jacobian matrix and the CCM- stiffness matrix $[K] = \mathrm{diag}([J],[K_{\mathrm{CCM}}])$ must be nonsingular. This implies that the CCM- stiffness matrix has to be constrained by adequate support conditions and must not rely solely on the Lagrange multipliers to suppress rigid body displacements and rotations. Moreover, the matrix $[D] + \frac{1}{4}\Delta t^2 [K]$ with $[D] = \mathrm{diag}([D_1],[D_2])$ has to be positive definite. Because $[K]$ involves the peridynamic Jacobian matrix, which is time-consuming to compute, more research is necessary in order to find an adequate, but less laborious criterion for the stability of the explicit time integration. Further complications arise due to the significant influence of the Arlequin weights on the critical timestep length according to [Fernier et al 2017]. As soon as the prerequisites for a stable time integration are known, new lumped density matrices $[D]$ and damping coefficients $c^{(n)}$ can be developed in order to achieve as fast as possible convergence to the steady state solution.

6.2.2 Progressions and further improvements with peridynamic finite elements

The developed elements could be the begin of the following progressions.

1. State-based Peridynamics. Replacing the implemented bond-based model by a state-based one would decouple bulk modulus and poisson ratio, thus making the method applicable to a broader range of materials. Thus, a distinction between volumetric and distortional deformations becomes possible, as the force densities become functions of the deformations of the respective families. This would enable to capture the plastic incompressibility condition [Madenci and Oterkus 2014, p.9], which is required for ductile material behavior, e.g. in the vicinity of the crack tip. Furthermore, the state-based Jacobian matrix would be interesting to analyze.

2. Extension to dynamics. Steady state dynamics in 1-D and (quasi) static problems were investigated in the scope of this thesis. By extending the equations in section 6.2.1 to mass- and damping matrices not solely designed to achieve the steady-state solution, the method could be applied to dynamic fracture.

3. Large deformations. Example 5.2.3 tested the applicability of the developed elements on large deformations. However, it does not pose a valid test, because no efforts were made to ensure that the bonds remain within the physical domain of the problem. In order to capture large deformation behavior correctly, a method to guarantee compatibility between horizon length δ and deformation must be found. An extension to stability problems would be interesting as well.

4. Independent horizon- and element length. The idea of this thesis was a fixed ratio $\frac{\delta}{\Delta} = 3$. This produced a fixed pattern of sets of cut, uncut- and middle elements. Following the idea of [Glaws 2014], this design choice could be resolved, such that the horizon becomes independent of the element length. This choice implies increased computational effort however, because the a priori-known sets of uncut, cut- and middle elements are not known in advance. Especially the case of a horizon radius being smaller than the element length will require an additional subelementation of the middle element.

5. Quadratic or higher order shape functions. The performance of elements with higher order shape functions, especially for the development of crack paths could be investigated. Higher order finite elements could be combined with a state-based model, where the forces in between two particles become functions of the deformations of the

respective end-point families. The additional deformation capabilities of higher order finite elements could have a positive effect on the accuracy of the deformation states. Furthermore, it would be interesting to compare the results w.r.t. to oscillations and the Petrov-Galerkin approach in [Bode et al 2020].

6. Averaging between the surface correction factors. In this thesis, the surface correction factor of a bond between $\mathbf{X}$ and $\mathbf{Y}$ was set equal the surface correction factor of the element containing $\mathbf{X}$ only. Attempts of averaging between the correction factors of both elements containing $\mathbf{X}$ and $\mathbf{Y}$ led to non-convergence of Newton's method. An implementation of averaging could improve the results from peridynamic finite elements further.

6.2.3 Linearization and coupling with frequency-domain solutions

The Arlequin method turned out to be an effective coupling between Peridynamics and CCM- subsystems. Extending the coupling between the 1-D peridynamic finite elements with analytical solutions to two dimensions could yield a broad selection of applications. Especially CCM-subsystems in the wavenumber domain with their capability to model the response of semi-infinite domains (see [Hackenberg 2017, p.51-59]) could be a worthwhile extension. However, as the CCM-subsystem's equations of motion are systems of linear differential equations which turn to algebraic equations in the Fourier domain, coupling to a linear peridynamic system would be desirable in order to save recomputation of the Jacobian matrix and apply modal superposition methods. This would require the development of linearized, two dimensional peridynamic finite elements.

A Appendix

A.1 Mathematical background

A.1.1 Coordinate transformation and functional determinant

The resulting force $\mathbf{r}$ of the family members $\mathbf{y}$ acting upon $\mathbf{x}$ is an integral over the deformed family $D_{\mathbf{x}}$. This equilibrium is written down in the deformed configuration.

$$\mathbf{r}(\mathbf{x}) = \iint\limits_{\Omega \cap D_{\mathbf{x}}} \mathbf{f}(\mathbf{x,y}) \, dy^1 dy^2 = \iint\limits_{\Omega \cap D_{\mathbf{x}}} \mathbf{f}(\mathbf{x,y}) \, da_y \tag{A.1}$$

In order to express the right hand side of the equation above in the reference configuration, substitution of $\mathbf{x}$ and $\mathbf{y}$ by $\mathbf{X}$ and $\mathbf{Y}$ is necessary. They are related by the map φ.

$$\begin{aligned}
\mathbf{x} &= \varphi(\mathbf{X}) = \mathbf{X} + \mathbf{u_X} \\
\mathbf{y} &= \varphi(\mathbf{Y}) = \mathbf{Y} + \mathbf{u_Y}
\end{aligned} \tag{A.2}$$

Equation A.2 applied to $\mathbf{f}$ leads to:

$$\mathbf{f}(\mathbf{x,y}) = \mathbf{f}(\,\varphi(\mathbf{X})\,,\,\varphi(\mathbf{Y})\,) =$$

$$= c \, \frac{\delta}{|\mathbf{Y} - \mathbf{X}|} \, \frac{|\mathbf{Y} + \mathbf{u_Y} - \mathbf{X} - \mathbf{u_X}| - |\mathbf{Y} - \mathbf{X}|}{|\mathbf{Y} - \mathbf{X}|} \, \frac{\mathbf{Y} + \mathbf{u_Y} - \mathbf{X} - \mathbf{u_X}}{|\mathbf{Y} + \mathbf{u_Y} - \mathbf{X} - \mathbf{u_X}|} \tag{A.3}$$

By using A.2 and A.3, the equilibrium in the deformed configuration can be expressed w.r.t. the undeformed reference configuration:

$$\mathbf{r}(\mathbf{x}) = \iint\limits_{\Omega \cap D_{\mathbf{x}}} \mathbf{f}(\mathbf{x,y}) \, dy^1 dy^2 = \iint\limits_{\Omega 0 \cap D_{\mathbf{X}}} \mathbf{f}(\,\varphi(\mathbf{X})\,,\,\varphi(\mathbf{Y})\,) \det D\varphi(\mathbf{Y}) \, dY^1 dY^2 \tag{A.4}$$

Since the base vectors $\mathbf{g}_j$ of the deformed configuration differ from the base vectors $\mathbf{e}_i$ of the reference configuration, the differential element $dy^1 dy^2$ has to be expressed in terms of the reference configuration by using the functional determinant of the map φ. The meaning

of the functional determinant is derived briefly in the following. (Please note: $\mathbf{r}$ does now denote a position vector).

$$dy^1 dy^2 = \left| dY^1\, \mathbf{g}_1 \,\times\, dY^2\, \mathbf{g}_2 \right| \tag{A.5}$$

The base vectors $\mathbf{g}_j$ of the deformed configuration (represented w.r.t. the cartesian basis) are obtained by computing the tangential space to a position vector $\mathbf{r}$ of the deformed configuration.

$$\mathbf{g}_j = \frac{\partial \mathbf{r}}{\partial \varphi^s}\, \frac{\partial \varphi^s}{\partial Y^j} \tag{A.6}$$

using A.2, one obtains

$$
\begin{aligned}
\mathbf{g}_1 &= \frac{\partial \mathbf{r}}{\partial \varphi^1}\frac{\partial \varphi^1}{\partial Y^1} + \frac{\partial \mathbf{r}}{\partial \varphi^2}\frac{\partial \varphi^2}{\partial Y^1} =
\begin{bmatrix} \dfrac{\partial \varphi^1}{\partial Y^1} \\[2mm] \dfrac{\partial \varphi^2}{\partial Y^1} \end{bmatrix}
=
\begin{bmatrix} \dfrac{\partial (Y^1 + u^1(Y^1,Y^2))}{\partial Y^1} \\[2mm] \dfrac{\partial (Y^2 + u^2(Y^1,Y^2))}{\partial Y^1} \end{bmatrix}
=
\begin{bmatrix} 1 + \dfrac{\partial u^1}{\partial Y^1} \\[2mm] \dfrac{\partial u^2}{\partial Y^1} \end{bmatrix} \\[6mm]
\mathbf{g}_2 &= \frac{\partial \mathbf{r}}{\partial \varphi^1}\frac{\partial \varphi^1}{\partial Y^2} + \frac{\partial \mathbf{r}}{\partial \varphi^2}\frac{\partial \varphi^2}{\partial Y^2} =
\begin{bmatrix} \dfrac{\partial \varphi^1}{\partial Y^2} \\[2mm] \dfrac{\partial \varphi^2}{\partial Y^2} \end{bmatrix}
=
\begin{bmatrix} \dfrac{\partial (Y^1 + u^1(Y^1,Y^2))}{\partial Y^2} \\[2mm] \dfrac{\partial (Y^2 + u^2(Y^1,Y^2))}{\partial Y^2} \end{bmatrix}
=
\begin{bmatrix} \dfrac{\partial u^1}{\partial Y^2} \\[2mm] 1 + \dfrac{\partial u^2}{\partial Y^2} \end{bmatrix}
\end{aligned}
\tag{A.7}
$$

The area of the differential element $dy^1 dy^2$ in the reference configuration is the cross product from equation A.5. To apply the cross product, the vectors from A.7 have to be expanded to three dimensions.

$$
dy^1 dy^2 = dY^1\, dY^2\, |\, \mathbf{g}_1 \times \mathbf{g}_2\, | = dY^1\, dY^2 \left\|
\begin{bmatrix} 1 + \dfrac{\partial u^1}{\partial Y^1} \\[2mm] \dfrac{\partial u^2}{\partial Y^1} \\[2mm] 0 \end{bmatrix}
\times
\begin{bmatrix} \dfrac{\partial u^1}{\partial Y^2} \\[2mm] 1 + \dfrac{\partial u^2}{\partial Y^2} \\[2mm] 0 \end{bmatrix}
\right\| =
\tag{A.8}
$$

$$
dY^1\, dY^2 \left[\left(1 + \frac{\partial u^1}{\partial Y^1}\right)\left(1 + \frac{\partial u^2}{\partial Y^2}\right) - \left(\frac{\partial u^2}{\partial Y^1}\right)\left(\frac{\partial u^1}{\partial Y^2}\right) \right] = dY^1\, dY^2\, \det D\varphi(\mathbf{Y})
$$

Up to now, u^1 and u^2 are not defined in terms of Y^1 and Y^2.
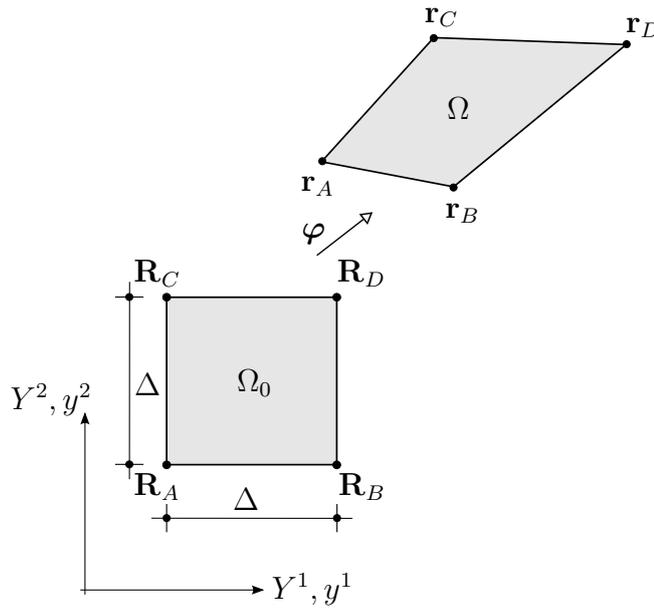
Figure A.1: Map from deformed to undeformed configuration

This relationship is obtained by expressing u^1, u^2 by the nodal displacements:

$$\begin{bmatrix} U_{A_1} \\ U_{B_1} \\ U_{C_1} \\ U_{D_1} \end{bmatrix} = \begin{bmatrix} r_{A_1} \\ r_{B_1} \\ r_{C_1} \\ r_{D_1} \end{bmatrix} - \begin{bmatrix} R_{A_1} \\ R_{B_1} \\ R_{C_1} \\ R_{D_1} \end{bmatrix} \quad ; \quad \begin{bmatrix} U_{A_2} \\ U_{B_2} \\ U_{C_2} \\ U_{D_2} \end{bmatrix} = \begin{bmatrix} r_{A_2} \\ r_{B_2} \\ r_{C_2} \\ r_{D_2} \end{bmatrix} - \begin{bmatrix} R_{A_2} \\ R_{B_2} \\ R_{C_2} \\ R_{D_2} \end{bmatrix} \tag{A.9}$$

A bilinear approach is made to connect the nodal displacements with the coordinates Y^1 and Y^2:

$$\begin{aligned} u^1 &= a_1 + b_1 Y^1 + c_1 Y^2 + d_1 Y^1 Y^2 \\ u^2 &= a_2 + b_2 Y^1 + c_2 Y^2 + d_2 Y^1 Y^2 \end{aligned} \tag{A.10}$$

with yet unknown coefficients a_1, b_1, c_1, d_1 and a_2, b_2, c_2, d_2. The coefficients are obtained by plugging in the nodal coordinates for Y^1, Y^2 solving the two linear equation systems:

$$\begin{bmatrix} 1 & R_{A_1} & R_{A_2} & R_{A_1} R_{A_2} \\ 1 & R_{B_1} & R_{B_2} & R_{B_1} R_{B_2} \\ 1 & R_{C_1} & R_{C_2} & R_{C_1} R_{C_2} \\ 1 & R_{D_1} & R_{D_2} & R_{D_1} R_{D_2} \end{bmatrix} \begin{bmatrix} a_1 \\ b_1 \\ c_1 \\ d_1 \end{bmatrix} = \begin{bmatrix} U_{A_1} \\ U_{B_1} \\ U_{C_1} \\ U_{D_1} \end{bmatrix} \tag{A.11}$$

and

$$
\begin{bmatrix}
1 & R_{A_1} & R_{A_2} & R_{A_1}R_{A_2} \\
1 & R_{B_1} & R_{B_2} & R_{B_1}R_{B_2} \\
1 & R_{C_1} & R_{C_2} & R_{C_1}R_{C_2} \\
1 & R_{D_1} & R_{D_2} & R_{D_1}R_{D_2}
\end{bmatrix}
\begin{bmatrix}
a_2 \\ b_2 \\ c_2 \\ d_2
\end{bmatrix}
=
\begin{bmatrix}
U_{A_2} \\ U_{B_2} \\ U_{C_2} \\ U_{D_2}
\end{bmatrix}
\tag{A.12}
$$

As soon as the coefficients are known, the functional determinant of the transformation from deformed to undeformed (see eq. A.8) can be computed:

$$
\det D\varphi(\mathbf{Y}) = \left(1 + \frac{\partial u^1}{\partial Y^1}\right)\left(1 + \frac{\partial u^2}{\partial Y^2}\right) - \left(\frac{\partial u^2}{\partial Y^1}\right)\left(\frac{\partial u^1}{\partial Y^2}\right) =
$$
$$
\left(1 + b_1 + d_1 Y^2\right)\left(1 + c_2 + d_2 Y^2\right) - \left(b_2 + d_2 Y^1\right)\left(c_1 + d_1 Y^2\right)
\tag{A.13}
$$

A.1.2 Continuity of the integrand

A brief proof of the continuity of the discretized integrand of the inner integral (comp. equation 3.5) shall be given. The aim is now to prove that equation A.14,

$$
\mathbf{f} = \begin{bmatrix} f^1 \\ f^2 \end{bmatrix} = c\,\frac{\delta}{|\mathbf{Y} - \mathbf{X}|}\left(|\mathbf{Y} + \mathbf{u_Y} - \mathbf{X} - \mathbf{u_X}| - |\mathbf{Y} - \mathbf{X}|\right)\frac{\mathbf{Y} + \mathbf{u_Y} - \mathbf{X} - \mathbf{u_X}}{|\mathbf{Y} + \mathbf{u_Y} - \mathbf{X} - \mathbf{u_X}|}
\tag{A.14}
$$

the force density of a bond, is still continuous if discretized displacement fields in terms of nodal displacements (finite element approach) are used instead of the original fields $\mathbf{u_X}$, $\mathbf{u_Y}$.

To keep the problem as simple as possible (though the argumentation can be extended to bonds which extend over two or three elements), it is assumed that a bond $\mathbf{X}$ - $\mathbf{Y}$ should lie within the same element. This element has eight nodal degrees of freedom u_{A_1}, u_{A_2}, ... , u_{D_2}. The discretization of $\mathbf{u_X}$ and $\mathbf{u_Y}$ is done with biliniar shape functions:

$$
\mathbf{u_X} = \begin{bmatrix} u^1(\mathbf{X}) \\ u^2(\mathbf{X}) \end{bmatrix} = N_A(\mathbf{X})\begin{bmatrix} u_{A_1} \\ u_{A_2} \end{bmatrix} + N_B(\mathbf{X})\begin{bmatrix} u_{B_1} \\ u_{B_2} \end{bmatrix} + N_C(\mathbf{X})\begin{bmatrix} u_{C_1} \\ u_{C_2} \end{bmatrix} + N_D(\mathbf{X})\begin{bmatrix} u_{D_1} \\ u_{D_2} \end{bmatrix}
\tag{A.15}
$$
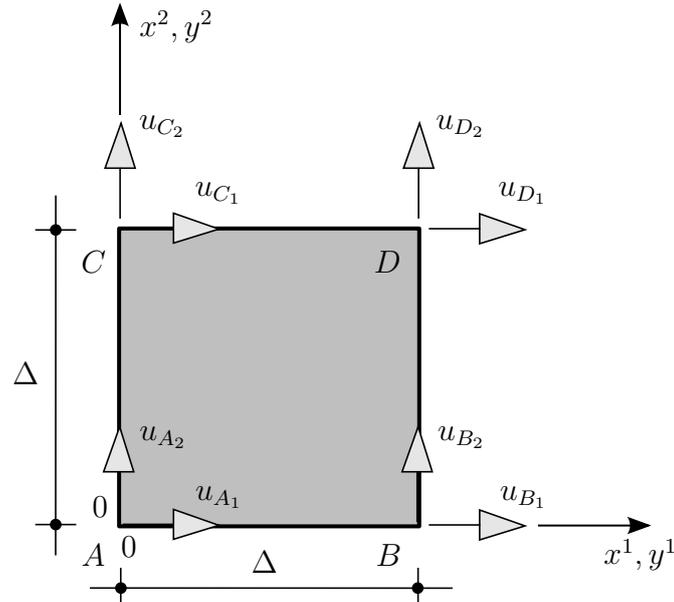
Figure A.2: Element and DOF-definitions

with

$$N_A(\mathbf{X}) = \frac{1}{\Delta}\left(1 - X^1\right)\left(1 - X^2\right)$$

$$N_B(\mathbf{X}) = \frac{1}{\Delta}\left(X^1\right)\left(1 - X^2\right)$$

$$N_C(\mathbf{X}) = \frac{1}{\Delta}\left(1 - X^1\right)\left(X^2\right) \tag{A.16}$$

$$N_D(\mathbf{X}) = \frac{1}{\Delta}\left(X^1\right)\left(X^2\right)$$

(Without a loss of general validity, the argumentation is done with an element of element length $\Delta = 1$, located at the origin of the coordinate system). The discretization of $\mathbf{u_Y}$ is done analogously. This means that the force density $\mathbf{f}$ of the bond is a map that projects a "point" $\mathbf{a} = [x^1, x^2, y^1, y^2, u_{A_1}, u_{A_2}, \ldots, u_{D_1}, u_{D_2}]$ from $\mathbb{R}^{12}$ to $\mathbb{R}^2$ (f^1, f^2).

The continuity of f^1 and f^2 is independent of each other. So, it is sufficient to investigate them separately. In the following, D denotes the set of departure of both f^1 and f^2.

$$f^1 : \mathbb{R}^{12} \supseteq D \to \mathbb{R}$$
$$f^2 : \mathbb{R}^{12} \supseteq D \to \mathbb{R}$$

Both f^1 and f^2 are scalars ($\in \mathbb{R}$), although the component functions building them originate from different spaces. The idea is now to break down f^1 and f^2 to their basic components. If the components in their respective variables are continuous, then also their combinations f^1 and f^2 will be continuous, because sums, products and quotients of continuous functions are continuous themselves [Meyberg and Vachenauer 2013, p.108]. The derivations are done exemplarily on f^1, but work for f^2 analogously.

$$f^1 \;=\; c\,\frac{1}{|\mathbf{Y}-\mathbf{X}|}\,\left(|\mathbf{Y}+\mathbf{u_Y}-\mathbf{X}-\mathbf{u_X}|-|\mathbf{Y}-\mathbf{X}|\right)\frac{Y^1+u^1(\mathbf{Y})-X^1-u^1(\mathbf{X})}{|\mathbf{Y}+\mathbf{u_Y}-\mathbf{X}-\mathbf{u_X}|} \quad\text{(A.17)}$$

Next, the absolute value functions in equation A.14 are expressed by the root function:

$$|\mathbf{Y}-\mathbf{X}| \;=\; \sqrt{(Y^1-X^1)^2+(Y^2-X^2)^2} \tag{A.18}$$

$$|\mathbf{Y}+\mathbf{u_Y}-\mathbf{X}-\mathbf{u_X}| \;=\; \sqrt{(Y^1+u^1(\mathbf{Y})-X^1-u^1(\mathbf{X}))^2+(Y^2+u^2(\mathbf{Y})-X^2-u^2(\mathbf{X}))^2}$$
$$\tag{A.19}$$

X^1 and Y^1 are both continuous, c is even and constant. Regarding eq. A.15, u_{A_1}, u_{B_1}, u_{C_1}, u_{D_1} are continuous too. Eq. A.16 consists of products of x^1 and x^2, and therefore are continuous again.

Equations A.18 and A.19 take the root of continuous functions. According to [Meyberg and Vachenauer 2013, p.107], the composition $f(g(x))$ is continuous, if f and g are continuous themselves. The continuity of the root's argument has been proven already, the root function $\sqrt{x}$ is continuous itself on $x \in \mathbb{R}_+$, so discretized deformed and undeformed length of the bonds are continuos. Last, eq. A.17 is again a composition of continuous functions and therefore continuous itself.

Although continuous, the force density function is not defined if one or both of the denominators of equation A.14 become zero. This could occur in two conceivable ways:

1. $\mathbf{X} = \mathbf{Y}$. Then, both expressions

$$\frac{1}{|\mathbf{Y}-\mathbf{X}|}$$

$$\frac{\mathbf{Y}+\mathbf{u_Y}-\mathbf{X}-\mathbf{u_X}}{|\mathbf{Y}+\mathbf{u_Y}-\mathbf{X}-\mathbf{u_X}|}$$

in eq. A.14 would not be defined. The behavior of the integrand in this case must be investigated.

2. Some combination of the dofs $[u_{A_1}, u_{A_2}, \ldots, u_{D_1}, u_{D_2}]$ could cause

$$\frac{\mathbf{Y} + \mathbf{u_Y} - \mathbf{X} - \mathbf{u_X}}{|\mathbf{Y} + \mathbf{u_Y} - \mathbf{X} - \mathbf{u_X}|}$$

to vanish, although $\mathbf{X} \neq \mathbf{Y}$

Case $\mathbf{X} = \mathbf{Y}$

An idea of the behavior of expression A.14 at $\mathbf{X} = \mathbf{Y}$ can be obtained from plotting the integrand. Below, the X^1 - and X^2 - component of the integrand for a fixed $\mathbf{X} = [4.5, 4.5]$ is depicted. The displacement field imprinted to the element is an isotropic expansion by a value of 1.
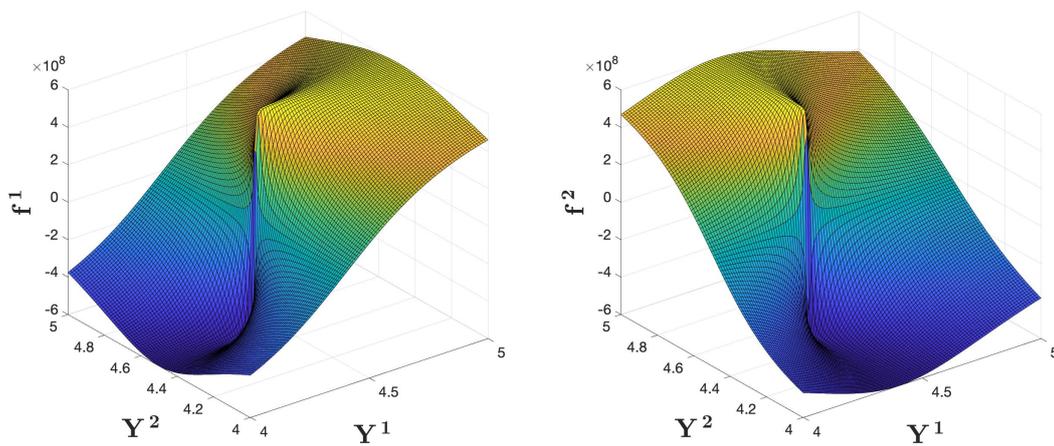
Figure A.3: Integrand with jump at $\mathbf{X} = \mathbf{Y} = \begin{bmatrix} 4.5 \\ 4.5 \end{bmatrix}$

Both plots in figure A.3 show a possible discontinuity at $\mathbf{X} = \mathbf{Y} = [4.5, 4.5]$. Yet it has to be figured out if this point represents a removable definition gap. In this case, the definition gap could be filled with an adequate function value to make the integrand continuous [Meyberg and Vachenauer 2013, p.107] and therefore easier for numerical quadrature to integrate. If the definition gap in $\mathbf{Y} = \mathbf{X}$ was removable, the limit

$$\lim_{\mathbf{Y} \to \mathbf{X}} f^1$$

must exist and be equal for any path $\mathbf{Y} \to \mathbf{X}$. Taking the limit above of eq. A.17 leads to:

$$\hat{f}^1 = \frac{2(X^1 - Y^1)}{\sqrt{(X^{1^2} - 2X^1Y^1 + Y^{1^2}) + (X^{2^2} - 2X^2Y^2 + Y^{2^2})}} = \frac{2(X^1 - Y^1)}{\sqrt{(X^1 - Y^1)^2 + (X^2 - Y^2)^2}}$$

$$(A.20)$$

Introducing $X^2 = Y^2$ allows to simplify the denominator:

$$\hat{f}^1 = \frac{2(X^1 - Y^1)}{\sqrt{(X^1 - Y^1)^2}} \tag{A.21}$$

Now, the limit $\lim\limits_{Y^1 \to X^1} \hat{f}^1$ is taken approaching X^1 from left and right:

$$\lim_{Y^1 \to X^1_-} \hat{f}^1 = -2$$
$$\lim_{Y^1 \to X^1_+} \hat{f}^1 = +2 \tag{A.22}$$

Because the limits from left and right in expression A.22 do not coincide, the definition gap in eq. A.14 cannot be removed. The same behavior holds for f^2. Thus, the integrand is not defined in this case.

Case X $\neq$ Y

The question is whether there is a combination of $[u_{A_1}, u_{A_2}, \ldots, u_{D_1}, u_{D_2}]$ that could render the distance between **X** and **Y** to zero. If so, the following relations must hold:

$$(Y^1 + u_\mathbf{Y}^1 - X^1 - u_\mathbf{X}^1)^2 \overset{!}{=} 0$$
$$(Y^2 + u_\mathbf{Y}^2 - X^2 - u_\mathbf{X}^2)^2 \overset{!}{=} 0 \tag{A.23}$$

Equation A.23 is sorted by **X** and **Y**:

$$Y^1 + u_\mathbf{Y}^1 = X^1 + u_\mathbf{X}^1$$
$$Y^2 + u_\mathbf{Y}^2 = X^2 + u_\mathbf{X}^2 \tag{A.24}$$

In a next step, the isoparametric approaches for the displacement vectors are introduced, exemplarily done with the X^1 - component of A.24.

$$Y^1 + (1 - Y^1)(1 - Y^2)\, u_{A_1} + Y^1(1 - Y^2)\, u_{B_1} + (1 - Y^1)Y^2\, u_{C_1} + Y^1Y^2\, u_{D_1} \overset{!}{=}$$
$$X^1 + (1 - X^1)(1 - X^2)\, u_{A_1} + X^1(1 - X^2)\, u_{B_1} + (1 - X^1)X^2\, u_{C_1} + X^1X^2\, u_{D_1} \tag{A.25}$$

In the further discussion, it is distinguished between a horizontal bond, for which a demonstrative explanation can be found, and an arbitrary orientated bond.

Horizontal bond

To simplify the expressions, it is assumed that $X^2 = Y^2$. This assumption is valid as the aim is to render the distance between $\mathbf{X}$ and $\mathbf{Y}$ to zero by an adequate combination of the element's dofs. So, the vertical difference has already vanished. In a next step, the horizontal difference between $\mathbf{X}$ and $\mathbf{Y}$ is abbreviated with s. For the current element under investigation (A.2), the only conditions of s are not to be zero in order to avoid $\mathbf{X}$ and $\mathbf{Y}$ to coincide and s being smaller equal Δ, as otherwise the bond would not lie within the element.

$$
\begin{aligned}
X^1 + s &= Y^1 \\
X^2 &= Y^2
\end{aligned}
\tag{A.26}
$$

Introducing eq. A.26 into A.25 leads to:

$$
s - s\left(1 - X^2\right) u_{A_1} + s\left(1 - X^2\right) u_{B_1} - s\,X^2\,u_{C_1} + s\,X^2\,u_{D_1} \overset{!}{=} 0
\tag{A.27}
$$

As $s \neq 0$, division by s is allowed. The expression is now a function of X^2 only.

$$
1 - \left(1 - X^2\right) u_{A_1} + \left(1 - X^2\right) u_{B_1} - X^2\,u_{C_1} + X^2\,u_{D_1} \overset{!}{=} 0
\tag{A.28}
$$

The aim is now to render the relative distance above to zero. In order to achieve that, the dofs u_{A_1} and u_{C_1} should be facing the dofs u_{B_1} and u_{D_1} (compare directions of dofs in fig. A.2 and fig. A.4). So, two signs in equation A.28 have to be modified:

$$
\left(1 - X^2\right) u_{A_1} + \left(1 - X^2\right) u_{B_1} + X^2\,u_{C_1} + X^2\,u_{D_1} \overset{!}{=} 1
\tag{A.29}
$$

Equation A.29 is visualized in figure A.4. It is sought a combination of the dofs and x^2 to fullfil eq. A.29. The colored areas denote the contribution of the respective terms. They add up to 1 if the right quadrilateral in figure A.4 is completely covered in colors. If so, the displacements would compress the element to a volume of zero, which is unphysical as the volume of the element may not vanish. This behavior is independent of X^2.

Arbitrary-orientated bond

For the investigation of an arbitrary bond, the center of the element is shifted to the origin of the coordinate system. X^1 and X^2 range now from -0.5 to 0.5 each. The shape functions
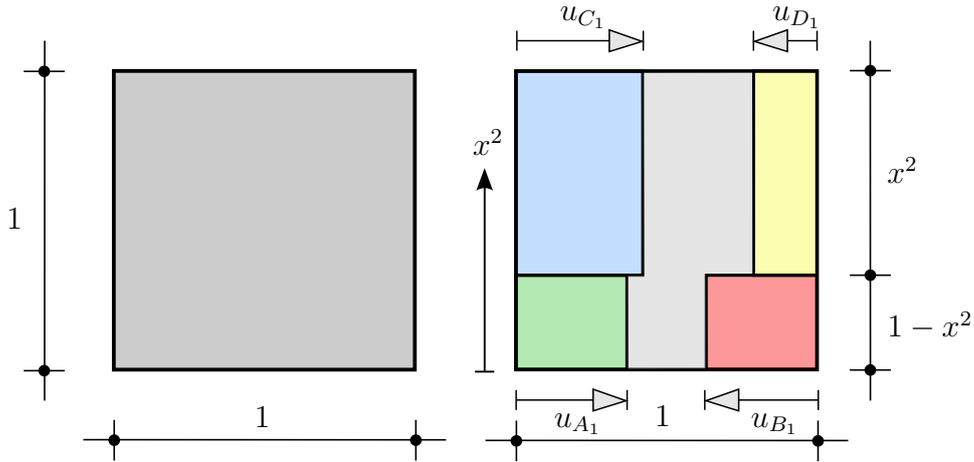
Figure A.4: Ratio of the dofs

transform to

$$
\begin{aligned}
N_A(\mathbf{X}) &= + (X^1 - \tfrac{1}{2})(X^2 - \tfrac{1}{2}) \\
N_B(\mathbf{X}) &= - (X^1 + \tfrac{1}{2})(X^2 - \tfrac{1}{2}) \\
N_C(\mathbf{X}) &= - (X^1 - \tfrac{1}{2})(X^2 + \tfrac{1}{2}) \\
N_D(\mathbf{X}) &= + (X^1 + \tfrac{1}{2})(X^2 + \tfrac{1}{2})
\end{aligned}
\tag{A.30}
$$

Two new variables are introduced in order to make the equations easier to interpret:

$$
\begin{aligned}
X^1 + s &= Y^1 \\
X^2 + p &= Y^2
\end{aligned}
\tag{A.31}
$$

It has to be found a combination of the dofs u_{A_1}, u_{B_1}, u_{C_1}, u_{D_1} and u_{A_2}, u_{B_2}, u_{C_2}, u_{D_2} which render both horizontal- and vertical difference d^1 and d^2 between $\mathbf{X}$ and $\mathbf{Y}$ to zero:

$$
\begin{aligned}
d^1 = \; & Y^1 - X^1 \\
& + (Y^1 - 1)(Y^2 - 1)u_{A_1} - (X^1 - 1)(X^2 - 1)u_{A_1} \\
& - (Y^1 + 1)(Y^2 - 1)u_{B_1} + (X^1 + 1)(X^2 - 1)u_{B_1} \\
& - (Y^1 - 1)(Y^2 + 1)u_{C_1} + (X^1 - 1)(X^2 + 1)u_{C_1} \\
& + (Y^1 + 1)(Y^2 + 1)u_{D_1} - (X^1 + 1)(X^2 + 1)u_{D_1} \overset{!}{=} 0
\end{aligned}
\tag{A.32}
$$

$$
\begin{aligned}
d^2 = \ & Y^2 - X^2 \\
& + (Y^1 - 1)(Y^2 - 1)u_{A_2} - (X^1 - 1)(X^2 - 1)u_{A_2} \\
& - (Y^1 + 1)(Y^2 - 1)u_{B_2} + (X^1 + 1)(X^2 - 1)u_{B_2} \\
& - (Y^1 - 1)(Y^2 + 1)u_{C_2} + (X^1 - 1)(X^2 + 1)u_{C_2} \\
& + (Y^1 + 1)(Y^2 + 1)u_{D_2} - (X^1 + 1)(X^2 + 1)u_{D_2} \overset{!}{=} 0
\end{aligned}
\tag{A.33}
$$

Equations A.31 are introduced into A.32 and A.33.

$$
\begin{aligned}
& \left(\ sp - \frac{p}{2} - \frac{s}{2} + sX^2 + pX^1 \right) u_{A_1} + \\
& \left(-sp - \frac{p}{2} + \frac{s}{2} - sX^2 - pX^1 \right) u_{B_1} + \\
& \left(-sp + \frac{p}{2} - \frac{s}{2} - sX^2 - pX^1 \right) u_{C_1} + \\
& \left(\ sp + \frac{p}{2} + \frac{s}{2} + sX^2 + pX^1 \right) u_{D_1} = -s
\end{aligned}
\tag{A.34}
$$

$$
\begin{aligned}
& \left(\ sp - \frac{p}{2} - \frac{s}{2} + sX^2 + pX^1 \right) u_{A_2} + \\
& \left(-sp - \frac{p}{2} + \frac{s}{2} - sX^2 - pX^1 \right) u_{B_2} + \\
& \left(-sp + \frac{p}{2} - \frac{s}{2} - sX^2 - pX^1 \right) u_{C_2} + \\
& \left(\ sp + \frac{p}{2} + \frac{s}{2} + sX^2 + pX^1 \right) u_{D_2} = -p
\end{aligned}
\tag{A.35}
$$

Equations A.34 and A.35 are composed of each four hypersurfaces with parameters X^1, X^2, s and p and one plane respectively. The hypersurfaces are multiplied with their respective dof and add up in any point $[X^1, X^2, s, p]$ to the change in the relative distance between $\mathbf{X}$ and $\mathbf{Y}$.
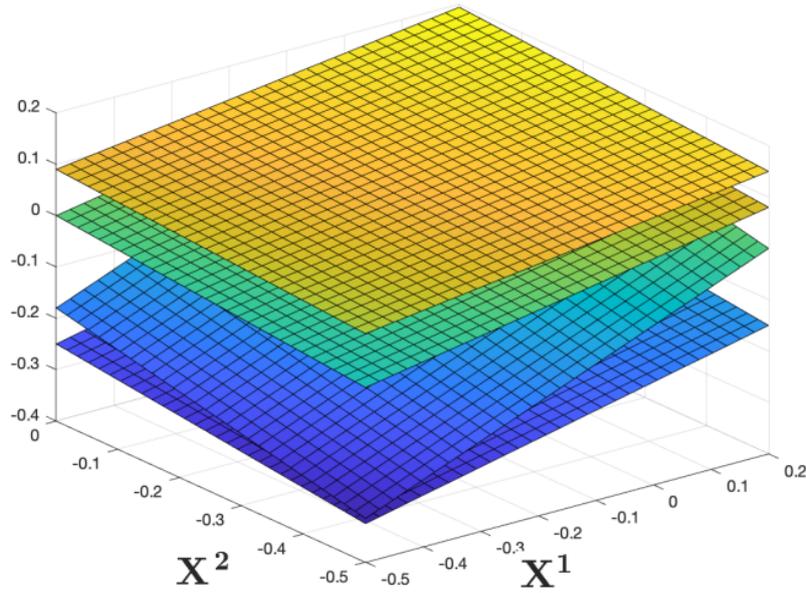
Figure A.5: Hypersurfaces for $s = 0.3$, $p = 0.5$, $u_{A_1} = 0.5$, $u_{B_1} = -0.4$, $u_{C_1} = -0.9$, $u_{D_1} = 0.3$

An exemplary solution valid for all parameters is obtained by introducing $\frac{1}{2}$ for u_{A_1} and u_{C_1}, $-\frac{1}{2}$ for u_{B_1} and u_{D_1}. Due to the signs of the respective terms, all expressions except for $\frac{s}{2}$ in eq. A.32 and $\frac{p}{2}$ in eq. A.33 will eliminate each other if all dofs have the same magnitude. Again, this case would be a compression of the element to zero area.

It has to be investigated now if d^1 and d^2 could become zero even without compressing the element into an unphysical state. The red line in figure A.6 denotes the cutting line
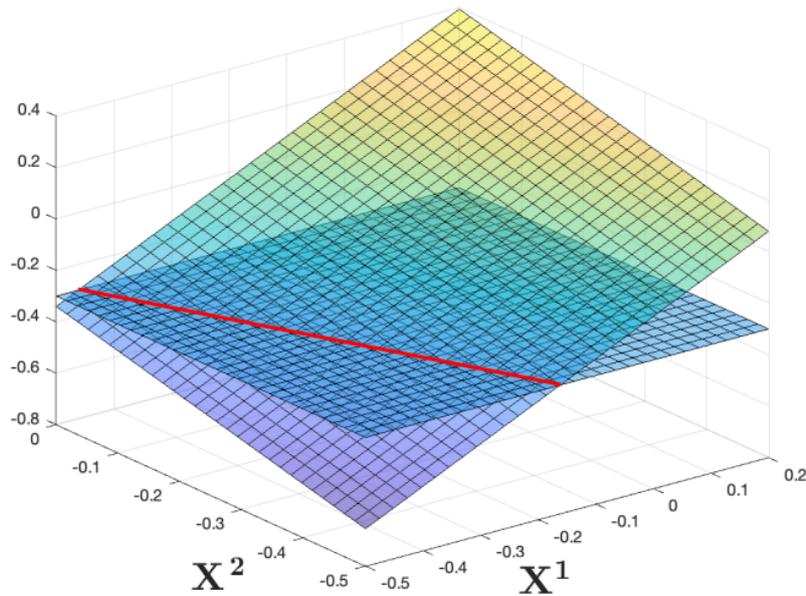
**Figure A.6:** Sum of hypersurfaces for $s = 0.3$, $p = 0.5$, $u_{A_1} = 0.5$, $u_{B_1} = -0.4$, $u_{C_1} = -0.9$, $u_{D_1} = 0.3$

between the sum of the four hypersurfaces multiplied with their respective dof and a plane which has the value $s = -0.3$. The surfaces are therefore a visualization of equation A.34, and the red line poses a physically reasonable solution to it. The equation defining the red line can be obtained by solving A.34 for X^2 in dependence of X^1 (for the chosen combination of $s = 0.3$ and $p = 0.5$):

$$X^2 = \frac{23}{126} - \frac{5}{3}X^1 \tag{A.36}$$

Exemplarily, a point $P = [X^1 = -0.2285, X^2 = -0.3890]$ on this line is chosen for further derivations:
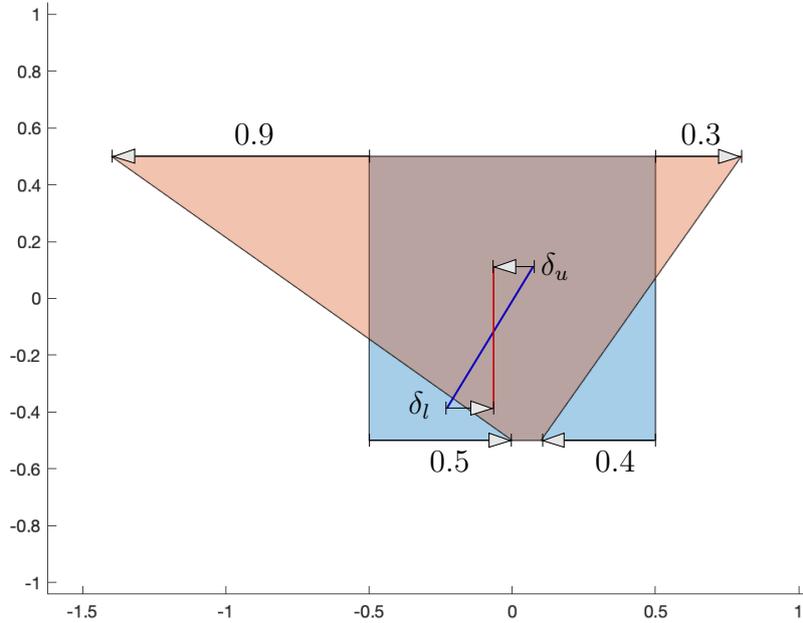
Figure A.7: Rotation of a bond $X^1 = -0.2285$, $X^2 = -0.3890$, $s = 0.3$, $p = 0.5$

Depicted in fig. A.7 in blue is the bond in the undeformed configuration, which is mapped to the red bond in the deformed configuration. This special bond under the depicted displacement field results in eq. A.32 to be fulfilled as:

$$
\begin{aligned}
d^1 &= Y^1 + u^1(Y^1) - X^1 - u^1(X^1) = -0.2285 + 0.3 - 0.1367 - (-0.2285 + 0.1625) \\
&= 0.0008 \approx 0
\end{aligned}
\tag{A.37}
$$

This displacement field can be interpreted as a rotation of the inclined bond into a vertical

position, expressed by the displacements of lower- and upper end of the bond:

$$\delta_l = 0.1625$$
$$\delta_u = 0.1367 \qquad\qquad\qquad (A.38)$$
$$\delta_l + \delta_u = 0.1625 + 0.1367 = 0.3 = s$$

In fact, every point on the red line in figure A.6 represents a bond which is rotated into a vertical alignment by the displacements of the dofs and therefore fulfills equation A.34. Please note that the center of rotation needs not to coincide with the midpoint of the respective bond.

However, using the same idea to render the A.35 to zero and still be physically reasonable will not work. It has been shown that a valid configuration of the dofs that sets A.34 to zero will turn the respective bonds into an upward-pointing direction. The only way now to fulfill A.35,

$$d^2 = Y^2 + u^2(Y^2) - X^2 - u^2(X^2) = 0 \qquad\qquad (A.39)$$

would mean to eliminate the distance between deformed end point $Y^2 + u^2(Y^2)$ and deformed start point $X^2 - u^2(X^2)$ of the bond.
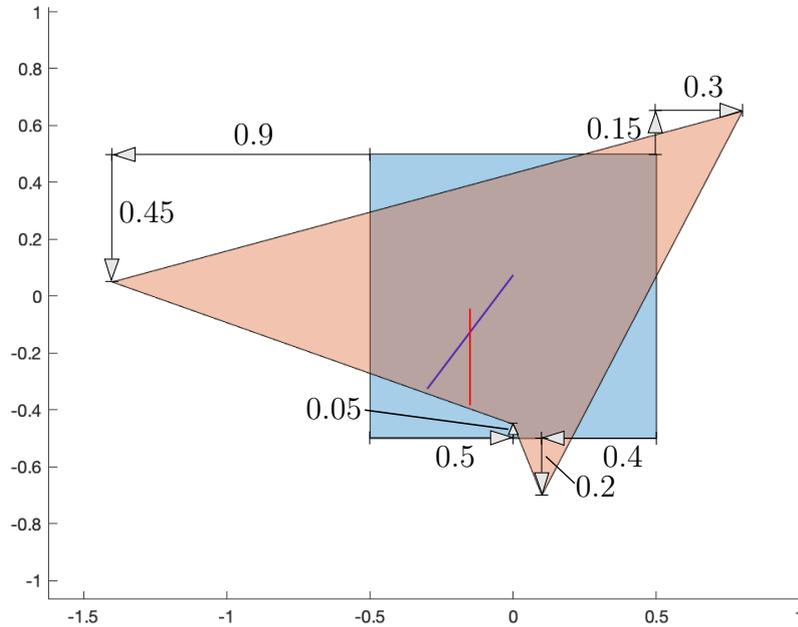
Figure A.8: Vertical shrinking of bond by $u_{A_1} = 0.5$, $u_{B_1} = -0.4$, $u_{C_1} = -0.9$, $u_{D_1} = 0.3$, $u_{A_2} = 0.05$, $u_{B_2} = -0.2$, $u_{C_2} = -0.45$, $u_{D_2} = 0.15$

In figure A.8, the displacements of vertical dofs of the element are changed in order to shrink the vertical distance between lower and upper end of the bond. It is visible that the deformed

bond (red) has already been reduced in its vertical length. But this displacement field is already unphysical. To prove this, the area spanned by the cross product of the base vectors underneath at the corner nodes is evaluated for the displacement state above. [Müller 2018, S.39]

$$\mathbf{G}_i = \frac{\partial}{\partial X^i}\mathbf{R} \tag{A.40}$$

$\mathbf{R}(X^1, X^2)$ is the position vector of any point $[X^1, X^2]$ in the element. Because an isoparametric approach was chosen, $\mathbf{R}(X^1, X^2)$ can be written as:

$$\begin{aligned}\mathbf{R}(X^1, X^2) = (X^1 - 1)(X^2 - 1)(\mathbf{X}_A + \mathbf{u}_A) - (X^1 + 1)(X^2 - 1)(\mathbf{X}_B + \mathbf{u}_B) - \\ - (X^1 - 1)(X^2 + 1)(\mathbf{X}_C + \mathbf{u}_C) + (X^1 + 1)(X^2 + 1)(\mathbf{X}_D + \mathbf{u}_D)\end{aligned} \tag{A.41}$$

Then, the base vectors become:

$$\mathbf{G}_1 = (X^2 - 1)(\mathbf{X}_A + \mathbf{u}_A) - (X^2 - 1)(\mathbf{X}_B + \mathbf{u}_B) - (X^2 + 1)(\mathbf{X}_C + \mathbf{u}_C) + (X^2 + 1)(\mathbf{X}_D + \mathbf{u}_D) \tag{A.42}$$

$$\mathbf{G}_2 = (X^1 - 1)(\mathbf{X}_A + \mathbf{u}_A) - (X^1 + 1)(\mathbf{X}_B + \mathbf{u}_B) - (X^1 - 1)(\mathbf{X}_C + \mathbf{u}_C) + (X^1 + 1)(\mathbf{X}_D + \mathbf{u}_D) \tag{A.43}$$

The X^3-component of all vectors above is 0.

$$\begin{aligned}X^1 = -0.5 \quad &, \quad X^2 = -0.5 \\ \mathbf{X}_A = \begin{bmatrix} -0.5 \\ 0.5 \end{bmatrix} \quad, \quad \mathbf{X}_B = \begin{bmatrix} 0.5 \\ -0.5 \end{bmatrix} \quad, \quad \mathbf{X}_C &= \begin{bmatrix} -0.5 \\ 0.5 \end{bmatrix} \quad, \quad \mathbf{X}_D = \begin{bmatrix} 0.5 \\ 0.5 \end{bmatrix} \\ \mathbf{U}_A = \begin{bmatrix} 0.5 \\ 0.05 \end{bmatrix} \quad, \quad \mathbf{U}_B = \begin{bmatrix} -0.4 \\ -0.2 \end{bmatrix} \quad, \quad \mathbf{U}_C &= \begin{bmatrix} -0.9 \\ -0.45 \end{bmatrix} \quad, \quad \mathbf{U}_D = \begin{bmatrix} 0.3 \\ 0.15 \end{bmatrix}\end{aligned} \tag{A.44}$$

Introducing A.44 into A.42 and A.43 and using A.40 yields:

$$\mathbf{A} = \mathbf{G}_1 \times \mathbf{G}_2 = \begin{bmatrix} 0 \\ 0 \\ -0.3 \end{bmatrix} \tag{A.45}$$

The third entry in eq. A.45, the area of a differential element in **A**, is a negative number. So, on the way to rendering the vertical distance (equation A.35) to zero, the material is forced to pass through itself, which is unphysical. Therefore, it can be stated that any displacement that results in an undefined integrand represents an unphysical displacement field.

A.1.3 Functional analysis

This section gives a short overview over some concepts from functional analysis used in this thesis. A more detailed description can be found in [Meyer-Spasche et al 2012], [Mehlhorn 1999] and [Werner 2006]. Because the vector spaces in this section are vector spaces of functions of $\mathbb{R}$, the elements of those vectors spaces are not written in bold letters.

The term vectorspace used here means a set V over a field K ($K = \mathbb{R}$). For two vectors $(u, v) \in V$ and a scalar $\alpha \in \mathbb{K}$, the operations

$$\text{addition} + \ : \ V \times V \to V, \ (u \, , \, v) \ \to \ u + v$$
$$\text{scalar multiplication} \cdot \ : \ \mathbb{K} \times V \to V, \ (\alpha \, , \, v) \ \to \ \alpha \cdot v$$

are defined [Meyer-Spasche et al 2012, p.1].

Norm

A map $\|\cdot\| \to \mathbb{R}$ by $v \to \|v\|$ is called a norm, iff

$$\|v\| \geq 0 \ \ \forall \ \ v \in V$$
$$\|v\| = 0 \ \ \text{iff} \ \ v = 0$$
$$\|\alpha \, v\| = |\alpha| \|u\| + \|v\| \ \forall \, u, v \in V$$
$$\|u + v\| \leq \|u\| + \|v\| \ \forall \, u, v \in V$$

[Meyer-Spasche et al 2012, p.9]. A norm on a vector space provides a tool to measure the "length" or size of the function space's elements. The norm of a vector cannot be negative per definition and will be zero for the zero element of the vector space. Please note that ∞ is not a number in $\mathbb{R}$ and therefore no valid result for the length of a vector either. Furthermore, different norms on the same space are possible.

Metric

With a norm $\|\cdot\|$, it is possible to define a metric on the vector space V in order to measure the distance between two elements u, v. A function d with

$$d(u,v) := \|u,v\|$$

is called a metric on V [Meyer-Spasche et al 2012, p.12].

Inner product

A map $< \cdot, \cdot > \rightarrow \mathbb{R}$ is called an inner product (scalar product), if

$$< \alpha\, u, v > = \alpha < u, v >$$
$$< u + w, v > = < u, v > + < w, v >$$
$$< u, u > = 0 \text{ iff } u = 0$$

holds for all u, v, $w \in V$, $\alpha \in \mathbb{R}$.

Hilbert space

A vector space with an inner product (scalar product) is called a Hilbert space, if it is complete under the norm induced by it's scalar product [Meyer-Spasche et al 2012, p.12]. Completeness means that every Cauchy sequence of elements of V converges to an element of V; the fact that the space is complete ensures that functions (vectors of V), which are often defined as limits of function series, do exist in V.

In the scope of this thesis, the two Hilbert spaces $\mathbf{L}^2$ and $\mathbf{H}^1$ are of importance. The space

$$\mathbf{L}^2 := \left\{ v(x) \,\Big|\, \int_\Omega |f(x)|^2 \, dx < \infty \right\} \tag{A.46}$$

is the vector space of all square integrable functions. Thus, the integral over the functions squared remains finite. It's inner product is defined as

$$< f, g >_{\mathbf{L}^2} = \int_\Omega f(x)g(x) \, dx \tag{A.47}$$

The scalar product of a function f of $\mathbf{L}^2$ with itself reads as

$$< f, f >_{\mathbf{L}^2} = \int_\Omega |f|^2 \, dx$$

This scalar product induces the norm $\|\cdot\|$ on $\mathbf{L}^2$:

$$\|f\|_{\mathbf{L}^2} \;=\; \left(\int_\Omega |f|^2 \, dx \right)^{\frac{1}{2}}$$

Please note that the inner product of two functions $< f, g >_{\mathbf{L}^2}$ can yield negative results; just the norm (length) of a vector has to be ≥ 0.

The Hilbert space $\mathbf{H}^1$ is also a Sobolev space, a vector space of functions with a weak derivative. A definition of the weak derivative can be found in [Werner 2006, p.226]. $\mathbf{H}^1$ is defined as:

$$\mathbf{H}^1 \;=\; \mathbf{W}^{1,2} \;:=\; \left\{ v(x) \in \mathbf{L}^2 \,\middle|\, D^\alpha v \in \mathbf{L}^2 \text{exist for all } |\alpha| \leq 1 \right\} \tag{A.48}$$

[Herzog 2013, p.11]. $D^\alpha v$ in eq. A.48 means the weak derivatives of v up to order k. The approach functions for real and virtual displacements in 3.7, as well as the approach functions for the Lagrange multipliers in 4.2 are taken from the Sobolev space $\mathbf{W}^{1,2}$. Although the weak form of Peridynamics does not require derivation of the approach functions like CCM, the H^1- coupling operator in equation 4.2 demands the fields λ and μ to be differentiable. Softening the requirement of classical differentiability of the approach functions to a weak differentiability allows the use of piecewise continuously-differentiable approach functions (hat-functions).

The inner product in $\mathbf{H}^1$ is defined as

$$< f, g >_{\mathbf{H}^1} = \int_\Omega f(x)\, g(x) \;+\; D^1 f(x)\, D^1 g(x) \, dx \tag{A.49}$$

inducing the norm:

$$\|\cdot\|_{\mathbf{H}^1} \;=\; \left(\int_\Omega |f(x)\, g(x)|^2 \, dx \;+\; \int_\Omega \left| D^1 f(x)\, D^1 g(x) \right|^2 \, dx \right)^{\frac{1}{2}} \tag{A.50}$$

The coupling problems in the scope of this work include one- and two dimensional domains Ω. On a two dimensional domain $\Omega \in \mathbb{R}^2$, the functions (fields) to be coupled will be vector-valued: $\mathbf{f}(\mathbf{x}) \in \mathbb{R}^2$. The Sobolev space $\mathbf{W}^{1,2}$ of vector valued functions is defined as:

$$\mathbf{H}^1(\Omega, \mathbb{R}^2) \;=\; \mathbf{W}^{1,2}(\Omega, \mathbb{R}^2) \;:=\; \left\{ \mathbf{f}(\mathbf{x}) \in \mathbf{L}^2(\Omega, \mathbb{R}^2) \,\middle|\, \nabla \mathbf{f} \in \mathbf{L}^2(\Omega, \mathbb{R}^{2\times 2}) \text{ exists} \right\} \tag{A.51}$$

The scalar product in $\mathbf{W}^{1,2}(\Omega, \mathbb{R}^2)$ for two vectors $\mathbf{f}(\mathbf{x})$, $\mathbf{g}(\mathbf{x})$ is defined as:

$$< \mathbf{f}, \mathbf{g} >_{\mathbf{H}^1} = \int_{\Omega} \mathbf{f}(\mathbf{x}) \cdot \mathbf{g}(\mathbf{x}) + \nabla \mathbf{f}(\mathbf{x}) : \nabla \mathbf{g}(\mathbf{x}) \, dA_{\mathbf{X}} \qquad (A.52)$$

The operator : denotes the twofold tensor contraction.

Hilbert spaces over the field $\mathbb{R}$ are isomorphic to their dual space. [Bronstein et al 2012, p.639]. This means, that the dual space of a Hilbert space is the Hilbert space itself with the same inner product and norm. The dual space V^* is the space of all continuous linear functionals $\varphi : V \to \mathbb{R}$. An example of a dual space would be the (finite dimensional) vector space of the contravariant vectors – the scalar product between co- and contravariant vectors yields a real number, an element of the field of the vector space. So, the contravariant vector can be seen as a continuous linear functional on the covariant vector. The set of all contravariant vectors would be the dual vectors space to the covariant vector space.

Riesz representation theorem

This connection between a Hilbert space V and it's dual space V^* by the inner product is ensured by Riesz representation theorem [Bronstein et al 2012, p.644]. The theorem states:

Let $(V, < \cdot, \cdot >)$ be a Hilbert space. Then, for each continuous linear map $l \in V^*$ with $l : V \to \mathbb{R}$, there is a $\mathbf{v}_l \in V$, such that $l(\mathbf{v}) = < \mathbf{v}_l, \mathbf{v} >$ for all $\mathbf{v} \in V$ and $\|l\|_{V \to \mathbb{R}} = \|\mathbf{v}_l\|_V$.

In orther words: Every linear continuous functional on a Hilbert space can be expressed by a scalar product. This theorem is very useful, because it states, that the coupling operator C of the Arlequin method can be expressed by a scalar product of the Hilbert space of the underlying function spaces.

All elements of Hilbert spaces must have finite norm [Dino Sejdinovic 2014, p.3], because otherwise, it would not be a normed space.

A.2 Newton's method

Discretization and derivation of equation 3.17 by the virtual degrees of freedom $\bar{v}_j^s$ leads to a system of $2N$ coupled, nonlinear equations:

$$\frac{\partial R}{\partial \bar{v}_j^s} \;=\; \frac{\partial R_i(\bar{u}_k^s)}{\partial \bar{v}_j^s} + \frac{\partial R_e}{\partial \bar{v}_j^s} \;=\; 0 \;\; , \;\; s = 1,2 \;\; , \;\; j = 1 \dots N \;\; , \;\; k = 1 \dots N \tag{A.53}$$

Every equation represents the equilibrium of outer and inner forces in either x_1 or x_2 direction in the nodes of the finite element mesh. The inner forces in the nodes are now a function of all the degrees of freedom $\bar{u}_k^s$. For simplification, the notation of A.53 is switched to a vector-one:

$$\mathbf{f} \;=\; \mathbf{f}_i(\bar{\mathbf{u}}) \,+\, \mathbf{f}_e \tag{A.54}$$

In general, no solution for this equation is available. An approximation to the solution can be computing a Taylor series expansion of A.54 and stoping after the linear term [Bronstein et al 2012, p.924].

$$\mathbf{f} : \mathbb{R}^{2N} \to \mathbb{R}^{2N}$$

$$\mathbf{f}(\bar{\mathbf{u}} + \mathbf{h}) \;=\; \mathbf{f}(\bar{\mathbf{u}}) \,+\, J(\bar{\mathbf{u}}) \cdot \mathbf{h} + \mathcal{O}(|\mathbf{h}|) \;\; , \;\; \bar{\mathbf{u}} \,, \mathbf{h} \in \mathbb{R}^{2N} \tag{A.55}$$

J denotes the Jacobian matrix.

$$J(\bar{\mathbf{u}}) \;=\; \begin{bmatrix} \dfrac{\partial R_1^1}{\partial \bar{u}_1^1} & \cdots & \dfrac{\partial R_1^1}{\partial \bar{u}_N^1} & \dfrac{\partial R_1^1}{\partial \bar{u}_1^2} & \cdots & \dfrac{\partial R_1^1}{\partial \bar{u}_N^2} \\[2mm] \vdots & \ddots & \vdots & \vdots & \ddots & \vdots \\[2mm] \dfrac{\partial R_N^1}{\partial \bar{u}_1^1} & \cdots & \dfrac{\partial R_N^1}{\partial \bar{u}_N^1} & \dfrac{\partial R_N^1}{\partial \bar{u}_1^2} & \cdots & \dfrac{\partial R_N^1}{\partial \bar{u}_N^2} \\[3mm] \dfrac{\partial R_1^2}{\partial \bar{u}_1^1} & \cdots & \dfrac{\partial R_1^1}{\partial \bar{u}_N^1} & \dfrac{\partial R_1^2}{\partial \bar{u}_1^2} & \cdots & \dfrac{\partial R_1^2}{\partial \bar{u}_N^2} \\[2mm] \vdots & \ddots & \vdots & \vdots & \ddots & \vdots \\[2mm] \dfrac{\partial R_N^2}{\partial \bar{u}_1^1} & \cdots & \dfrac{\partial R_N^1}{\partial \bar{u}_N^1} & \dfrac{\partial R_N^2}{\partial \bar{u}_1^2} & \cdots & \dfrac{\partial R_N^2}{\partial \bar{u}_N^2} \end{bmatrix} \tag{A.56}$$

Neglecting the terms of higher order leads to finding the roots of:

$$\mathbf{f}(\bar{\mathbf{u}}) \, + \, J(\bar{\mathbf{u}}) \cdot \mathbf{h} = \mathbf{0} \tag{A.57}$$

This expression can be seen as a fixpoint–iteration. At timestep n, it can be written as:

$$\mathbf{f}(\bar{\mathbf{u}}_n) \, + \, J(\bar{\mathbf{u}}_n) \cdot (\bar{\mathbf{u}}_{n+1} - \bar{\mathbf{u}}_n) = \mathbf{0} \tag{A.58}$$

Although direct computation of $\bar{\mathbf{u}}_{n+1}$ via inversion of $J(\bar{\mathbf{u}}_n)$ is possible, the numerical effort of solving the linear equation system below is lower.

$$J(\bar{\mathbf{u}}_n) \cdot \Delta\bar{\mathbf{u}} = -\mathbf{f}(\bar{\mathbf{u}}_n) \tag{A.59}$$

$\bar{\mathbf{u}}_{n+1}$ is obtained afterwards by

$$\bar{\mathbf{u}}_{n+1} = \bar{\mathbf{u}}_n + \Delta\bar{\mathbf{u}}$$

A.3 Numerical derivation with complex step derivative

The complex step derivative is a forward difference method using complex arithmetics in order to obtain a numerical first derivative of an analytic function $f(x)$, which is real valued for $x \in \mathbb{R}$ [Moler 2013]. It is obtained from a Taylor series expansion of f with an imaginary step $i\,h$:

$$f(x_0 + i\,h) \, = \, f(x_0) \, + \, f'(x_0)\,(i\,h) + \frac{1}{2}f''\,(i\,h)^2 + \frac{1}{6}f'''\,(i\,h)^3 \, + \, ... \tag{A.60}$$

Because $f(x) \in \mathbb{R}$ for $x \in \mathbb{R}$ holds, the expressions above containing uneven exponents of $(i\,h)$ are imaginary, whereas even exponents yield real - valued ones. Comparing the imaginary parts left and right of the equal sign yields an expression for the first derivative and terms of higher order:

$$\text{Im}\Big(f(x_0 + i\,h)\Big) \, = \, f'(x_0) \cdot h - \frac{1}{6}f'''\,h^3 \, + \, ... \tag{A.61}$$

Division by h and solving for f' provides an approximation of the first derivative:

$$f'(x_0) = \frac{\text{Im}\Big(f(x_0 + i\,h)\Big)}{h} + \mathcal{O}(h^2) \tag{A.62}$$

The complex step derivative has two advantages over forward differences; at first, the order of the error is $\mathcal{O}(h^2)$ for complex step derivative instead of $\mathcal{O}(h^1)$ for finite difference approximation [Bollhöfer and Mehrmann 2013, p.48]. Moreover, in order to obtain a good approximation of the first derivative with forward differences

$$\frac{f(x+h) - f(x)}{h}$$

a small h (up to machine precision) would be desirable. Then, the expression above is a difference of two large floating point numbers of approximately the same size, which will result in a loss of significant digits [Bollhöfer and Mehrmann 2013, p.37]. Thus, in a finite difference scheme, the step size h cannot be chosen arbitrarily small. As the derivative in the complex step algorithm is obtained by a quotient only (see eq. A.62), cancellation errors will not occur and a small step size up to machine precision is possible.

A.4 Numerical integration

A.4.1 Gauss-Legendre quadrature

Gauss-Legendre quadrature is based on approximating the integrand $f(t)$ between a and b by a polynomial $p(t)$.

$$\int_a^b f(t)dt \approx \int_a^b p(t)\,dt \tag{A.63}$$

The integral over $p(t)$ between a and b can be transformed to an integral between -1 and 1 by the following transformation [Simeon 2009, p.5]:

$$\begin{aligned} t = \psi(x) &= \frac{a+b}{2} + \frac{b-a}{2}x \\ \int_a^b p(t)\,dt &= \frac{b-a}{2}\int_{-1}^1 p\left(\frac{a+b}{2} + \frac{b-a}{2}x\right)dx \end{aligned} \tag{A.64}$$

Any integral over a polynomial $p(x)$ of order up to $2n-1$ is supposed to be equal to a sum n products of weights α_i and respective function evaluations of $f(x_i)$ respectively $p(x_i)$, where x_i denotes the support points of the quadrature. Thus $2n$ unknowns, n support points and n weights have to be determined.

$$\int_{-1}^1 p(x)\,dx \stackrel{!}{=} \sum_{i=1}^n p(x_i)\,\alpha_i \tag{A.65}$$

The key idea of Gauss-Legendre quadrature is picking the support points not "arbitrarily", but making use of two properties of Legendre polynomials P. First, a Legendre polynomial $P_{(n)}$ of order n has n real roots within [-1, 1]. Second, the first $n - 1$ Legendre polynomials $P_{(1)}$ ... $P_{(n-1)}$ can be considered as $n - 1$ orthogonal base vectors of the vector space of polynomials. $P_{(n)}$ is orthogonal to the first $n - 1$ Legendre polynomials. I.e. it holds:

$$\int_{-1}^{1} P_{(i)}(x) \, P_{(j)}(x) \, dx \;=\; \delta_{ij} \tag{A.66}$$

Suppose $p(x)$, the polynomial to be integrated from eq. A.65, be of order $2n - 1$. By polynomial division, it can be broken down in a product $q(x) L_{(n)}(x)$ and a remainder $r(x)$, where $q(x)$ and $r(x)$ are both of order $n - 1$. Replacing $p(x)$ in equation A.65 by this broken-down expression yields:

$$\int_{-1}^{1} p(x) \, dx \;=\; \int_{-1}^{1} q(x) P_{(n)}(x) \, dx \;+\; \int_{-1}^{1} r(x) \, dx \tag{A.67}$$

Remembering the orthogonality of Legendre polynomials, expression

$$\int_{-1}^{1} q(x) P_{(n)}(x) \, dx \;=\; 0 \tag{A.68}$$

must be zero, as $q(x)$ is of order $n - 1$ and thus built up from Legendre polynomials of maximum order $n - 1$. Thus, it holds [Gillow 2016, p.17]:

$$\int_{-1}^{1} p(x) \, dx \;=\; \overbrace{\int_{-1}^{1} q(x) P_{(n)}(x) \, dx}^{0} \;+\; \int_{-1}^{1} r(x) \, dx \tag{A.69}$$

Remaining is the integral over a polynomial $r(x)$ of order $n - 1$. Now, a quadrature of the right side of equation A.69 is demanded:

$$\overbrace{\int_{-1}^{1} q(x) P_{(n)}(x) \, dx}^{0} \;+\; \int_{-1}^{1} r(x) \, dx \;\overset{!}{=}\; \overbrace{\sum_{i=1}^{n} q(x_i) P_{(n)}(x_i) \, \alpha_i}^{0} \;+\; \sum_{i=1}^{n} r(x_i) \, \alpha_i \tag{A.70}$$

By choosing the support points x_i to be equal to the roots of the n'th Legendre polynomial, cancellation of the $q(x_i) P_{(n)}(x_i)$ is guaranteed. It remains equation

$$\int_{-1}^{1} r(x) \, dx \;\overset{!}{=}\; \sum_{i=1}^{n} r(x_i) \, \alpha_i \tag{A.71}$$

Expression A.71 is supposed to hold for arbitrary polynomials $r(x)$ up to order $n - 1$, thus also for $1, x, \ldots, x^{n-1}$. Computation of the weights α_i therefore is possible by e.g. inversion

of the Vandermonde matrix [Simeon 2009, p.10].

$$
\begin{bmatrix}
x_0^0 & x_1^0 & ... & x_{n-1}^0 \\
x_0^1 & x_1^1 & ... & x_{n-1}^1 \\
... & ... & ... & ... \\
x_0^{n-1} & x_1^{n-1} & ... & x_{n-1}^{n-1}
\end{bmatrix}
\begin{bmatrix}
\alpha_1 \\
\alpha_2 \\
... \\
\alpha_n
\end{bmatrix}
=
\begin{bmatrix}
\int_{-1}^1 x^0 dx \\
\int_{-1}^1 x^1 dx \\
... \\
\int_{-1}^1 x^{n-1} dx
\end{bmatrix}
\tag{A.72}
$$

Furthermore, the choice of the support points being the roots of the Legendre polynomial makes the following expression hold:

$$
\int_{-1}^1 p(x)\, dx = \sum_{i=1}^n q(x_i) P_{(n)}(x_i)\, \alpha_i + \sum_{i=1}^n r(x_i)\, \alpha_i
\tag{A.73}
$$

Remembering the claim from expression A.65 thus provides:

$$
\sum_{i=1}^n p(x_i)\, \alpha_i = \int_{-1}^1 p(x)\, dx = \sum_{i=1}^n r(x_i)\, \alpha_i
\tag{A.74}
$$

If an integration of $p(x)$ in terms of n summations exists, then it must be equal to the quadrature of the remainder $r(x)$. As it was shown, that the quadrature of the remainder equals the analytical evaluation of the integral of $q(x)$, the quadrature of $p(x)$ equals its analytical evaluation. Thus, the integral over the $2n-1$ polynomial $p(x)$ can be expressed exactly by a sum of n products of evaluations of $p(x_i)$ at the roots of the n'th Legendre polynomial and the weights computed from eq. A.72.

One concluding remarks about Gaussian quadrature. Despite its excellent capabilities of integrating polynomials, it relies on the requirement that $f(x)$ from equation A.63 can be approximated sufficiently by a polynomial of order $2n-1$. If $f(x)$ is not continuous, e.g. because it was truncated by a peridynamic horizon, a large number of Legendre-polynomial roots and thus Legendre polynomials of high order will be necessary in order to approximate the discontinuous function adequately. Therefore, direct application of Gauss quadrature may produce poor results, and a subdivision of the integrand into continuous subsections could turn out to be more efficient than increasing the number of quadrature points.

A.4.2 tanh-sinh quadrature of the middle element

tanh-sinh quadrature is an alternative numerical quadrature invented 1974 by Hidetosi Takahasi and Masatake Mori [Takahasi and Mori 1974], which is able to yield reliable results for integrands with endpoint-singularities [Bailey 2006, p.1]. It does not rely on polynomial fit-

ting of the integrand like e.g. Gauss-Legendre quadrature [Takahasi and Mori 1974, p.722], but utilizes the fact, "that for certain bell-shaped integrands, approximating the integral by a simple step-function summation is remarkably accurate" [Bailey 2006, p.1].

The effect of the tanh-sinh-quadrature is based on integration by substitution:

$$I \; = \; \int_{-1}^{1} f(x)\, dx \; = \; \int_{a}^{b} f(\psi(t))\, \psi'(t)\, dt \tag{A.75}$$

Replacing x by $\psi(t)$ introduces a multiplication of the former integrand with $\psi'(t)$. If $\psi'(t)$ was decaying strong enough to 0 with increasing t respectively $-t$, it is possible to bring the integrand $f(\psi(t))\,\psi'(t)$ into a smooth bell-shaped form. The transformation rule of the tanh-sinh quadrature inherits this property:

$$\begin{aligned} \psi(t) \; &= \; \tanh(\lambda\, \sinh(t)) \\ \psi'(t) \; &= \; \frac{\lambda \cosh(t)}{\cosh^2(\lambda\, \sinh(t))} \\ \text{with}\, \lambda \; &= \; \frac{\pi}{2} \end{aligned} \tag{A.76}$$

Both functions ψ and ψ' are depicted in figure A.9:
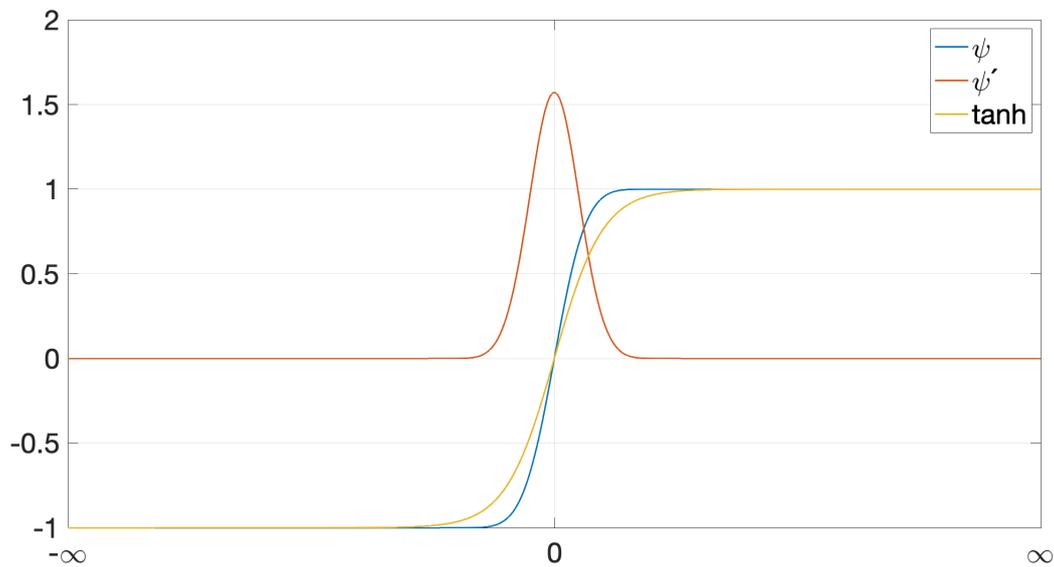
**Figure A.9:** ψ,ψ' and $\tanh$ for comparison

The smooth, bell like shape of the orange $\psi'(t)$ is obvious. Multiplying $f(\psi(t))$ with this function can be interpreted as applying a bell-shaped filter upon the integrand. To examine

it's decay rate, $\psi'(t)$ is rewritten in terms of exponential functions:

$$\frac{\lambda \cosh(t)}{\cosh^2(\lambda \sinh(t))} = \frac{\frac{\pi}{2} \cosh(t)}{\cosh^2(\frac{\pi}{2} \sinh(t))} = \frac{\pi (e^{-t} + e^t)}{\left(e^{-\frac{\pi}{4}(e^t - e^{-t})} + e^{\frac{\pi}{4}(e^t - e^{-t})}\right)^2} \tag{A.77}$$

For $|t|$ large enough, the components e^{-t} in equation eq. A.77 can be neglected, such that the following proportionality holds:

$$\psi'(t) \sim \frac{\pi e^t}{e^{\frac{1}{2}\pi e^t}} \approx e^{-\frac{\pi}{2} e^t} \tag{A.78}$$

Due to this double-exponential decay of $\psi'(t)$ for large $|t|$, most singularities and infinite derivatives at the ends of the integration domain are effectively suppressed, even rendering the complete integrand $f(\psi(t))\,\psi'(t)$ decaying with double-exponential rate [Ye 2006, p.24]

Depicted in blue is $\psi(t)$. The $\tanh(t)$ - function in yellow, quickly approaching its asymptotes $1/-1$ itself, serves as comparison, pointing out the even faster convergence of $\psi(t)$. From the definition of the substitution (eq. A.75), the limits of the substituted integral can be computed. It must hold:

$$\begin{aligned} +1 &\stackrel{!}{=} \psi(a) \\ -1 &\stackrel{!}{=} \psi(b) \end{aligned} \tag{A.79}$$

Solving for a and b is done by the inverse of ψ:

$$\begin{aligned} a &= \lim_{p \to -1} \psi^{-1}(p) = \lim_{p \to -1} \operatorname{arcsinh}(\frac{1}{\lambda} \operatorname{arctanh}(p)) \\ b &= \lim_{p \to +1} \psi^{-1}(p) = \lim_{p \to +1} \operatorname{arcsinh}(\frac{1}{\lambda} \operatorname{arctanh}(p)) \end{aligned} \tag{A.80}$$

The arctanh - function can be expressed by the ln - function [Rade and Westergren 2013, p.121]:

$$\operatorname{arctanh}(p) = \frac{1}{2} \ln \frac{1+p}{1-p} \tag{A.81}$$

With the asymptotic behavior of the ln - function

$$\begin{aligned} \lim_{p \to -1} \ln \frac{1+p}{1-p} &= -\infty \\ \lim_{p \to +1} \ln \frac{1+p}{1-p} &= +\infty \end{aligned} \tag{A.82}$$
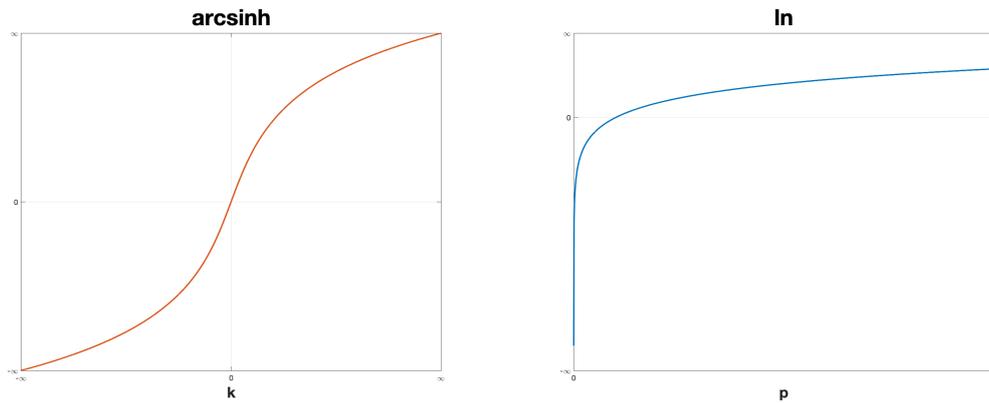
Figure A.10: $\operatorname{arcsinh}(k)$ and $\ln(p)$

and the plot of the arcsinh- function in fig. A.10, the values for a and b can be derived:

$$
\begin{aligned}
a &= \lim_{p \to -1} \psi^{-1}(p) = \lim_{p \to -1} \operatorname{arcsinh}(\frac{1}{2\lambda} \ln \frac{1+p}{1-p}) = +\infty \\
b &= \lim_{p \to +1} \psi^{-1}(p) = \lim_{p \to +1} \operatorname{arcsinh}(\frac{1}{2\lambda} \ln \frac{1+p}{1-p}) = -\infty
\end{aligned}
\tag{A.83}
$$

So, the tanh-sinh quadrature maps the original interval $[-1, 1]$ to the interval $(-\infty, \infty)$. Up to now, it has been explained that regions close to the interval ends, which are possibly blowing up into singularities, are multiplied with the double-exponentially decreasing ψ' and therefore suppressed by the faster decrease rate of ψ'. Yet, the discretization of the integrand $f(\psi(t))\,\psi'(t)$ has to be examined.

The Euler Maclaurin Summation formula is an asymptotic error analysis for the trapezoidal rule [Ata and Sahin 2018, p.30], expressing the error induced by the approximation of an integral via trapezoidal rule by the derivatives of the integrand at the beginning and end of the interval $[a, b]$: [Abramowitz and Stegun 1948, p.16]. It is defined:

$$
\begin{aligned}
h &= \frac{b - a}{N - 1} \\
x_i &= a + (i - 1)\,h \quad, \quad i \in [1, N]
\end{aligned}
\tag{A.84}
$$

$$\int_a^b f(x)\,dx = \frac{h}{2}f(x_1) + h\sum_{k=2}^{N-1} f(x_k) + \frac{h}{2}f(x_N) +$$

$$+\ \frac{h^2}{2\cdot 3!}[\,f'(x_1) - f'(x_N)\,] -$$

$$-\ \frac{h^4}{6\cdot 5!}[\,f'''(x_1) - f'''(x_N)\,] +$$

$$+\ \frac{h^6}{30\cdot 7!}[\,f^{(V)}(x_1) - f^{(V)}(x_N)\,] -$$

$$-\ ...$$

(A.85)

In the scope of the tanh-sinh quadrature, the domain of integration $(-\infty,\,\infty)$ is discretized with N equidistantly distributed support points. Although the asymptotic expansion in A.85 is usually not convergent, the integrand $f(\psi(t))\,\psi'(t)$ is decaying double-exponentially, such that the error terms in A.85, consisting of exactly those endpoint derivatives, become extraordinary small and therefore can be omitted. Thus, it can be concluded that a bell shaped integrand can be approximated extraordinary exactly by the trapezoidal rule. A more detailed examination of the tanh-sinh quadrature and it's mechanism can be found in [Takahasi and Mori 1974], [Vanherck et al 2020] and [Ye 2006].

The discretization of integral eq. A.75 necessitates to approximate the infinite domain $(-\infty,\infty)$ by a finite window $[-n\cdot h, n\cdot h]$. Again, due to the bell-shape of $\psi'(t)$, a relatively small number n leads to remarkable precision.

$$\int_{-1}^{1} f(x)\,dx = \int_{-\infty}^{\infty} f(\psi(t))\,\psi'(t)\,dt \approx \sum_{j=-n}^{n} f(x_j)\,w_j$$

(A.86)

with

$$N = (2n+1)$$
$$t_j = j\,h$$

(A.87)

and the abscissas and weights:

$$x_j = \psi(t_j) = \tanh(\frac{1}{2}\,\pi\,\sinh(j\,h)\,)$$

$$w_j = \psi'(t_j) = \frac{\frac{1}{2}\,h\,\pi\,\cosh(j\,h)}{\cosh(\frac{1}{2}\,\pi\,\sinh(j\,h)\,)^2}$$

(A.88)

Due to the map $x_j = \psi(t_j)$, the support points in the x-domain are not distributed equidis-

tant, but concentrated close to the ends of the integration domain. The discretization of $(-\infty, \infty)$ by the finite window $[-t_n, t_n]$ introduces a truncation error [Vanherck et al 2020, p.3] additionally to a discretization error. Yet, according to [Vanherck et al 2020, p.3], the choice of ψ and ψ' above yields the optimal choice of the transformation, as an even faster decay would lead to a higher discretization error, while a slower decay would introduce higher truncation errors.

Implementation

In the beginning, neither the necessary length of the window $[-n \cdot h, n \cdot h]$, nor the necessary interval length h are known. Therefore, the algorithm works iteratively, approximating the value of the integral I by a series I_k. At first, four parameters have to be defined, compare [emece67 2017]:

1. ϵ_w: This threshold is the smallest value the "weights" of the tanh-sinh-quadrature, $\psi'(t)$, are allowed to be. Usually, it is set to the current machine precision. This prevents the case that $\psi'(t)$ becomes indistinguishable from 0 for the machine.

2. $|\epsilon_{Abz}|$: This threshold is the largest value allowed for the abszissas $\psi(t)$, for example $1 - eps$, with eps being the machine precision. This threshold prevents the abszissas to become numerically 1 and therefore prevents evaluation of the integrand at a singularity.

3. k_{max}: The maximum number of levels of iteration k.

4. ϵ_I: If $|I_{k-1} - I_k| \leq \epsilon_I$, the iteration stops.

In every iteration level k, the interval length h in the t domain is halved. Afterwards, with progressing counter ii, the t-axis is developed with more and more subintervals of length h until either the respective weights $\psi'(ii \cdot h)$ become too small or the abszissas $\psi(ii \cdot h)$ become 1. The iteration kk stops as soon as the difference between two successive I_{kk} becomes smaller than the defined threshold ϵ_I or the maximum number of iterations is reached.

One potential pitfall regarding Peridynamics has to be mentioned. The size of material parameters c in the scope of this work is in the order of magnitude of 10^{10}. The integrand f, involving a product with c and expressed by the data type double, has therefore already used up 10 of the 16 digits available. Because of that, the accuracy of a double might not be sufficient to resolve the threshold ϵ_I, at least not for ϵ_I being close to eps. Therefore, the multiplication with c should be done after the tanh-sinh- quadrature has converged.

Algorithm 1: tanh-sinh quadrature

---

initialization;

$I_0 = 0$

for $k = 1{:}1{:}k_{max}$ **do**

    $h = \frac{1}{2^k}$

    $ii = 1$

    $a_{ii} = 0$

    $w_{ii} = 1$

    $I_k = 0$

    while $a_{ii} \leq (1 - eps)$ *&* $w_{ii} > \epsilon_w$ **do**

        if $ii = 1$ **then**

            $w_{ii} = (h\,\pi\,\cosh((ii - 1) \cdot h)) / (2\cosh\left(\frac{\pi}{2}\sinh(h \cdot (ii - 1))^2\right))$;

            $a_{ii} = \tanh\left(\frac{\pi}{2}\sinh\left(h \cdot (ii - 1)\right)\right)$;

            $I_k = f(a_{ii}) \cdot w_{ii}$;

            ii = ii + 1;

        else

            $w_{ii} = (h\,\pi\,\cosh((ii - 1) \cdot h)) / (2\cosh\left(\frac{\pi}{2}\sinh(h \cdot (ii - 1))^2\right))$;

            $a_{ii_1} = \tanh\left(\frac{\pi}{2}\sinh\left(h \cdot (ii - 1)\right)\right)$;

            $a_{ii_2} = \tanh\left(\frac{\pi}{2}\sinh\left(-h \cdot (ii - 1)\right)\right)$;

            $I_k = I_k + (f(a_{ii_1}) + f(a_{ii_2})) \cdot w_{ii}$;

            ii = ii + 1

        if $|I_k - I_{k-1}| \leq \epsilon_I$ **then**

            break **while**

            break **for**

A.5 Bilinear approach functions

Considered is a meshgrid built from quadrilateral, four-node elements. The meshgrid consists of M finite element nodes. The approximated displacement field $\mathbf{U}^h$ can be expressed by the finite sum

$$\mathbf{u}^h(\mathbf{X}) = \tilde{\mathbf{u}}^h(\mathbf{X}) + \sum_{n=1}^{M} \mathbf{A}_n(\mathbf{X}) \cdot \bar{\mathbf{u}}_n$$

with $\tilde{\mathbf{u}}^h(\mathbf{X})$ being a constant displacement field fulfilling potential Dirichlet boundary conditions, $\mathbf{A}_n(\mathbf{X})$ being the matrix of approach functions and $\bar{\mathbf{u}}_n$ being the displacements of node n.

The matrix $\mathbf{A}_n(\mathbf{X})$ is given by:

$$\mathbf{A}_n(\mathbf{X}) = \begin{bmatrix} \bar{N}_n(X^1)\bar{N}_n(X^2) & 0 \\ 0 & \bar{N}_n(X^1)\bar{N}_n(X^2)) \end{bmatrix}$$

The one-dimensional approach functions (on global level) $\bar{N}_n(X^1)$ is defined as:

$$\bar{N}_n(X^1) = \begin{cases} +\dfrac{1}{\Delta}\left(X^1 - X_n^1\right) + 1 & \text{for } X_n^1 - \Delta \leq X^1 \leq X_n^1 \\ -\dfrac{1}{\Delta}\left(X^1 - X_n^1\right) + 1 & \text{for } X_n^1 < X^1 \leq X_n^1 + \Delta \\ 0 & \text{else} \end{cases}$$

(The function $\bar{N}_n(X^2)$ would be defined analogously by replacing X^1 by X^2). A global approach function $\bar{N}(X^1,X^2)$ is generated by a product of $\bar{N}_n(X^1)$ and $\bar{N}_n(X^2)$. Because $\bar{N}(X^1$ is defined piecewise, $\bar{N}(X^1,X^2)$ is defined piecewise as well:

$$\bar{N}_n(X^1, X^2) = \begin{cases} \left[\dfrac{1}{\Delta}(X^1 - X_n^1) + 1\right]\left[\dfrac{1}{\Delta}(X^2 - X_n^2) + 1\right] & \text{for}\left[X_n^1 - \Delta \leq X^1 \leq X_n^1\right]\wedge \\ & \left[X_n^2 - \Delta \leq X^2 \leq X_n^2\right] \\ \left[-\dfrac{1}{\Delta}(X^1 - X_n^1) + 1\right]\left[\dfrac{1}{\Delta}(X^2 - X_n^2) + 1\right] & \text{for}\left[X_n^1 < X^1 \leq X_n^1 + \Delta\right]\wedge \\ & \left[X_n^2 - \Delta \leq X^2 \leq X_n^2\right] \\ \left[\dfrac{1}{\Delta}(X^1 - X_n^1) + 1\right]\left[-\dfrac{1}{\Delta}(X^2 - X_n^2) + 1\right] & \text{for}\left[X_n^1 - \Delta \leq X^1 \leq X_n^1\right]\wedge \\ & \left[X_n^2 < X^2 \leq X_n^2 + \Delta\right] \\ \left[-\dfrac{1}{\Delta}(X^1 - X_n^1) + 1\right]\left[-\dfrac{1}{\Delta}(X^2 - X_n^2) + 1\right] & \text{for}\left[X_n^1 < X^1 \leq X_n^1 + \Delta\right]\wedge \\ & \left[X_n^2 < X^2 \leq X_n^2 + \Delta\right] \\ 0 & \text{else} \end{cases}$$

$$\tag{A.89}$$

The derivatives of $\bar{N}_n(X^1, X^2)$ w.r.t. X^1 and X^2 are given by:

$$\frac{\partial \bar{N}_n}{\partial X^1} = \begin{cases} \frac{1}{\Delta}\left[\frac{1}{\Delta}(X^2 - X_n^2) + 1\right] & \text{for}\left[X_n^1 - \Delta < X^1 < X_n^1\right] \wedge \\ & \qquad\qquad \left[X_n^2 - \Delta < X^2 < X_n^2\right] \\ -\frac{1}{\Delta}\left[\frac{1}{\Delta}(X^2 - X_n^2) + 1\right] & \text{for}\left[X_n^1 < X^1 < X_n^1 + \Delta\right] \wedge \\ & \qquad\qquad \left[X_n^2 - \Delta < X^2 < X_n^2\right] \\ \frac{1}{\Delta}\left[-\frac{1}{\Delta}(X^2 - X_n^2) + 1\right] & \text{for}\left[X_n^1 - \Delta < X^1 < X_n^1\right] \wedge \\ & \qquad\qquad \left[X_n^2 < X^2 < X_n^2 + \Delta\right] \\ -\frac{1}{\Delta}\left[-\frac{1}{\Delta}(X^2 - X_n^2) + 1\right] & \text{for}\left[X_n^1 < X^1 < X_n^1 + \Delta\right] \wedge \\ & \qquad\qquad \left[X_n^2 < X^2 < X_n^2 + \Delta\right] \\ 0 & \text{else} \end{cases} \qquad (\text{A.90})$$

and

$$\frac{\partial \bar{N}_n}{\partial X^2} = \begin{cases} \left[\frac{1}{\Delta}(X^1 - X_n^1) + 1\right]\frac{1}{\Delta} & \text{for}\left[X_n^1 - \Delta < X^1 < X_n^1\right] \wedge \\ & \qquad\qquad \left[X_n^2 - \Delta < X^2 < X_n^2\right] \\ \left[-\frac{1}{\Delta}(X^1 - X_n^1) + 1\right]\frac{1}{\Delta} & \text{for}\left[X_n^1 < X^1 < X_n^1 + \Delta\right] \wedge \\ & \qquad\qquad \left[X_n^2 - \Delta < X^2 < X_n^2\right] \\ \left[\frac{1}{\Delta}(X^1 - X_n^1) + 1\right]\left[-\frac{1}{\Delta}\right] & \text{for}\left[X_n^1 - \Delta < X^1 < X_n^1\right] \wedge \\ & \qquad\qquad \left[X_n^2 < X^2 < X_n^2 + \Delta\right] \\ \left[-\frac{1}{\Delta}(X^1 - X_n^1) + 1\right]\left[-\frac{1}{\Delta}\right] & \text{for}\left[X_n^1 < X^1 < X_n^1 + \Delta\right] \wedge \\ & \qquad\qquad \left[X_n^2 < X^2 < X_n^2 + \Delta\right] \\ 0 & \text{else} \end{cases} \qquad (\text{A.91})$$

Because those derivatives have to be understood in a weak sense, thus no derivative is defined in the nodes $\mathbf{X}_n$, the $\leq$ have been replaced by $<$ in eq. A.90 and eq. A.91.

A.6 Differentiation of nodal force

Deriving an internal nodal force by a degree of freedom yields the respective entry of the Jacobian matrix. The omitted steps in subsection 3.1.5 are written down below:

$$J_{17} = \frac{\partial R_1^1}{\partial \bar{u}_3^2} = \iint\limits_{\Omega^0} \iint\limits_{\Omega^0 \cap D_{\mathbf{X}}} (N_1(\mathbf{Y}) - N_1(\mathbf{X})) \frac{\partial f^1}{\partial \bar{u}_3^2} \, dA_Y \, dA_X =$$

$$= \iint\limits_{\Omega^0} \iint\limits_{\Omega^0 \cap D_{\mathbf{X}}} \left(N_1(\mathbf{Y}) - N_1(\mathbf{X})\right) \left(\frac{1}{L} \frac{l^1 \, l^2}{(l)^2}(N_3(\mathbf{Y}) - N_3(\mathbf{X})) - \epsilon \frac{l^1 \, l^2}{(l)^3}(N_3(\mathbf{Y}) - N_3(\mathbf{X}))\right) dA_Y \, dA_X =$$

$$= \iint\limits_{\Omega^0} \iint\limits_{\Omega^0 \cap D_{\mathbf{X}}} \left(\frac{1}{L} \frac{l^1 \, l^2}{(l)^2} - \epsilon \frac{l^1 \, l^2}{(l)^3}\right) \left(N_1(\mathbf{Y}) - N_1(\mathbf{X})\right) \left(N_3(\mathbf{Y}) - N_3(\mathbf{X})\right) dA_Y \, dA_X$$

$$(A.92)$$

A.7 4 - node quadrilateral CCM - elements

The stiffness matrix of a 4-node plane stress element is taken from [Ye]. (The order of the dofs in [Ye] was rearranged in order to fit the order of the local dofs in this thesis).

$$
\begin{bmatrix} r_1^1 \\ r_2^1 \\ r_3^1 \\ r_4^1 \\ r_1^2 \\ r_2^2 \\ r_3^2 \\ r_4^2 \end{bmatrix} =
\begin{bmatrix}
C_1 & & & & & & & \\
C_4 & C_1 & & & & \text{sym.} & & \\
C_7 & -\frac{C_1}{C_2} & C_1 & & & & & \\
-\frac{C_1}{C_2} & C_7 & C_4 & C_1 & & & & \\
C_2 & -C_5 & C_5 & -C_2 & C_3 & & & \\
C_5 & -C_2 & C_2 & -C_5 & C_6 & C_3 & & \\
-C_5 & C_2 & -C_2 & C_5 & C_8 & -\frac{C_3}{C_2} & C_3 & \\
-C_2 & C_5 & -C_5 & C_2 & -\frac{C_3}{C_2} & C_8 & C_6 & C_3
\end{bmatrix}
\begin{bmatrix} u_1^1 \\ u_2^1 \\ u_3^1 \\ u_4^1 \\ u_1^2 \\ u_2^2 \\ u_3^2 \\ u_4^2 \end{bmatrix}
\qquad (A.93)
$$

with

$$C_1 = \left(\frac{b}{3a} + \frac{1-\nu}{6} \frac{a}{b} \right) \left(\frac{E\,t}{1-\nu^2} \right)$$

$$C_2 = \left(\frac{\nu}{4} + \frac{1-\nu}{8} \right) \left(\frac{E\,t}{1-\nu^2} \right)$$

$$C_3 = \left(\frac{a}{3b} + \frac{1-\nu}{6} \frac{b}{a} \right) \left(\frac{E\,t}{1-\nu^2} \right)$$

$$C_4 = \left(-\frac{b}{3a} + \frac{1-\nu}{12} \frac{a}{b} \right) \left(\frac{E\,t}{1-\nu^2} \right)$$

$$C_5 = \left(\frac{\nu}{4} - \frac{1-\nu}{8} \right) \left(\frac{E\,t}{1-\nu^2} \right) \tag{A.94}$$

$$C_6 = \left(\frac{a}{6b} - \frac{1-\nu}{6} \frac{b}{a} \right) \left(\frac{E\,t}{1-\nu^2} \right)$$

$$C_7 = \left(\frac{b}{6a} - \frac{1-\nu}{6} \frac{a}{b} \right) \left(\frac{E\,t}{1-\nu^2} \right)$$

$$C_8 = \left(-\frac{a}{3b} + \frac{1-\nu}{12} \frac{b}{a} \right) \left(\frac{E\,t}{1-\nu^2} \right)$$

where t denotes the thickness, a the length and b the height of the element.

A.8 Plane stress- and plane strain relations

The connections between stresses and strains in Voigt notation for plane stress and plane strain are given by:

Plane stress

$$\begin{bmatrix} \sigma_{11} \\ \sigma_{22} \\ \sigma_{12} \end{bmatrix} = \frac{E}{1-\nu^2} \begin{bmatrix} 1 & \nu & 0 \\ \nu & 1 & 0 \\ 0 & 0 & \frac{1}{2}(1-2\nu) \end{bmatrix} \begin{bmatrix} \epsilon^{11} \\ \epsilon^{22} \\ 2\epsilon^{12} \end{bmatrix} \tag{A.95}$$

Plane strain

$$\begin{bmatrix} \sigma_{11} \\ \sigma_{22} \\ \sigma_{12} \end{bmatrix} = \frac{E}{(1+\nu)(1-2\nu)} \begin{bmatrix} 1 & \nu & 0 \\ \nu & 1 & 0 \\ 0 & 0 & \frac{1}{2}(1-2\nu) \end{bmatrix} \begin{bmatrix} \epsilon^{11} \\ \epsilon^{22} \\ 2\epsilon^{12} \end{bmatrix} \tag{A.96}$$

Bibliography

[Abramowitz and Stegun 1948]   ABRAMOWITZ, Milton ; STEGUN, Irene A.: *Handbook of mathematical functions with formulas, graphs, and mathematical tables.* Volume 55. US Government printing office, 1948

[Ascher and Petzold 1998]   ASCHER, Uri M. ; PETZOLD, Linda R.: *Computer methods for ordinary differential equations and differential-algebraic equations.* Volume 61. Siam, 1998

[Ata and Sahin 2018]   ATA, Kayhan ; SAHIN, Mehmet: An integral equation approach for the solution of the Stokes flow with Hermite surfaces. In: *Engineering Analysis with Boundary Elements* 96 (2018), p. 14–22

[Axthelm 2020]   AXTHELM, Rebekka: *Numerik für Ingenieure.* 2020. – URL `http://axtr.xthelm.de/Lehre/MNEU/Unterlagen/skript_mneu.pdf`. – Zürcher Hochschule für Angewandte Wissenschaften, retrieved on [21.05.2021]

[Bailey 2006]   BAILEY, David H.: Tanh-sinh high-precision quadrature. (2006). – URL `https://www.davidhbailey.com/dhbpapers/dhb-tanh-sinh.pdf`. – davidhbailey.com, retrieved on [21.05.2021]

[Becker 2011]   BECKER, Moritz: *Balkentheorien nach Bernoulli und Timoshenko.* Lehrstuhl für Baumechanik, Arcisstraße 21, 80333 München, Technische Universität München, Lehrstuhl für Baumechanik, Master thesis, april 2011

[Bobaru et al 2016]   BOBARU, Florin ; FOSTER, John T. ; GEUBELLE, Philippe H. ; SILLING, Stewart A.: *Handbook of peridynamic modeling.* CRC press, 2016

[Bode et al 2020]   BODE, T ; WEISSENFELS, C ; WRIGGERS, P: Peridynamic Petrov–Galerkin method: a generalization of the peridynamic theory of correspondence materials. In: *Computer Methods in Applied Mechanics and Engineering* 358 (2020), p. 112636

[Bollhöfer and Mehrmann 2013]   BOLLHÖFER, Matthias ; MEHRMANN, Volker: *Numerische Mathematik: Eine projektorientierte Einführung für Ingenieure, Mathematiker und Naturwissenschaftler.* Springer-Verlag, 2013

[Bower 2008]   BOWER, Allan F.: *Analytical techniques and solutions for linear elastic solids.* 2008. – URL `http://solidmechanics.org/text/Chapter5_2/Chapter5_2.htm`. – solidmechanics.org, retrieved on [21.05.2021]

[Bronstein et al 2012]   BRONSTEIN, Ilja N. ; HROMKOVIC, Juraj ; LUDERER, Bernd ; SCHWARZ, Hans-Rudolf ; BLATH, Jochen ; SCHIED, Alexander ; DEMPE, Stephan ; WANKA, Gert ; GOTTWALD, Siegfried: *Taschenbuch der Mathematik.* Volume 1. Springer-Verlag, 2012

[Chen and Gunzburger 2011]   CHEN, Xi ; GUNZBURGER, Max: Continuous and discontinuous finite element methods for a peridynamics model of mechanics. In: *Computer Methods in Applied Mechanics and Engineering* 200 (2011), Nr. 9-12, p. 1237–1250

[Dang and Meguid 2010]   DANG, Hoang K. ; MEGUID, Mohamed A.: Evaluating the performance of an explicit dynamic relaxation technique in analyzing non-linear geotechnical engineering problems. In: *Computers and Geotechnics* 37 (2010), Nr. 1-2, p. 125–131

[Dhia 1998]   DHIA, Hachmi B.: Multiscale mechanical problems: the Arlequin method. In: *Comptes Rendus de l'Academie des Sciences Series IIB Mechanics Physics Astronomy* 12 (1998), Nr. 326, p. 899–904

[Dhia 2008]   DHIA, Hachmi B.: Further insights by theoretical investigations of the multiscale Arlequin method. In: *International Journal for Multiscale Computational Engineering* 6 (2008), Nr. 3

[Dhia and Rateau 2005]   DHIA, Hashmi B. ; RATEAU, Guillaume: The Arlequin method as a flexible engineering design tool. In: *International journal for numerical methods in engineering* 62 (2005), Nr. 11, p. 1442–1462

[Dino Sejdinovic 2014]   DINO SEJDINOVIC, Arthur G.:   What is an RKHS.   In: *Lecture Notes*   (2014). –   URL https://www.gatsby.ucl.ac.uk/~gretton/coursefiles/RKHS_Notes1.pdf. – Gatsby Computational Neuroscience Unit, retrieved on [21.05.2021]

[Dong et al 2020]   DONG, Yijia ; SU, Chao ; QIAO, Pizhong: A stability-enhanced peridynamic element to couple non-ordinary state-based peridynamics with finite element method for fracture analysis. In: *Finite Elements in Analysis and Design* 181 (2020), p. 103480

[emece67 2017]   EMECE67: *The Tanh-Sinh quadrature.* The Museum of HP Calculators. january 2017. – URL https://www.hpmuseum.org/forum/thread-7690.html. – retrieved on [21.05.2021]

[Fernier et al 2017]   FERNIER, Alexandre ; FAUCHER, Vincent ; JAMOND, Olivier: Multi model arlequin method for fast transient dynamics in explicit time integration. In: *13e colloque national en calcul des structures*, 2017

[Fries et al 2013]   FRIES, Thomas-Peter ; BAYDOUN, Malak ; WEBER, Nikolai: 3d crack propagation with the xfem and a hybrid explicit-implicit crack description. In: *International Conference on Extended Finite Element Methods XFEM*, 2013

[Gerstle 2015]   GERSTLE, Walter H.: *Introduction to practical peridynamics: computational solid mechanics without stress and strain.* Volume 1. World Scientific Publishing Company, 2015

[Gillow 2016]   GILLOW, Kathryn: *Quadrature.* University of Oxford, Mathematical Institute, Practical Numerical Analysis (2016-2017). 2016. – URL https://courses.maths.ox.ac.uk/node/371/materials. – retrieved on [21.05.2021]

[Glaws 2014]   GLAWS, Andrew T.: *Finite element simulations of two dimensional peridy-namic models*, Virginia Tech, Master thesis, 2014

[Guidault and Belytschko 2007]   GUIDAULT, P-A ; BELYTSCHKO, Ted: On the L2 and the H1 couplings for an overlapping domain decomposition method using Lagrange multipliers. In: *International journal for numerical methods in engineering* 70 (2007), Nr. 3, p. 322–350

[Gálvez et al 1998]   GÁLVEZ, J. C. ; CENDÓN, D. A. ; PLANAS, J. ; GUINEA, G. V. ; ELICES, M.: Fracture of concrete under mixed loading-experimental results and numerical prediction. In: *Proceedings of FRAMCOS* Volume 3, 1998, p. 729–738

[Hackenberg 2017]   HACKENBERG, Manuela: *A Coupled Integral Transform Method - Finite Element Method Approach to Model the Soil-Structure-Interaction*, Technische Universität München - Lehrstuhl für Baumechanik, Ph.D. thesis, 2017

[Hartmann 2008]   HARTMANN, Ralf: *Numerical analysis of higher order discontinuous Galerkin finite element methods.* Institute of Aerodynamics and Flow Technology, DLR (German Aerospace Center). 2008. – URL `https://elib.dlr.de/57074/1/Har08b.pdf`. – retrieved on [21.05.2021]

[Herzog 2013]   HERZOG, R: Skript zur Vorlesung Einführung in Sobolevräume. (2013). – URL `https://www.tu-chemnitz.de/mathematik/part_dgl/teaching/SS2014_Numerik_von_PDEs/Skript_Sobolevräume.pdf`. – Technische Universität Chemnitz, Professur Numerische Mathematik, retrieved on [21.05.2021]

[Huang et al 2019]   HUANG, Xiaohua ; BIE, Zhiwu ; WANG, Lifeng ; JIN, Yanli ; LIU, Xuefeng ; SU, Guoshao ; HE, Xiaoqiao: Finite element method of bond-based peridynamics and its ABAQUS implementation. In: *Engineering Fracture Mechanics* 206 (2019), p. 408–426

[John 2009]   JOHN, Volker: *Numerik partieller Differentialgleichungen - eine elementare Einführung.* Weierstraß-Institutfür Angewandte Analysis und Stochastik. 2009. – URL `https://www.wias-berlin.de/people/john/LEHRE/NUM_KONV_PROB/num_konv_prob_4.pdf`. – retrieved on [21.05.2021]

[Kilic and Madenci 2010]   KILIC, B. ; MADENCI, Erdogan: An adaptive dynamic relaxation method for quasi-static simulations using the peridynamic theory. In: *Theoretical and Applied Fracture Mechanics* 53 (2010), Nr. 3, p. 194–204

[Klingbeil 1966]   KLINGBEIL, Eberhard: *Tensorrechnung für Ingenieure.* Volume 197. Bibliographisches Institut, Hochschultaschenbücher-Verlag, 1966

[Littlewood et al 2014]   LITTLEWOOD, David J. ; SILLING, Stewart A. ; SELESON, Pablo D. ; MITCHELL, John A.: Integrating Meshfree Peridynamic Models with Classical Finite Element Analysis. / Sandia National Lab.(SNL-NM), Albuquerque, NM (United States). 2014. – Research Report

[Madenci and Oterkus 2014]   MADENCI, Erdogan ; OTERKUS, Erkan: Peridynamic theory. In: *Peridynamic Theory and Its Applications.* Springer, 2014

[Mehlhorn 1996a]   MEHLHORN, G: *Der Ingenieurbau: Baustatik, Baudynamik.* Ernst & Sohn, Berlin, 1996 (BOOK)

[Mehlhorn 1996b]   MEHLHORN, G: *Der Ingenieurbau: Werkstoffe.* Volume 202. Ernst & Sohn, Berlin, 1996

[Mehlhorn 1999]   MEHLHORN, G: *Der Ingenieurbau: Mathematik.* Ernst & Sohn, Berlin, 1999

[Messmer 2020]   MESSMER, Thea: *Modellierung von Randbedingungen mit zweidimensionalen peridynamischen Finiten Elementen,* Technical University of Munich, Master thesis, 2020

[Meyberg and Vachenauer 1999]   MEYBERG, Kurt ; VACHENAUER, Peter: *Höhere Mathematik 2: Differentialgleichungen · Funktionentheorie Fourier-Analysis · Variationsrechnung.* Springer, 1999

[Meyberg and Vachenauer 2013]   MEYBERG, Kurt ; VACHENAUER, Peter: *Höhere Mathematik 1: Differential-und Integralrechnung Vektor-und Matrizenrechnung.* Springer-Verlag, 2013

[Meyer-Spasche et al 2012]   MEYER-SPASCHE, R ; BAUER, C ; DALL'ACQUA, A: Introduction to Functional Analysis for Engineers. (2012). – Max-Planck-Institut für Plasmaphysik

[Moler 2013]   MOLER, Cleve: *Complex Step Derivative.* 2013. – URL `https://blogs.mathworks.com/cleve/2013/10/14/complex-step-differentiation/`. – blogs.mathworks.com, retrieved on [21.05.2021]

[Mousavi and Sukumar 2010]   MOUSAVI, SE ; SUKUMAR, N: Generalized Duffy transformation for integrating vertex singularities. In: *Computational Mechanics* 45 (2010), Nr. 2-3, p. 127

[Müller 2018]   MÜLLER, Gerhard: Continuum Mechanics and Tensor Analysis. (2018). – Technische Universität München, Lehrstuhl für Baumechanik

[Nolting 2006]   NOLTING, Wolfgang: *Grundkurs Theoretische Physik 2.* Springer, 2006

[Parisch 2003]   PARISCH, Horst: Festkörper-Kontinuumsmechanik. In: *BG Teubner* 144 (2003)

[Peterson et al 2018]   PETERSON, Kara J. ; BOCHEV, Pavel B. ; KUBERRY, Paul A.: Explicit Partitioned Methods for Interface Coupling. / Sandia National Lab.(SNL-NM), Albuquerque, NM (United States). 2018. – Research Report

[Rade and Westergren 2013]   RADE, Lennart ; WESTERGREN, Bertil: *Springers mathematische Formeln: Taschenbuch für Ingenieure, Naturwissenschaftler, Informatiker, Wirtschaftswissenschaftler.* Springer-Verlag, 2013

[Silling 2000]   SILLING, Stewart A.: Reformulation of elasticity theory for discontinuities and long-range forces. In: *Journal of the Mechanics and Physics of Solids* 48 (2000), Nr. 1, p. 175–209

[Silling and Askari 2005]   SILLING, Stewart A. ; ASKARI, Ebrahim: A meshfree method based on the peridynamic model of solid mechanics. In: *Computers & structures* 83 (2005), Nr. 17-18, p. 1526–1535

[Silling et al 2007]   SILLING, Stewart A. ; EPTON, M ; WECKNER, O ; XU, Ji ; ASKARI, E23481501120: Peridynamic states and constitutive modeling. In: *Journal of Elasticity* 88 (2007), Nr. 2, p. 151–184

[Simeon 2009]   SIMEON, Bernd: *Numerische Mathematik Skriptum zur Vorlesung im Sommersemester 2009 TU München, Zentrum Mathematik.* 2009

[Steeb 2021]   STEEB, Holger: *Finite-Elemente-Methode.* 2021. – URL https://www.mib.uni-stuttgart.de/ls2/100-online/HMIB/kap8/kap8.html. – Universität Stuttgart, Institut für Mechanik, retrieved on [21.05.2021]

[Takahasi and Mori 1974]   TAKAHASI, Hidetosi ; MORI, Masatake: Double exponential formulas for numerical integration. In: *Publications of the Research Institute for Mathematical Sciences* 9 (1974), Nr. 3, p. 721–741

[Trageser and Seleson 2020]   TRAGESER, Jeremy ; SELESON, Pablo: Bond-based peridynamics: A tale of two Poisson's ratios. In: *Journal of Peridynamics and Nonlocal Modeling* 2 (2020), Nr. 3, p. 278–288

[Vanherck et al 2020]   VANHERCK, Joren ; SORÉE, Bart ; MAGNUS, Wim: Tanh-sinh quadrature for single and multiple integration using floating-point arithmetic. In: *arXiv preprint arXiv:2007.15057* (2020)

[Wang and Tian 2012]   WANG, Hong ; TIAN, Hao: A fast Galerkin method with efficient matrix assembly and storage for a peridynamic model. In: *Journal of Computational Physics* 231 (2012), Nr. 23, p. 7730–7738

[Werner 2006]   WERNER, Dirk: *Funktionalanalysis.* Springer, 2006

[Ye 2006]   YE, Lingyun: *Numerical quadrature: theory and computation*, Dalhousie University, Ph.D. thesis, 2006

[Ye]   YE, Wenjing: *4 Node Rectangular Element for Plane Stress Analysis.* – URL https://slideplayer.com/slide/5716165/19/images/15/4-NodeRectangularElementforPlaneStressAnalysis.jpg. – Department of Mechanical Engineering, Hong Kong University of Science and Technology, MECH593 Introduction to Finite Element Methods, retrieved on [21.05.2021]

[Zhan and Liu 2015]   ZHAN, Chun-xiao ; LIU, Yi-hua: Plane elasticity solutions for beams with fixed ends. In: *Journal of Zhejiang University-SCIENCE A* 16 (2015), Nr. 10, p. 805–819